BRNO UNIVERSITY OF TECHNOLOGY

Central European Institute of Technology BUT

DOCTORAL THESIS

Brno, 2024

M.Tech. Jyoti Jyoti

This page is left intentionally

BRNO UNIVERSITY OF TECHNOLOGY

VYSOKÉ UČENÍ TECHNICKÉ V BRNĚ

CENTRAL EUROPEAN INSTITUTE OF TECHNOLOGY BUT

STŘEDOEVROPSKÝ TECHNOLOGICKÝ INSTITUT VUT

NOVEL MATERIALS FOR SENSING AND BIOSENSING

NOVÉ MATERIÁLY PRO SNÍMÁNÍ A BIOSENZOVÁNÍ

DOCTORAL THESIS
DIZERTAČNÍ PRÁCE

AUTHOR — M.Tech. Jyoti Jyoti
AUTOR PRÁCE

SUPERVISOR — prof. RNDr. Martin Pumera, Ph.D.
ŠKOLITEL

BRNO 2024

This page is left intentionally

Abstract

The 2D material-based 3D-printed electrodes and nano/micromotors have emerged as the cutting-edge technologies. It has drawn widespread attention due to their distinctive characteristics that make them suitable for sensing and biosensing applications. The research offers valuable insights through systematic experimentation to promote advancements in sensing technologies. The 3D-printed nanocarbon electrodes have eliminated the need for the conventional electrodes by providing the benefits such as ease of fabrication, quick production, excellent precision and customization of the shapes depending upon our requirements. Consequently, the findings of this thesis highlight the versatility of 3D-printed nanocarbon electrodes in applications involving phenols, pesticides and biosensing, particularly DNA sensing. Next, we explored the active quantum materials-based micromotors for DNA detection as well the food safety applications. This next-generation technology combines the appealing features of the quantum materials along with their autonomous mobility as micromotors, which makes the detection fast and offers inexpensive platforms for sensing and bio-analysis.

Thus, by addressing challenges related to analyte use, particularly those with rapid action and toxicity, the study explores advanced detection methods, incorporating modern technologies to offer innovative solutions. The findings contribute to the ongoing evolution of technologies crucial for addressing contemporary challenges in analytical chemistry and bioanalytical chemistry.

Abstrakt

Materiály na bázi 2D použité ve 3D tištěných elektrodách a nano/mikromotorech se staly špičkovými technologiemi. Získaly širokou pozornost díky svým výjimečným charakteristikám, které je předurčují pro použití v senzorových a biosenzorových aplikacích. Výzkum nabízí cenné vhledy prostřednictvím systematického výzkumu za účelem podpory pokroku v senzorových technologiích. 3D tištěné elektrody z nanouhlíku eliminují potřebu konvenčních elektrod tím, že poskytují výhody jako snadnou výrobu, rychlou produkci, vynikající přesnost a přizpůsobení tvarů v závislosti na našich požadavcích. V důsledku toho zjištění této práce zdůrazňují univerzálnost 3D tištěných elektrod z nanouhlíku v aplikacích, které zahrnují fenoly, pesticidy a biosensing, zejména detekci DNA. Dále jsme zkoumali aktivní kvantové materiály na bázi mikromotorů pro detekci DNA, stejně jako aplikace pro bezpečnost potravin. Tato technologie příští generace kombinuje atraktivní vlastnosti kvantových materiálů spolu s jejich autonomní pohyblivostí jako mikromotory, což detekci urychluje a nabízí cenově dostupné platformy pro senzoriku a bioanalýzu. Řešením výzev souvisejících s využitím analytu, zejména těch s rychlou akcí a toxicitou, práce zkoumá pokročilé metody detekce, které zahrnují moderní technologie nabízející inovativní řešení. Zjištění přispívají k probíhající evoluci technologií nezbytných pro řešení současných výzev v analytické chemii a bioanalytické chemii.

This page is left intentionally

Keywords

3D-printed electrodes, additive manufacturing, Fused deposition modelling, DNA sensing, active quantum micromotors, FRET phenomena, SEM, EDS, XPS, Fluorescence Spectroscopy, *Salmonella typhimurium*

Klíčová slova

3D tištěné elektrody, aditivní výroba, fúzní depoziční modelování, snímání DNA, aktivní kvantové mikromotory, FRET jevy, SEM, EDS, XPS, fluorescenční spektroskopie, *Salmonella typhimurium*

This page is left intentionally

Declaration

I hereby declare that I have written this work, entitled “Novel Materials for Sensing and Biosensing”, under the guidance of my thesis supervisor, Prof. RNDr. Martin Pumera, Ph.D., and relying on technical literature and other sources of information, which are all properly cited and outlined in the references.

Jyoti

This page is left intentionally

Acknowledgements

Dear God, I offer this Ph.D. thesis not just as my achievement but as a tribute to the countless blessings you showered upon me. Thank you to the tough times that made me stronger, the wise people who showed me the way, and the loving people who always had my back. Thank you for providing me the strength to fulfill my late father's dream. I couldn't have done it without all of you.

First and foremost, I would like to thank my Ph.D. supervisor, Prof. RNDr. Martin Pumera. From the beginning of planning my research to handing in my thesis, his constant help and great advice really made a big difference in my academic journey. His immense knowledge, motivation and patience have given me more power and spirit to excel in research writing. Our biweekly meetings were invaluable for my academic progress, providing essential checkpoints and continuous encouragement. They played a pivotal role in keeping me on track and motivated throughout the journey. I'm truly thankful for his significant contributions to my development. His professional mentorship not only enriched my understanding but also opened doors for collaborative learning with other research groups, which has broadened my academic experience.

I am deeply thankful for the collaborative efforts and guidance provided by Assoc. Prof. RNDr. Miroslav Fojta, Ph.D., and Hana Pinkova from the Institute of Biophysics. Their invaluable contribution not only facilitated our work in biosensing but also opened new horizons for exploration. Additionally, this collaboration has not only been instrumental in advancing biosensing techniques but has also provided me with a solid foundation to pioneer my journey in this field.

Next, I extend my heartfelt gratitude to Prof. Alberto Escarpa and Dr. Beatriz Jurado-Sánchez for their exceptional support and mentorship during my internship. Their generosity in providing access to research facilities and the laboratory significantly enriched my learning experience. Being part of their team was a valuable opportunity that enhanced my understanding and skills in the field of micromotors for food safety. Without their unwavering support, conducting this research would not have been possible. I sincerely appreciate their guidance, and they hold a special place in my academic journey.

I express my profound gratitude to Dr. Edurne Redondo, my first mentor in the Ph.D. journey. She not only introduced me to the intricacies of 3D-printing but also guided me through every step, such as correcting my initial project proposal and helping shape my manuscripts. She patiently imparted her knowledge and wisdom. Her mentorship and support have been invaluable, and she holds a very special place in my heart. Expressing my gratitude for his tremendous patience and kindness is beyond words.

I extend my sincere gratitude to Dr. Jose Munoz for his invaluable mentorship and for introducing me to cutting-edge technology, specifically micromotors. His expertise, valuable insights, and spontaneous ideas during our discussions significantly shaped my projects. Working together has enhanced my research. I feel fortunate to have had such a dedicated and inspiring mentor by my side.

I am grateful for the friendly and inspiring atmosphere in the Future Energy Group, which significantly contributed to my learning experience. Despite our diverse backgrounds, the strong connections we formed through lab work and the overall friendly environment make it the best place to work. My sincere thanks to all the group members I came across. I am grateful to Katka Pala for her exceptional organizational skills and support. Nothing would have been possible without her in the lab.

I express my heartfelt appreciation to all the individuals mentioned above for their engaging daily discussions and collaborative work in the lab, which made the research journey more stimulating and enriching. Additionally, I acknowledge the financial support provided by the CzechNanoLab research infrastructure supported by LM2018110 MEYS CR, for facilitating the measurements and sample fabrication at CEITEC Nano Research Infrastructure.

Last but certainly not least, my heartfelt gratitude goes to my uncle (Mr. Shagan Singh) and aunt (Mrs. Manjeet Kaur), who have been the pillars of support throughout my life's journey. Their guidance and education have paved the way for me to pursue and achieve my dreams. I am deeply indebted to them for their unwavering encouragement and belief in my potential. They have always supported me financially so that I only pay attention to my studies and achieve my objective without any obstacles on the way. Next, I am grateful for my mother (Mrs. Satwinder Kaur), grandparents, siblings, brother- in-laws, sister-in-law, nieces, nephew and friends who remembered me in their prayers for the ultimate success. I owe a great deal of my success to them. I am also grateful to my altruistic friend Nishant, who has been a guiding light throughout the entire journey of my Ph.D. I consider myself nothing without them. They gave me enough moral support, encouragement, and motivation to accomplish my personal goals. Lastly, I express my gratitude to N. Senthilnathan for dedicating valuable time to review and correct my thesis.

Jyoti

Table of Contents

Summary of the Thesis

In the rapidly advancing field of sensing and biosensing applications, the quest for innovative materials has become paramount. This thesis explores the integration of 2D materials, specifically 3D-printed carbon electrodes for chemical sensing and biosensing applications. Furthermore, Graphene quantum dots based nano/micro motors have been employed as highly effective biosensors.

2D materials represent a unique class of nanomaterials with broad implications across various fields of research. It consists of ultra-thin structures with one or a few atoms of thickness, which has caught attention and found diverse applications. These structures exhibit improved electronic, optical, chemical, and physical properties linked to key characteristics like phase, crystallinity, exfoliation, stability, and size. These properties, influenced by the synthesis method, have significantly enhanced the performance of sensing and biosensing systems in both electrochemical and optical transduction modes. Additionally, they are promising candidates for biomedical applications, notably in areas of drug delivery and drug potentiation as well as photothermal and photodynamic therapies. The high surface area to volume ratio of these materials has also inspired research in developing nanocomposite scaffolds with enhanced mechanical and biological properties. 2D nanomaterials such as graphene and its derivatives have long been of interest to researchers in this area.

Besides graphene, emerging materials like graphene quantum dots materials have drawn a lot of attention for various sensing applications. Quantum dots are semiconductor nanocrystals with diameters ranging from 1 to 10 nanometres. They exhibit distinctive electronic characteristics, falling between the properties of bulk semiconductor materials and discrete molecules. This is largely attributed to the high ratio of surface area to volume in these particles. Quantum dots exhibit unique properties that make them promising candidates for diverse applications and devices, including solar cells, fluorescent probes, optical switches, light sources, etc. Owing to their distinct electronic properties and adjustable emission spectra, quantum dots have become a subject of substantial interest. Their small size makes them suitable for various medical applications, including imaging and biosensors. Hence, the application of 2D materials and quantum Dots for sensing and biosensing holds great promise in propelling the advancement of sensing technologies. This innovative approach opens

avenues for more sensitive and efficient detection methods, marking a significant footstep in the evolution of biosensing applications.

List of Publications

First author articles

1. **Jyoti**, Jose Muñoz, and Martin Pumera*. Quantum Material-Based Self-Propelled Microrobots for the Optical "On-the-Fly" Monitoring of DNA. **ACS Applied Material Interfaces** 2023, 15, 58548

2. **Jyoti**, Miroslav Fojta, Monika Hermanova, Hana Pivonkova, Osamah Alduhaish, Martin Pumera*. Genosensing on a 3D-printed nanocarbon electrode. **Electrochemistry Communications** 2023, 151, 107508

3. **Jyoti**, Edurne Redondo, Osamah Alduhaish, Martin Pumera*. 3D-printed Electrochemical Sensor for Organophosphate Nerve Agents. **Electroanalysis** 2023, 35, 139

4. **Jyoti**, Edurne Redondo, Osamah Alduhaish, Martin Pumera*. 3D-printed nanocarbon sensors for the detection of chlorophenols and nitrophenols: Towards environmental applications of additive manufacturing. **Electrochemistry Communications** 2021, 125, 106984

5. **Jyoti**, Alberto-Rodríguez Castillo, Beatriz Jurado-Sánchez, Martin Pumera*, Alberto Escarpa. Active Quantum Materials for Food Safety: Salmonella Identification by Dynamic Active Microrobots. **Manuscript under Revision**

Co-author articles

6. Lujun Wang, Siowwoon Ng, **Jyoti**, and Martin Pumera*. Al_2O_3/Covalent Organic Framework on 3D-Printed Nanocarbon Electrodes for Enhanced Biomarker Detection. **ACS Applied Nano Materials** 2022, 5, 9719

This page is left intentionally

Organization of the Thesis

This thesis is a paper-based thesis. The entire dissertation comprises seven chapters. On the basis of this, it is broadly divided into two main parts. In the first part, we explore the significance of 3D-printed electrodes for sensing and biosensing applications, while the second part focuses on the importance of nano/micromotors for biosensing applications.

Starting with **Chapter 1**, we laid out the goals and motivations behind the thesis. **Chapter 2** introduces 3D-printed technology and its challenges. Taking a step further, the next section will introduce micro/nano motors and their applications in biosensing. Moving on to **Chapter 3**, we dig into the background and literature review of 3D-printed technology and micro/nanomotors in sensing and biosensing applications.

Hence, **Part I** of the thesis, spanning from Chapters 4.1 to 4.3, is dedicated to the exploration of 3D-printed nanocarbon sensors. **Chapter 4.1** discusses the importance of these sensors for detecting chlorophenols and nitrophenols. In **Chapter 4.2**, we extend this exploration to 3D-printed electrochemical sensors designed for detecting organophosphate nerve agents. **Chapter 4.3** focuses on Geno-sensing using a 3D-printed nanocarbon electrode to showcase the feasibility of 3D-printed electrodes in biosensing.

Part II comprises Chapters 5.1 and 5.2, which shift the focus to nano/micromotors. **Chapter 5.1** explores self-propelled microrobots based on quantum materials for optical 'on-the-fly' monitoring of DNA. **Chapter 5.2** highlights the utilization of active quantum materials for ensuring food safety, specifically in identifying Salmonella using Dynamic Active Microrobots.

The thesis concludes with **Chapter 6**, summarizing the key findings and insights, followed by **Chapter 7**, which contains the appendix of the thesis.

Chapter 1

Objective of the Thesis

The primary objective of this thesis is to investigate and assess the potential of novel materials, explicitly focusing on 2D material-based 3D-printed electrodes and nano/micromotors in the domain of chemical sensing and biosensing applications. Our aim is to contribute valuable insights through systematic experimentation and analysis, fostering enhanced performance and advancements in chemical and biosensor technologies. This research endeavours to address the challenges posed by the extensive use of analytes in various industries, particularly those with rapid action and toxicity. By exploring advanced detection methods and the integration of modern technologies like 3D-printed technology and nano/micromotors, the goal is to offer innovative solutions that enhance sensitivity, precision, and diagnostic capabilities in environmental and medical applications.

The rapid spread of toxic substances such as organophosphates and phenolic compounds across various industries, including chemical, cosmetic, and agricultural, presents a grave danger to our planet [1,2]. Notably, the extensive use of pesticides and organophosphates in farming helps the farmers to safeguard the crops. Unfortunately, these substances have now accumulated in our environment, posing a severe threat not only to nature but also to our well-being. The consequences of this contamination, ranging from cancer and chronic obstructive pulmonary disease to congenital disabilities and infertility, have sparked widespread concern among the public [3,4].

To address these issues, various detection techniques exist, ranging from traditional methods like gas chromatography and high-performance liquid chromatography, involving a preparation step before analysis, to more advanced methods such as sensors-electrochemical, optical, piezoelectric, and molecular imprinted polymer [5,6].

Through systematic experimentation and analysis, the aim is to contribute valuable insights into the utilization of novel materials, paving the way for enhanced performance and advancements in chemical and biosensor technologies. The applications of modern technologies, such as 3D-printed technology and nano/micromotors, in sensing and biosensing applications are driven by the compelling need for high performance, sensitivity, and precision in diagnostic and analytical processes [7]. Hence, this thesis highlights the potential of novel materials, specifically 2D material-based 3D-printed electrodes and nano/micromotors, in the field of chemical sensing and biosensing applications.

Part I: 3D printed Electrodes for Sensing and Biosensing Applications

Recently, 2D materials have gained significant attention due to their extraordinary properties, with notable examples like graphene, transition-metal dichalcogenides (e.g., MoS_2), and two-dimensional inorganic compounds (MXenes). Simultaneously, the widespread availability and affordability of 3D printers, combined with user-friendly design software, have revolutionized 3D-printing into a globally accessible and cost-effective fabrication tool. The integration of 3D-printing with 2D materials has resulted in the creation of new composites, offering a promising platform for the next generation of technologies. This technique allows the manufacturing of complex and functional structures in customized shapes (such as curves, spheres, etc.) through a highly automated system with minimal human intervention [8–10]. 3D-printing with 2D materials offers the benefits of flexible design by retaining the unique qualities of the 2D material. Exploring the use of 2D materials in 3D-printing is an area with a lot of untapped potential. 2D nanomaterials enhance sensor sensitivity, which is crucial for detecting low concentrations in medical and environmental applications. Their use enables miniaturized and portable sensing devices, which are ideal for on-site applications like point-of-care diagnostics and environmental monitoring.

3D-printed devices can offer a series of benefits, such as i) simple manufacturing process; ii) rapid production (scalability) reducing the generation of waste; iii) high accuracy, repeatability and resolution; iv) customization of shape and geometries (freeform production); v) few human interventions once the prototype is designed and uploaded to the system; vi) availability of a wide range of materials to be processed, making possible to provide multifunctional attributes; and vii) high durability without losing efficiency and sensitivity (robustness)[11]. Such

advantages have motivated us to opt for 3D-printed carbon electrodes for electrochemical approaches. This integration of the 3D-printed techniques with 2D nanomaterials offers a versatile platform for creating highly specific biosensors tailored for various targets, such as DNA patterns, proteins, or germs. Therefore, this part of the thesis specifically highlights the recent progress in 3D-printing of the 2D materials family primarily carbon and implementing it for sensing and biosensing applications [12].

Part II: Nano/micromotors for Biosensing Applications

Inspired by nature, scientists are developing tiny machines, micro/nanomotors, that convert energy into motion. The motion of synthetic micro/nanomotors can be either chemically self-propelled or propelled by various external energy, including magnetic or electrical fields, light, or ultrasound [13,14].

The self-propelled behaviour of the nano/micromotors has opened the door for developing new motion-based detection platformsleads to improve mass transport and accelerates reaction kinetics, making biosensing processes faster and more efficient. The incorporation of micromotors in biosensing applications contributes to the development of autonomous biosensing devices. These devices can navigate complex environments, ensuring comprehensive and thorough sampling, especially in challenging biological or environmental conditions [15–17].

The micro/nanomachines show promising potential in a wide range of fields, including chemo/bioanalysis [18,19], environment [20,21] , cargo delivery [22–24], biomedicine [25,26] and defence [27] due to their semi-intelligent and versatile operations. Micro/nanomachines, with their unique structures and motion modes, can perform various applications like transport, release, adsorption, and binding. This innovative use of micro/nanomachines is revolutionizing modern analytical chemistry, introducing motion-based sensing techniques that enable quick analysis and enhanced assay sensitivity [28].

The evolution of advanced fabrication schemes employed in crafting these nanomachines introduces novel functionalities and capabilities. These recent advancements have expanded the field of sensing possibilities and bioanalytical applications. These involve not only new sensing applications in previously inaccessible microscale environments but primarily focus on new sensing approaches based on motor movement. Therefore, these self-propelled

nanomotors hold significant promise in pioneering novel sensing and biosensing protocols, particularly those involving ‘on-the-fly’ recognition events [29].

Chapter 2

Introduction

2.1 2D materials towards 3D-printing

2.2 Nano/micromotors towards sensing

2.3 State of the Art

2.4 Material Characterization

2.1 2D materials towards 3D-printing

2D Nanomaterials

Ultrathin two-dimensional (2D) nanomaterials are a new class of nanomaterials with sheet-like structures and transverse dimensions larger than 100 nm, while the thickness is typically less than 5 nm [30]. Due to their unique shapes, 2D nanomaterials possess large surface and anisotropic physical/chemical properties [31].

The quest for 2D materials began with the discovery of graphene in 2004 [32]. Since that time, several additional members have joined this extensive group of nanomaterials, including TMDs, MXenes, BP, and h-BN, as explained below [33–40]. These thin layers can be obtained through different methods, depending on the approach you choose [41–44]. The inherent qualities of 2D materials showcase significant potential for incorporating them into printed composites. This is because of their atomic thickness, mechanical flexibility, transparency, and electrical conductivity. **Figure 1** provides a general illustration of these materials.

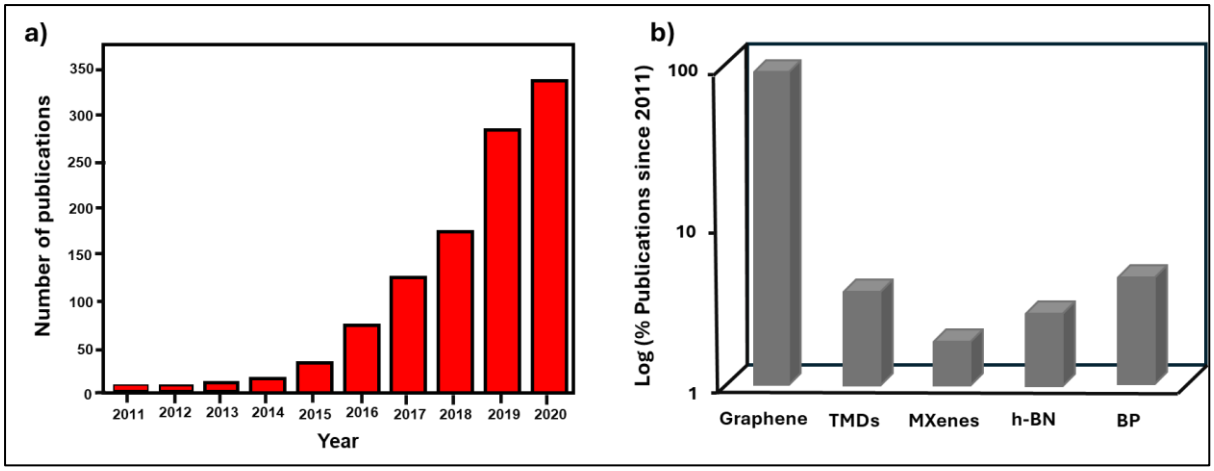

Figure 1. Statistics bibliography research by Web of Science: (a) Number of publications per year under the topics of 3D-printing combined with 2D materials, Graphene, MXenes, TMDCs, MoS_2, Black phosphorous and Boron nitride and (b) Relative percentage of publications since 2010 per 2D materials in the 3D field [12].

Graphene is the most known allotrope of carbon. It consists of a single atomic layer of sp^2 hybridized carbon atoms in a honeycomb 2D structure. The properties of graphene are extraordinary, such as its mechanical strength, good flexibility, high thermal conductivity, high carrier density, and optical transparency [45–49]. Moreover, numerous studies have demonstrated graphene's capability to introduce various functional groups onto its surface through functionalization. This valuable characteristic allows the material to be tailored for specific applications and enhances cohesion when used in the development of new-generation composites [50,51]. Graphene also possesses distinctive biochemical properties, including antibacterial characteristics and high resistance to a wide range of chemicals, such as strong acids or bases, reductants, and oxidants [52,53]. The primary industrial technique for the rapid and cost-effective production of this material involves obtaining it from graphite through liquid phase exfoliation (LPE). This process enables the layering of the graphite flakes, resulting in a material with only a few layers [54]. Alternative approaches involving partial modification of the material's chemical composition include oxidative intercalation (yields Graphene Oxide, GO) and subsequent partial structural restoration through chemical reduction (results reduced Graphene Oxide, rGO). This results in a material that is easy to handle and dispersible in water [55–58] and commonly used in bio-applications.

3D-printing: Additive Manufacturing

3D-printing is a revolutionary technology that uses a geometric blueprint to construct physical objects by adding material layer by layer [59]. This game-changing process has achieved remarkable advancements since the first commercialization of 3D printing in 1980 by Charles Hull [60]. Today, 3D-printing finds itself employed in a wide range of diverse sectors, from crafting artificial heart pumps and unique jewellery pieces [61] to producing cutting-edge products like 3D-printed corneas, PGA rocket engines [62], a steel bridge in Amsterdam [63], and even items in the aviation and food industries [64].

3D-printing, also known as additive manufacturing, is a recent technology that consists of a layer-by-a-layer deposition process guided by computer-aided design (CAD) software. [11] This novel technique has many advantages in comparison with traditional electrode manufacturing techniques, which include the rapid production of devices with low waste generation, high accuracy, repeatability, high resolution, and high durability. Furthermore, it offers the possibility of customization of the shape and geometry of the produced objects through a highly automated system with the least human intervention.[8,65] Among conventional materials such as carbon materials (graphene [66–68], carbon nanotubes [69–71], mesoporous carbon [72,73], etc.) have been extensively exploited for chemical sensing and biosensing in the past, can be printed now by using the 3D printed technology as shown in **Figure 2** with minimal waste.

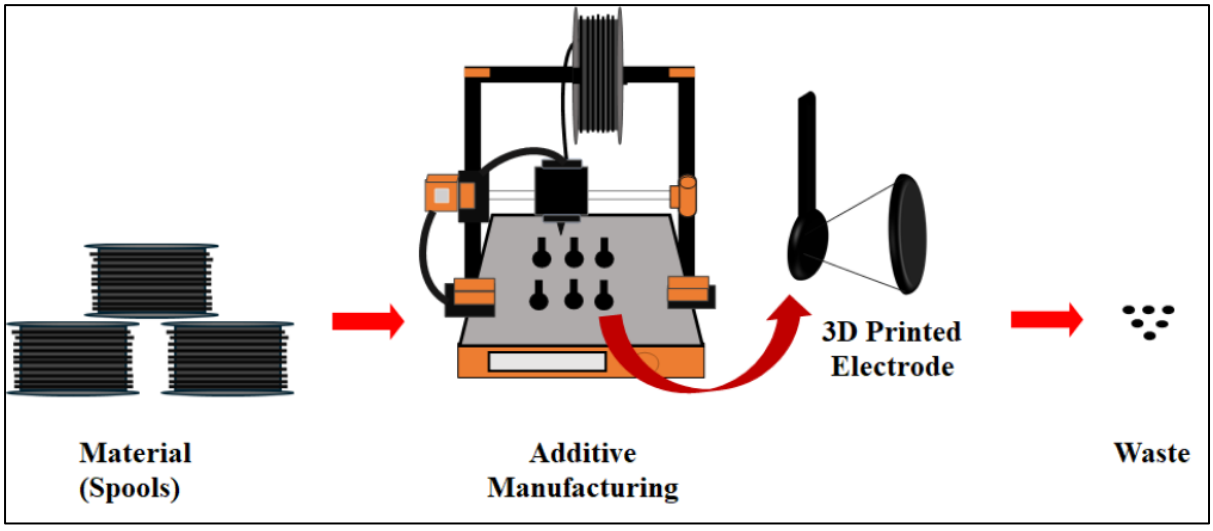

Figure 2. Depicting the additive manufacturing technology with minimum waste.

There are various kinds of 3D-printing techniques available, each with its unique advantages. These methods can be broadly categorized into seven groups: binding jetting, directed energy

deposition, material extrusion, material jetting, powder bed fusion, sheet lamination, and vat photopolymerization. There are no debates about which machine or technology functions better because each of them has its own targeted applications. Nowadays, 3D-printing technologies are no longer limited to prototyping usage but are increasingly also being used to make a variety of products [74]. However, in this context, we are addressing material extrusion-based 3D-printing technology, which operates on the fundamental principle of Fused Deposition Modeling (FDM).

Fused Deposition Modeling (FDM): In the early 1990s, an innovative material extrusion system emerged for the 3D-printing is known as FDM. This groundbreaking method utilizes a polymer as its primary material [75] and operates by heating and extruding thermoplastic filament to form objects layer by layer, from the bottom to the top. The process of FDM involves heating the thermoplastic inside the extruder until it becomes semi-liquid, which is then carefully layered along the extrusion path [76]. In cases where additional support is necessary, a removable material is deposited by the 3D printer to act as a scaffold.

Materials Used for 3D-Printing Technology in the Manufacturing Industry

In order to produce high-quality devices, 3D-printing requires high-quality materials that meet precise standards. The ability to fabricate key elements using a wide range of materials, including ceramic, metallic, polymers, and their combinations in the form of hybrid, composites or functionally graded materials (FGMs) [77]. But here, we are mainly focussed on the polymers and the metals as follows:

Polymers

The implementation of 3D-printing technologies has revolutionized the production of polymer components, ranging from prototypes to complex structures with intricate geometries [78]. By FDM, one can quickly fabricate 3D-printed objects by depositing layers of extruded thermoplastic filament, such as polylactic acid (PLA), acrylonitrile butadiene styrene (ABS), polypropylene (PP) or polyethylene (PE) [78]. The versatility of 3D-printing with polymers, whether in a liquid state or with a low melting point, has made it a widely used technique in the industry due to its economic efficiency, lightweight nature, and adaptable processing

methods [79]. In the field of biomaterials and medical device production, polymer materials play a significant role as inert substances, aiding in the successful functioning of devices while also providing essential support [80].

Metals

3D-printing with metal materials has gained significant attention in a variety of industries, including aerospace, automobile, medical, and manufacturing [81] due to its advantages. Aluminium alloys, cobalt-based alloys, nickel-based alloys, stainless steels, and titanium alloys are among the metals that are commonly used in 3D-printing due to their exceptional physical properties [80,82–86]. These materials have a broad range of applications, from printing human organs to creating aerospace parts, thanks to their outstanding physical properties. For example, cobalt-based alloys are particularly well-suited for 3D-printing in dental applications because of their high specific stiffness, resilience, recovery capacity, elongation, and heat-treated conditions [80]. Nickel-based alloys, often used in 3D-printing for aerospace parts, offer exceptional corrosion resistance and can withstand temperatures of up to 1200 °C, making them ideal for challenging environments. Additionally, 3D-printing with titanium alloys is advantageous for applications in aerospace components and the biomedical industry, thanks to their unique properties such as elasticity, corrosion resistance, oxidation resistance, and low density [85,86].

Advances on 2D Materials towards 3D-printing

In recent years, the exceptional properties of 2D materials have led to their widespread use in various industries. Pioneering examples, such as graphene and transition-metal dichalcogenides (TMDs) like MoS_2, along with other 2D inorganic compounds like MXenes, h-BN, and BP, have paved the way for their applications. Furthermore, with the availability of inexpensive 3D-printers and design software, 3D-printing has become a popular and accessible means of fabrication worldwide. Harnessing this technology to create new composites utilizing 2D materials offers a promising platform for advancing into the next generation of technology.

2.2 Nano/micromotors towards sensing

Micromotors have witnessed remarkable potential in the scientific field, which can efficiently convert different types of energy into independent movement [87–90]. With their unique ability,

these emerging microdevices have gained widespread usage in a variety of fields, such as drug delivery, analytical sensing, and tissue regeneration [91–98]. In particular, their autonomous behaviour makes them highly suitable for sensing tasks, even in tiny sample volumes [99–104]. Moreover, the dynamic movement of micromotors allows for efficient mixing of sample solutions, reducing analysis time and simplifying sample treatment [105]. Given its immense benefits, there has been extensive research on optimizing micromotors for sensing applications [106–108]. **Figure 3** illustrates the general process of the micromotors. On the basis of the propulsion mechanisms, micromotors are divided into two broad categories: fuel-based mechanisms and fuel-free mechanisms.

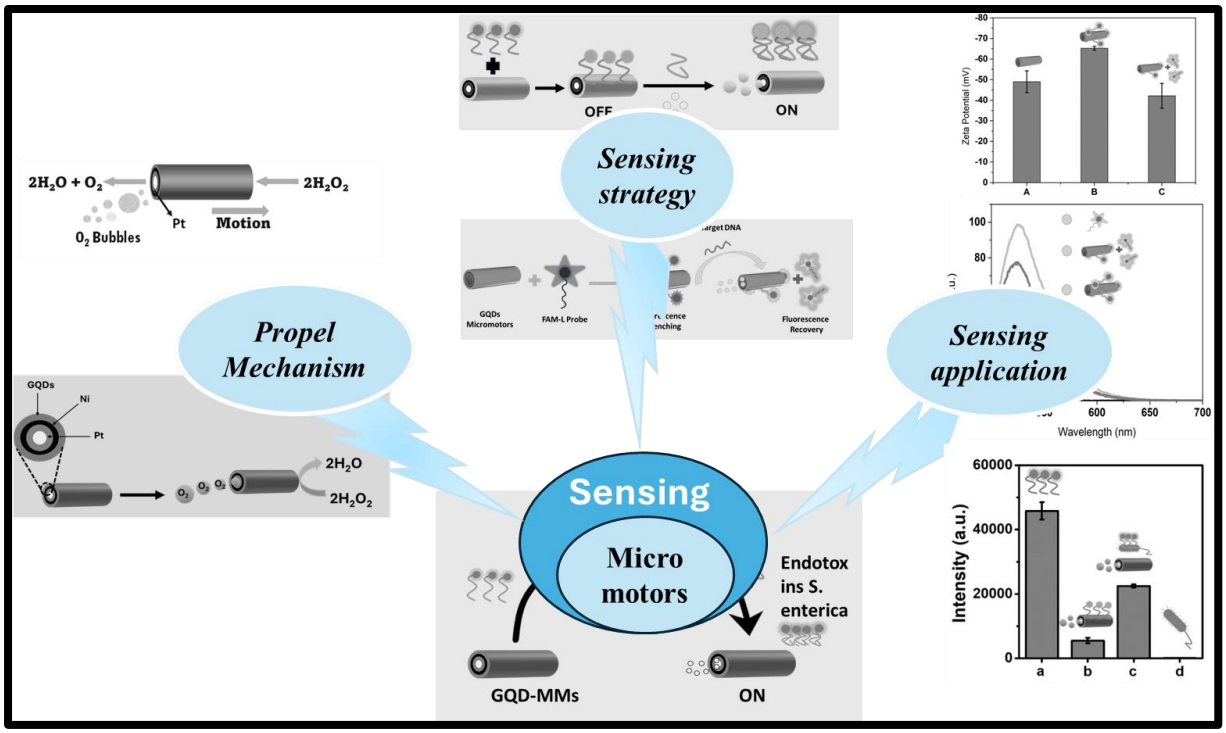

Figure 3. The scheme that describes the general flow and information about micro motors

Fuel-Based Mechanism

Bubble-Propelled Micromotors

Bubble-propelled micromotors fall under the category of self-diffusiophoresis. Self-diffusiophoresis is a phenomenon in which the motion of motile particles is driven by the gradient of their surface potential. In the case of bubble-propelled micromotors, the surface potential of the micromotor is created by the catalytic decomposition of a chemical fuel. The autonomous locomotion of bubble-driven micromotors primarily relies on the recoil force

resulting from bubble generation. This propulsion is achieved when the bubbles grow and collapse on the surface, and the impulse generated by the bubbles detaches from the surface of the micromotor [109,110].

Bubble-driven micromotors commonly utilize H_2O_2 solution as the primary medium fuel in their systems. The catalytic decomposition of H_2O_2 into O_2 and H_2O, facilitated by the innermost layer (Pt or Au) in bubble-driven micromotors, generates an excess of O_2 bubbles. These bubbles contribute to the recoil force that propels the micromotors.

The motions of these microdevices are categorized into three broad categories. The first type is linear or quasi-linear, where the microdevices follow a curved path with a significantly larger radius compared to their length. Circular motion, on the other hand, involves the micromotor moving in a circular path with a diameter similar in magnitude to its length. The third type is screw-like, where the micromotor's movement can be described as a combination of small circular motions around a central axis and a self-propelled tip moving parallel to the circular plane, resulting in a conical or screw-like pattern. These motion patterns are commonly observed and attributed to the unique shapes of micromotor tubes [111]. Notably, the velocity of these micromotors is influenced by factors such as the bubble radius and the frequency of bubble generation, both of which are dependent on the concentration of the fuel. The motion patterns can also be described by using the Reynolds number [111].

Fuel-free Mechanism

Fuel-free micromotors are dependent on external stimuli like magnetic, light, or ultrasonic and electric fields to move forward. This unique propulsion method brings various advantages, such as the ability to control remotely, durability, and compatibility with biological systems, making them highly promising for a wide range of uses. The integration of magnetic components into these micromotors is vital in achieving directional control, providing immense potential for numerous fields. Specifically, magnetic fields have been widely utilized for remote control and serve as a reliable power source for driving these tiny motors forward.[112]

Ultrasonic waves can also be used to propel micromotors, harnessing the difference in pressure caused by two intersecting waves. This technique shows great potential. In addition, electric fields can be utilized to generate fuel-free motion [113–115]. By leveraging the electroosmotic properties in low-frequency electric fields, micromotors can be propelled. Similarly, high-frequency electric fields can drive rotary micromotors by interacting with electrically polarized nano-entities; however, while these methods offer benefits like strong propulsion and minimal

medium requirements, their complex manufacturing processes and reliance on high-energy external fields present challenges.

Sensing Strategy

Fluorescence-based sensing strategy

The widely used fluorescence-based strategy in traditional sensing has been integrated with the micromotor platform for novel sensing approaches. Fluorescence is the light emitted by the fluorophore when it absorbs light or other electromagnetic radiation and offers easy readout by the naked eye. Combining this fluorescence-based sensing strategy with micromotors enhances sensitivity, providing a powerful sensing platform. The integration allows for highly sensitive detection of small-volume raw samples in a short time, ensuring easy operation, remarkable selectivity, and high accuracy. The fluorescence-based micromotor sensing strategy can be categorized into different transition patterns of the fluorescence signal, including ‘off–on’ and ‘on–off’ detection strategies. In the ‘off–on’ strategy, the fluorescence signal changes from ‘off’ in the absence of targets to ‘on’ in their presence. A common ‘off–on’ detection strategy employs the immunofluorescence technique. In this scenario, micromotors are often equipped with antibodies to capture targets. The presence of captured targets is then detected through fluorescent signals using fluorescent labels.

The micromotor platform is revolutionizing sensing by incorporating the widely utilized conventional fluorescence-based approach. This strategy uses the emission of fluorescent light when fluorophores are exposed to electromagnetic radiation, allowing for effortless and accurate readings. By integrating this method, the platform boosts improved sensitivity and a robust sensing capability. This enables susceptible detection in small-volume samples with ease of operation, exceptional selectivity, and enhanced accuracy. The fluorescence-based micromotor technique utilizes transition patterns, such as ‘off-on’ and ‘on-off’, to detect targets. In the ‘off-on’ approach, the fluorescence shifts from ‘off’ to ‘on’ in the presence of targets. This technique typically involves the use of micromotors with antibodies to capture the targets, commonly known as immunofluorescence [116].

Applications of Biosensor Micromotors

Micromotors have captured widespread interest in sensing applications due to their ability to navigate autonomously and their compact size. Their unique capabilities have revolutionized the sensing in environmental science, food safety, and biomedical fields. In this section, we will delve into recent developments in micromotor-based sensing, specifically in the areas of environmental science, food safety, and biomedical applications.

Environmental science

The rapid growth of the industry has led to excessive discharge of harmful pollutants into water and air. This poses a grave danger to human well-being and requires urgent attention. In the field of environmental science, extensive efforts are being made to develop effective detection technologies as a foundational step towards remediation [117,118]. One standout option that has garnered significant interest is the use of micromotors. Their tiny size and ability to move independently make them ideal for discreet and continuous mixing. In the area of environmental sensing, micromotors have proven to be highly efficient in detecting all sorts of pollutants, from toxins and bacteria to heavy metal ions, even in situations with limited sample volumes. Clearly, micromotors have established themselves as invaluable tools for environmental monitoring.

Food safety

Concern for food safety is a global issue, prompting extensive research efforts to address the problem. According to a study by Escarpa and his colleagues [119], micromotors present a promising solution. They used bubble-propelled Mg/Au Janus micromotors to detect and remove diphenyl phthalate (DPP), an organic pollutant commonly found in food samples. The self-propelled movement of these micromotors allowed for efficient detection in a variety of samples, showcasing their adaptability and reproducibility. Furthermore, micromotors have been utilized to detect bacteria in food early. Escarpa and his team [120] developed graphene oxide, which is composed of micromotors that exhibit high performance in monitoring mycotoxins, showing superior sensitivity and reliability compared to traditional sensors. They also introduced an ‘on-off’ QD-composed micromotor system for precise control and detection of food contaminants.

Biomedical fields

Micromotors have quickly established themselves as valuable sensors in biomedical applications due to their compact size and independent movement. This allows for non-invasive

detection in small bio samples, making them ideal for use in medical contexts. Multiple micromotors have been proposed for biosensing, with each one employing specific recognition strategies to target probes or facilitate antigen-antibody interactions. For instance, *Yu et al.* [121] introduced a micromotor-based sensing platform for cancer biomarkers. This platform enables *in situ* immunoassays by counting tag numbers and observing speed changes resulting from selective antibody recognition. Additionally, *Wang* and colleagues [122] have successfully developed a colourimetric micromotor-based immunoassay for cortisol detection. Their work highlights the efficacy and faster detection process of using micromotors, ultimately creating a rapid and efficient naked-eye platform for cortisol detection.

2.3 State of the Art

Sensors

A sensor is a device that transforms physical inputs into interrelated outputs, usually in the form of electrical or optical signals that humans or electronic instruments can read. These remarkable tools, along with their accompanying interfaces, play a vital role in detecting and measuring various physical and chemical properties of compounds, such as temperature, pH, force, odour, pressure, the presence of specific chemicals, flow, position, and light intensity [123].

Classification of sensors

Mainly into two categories: Chemical Sensors and Biosensors

Chemical sensors

A chemical sensor is a device that converts a chemical or physical property of a specific analyte into a measurable signal, in which magnitude is in relation to the concentration of the analyte [124]. Unlike biosensors, chemical sensors face challenges in detecting phenolic compounds, which is attributed to low sensitivity and selectivity. Addressing these issues, nanomaterials, mainly carbon, metal, quantum dots, and transition-metal dichalcogenides, enhance signal amplification in chemical sensors. Indeed, the rise of nanotechnology is facilitating opportunities for the fabrication of innovative sensors using various nanomaterials such as

carbon, metal, quantum dots, and transition-metal dichalcogenides in sensing applications [125–127].

Based on the different transduction principles, chemical sensors can be mainly classified into two main classes: sensors with optical transducers (i.e. optical sensors) and sensors with electrical transducers (i.e. electrochemical sensors) [126,128,129]. Nanomaterials have been extensively used for optical and electrochemical sensing and have shown attractive results due to their unique advantages, such as good optical, electronic, and mechanical properties, much higher specific surface and versatility in surface modification [125,127,130–132].

Electrochemical sensor:

Electrochemical sensors have been gaining attention in the field of analytical chemistry due to their unique and desirable properties. These sensors offer a reliable and cost-effective solution for the analysis of phenolic compounds [133,134], with their fast response time, ease of use, high sensitivity, low instrumentation costs, small sample volumes, and portable design. Consequently, they have attracted considerable attention in the literature, and numerous research articles have been dedicated to their development and application in pharmaceutical and biomedical analysis [135,136]. In fact, significant advancements have been made in electroanalytical chemistry in recent decades, thanks to the development of ultra-microelectrodes, inexpensive and disposable electrodes, molecular devices, and cleverly designed electrochemical sensors. Therefore, electrochemical sensors are highly valuable tools in the field of analytical chemistry, with their unique capabilities and constant evolution proving them to be essential for reliable and efficient analysis.

Biosensors

A biosensor is a powerful tool made by combining a bioreceptor and physicochemical detector with a transducer [137]. The bioreceptor, which can be a biomolecule like an antibody, aptamer, enzyme, nucleic acid, or cell, is responsible for detecting the desired target analyte. Through precise biorecognition, these sensors boast high selectivity for their designated analyte, shielding against problematic signal interference from other substances [138]. Ultimately, the transducer translates biorecognition into a measurable signal. In order to create a robust biosensor, it is necessary to first immobilize the bioreceptor onto the transducer surface through either a reversible or irreversible method. There are several strategies available to achieve this, such as surface adsorption, covalent binding, cross-linking, entrapment (using beads or fibres), bioaffinity, and chelation or metal binding. The selection of a specific strategy depends on

various factors, including the type of sample, desired selectivity, and level of complexity [138]. In a biosensor, the transducer plays a crucial role in converting the energy generated by a physical change during a reaction into a different form. This transformation, known as 'signalization', allows the biorecognition event to be measured. Today, transducers come in an array of types, including optical, electrochemical, quartz crystal piezoelectric, calorimetric, and thermal variations. Studies have shown that the majority of transducers operate by producing either optical or electrical signals, which are proportional to the interactions between the analyte and bioreceptor. A schematic diagram of the main components of a biosensor is shown in **Figure 4.**

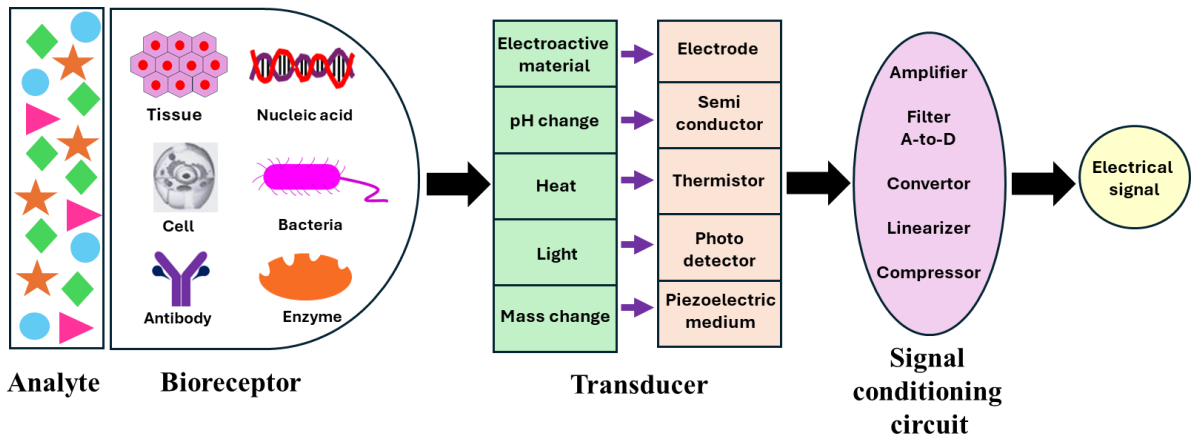

Figure 4: Schematic diagram of a biosensor.

Biosensors have taken the world by storm, serving as valuable tools for analysis and diagnosis. With their unparalleled performance, they have surpassed all other methods currently in use. Their operational simplicity, affordability, and lack of skill requirements have made them accessible to the average person for everyday use. As a result, they have found their way into a diverse range of fields, including self-monitoring for diabetes and heart conditions, forensic investigations such as drug discovery, agricultural and environmental detection, the food industry, and biodefense [139]. Undoubtedly, the success of biosensors in today's market hinges on their ability to continuously improve features such as selectivity, sensitivity, stability, reproducibility, and portability while keeping costs low. Various output signals, based on transducers, have been utilized to enhance the performance of biosensors such as optical (such as absorbance, luminescence, chemiluminescence, and surface plasmon) [140], mass (piezoelectric and magnetoelectric) [141], and thermometric [142].

Electrochemical Biosensors:

According to IUPAC, an electrochemical biosensor is a sophisticated device that combines a biological recognition element with an electrochemical transducer to provide precise and partial quantitative data on a specific analyte [143]. In other words, the sensor uses the power of an enzyme or antibody to directly interact with the electrochemical component and produce critical information on the substance being analysed. As research has shown, there is a diverse range of electrochemical detection methods available, such as amperometry, potentiometry, voltammetry, and more. These techniques utilize different electrical principles to achieve their results and contribute to the numerous applications of electrochemistry, including field-effect transistors, spectroscopy, and surface plasmon resonance. In addition, emerging techniques like ellipsometry, waveguide-based technology, and even atomic force microscopy have been combined with electrochemistry, showcasing the potential for continuous innovation in this field.

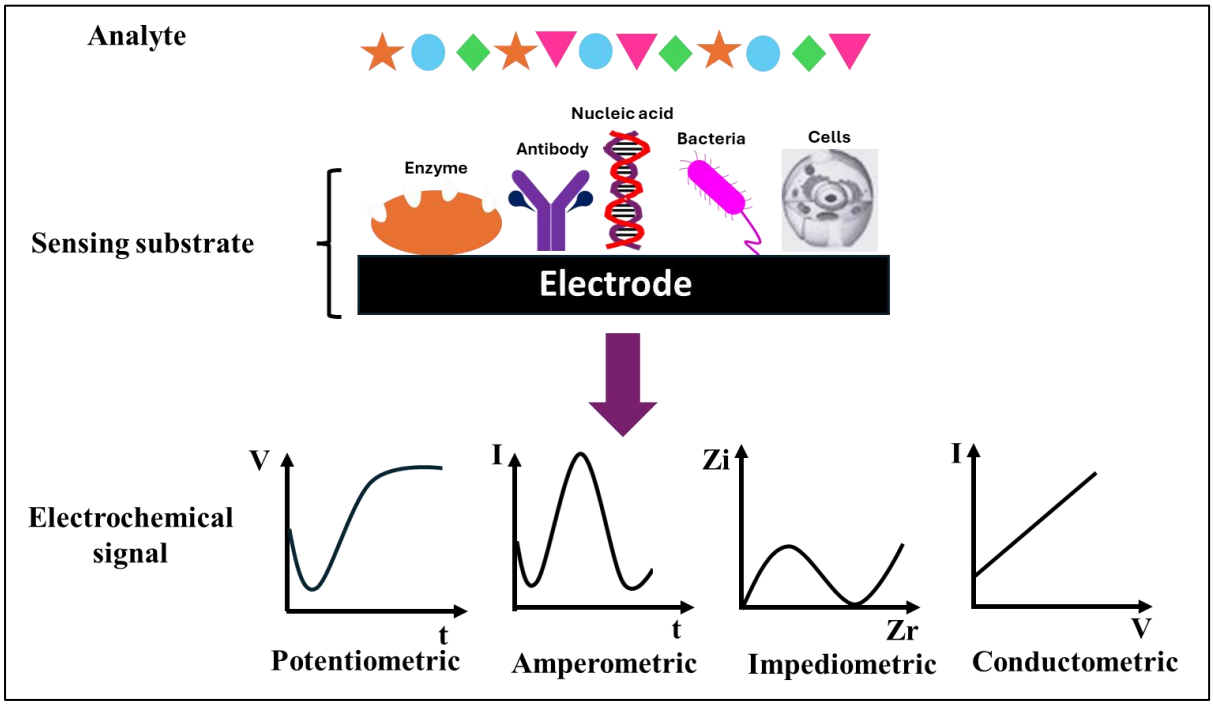

Figure 5: A schematic diagram of an electrochemical biosensor.

Förster Resonance Energy Transfer (FRET) based Optical Biosensors:

FRET is a powerful tool in biosensor development as it enables the precise and sensitive detection of biomolecules without having to alter or label them. By measuring the fluorescence of the acceptor molecule, FRET can pinpoint the exact proximity of both the donor and acceptor fluorophore. Therefore, even slight changes in the environment that affect the distance between the two molecules are immediately reflected in the level of fluorescence. As a result, FRET allows for the detection of subtle variations in the environment, such as the presence of a

specific biomolecule, without requiring direct labelling or modification of that biomolecule [144,145]. Furthermore, FRET is a non-radiative process, eliminating the risk of producing ionizing radiation [146].

Moreover, the use of FRET biosensors offers a distinct advantage in terms of specificity. These sensors possess the ability to accurately detect a specific biomolecule or environmental change without being influenced by other substances or alterations that may be present. This exceptional specificity is achieved by skilfully designing the biosensor to possess a strong affinity for the target biomolecule and engineering the donor and acceptor molecules to be in close proximity [147]. Not only are FRET biosensors highly specific, but they are also incredibly sensitive and adaptable. These versatile sensors have the capability of detecting numerous biomolecules and changes in the environment. Furthermore, they have a diverse range of applications, such as monitoring protein-protein interactions, measuring enzyme activity, and tracking changes in pH [148–155].

FRET is a fascinating phenomenon found in photochemical and quantum mechanical processes. It involves the transfer of energy from a photon-excited donor fluorophore to an electron-acceptor fluorophore in its ground state within a distance of 1-10 nm. This discovery was named after German scientist Theodor Förster, who first described it [156]. FRET is widely used as a valuable tool in biochemistry and biophysics to measure molecular interactions, such as protein-DNA and protein-protein interactions, as well as changes in protein structure. To track the formation of a conjugate between two molecules, FRET makes use of a donor and acceptor fluorophore, respectively. These labelled fluorophores play an essential role in revealing important molecular dynamics.

Moreover, the emission of the acceptor is mainly detected through intermolecular FRET between the donor and acceptor when they come into close proximity (1–10 nm) with each other. By labelling the target protein with a donor and acceptor at two distinct sites, conformational changes in the protein can be monitored. As the protein twists or bends, FRET changes are observed as the relative orientation and distance between the donor and acceptor fluorophores change. This powerful technique can also be utilized to detect ligand binding through fluorescent indicators [157–159], as changes in protein conformation or molecular interactions can be detected through FRET. With FRET, researchers can measure the distance between the two components and deduce whether the individual molecule has undergone conformational changes or undergone interactions with other molecules.

Principle of FRET: FRET, or Förster resonance energy transfer, is an essential phenomenon in photo-physiochemistry. It operates through a distance-dependent mechanism and involves the transfer of energy from a photon-activated donor fluorophore to an appropriate ground-state electron acceptor fluorophore. This transfer occurs through dipole-dipole interactions when the two molecules are in close proximity [160]. The fundamental principle of FRET hinges on the donation of energy from a donor to an acceptor molecule through dipole-dipole interactions and non-radiative energy transfer over time and space. This transfer is only possible when the molecules are within 1-10 nm of each other and when their electronic energy levels align [161]. The first step in the process is the excitation of the donor fluorophore molecule, achieved by absorbing a specific frequency of light's energy (expressed as $E = h\upsilon$) at a particular wavelength. This excitation causes the donor molecule to transmit a portion of its energy to the acceptor molecule, provided that the two are in close proximity. Consequently the donor molecule's fluorescence emission decreases while the acceptor molecule's fluorescence emission increases. The effectiveness of this energy transfer lies in various factors, such as the distance between the donor and acceptor molecules, their overlapping spectral profiles, and their relative orientation. To better visualize this energy transfer and the fluorescence phenomenon, **Figure 6 (B)** displays a Jablonski diagram of a donor-acceptor pair undergoing FRET. This diagram serves as a representation of the intricate processes occurring within FRET. Jablonski's diagram showcases the dynamic interplay of energy levels and their transitions between a donor and acceptor molecule. This diagram outlines four distinct energy levels: the ground state (S_0), the first excited singlet state (S_1), the first excited triplet state, and a non-fluorescent ground state (S_0) following emission. When the donor molecule absorbs light, it is propelled into the first excited singlet state (S_1). At this point, it can either return to the ground state (S_0) through spontaneous emission, creating fluorescence, or it can engage in FRET, channelling its energy to the acceptor molecule. In FRET, energy is passed from an excited donor molecule (S_1) to a ground-state acceptor molecule (S_0). This results in the acceptor molecule being excited to its first excited singlet state (S_1) while the donor molecule returns to its ground state (S_0) without releasing fluorescence. Following this transfer, the acceptor molecule then emits fluorescence as it returns to its ground state (S_0). The Jablonski diagram depicted in **Figure 6** [162–171] offers a visual representation of FRET efficiency, which heavily relies on the degree of spectral overlap between the donor and acceptor fluorophores, as well as the distance and orientation of these molecules.

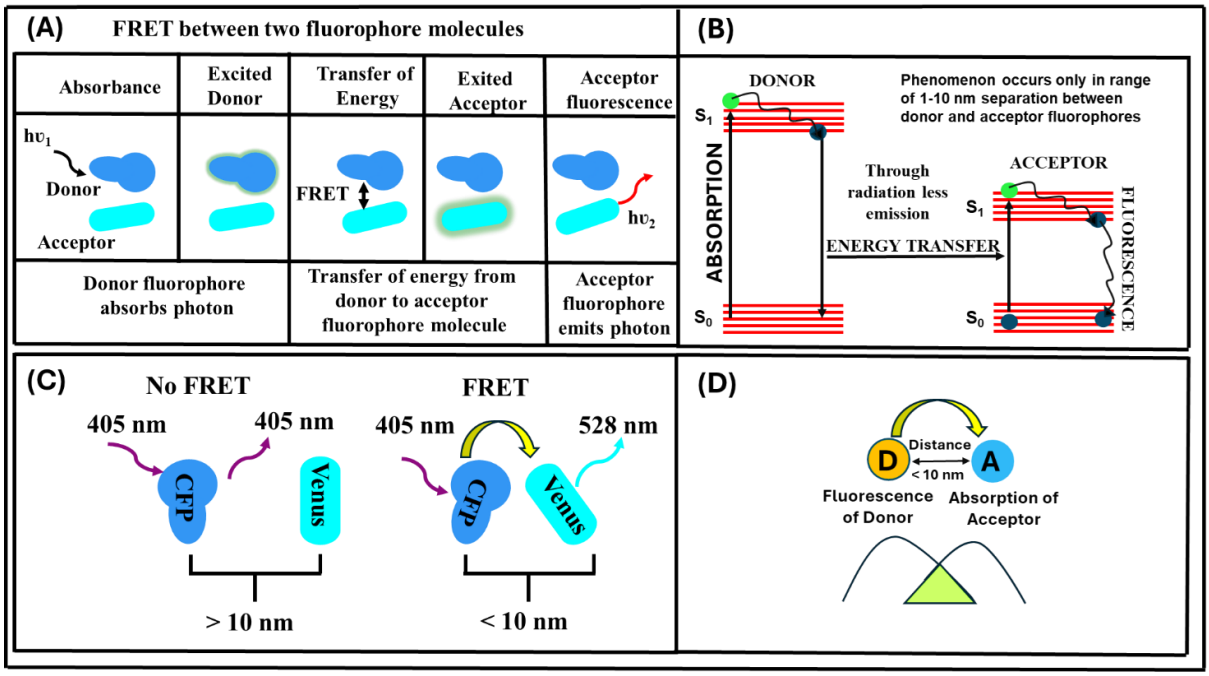

Figure 6. (A) Energy transfer between two fluorophore molecules. **(B)** Jablonski diagram fordonor–acceptor pair in FRET. **(C)** The orientation of the donor-acceptor pair is parallel to each other for maximum transfer of energy, as represented by the spectral overlapping of the emission spectra of the donor (D) and the absorption spectra of an acceptor (A). **(D)** Overlapping integral during FRET.

Donor and Acceptor Fluorophores: In FRET, the donor is a fluorophore molecule that emits radiation when excited by a photon with the right frequency and wavelength. This energy is then transferred to an acceptor molecule through non-radiative means. Donor molecules can range from fluorescent proteins to nanomaterials like quantum dots or dyes, and they all can transfer energy through FRET. On the other end, the acceptor molecule receives this energy from the donor and can also be a variety of fluorescent molecules, such as proteins, quantum dots, or dyes [172].

2.4 Material Characterization

Various techniques have been implemented to characterize the material of the 3D-printed carbon electrodes and the micro/nanorobots. Such as scanning electron microscopy (SEM), X-ray photoelectron spectroscopy (XPS), Energy-dispersive X-ray spectroscopy (EDS, also abbreviated EDX or XEDS) and Fourier transform infrared spectroscopy (FTIR) etc. with the prime focus on the SEM. All these instruments are available in the CEITEC, BUT.

Scanning Electron Microscopy (SEM)

An SEM is an electron microscope with the capability to produce images by scanning a sample surface with its focused beam of electrons. Electrons interact with the atoms in the sample, causing it to produce several signals that contain many details about surface topography and the composition of the sampling system. It also provides information about the type of morphology (texture), chemical composition, and the crystalline structure and orientation of the material constituting the sample [173].

Fundamental Principles of Scanning Electron Microscopy (SEM): It is based on the fact that if kinetic energy applies to a sample, then signals are produced on the interaction of electrons. These interactions can be divided into two major categories: elastic interactions and inelastic interactions. Elastic scattering is caused by the deflection of an incident electron from a specimen's atomic nucleus or outer shell electrons with similar energy. This type of interaction is known for its low energy loss during collision and wide-angle scattering of electrons. Backscattered electrons (BSE) are elastically scattered incident electrons with an angle of more than 90° and produce a useful signal for imaging the sample. Inelastic scattering happens through the different interactions involving the incident electrons with the electron and atoms of the sample, which leads to a substantial energy transfer from a primary beam electron into that atom (**Figure 7**). The extent of energy dissipation relies on whether the electrons in the specimen are excited singly or collectively, as well as on the binding energy between the electron and the atom.

Consequently, specimen ionization causes the excitation of electrons in specimens, resulting in the production of secondary electron (SE); it is commonly defined as having energies lower than 50 eV and is used for imaging or analysis of the sample. The secondary and backscattered electrons generate an image. Secondary electrons emitted from the specimen are responsible for revealing morphology and topography, while the backscattered electrons depict contrast that is connected to the composition of elements. Apart from these signals used for image formation, many other signals are also produced when an electron beam strikes a sample, such as characteristic x-rays, Auger electrons and cathodoluminescence [174].

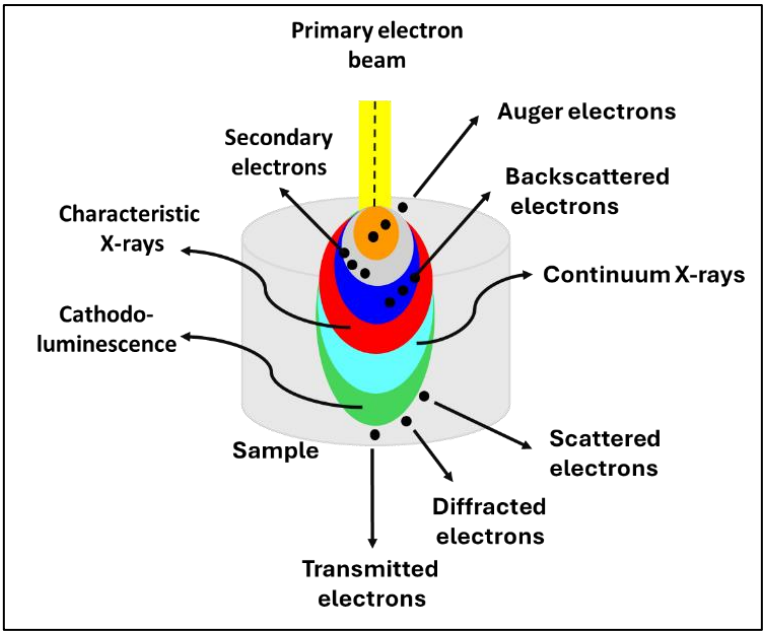

Figure 7. Schematic diagram of the working principle of SEM

Figure 8 shows the electrons sourced from tungsten filament lamps located at the top of the column and the electromagnetic lenses used. The electrons are released after heat energy is applied to the electron source, allowing them to move at a high velocity towards the anode, which is positively charged. The electron beam triggers the primary scattered (Primary) electrons with high energies, whereas the secondary ones are emitted from the specimen surface at low-energy levels. The electron beam is directed at the specimen, and it interacts with the sample to produce signals that reveal information about the topography of surfaces and also component elements.

The sample does not require any special handling for visualization under the SEM; even dried samples that have been air-dried can be viewed directly. However, the microbial specimens must be fixed, dehydrated, and dried to retain the cell structures, which cannot collapse under a high vacuum in the microscope. Next, the samples are coated with a thin layer of heavy metal elements that enable the spatial scattering of electric charges on the surface specimen for better image production high clarity.

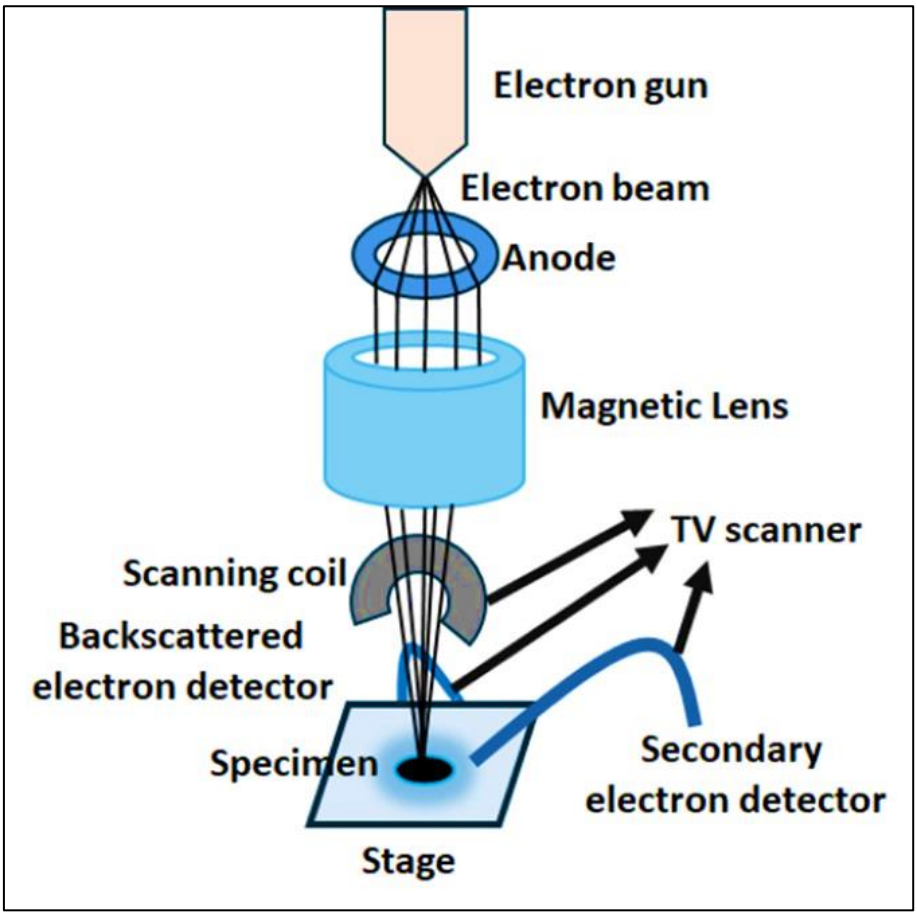

Figure 8. Schematic diagram of SEM instrumentation

The microscope scans a thin section by moving a beam of electrons back and forth. When these electrons hit the specimen, the surface emits secondary electrons, which are captured by a special detector. As the secondary electrons reach and penetrate the detector, they impact a scintillator (a luminescence material that fluoresces if charged particles or high-energy photons strike it). This produces a flash of light that is converted into an electric current by a photomultiplier and activates the cathode ray tube by sending the signal. This gives an image that can be viewed as well as photographed [175].

Energy-dispersive X-ray spectroscopy (EDX)

Energy-dispersive X-ray spectroscopy (EDS, also known as EDX or XEDS) is an analytical tool that allows the study of the elemental composition of a sample. When the sample is excited

by an electron beam, it will emit some of its absorbed e-beam energy by releasing one electron from the shell and leaving a positive hole in space. When this electron moves out, another electron is attracted to take its place from an outer shell. When the electron goes from an outer higher-energy shell of an atom to the inner lower-energy shell, then there is a release of energy in the form of X-ray, which is produced from this energy difference. This X-ray's energy is unique to the specific elements and their transition. The X-rays produced during the process are captured by a silicon drift detector, which detects the signal and analyses it with corresponding software. Indeed, the chemical data information may be represented in either the elemental mapping or line scans. Thus, the X-rays can be used to determine every element that is present in such a sample. It is worth noting that EDX can be applied in either qualitative or quantitative measurements, allowing a user to identify the types of elements and determine the concentration percentage of each element. And likewise, the standard SEM method needs simple sample prep and is also non-destructive [176,177].

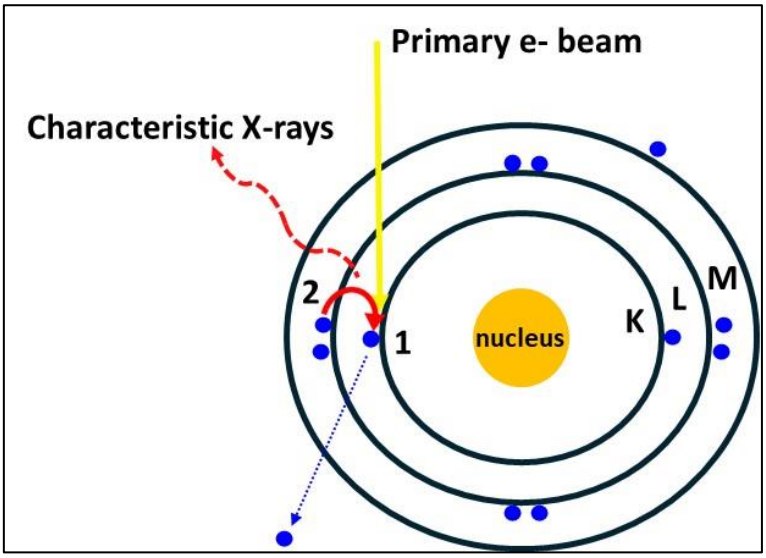

Figure 9. Schematic diagram of the working principle of EDX

X-ray photoelectron spectroscopy (XPS)

X-ray photoelectron spectroscopy is a very surface-sensitive analytical technique where the kinetic energies of released electrons are recorded after exposing a sample to X- rays. The two main features of this technique that make it essential as an analytical method are its surface sensitivity and its ability to expose chemical state information from the elements in the sample. All components other than hydrogen can be determined. At the same time, XPS has been

applied to probe the surface of almost every material, ranging from plastics or textiles through soils to soils and semiconductors [178, 179].

The sample is exposed to soft X-rays (**Figure 10**) with energies lower than ~6 keV, and the kinetic energy of the emitted electrons is analysed. There is a complete transfer of energy from the x-ray to a core-level electron to emit a photoelectron. This is mathematically expressed in Eq. (1), stating that the energy of the x-ray (hν) equals the binding energy (BE) of the electron, which represents how tightly it is bound to the atom/orbital, plus the kinetic energy (KE) of the emitted electron, and the spectrometer work function (Φ_{spec}), a constant value [179].

$$h\nu = BE + KE + \Phi_{spec}. \qquad \text{Eq. 1}$$

To determine the binding energy of an electron, Eq. (1) can be rearranged to get Eq. (2), where the terms on the right are either known (hν and Φ_{spec}) or measured in the XPS experiment (KE),

$$BE = h\nu - KE - \Phi_{spec}. \qquad \text{Eq. 2}$$

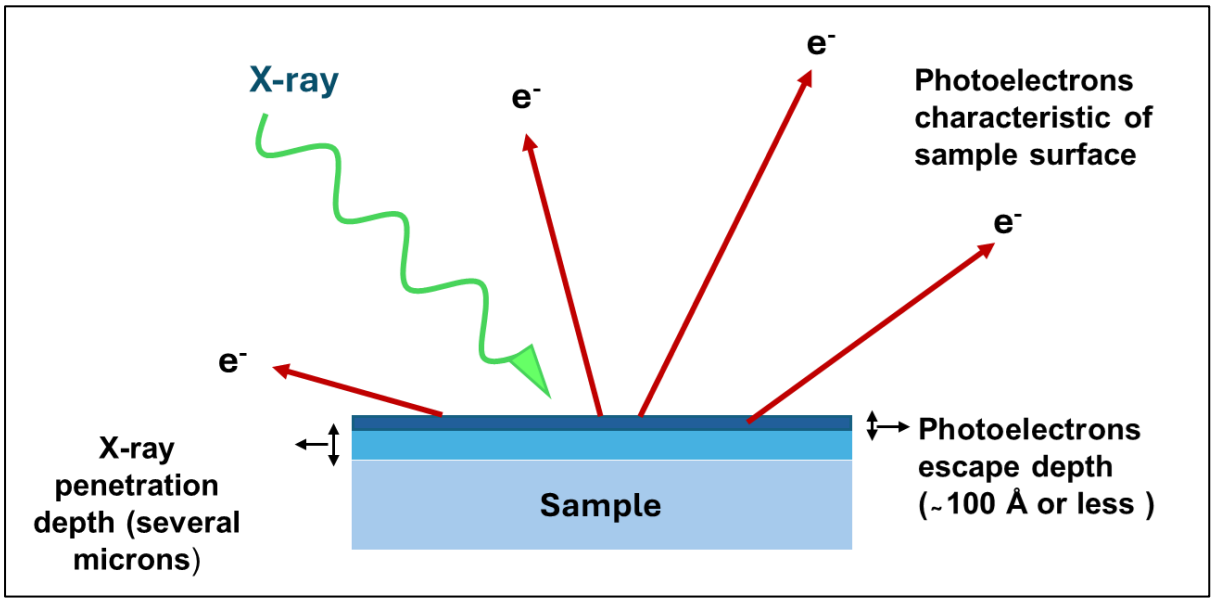

Figure 10. Schematic diagram of the photoemission measurement principle.

Photoluminescence

Photoluminescence spectroscopy, commonly known as PL, is a noncontact and non-destructive method used to explore the electronic structure of materials. During the process, light is directed onto a sample, leading to photo-excitation, where the material absorbs energy and enters an excited state. The excess energy is then dissipated through the emission of light, known as luminescence, referred explicitly to as photoluminescence in the context of photo-

excitation. This phenomenon involves electrons moving into excited states within the material, and upon returning to their ground states, they release excess energy, potentially as light through a radiative process or without light in a nonradiative process. The energy of the emitted light (photoluminescence) is associated with the difference in energy levels between the excited and ground states of electrons. The relative contribution of the radiative process influences the amount of emitted light. Overall, photoluminescence spectroscopy offers valuable insights into material properties without physically touching or damaging the sample [180,181].

Forms of Photoluminescence: Fluorescence and phosphorescence

Photoluminescence encompasses fluorescence (lasting 10^{-9}-10^{-7} seconds) and phosphorescence (lasting 10^{-3}-10^{-2} seconds after the incident light removal). The Jablonski diagram illustrates the quantum mechanics of these processes. In fluorescence, a molecule in the singlet ground state (S_0) absorbs a photon, promoting it to a singlet excited state (S_1). The emission of light happens when the molecule returns from S_1 to S_0 in less than 10 nanoseconds, facilitated by their same spin multiplicity.

Phosphorescence occurs when a molecule, typically containing atoms with higher mass and significant spin-orbit coupling, experiences intersystem crossing (ISC) between singlet S_1 and triplet T_1 electronic states. Due to the conservation of angular momentum, spin-orbit coupling allows phosphorescence to take place as a radiative transition from the T_1 to the S_0 state. This explains why phosphorescence operates on a much slower timescale, ranging from microseconds to thousands of seconds, compared to fluorescence [182–184]. In summary, fluorescence is the emission of light from a molecule's first excited singlet state (S_1) following the absorption of a photon, while phosphorescence involves light emission from a molecule's triplet state (T_1) after intersystem crossing from S_1 as shown in **Figure 11**.

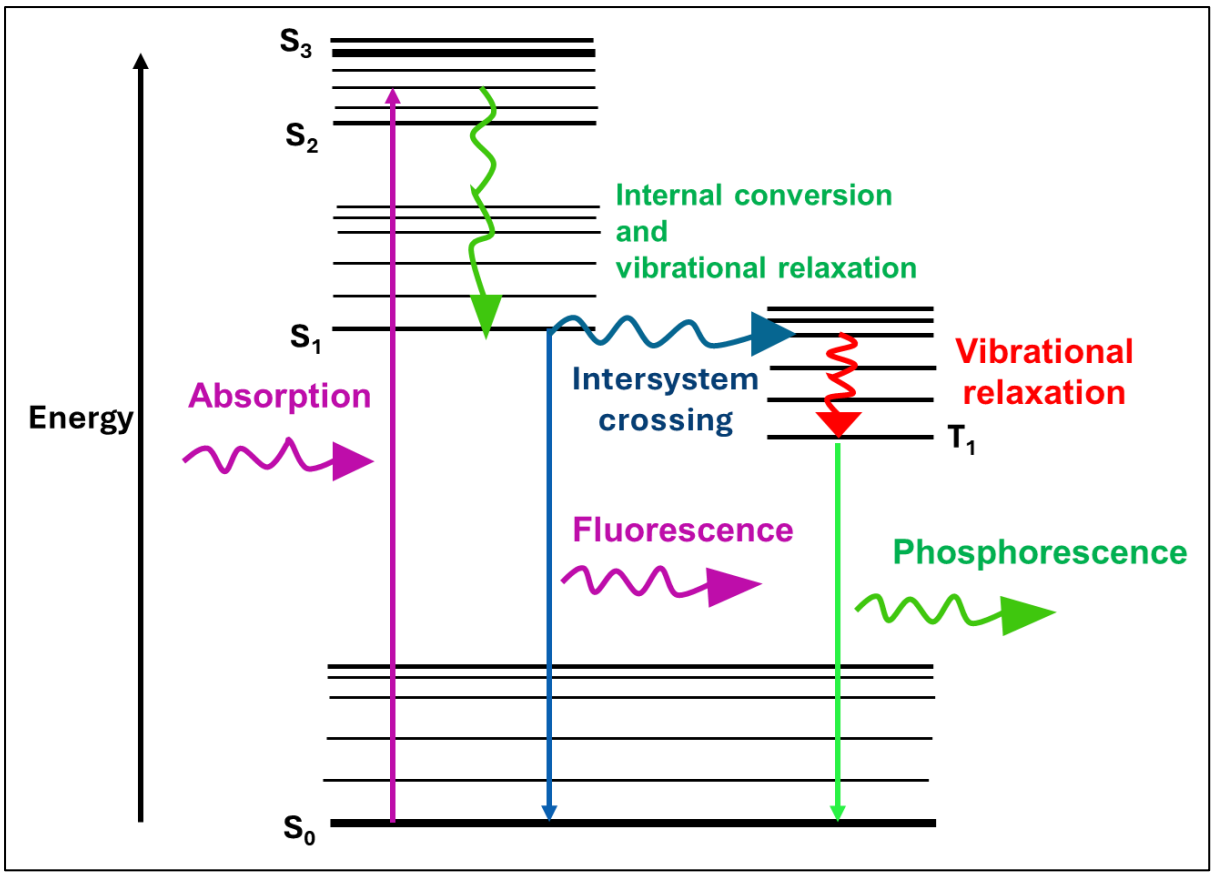

Figure 11. Energy diagram of fluorescence and phosphorescence.

Excitation and Emission

The definite wavelengths needed to activate a photoluminescent material and the colours it emits vary based on the material's properties, which are measured in nanometres (nm).

Excitation: Ultraviolet (UV) wavelengths are commonly employed for this purpose. Usually, UV excitation light sources utilize longwave UV at 365 nm (UVA 315 to 400 nm) or shortwave UV at 254 nm (UVC 200-280 nm). **Emission:** Photoluminescent materials generally produce colours within the visible spectrum, ranging from violet (400 nm) to red (750 nm). It's worth noting that some materials may emit light outside the visible colour spectrum, in the UV or near-IR range (above 750 nm).

Chapter 3

Background and Literature Review

3.1 Chemical Sensing

Phenolic Compounds Detection

Phenolic compounds play a crucial role in industrial development, serving as raw materials for resins, plastics, germicides, pharmaceuticals, textiles, dyes, and petrochemical products [185–188]. However, the release of these toxic compounds into the environment poses health risks to the heart, kidneys, and liver [189–193]. Addressing the high toxicity and persistency of phenolic compounds, scientists focus on their removal from water and wastewater using methods such as distillation, adsorption, incineration, solvent extraction, chemical oxidation, and membrane separation [66]. Various materials are employed to enhance the efficiency of these processes.

Commonly used methods for detecting phenolic contaminants include chromatography/mass spectrometry [194], spectral analysis [195], and capillary electrophoresis [196]. For instance, *Liu et al.* employed high-performance liquid chromatography coupled with tandem mass

spectrometry (HPLC-ESI-MS/MS) for the analysis of trace bromophenols in river and seawater samples [197]. The method successfully detected six bromophenols in samples with concentrations ranging from pM to nM. *Chen et al.* developed an analysis method using surface-enhanced Raman spectroscopy and principal component analysis for 2,4-dichlorophenol (2,4-DCP), 2,4,5-trichlorophenol (2,4,5-TCP), and 2,3,4,6-tetrachlorophenol (2,3,4,6-TeCP) [198].

The suggested approach enables the simultaneous detection of three phenolic contaminants with a low limit of detection (LOD). *Ali et al.* utilized multi-walled carbon nanotubes-based solid-phase extraction and capillary electrophoresis to analyse 4-cyanophenol and 3-nitrophenol [199]. This method proved effective for extracting and estimating phenolic contaminants in municipal wastewater.

Nevertheless, these techniques demand costly instruments and intricate procedures, rendering them time-consuming, expensive, and unsuitable for on-site rapid detection. In contrast to traditional instrumental methods, electrochemical sensors, consisting of identification elements and signal transducers, have become the prevailing choice for analysis. This is attributed to their simplicity, cost-effectiveness, rapid response, high sensitivity, portability, and miniaturization, making them suitable for real-time and on-site quantitative and qualitative analysis in complex matrices.

Carbon materials provide optimal solutions to challenges (sensitivity and selectivity), offering abundance, high biocompatibility, and diverse properties stemming from carbon–carbon molecular orbital hybridization. They play a pivotal role in various fields, notably electrochemical sensing, energy storage, and conversion. Graphene-like carbon materials, such as graphene and carbon nanotubes, are extensively explored in electrochemical sensors, particularly for phenolic compound detection [200].

Predominantly utilized in electrochemical sensors, carbonaceous materials address critical challenges like sensitivity and specificity. Various carbonbased electrodes such as glassy carbon, graphite, carbon black, fullerenes, carbon nanotubes, graphene-related materials, and nanostructured porous carbon materials ensure inert electrochemistry, electrocatalytic diversity, and cost-effectiveness. Beyond electrochemical sensors, these materials are commonly used in optical sensors. Graphene-based materials and carbon nanotubes, with unique optical properties, high conductivity, and easy functionalization, stand out for sensing applications, offering enhanced selectivity, chemical stability, and biocompatibility [191].

There is no denying that graphene-based materials possess extraordinary qualities, such as impressive adsorption capacity, superior electrical conductivity, and noteworthy optical

properties [201–203]. In parallel, conducting polymers have emerged as promising materials for phenolic compound removal, leveraging their outstanding optical, electric, electrical, and magnetic properties [204–209]. Additionally, conducting polymers exhibit excellent electrocatalytic properties and rapid electron transfer capabilities due to their inherent conductivity [210,211].

Conducting polymers find extensive applications in batteries [212], electrochromic devices [213], actuators [214,215], and supercapacitors [216]. Beyond phenolic compound removal, materials based on graphene and conducting polymers exhibit significant potential in sensing applications [217–219]. These materials have been widely utilized in sensors for detecting phenolic compounds, achieving detection capabilities down to the femtomolar range.

An electrochemical sensor (Cyclic voltammetry (CV)) for 4-nitrophenol (4-NP) was developed by incorporating polycarbazole (PCZ) polymer, graphene (Gr), and nitrogen on a glassy carbon electrode (GCE). Comparative analysis with other electrodes revealed that the PCZ/nitrogen-doped Gr-GCE exhibited superior electrochemical catalytic activity for 4-NP due to the catalytic ability of nitrogen atoms enhancing the electrical properties of Gr, along with a synergistic effect between PCZ and nitrogen-doped Gr. The peak current demonstrated direct proportionality to 4-NP concentration within the range of 0.8 to 20 µM, achieving a low detection limit (LOD) of 0.062 µM [220].

Similarly, a CV was developed for 4-nitrophenol (4-NP) by synthesizing polyaniline (PANI) in graphene oxide (GO) dispersion in the presence of 4-NP for molecularly imprinted polymer (MIP) fabrication. MIP offers exceptional specificity and durability in harsh chemical environments. The sensor's response was linear for 4-NP concentrations ranging from 0.06 to 1.4 mM, with a low detection limit (LOD) of 20 µM [221]. To enhance the sensitivity of differential pulse voltammetry (DPV) sensor for 4-NP detection, PANI was reinforced with interconnected and porous hybrid GO–iron tungsten nitride nanoflakes. The electrocatalytic performance of the PANI–GO–iron tungsten nitride-modified glassy carbon electrode (GCE) surpassed that of PANI-modified GCE. Both oxidation and reduction signals increased with 4-NP concentrations ranging from 0.03–3 µM and 0.01–4 µM, respectively. The LOD values for oxidation and reduction peak currents were excellent at 5.2 nM and 2.4 nM, respectively [222].

Another DPV sensor was developed by drop coating a mixture of partially RGO– PANI on the surface of GCE, but this time for the detection of phenol. As both RGO and PANI have good electrical conductivity and electrochemical activity, their combination resulted in better electrochemical properties. The current response was linear to the phenol concentration over 0.01–10 µM with a correlation coefficient of 0.9922. The LOD was calculated to be 4.5 nM

[223]. A work has reported a SWV sensor for 2,4-DCP based on the combination of Gr and PANI that have outstanding electroanalytic activities toward an analyte with diamond, which is an anti-passivating agent that has a high resistance to fouling, on the surface of GCE. The oxidation peaks showed a linear relationship to the analyte concentration from 5 to 80 µM, and the calculated LOD was 0.25 µM [224].

In the development of an amperometric (AMP) sensor for 2-nitrophenol (2-NP), graphene (Gr) and polyaniline (PANI) were incorporated with cerium tungstate on the surface of a glassy carbon electrode (GCE). This sensor, characterized by non-toxicity, a large surface area, chemical stability, and strong absorption capability, demonstrated wide linearity within the range of 1 nM to 1 mM. It achieved a low limit of detection (LOD) of 0.87 nM and exhibited excellent selectivity towards 2-NP when tested against various interferents [225].

Organophosphates Detection

Pesticides, widely employed for pest control in agriculture, include organophosphate pesticides (OPs), known for their high efficacy in insect eradication [226]. Common OPs comprise chlorpyrifos, diazinon, malathion, and parathion [227]. Unregulated pesticide usage leads to environmental contamination and residue presence in various food commodities [228]. Researchers have reported OPs residues, such as chlorpyrifos in cabbage, tomatoes, cayenne pepper, and carrots, and diazinon exceeding thresholds in long beans [229–231]. While gas chromatography (GC) and high-performance liquid chromatography (HPLC) remain reliable for detecting OPs due to their high selectivity and sensitivity [232,233], they require trained personnel, extended preparation and analysis times, and expensive equipment. They are unsuitable for on-site detection [234]. Thus, there is a need for a simple, rapid, and cost-effective on-site detection method for OPs in food commodities to ensure public safety. Electrochemical sensors offer a solution that is relatively inexpensive, adaptable to cloudy samples, and easily portable [235].

Various amperometric sensors have been developed for the detection of organophosphates in fruits and vegetables. Detection methods for organophosphate compounds commonly involve the use of the enzyme acetylcholinesterase (AChE) as a receptor. AChE catalyzes the hydrolysis of acetylthiocholine chloride, resulting in the production of thiocholine [236]. Thiocholine, an electroactive compound, can be detected using an amperometric method. *Mahmoudi et al.* [237] demonstrated high-sensitivity detection of paraoxon compounds using AChE. The method successfully detected paraoxon in spinach and cabbage samples at a

concentration of 10 nM. *Xu et al.* [238] developed a highly sensitive electrochemical sensor for detecting chlorpyrifos with a low limit of detection (LOD) of 70 pg/mL. The method leverages the synergistic effect of copper oxide nanoflowers (CuO NFs) and carboxyl-functionalized single-walled carbon nanotubes (c-SWCNTs). CuO NFs enhance the electrode surface area and electron transfer, while c-SWCNTs improve the effectiveness and stability of aptamer immobilization as a receptor. *Mishra et al.* [239] created a portable electrochemical sensor embedded in gloves for detecting organophosphate compounds on food surfaces. This method effectively detects solutions of methyl parathion (MP) and methyl paraoxon (MPOx) with a concentration of 200 µM on fruits and vegetables. In 2017, *Surucu et al.* developed an efficient electrochemical strategy for qualitative analysis of fenitrothion in tomato samples. The assay utilized a modified pencil graphite electrode with a composite film of reduced graphene oxide (RGO) and poly(E)-1-(4-((4-(phenylamino)phenyl)diazenyl)phenyl)ethanone (DPA). The method demonstrated high efficiency and selectivity for fenitrothion [240]. In 2018, *Xu et al.* introduced a novel electrochemical approach for detecting methyl parathion and paraoxon. The method involved the use of N-carbamoylmaleimide functionalized carbon dots (N-MAL CDs) deposited on the surface of a screen-printed carbon electrode (SPE), denoted as N-MAL CDs/SPE [241]. In 2017, J. *Mehta et al.* reported screen printed immunosensor modified with graphene quantum dots for the detection of the parathion. The use of GQDs has enabled the development of a highly sensitive and reliable immunosensor for parathion detection. This sensor demonstrated a dynamic linear response and an impressively low detection limit of 46 pg/L [242].

Further, in 2018, *G. Bolat et al.* reported highly sensitive electrochemical detection of the fenitrothion pesticide using a disposable pencil graphite electrode modified with self-assembled peptide-nanotubes. The electrochemical response of this sensor was linear with a lower detection limit of 0.0196 µM [243]. *Zhang et.al*. reported a stable biosensor for organophosphorus pesticide detection based on chitosan-modified graphene in 2020 with a detection limit of 54 pM [244].

3.2 Biosensors

A fundamental biosensor comprises a receptor, transducer, and processor. The recognition layer is formed by sensing elements like whole cells, antibodies, enzymes, or nucleic acids. These are integrated with the transducer through immobilization techniques like adsorption, cross-linking, or covalent binding. Transducers are selected based on the measurement

parameters, such as amperometric (current measurement at constant potential) [245], potentiometric (potential measurement at constant current) [246], piezoelectric (measurement of changes in mass), thermal (measurement of changes in temperature) [247], or optical (detection of changes in light transmission) [248]. Traditional analytical techniques involve multiple steps, extensive labour, time, and expensive instruments. In contrast, biosensors offer a quick, simple, and cost-effective alternative suitable for deployment in small hospitals and laboratories in remote areas lacking sophisticated instrument facilities.

Currently, quantitative real-time polymerase chain reaction (qPCR) stands as a standard method, utilizing a fluorescent signal in conjunction with DNA polymerase chain reaction for DNA quantification [249–253]. Despite its capability to detect the presence of 1–10 copies/mL of DNA samples, PCR remains limited to professional laboratories due to the requirement for specialized instrumentation [254,255]. Alternative approaches are under development to streamline DNA detection for point-of-care testing, including colourimetric [256], microfluidic platform-based optical detection [257], and electrochemical methods [258]. Among these techniques, electrochemical methods stand out for their ultra-sensitivity and well-established nature [259]. In electrochemical DNA sensors, nucleic acid hybridization is combined with electrochemical reactions to detect target DNA selectively [260,261]. However, the direct application of electrochemical methods for detecting a single copy of DNA in biological samples may be challenging. To overcome this, signal amplification approaches are utilized to enhance sensitivity and selectivity for low-concentration targets [262]. Moreover, electrochemical sensors present a promising avenue for both laboratory and point-of-care approaches, offering the potential for miniaturization and quantitative measurements [263,264].

Electrochemical transduction systems are known for their robustness, ease of use, portability, and cost-effectiveness. Electrodes in electrochemical biosensors are made from various materials such as glassy carbon, carbon paste, graphite composites, carbon/graphite formulations, carbon nanotubes, graphene, and gold. Screen-printed electrodes (SPEs) have gained popularity due to their easy and reproducible fabrication, both in laboratory and commercial settings [265]. Commercially available SPEs, functionalized or not, and in-house production facilities in many laboratories contribute to their widespread use. The configuration of the electrode, the chosen materials, and the immobilization of the bioreceptor on the electrode surface are all critical factors in ensuring the effectiveness of electrochemical biosensors.

A lot of work has been reported in the past for the detection of biomolecules such as DNA and bacterial detection, etc. In recent years, nucleic acids have found widespread application in various biosensors and bioanalytical assays due to their diverse physical, chemical, and biological properties [266]. In biosensors based on nucleic acids, the sensing elements are typically oligonucleotides with a known sequence of bases or fragments of DNA or RNA. Nucleic acid biosensors operate through highly specific hybridization of complementary DNA/RNA strands or serve as highly specific receptors for biochemical/chemical species [267,268]. These biosensors are particularly promising as they offer the potential for obtaining sequence-specific information in a faster, simpler, and more cost-effective manner than traditional methods. Unlike enzymes or antibodies, nucleic acid recognition layers can be easily synthesized and regenerated for multiple uses. Combining nucleic acid biosensors with polymerase chain reaction (PCR) methods, as demonstrated by Bell and Ranford-Cartwright, can enhance sensitivity and specificity [269,270].

Detection techniques play a crucial role in biosensor design, selected based on their specific applications. Among the various devices developed, electrochemical DNA biosensors have garnered significant attention due to their high sensitivity and rapid response. These devices are particularly valuable for sequence-specific DNA sensing. The miniaturization and advanced technology of electrochemical devices make them excellent tools for DNA diagnostics. Electrochemical detection of DNA hybridization typically involves monitoring current at a fixed potential. Various electrical modes have been developed for the detection of both label-free and labelled objects [271–278]. The immobilization of the nucleic acid probe onto the transducer surface plays a pivotal role in the overall performance of DNA biosensors and gene chips [279,280].

In 2018, *J. Lee et al.* introduced a versatile gold/iron-oxide nanoparticle-carbon nanotube (CNT) hybrid nanomaterial as a platform for virus DNA sensing. The limits of detection for influenza virus and norovirus were estimated to be around 8.4 pM and 8.8 pM, respectively. [281] *M. Shariati et al.* developed an exceptionally sensitive label-free biosensor for human papillomavirus DNA using gold nanotubes on nanoporous polycarbonate in electrical alignment, achieving a remarkable limit of detection (LOD) of 1 fM. [282] *J. Xu et al.* presented a label-free and highly sensitive electrochemical detection method for pathogenic DNA, achieving an estimated limit of detection of 1 fM. [283] *M. Khater et al.* conducted the electrochemical detection of a plant virus using gold nanoparticle-modified electrodes, achieving an estimated limit of detection (LOD) of 100 nM. [284] *C. Singhal et al.* presented a

paper-based DNA biosensor for detecting the chikungunya virus, employing gold shells coated magnetic nanocubes. The sensor achieved a detection limit of 0.1 nM with a linear range spanning from 0.1 nM to 100 μM. [285] *Y. Xiang et al.* presented 'Quantum Dot layer-by-layer assemblies as signal amplification labels for ultrasensitive electronic detection of uropathogenic', achieving a detection limit of 0.22 fM based on signal-to-noise characteristics.[286]

3.3 2D Materials towards 3D-printing

Compared to other nanomaterials, 2D nanostructures demonstrate promising applications for *in vitro* detection of small biological molecules, neurotransmitters, and proteins, serving as biomarkers. They are cost-effective, easily synthesized, and offer rapid response times for screening various disorders, including potentially fatal cancers [287]. These nanostructures enhance the sensitivity, selectivity, and stability of sensing platforms [288]. 2D nanoarchitectures coupled with advanced nanotechnology improve real-time detection of gases, pollutants, and small biomolecules, contributing to both *in vitro* and *in vivo* diagnosis [289]. Point-of-care testing devices, with portability, flexibility, non-invasiveness [290], low cost, time-effectiveness, improved sampling frequency, and implantability [291], have revolutionized the sensing systems. Trials involving wireless transmission of analytical data to medical centres have been successful. Still, the development of ready-to-use and reusable sensors lags due to device complexity and high costs [292]. With technological progress, sensors have become integral to various facets of human life. The identification and sensing of proteins, enzymes, antibodies, and other biomolecules hold significant biological, technological, and pharmaceutical importance. In this regard, the utilization of 3D-printed sensors incorporating 2D materials has emerged as an excellent option due to their straightforward processing and frequently adjustable properties. In this context, graphene emerges as a promising platform for the biological recognition of glucose in real samples [293]. Zhang and colleagues developed a highly sensitive non-enzymatic glucose biosensor using a simple screen-printing method. Specifically, graphite electrodes were modified with a microflower structure composed of copper oxide/few-layer graphene, leading to a substantial enhancement in sensor performance. These sensors effectively mitigated interference from real sample components, such as dopamine and ascorbic acid. The 3D-printing approach simplified the fabrication process without compromising sensor efficacy. While reports on printed biosensors with 2D materials

are limited, they primarily focus on graphene-related materials for detecting biomolecules or monitoring human body activities through pressure sensors.

Yet, MXenes demonstrate promise as a material platform for printable and wearable sensors, as pioneered by *Guo et al.* [294]. Guo and collaborators introduced a groundbreaking flexible and degradable pressure sensor, marking the first instance of predicting patients' health status by electronically mapping the skin (i.e., electronic skin). The adjustable pressure sensor could be affixed to human skin for various biomonitoring tasks, including measuring wrist physical force, showcasing potential applications for predicting the healthcare status of early-stage Parkinson's disease. *Cheng et al.* [295] employed a straightforward abrasive paper stencil printing process to create an MXene-based piezo-resistive sensor with randomly distributed spinous microstructures. This sensor is designed to monitor body activities and medical states when placed on joints or muscles. In the realm of wearable sensors, temperature sensors are experiencing rapid advancements for on-skin temperature monitoring, allowing for real-time tracking. Wang and colleagues pioneered a stretchable temperature sensor using a cellular graphene/polydimethylsiloxane composite through a direct 3D ink-writing technique [296]. The authors claimed high-temperature sensitivity (0.008 ˚C) towards printed composites. Notably, the sensitivity of the printed grid structure remained stable even under significant external deformations, highlighting the considerable potential of flexible devices.

3.4 Nano/micromotors for Sensing

The progress made in nanotechnology has sparked the development of powerful artificial nano/micromotors that utilize energy to perform complex tasks on a miniature level.[14,297–299] The use of nano/micro motors to drive tiny machinery is a fascinating area of study, offering potential possibilities. These micromotors are capable of propelling liquids using various energy sources, converting them into powerful mechanical movement. This marks a significant advancement in the development of practical nanomachines, showcasing their ability to harness energy and take on a range of applications. Over the recent years, these nano/microscale motors have become increasingly prevalent. These miniature marvels utilized a variety of propulsion techniques and emerged as innovative contributors to this evolving field. Tubular micromotors, with lengths ranging from 5 to 15 μm and adjustable tube openings (1 to 5 μm diameter), have shown promising potential for developing selective assays in complex media. These micromotors typically feature an outer layer made of polymer or (carbon/2D) nanomaterials,

while the inner layer serves as a catalyst (platinum, manganese dioxide, silver, or zinc). An intermediate layer (usually nickel) can be included to control motion through a magnetic field; this is crucial for analytical applications mimicking the way magnetic particle-based assays work. Synthesis methods like template electrosynthesis or rolled-up approaches are commonly employed, with template electrosynthesis being preferred for its low cost, simplicity, and versatility in analytical applications. Janus micro motors, with their unique spherical morphology, combine different physical and chemical characteristics into one single unit to perform complex analytical tasks with proficiency. It can be composed of various materials (carbon nanomaterials, 2D nanomaterials, polystyrene, responsive polymers, magnesium) coated or incorporating catalytic metals, quantum dots, or magnetic materials. Different synthetic routes, including sputtering metallic films on microbeads, pickering emulsion, polymer self-assembly, or bipolar electrochemistry, contribute to their high versatility. Janus micromotors offer substantial possibilities in analytical chemistry, allowing easy tuning of their structure to incorporate multifunctional abilities, as demonstrated in previous publications from our research group [300–302].

In the era of rapid industrialization, the excessive release of harmful pollutants into water and air poses a significant threat to human health. Addressing this issue, researchers are actively pursuing advanced technologies for pollution detection, a crucial step in environmental remediation [117,118]. The evolution of micromotors has garnered attention in ecological science due to their remarkable advantages, such as small size and autonomous movement, enabling non-invasive and continuous mixing. These features make micromotors effective in efficiently detecting various pollutants in different sample types, even in low volumes. Tailored functional micromotors have been successfully applied in environmental science to sense toxins, bacteria, heavy metal ions, and more. For instance, Wang and team introduced an enzyme-powered micro fish micromotor, proving its efficacy as a potent tool for water quality testing through a speed-sensing strategy [303]. Similar to the correlation between the lifetime and swimming behaviour of live fish in natural settings with water quality, these micromotors swimming performance and lifespan were influenced by toxins in the water. Specifically, the micromotors were propelled by bubbles generated from catalase catalysis during H_2O_2 decomposition. Toxins could inhibit the enzyme catalase, the biocatalytic engine of the micromotor, causing a time-dependent loss in catalase activity and impacting motion performance. By observing the velocity, the enzyme-powered microfish offered optically sensitive visualization of changes in motion performance in the presence of pollutants like Hg^{2+}, Cu^{2+}, sodium azide, and

aminotriazole. Remarkably, this artificial microfish addressed ethical and reproducibility concerns, making it a powerful tool for real-time water quality testing. They later utilized bubble-propelled dye-coated micromotors for rapid detection of nerve agents like sarin and soman simulants, employing an 'on–off' fluorescent strategy [304]. The 'on–off' signal changes were induced by the quenching effect of nerve agents on the fluorescent dye. Autonomous locomotion significantly enhanced the fluorescence quenching efficiency of nerve agents, enabling real-time detection. In contrast to traditional static methods for nerve agent detection, these micromotors offered a real-time on-site sensing approach, showing great potential for detecting various chemical agents.

Utilizing the luminescence quenching mechanism, a bubble-propelled micromotor system with 'on–off' luminescence was introduced for efficient sensing of trinitrotoluene (TNT), a highly toxic substance with potential carcinogenic and mutagenic effects [305]. In another approach, Liu and colleagues [306] devised an 'on–off' fluorescent MnO_2-catalyzed bubble-powered micromotor for detecting Fe^{3+} in water with high sensitivity and excellent selectivity. These micromotors featured a hollow tubular structure with an outer layer of Eu-MOF and an inner layer of ethylendiaminetetraacetic acid (EDTA). Notably, EDTA, with its abundant functional groups, exhibited a strong affinity for heavy metal ions, including Fe^{3+}. This design allowed the micromotors to integrate the detection and removal of Fe^{3+} in the water sample, serving as a dual-functional tool for sensing and removing various targets in environmental sciences.

In addition to heavy metal ions and toxin detection, monitoring water pH is a crucial aspect of environmental science. Micromotor sensors, exhibiting pH-responsive fluorescent variations, serve as valuable tools for real-time pH sensing [307]. Leveraging this pH-responsive sensing strategy, Li and colleagues [308] introduced a biodegradable Fluorescein Isothiocyanate (FITC) based micromotor for gas sensing. These micromotors could detect gases such as ammonia (NH_3) and hydrogen chloride (HCl) capable of affecting solution pH, which operates exclusively in aqueous environments. The autonomous movement of micromotors accelerated solution mixing. As the fluorescence intensity of FITC correlated with the pH value, the micromotors displayed strong fluorescence in an NH_3 gas environment while showing minimal fluorescence in an HCl gas environment. Notably, these micromotors, primarily composed of a biodegradable polymer and enzyme-powered, minimized environmental pollution. Micromotor-based sensing platforms mark a new era in environmental science, overcoming previous sensing strategy limitations through their tiny size and autonomous movement.

Solovev et al. [309] developed a catalytic reaction-driven tubular micro/nanomotor using a Ti/Fe/Pt nanomembrane rolled into a tubular structure. This unmodified micro/nanomotor demonstrated substantial towing force through the bubble recoiling mechanism, efficiently capturing and transporting various particles. The tubular micro/nanomotors, floating on the solution and moving at the water-air interface [310], exhibited the capability to catch floating metallic nanoplates, assembling them into regular arrays. This delivery property was extended to capture and directionally transport microparticles and cells in microfluidic channels [311]. The easy modification of these micro/nanomotors allows for diverse biofunctions, including selective capture, transport, isolation, and release of biomolecules. *Kagan et al.* [16] created a tubular micro/nanomotor using the template-assisted electrodeposition method for effectively isolating nucleic acid targets through surface modification. Half-coated with Au, the tubular micro/nanomotors were then modified with a binary self-assembled monolayer consisting of a thiolated capture probe and short-chain 6-mercapto-1-hexanol. The modified tubular micro/nanomotors exhibited enhanced collection efficiency by selectively collecting surrounding targets, including single-stranded DNA, through local convection induced by bubble ejection.

Additionally, these biofunctionalized tubular micro/nanomotors, carrying the target DNA, moved forward to escape untreated samples, such as human serum, achieving selective capture, delivery, and isolation of target DNA in a complex sample solution. A similar approach was employed for rolled-up tubular micro/nanomotors [17]. Metallic tubular micro/nanomotors were fabricated and subjected to a deposition process, coating half of the tube with Au. The Au surface was then modified with streptavidin, enabling the capture of biotinylated beads. In another study, *Orozco et al.* [312] utilized a molecular imprinting method to create polymer-based catalytic reaction-driven tubular micro/nanomotors with biofunctions. Molecular imprinting occurred during the electrodeposition of the outer poly(3,4-ethylenedioxythiophene) (PEDOT) layer, allowing direct biofunctionalization with binding sites after template etching. The outer wall's recognition properties were maintained under harsh operating conditions, such as high temperature, pressure, and extreme pH [312]. Subsequently, researchers used biofunctionalized tubular micro/nanomotors to capture and isolate anthrax simulant spores. Visual confirmation of spore elimination was achieved via biofunctionalized tubular micro/nanomotors [313].

Micromotors hold immense potential in the field of sensing due to their self-propulsion behaviour. Here, we have provided an overview of the development of these micromotors and

their applications in sensing. Initially, we introduced propulsion mechanisms that allow the micromotors to move autonomously [307], followed by highlighting their sensing strategies. It also covered applications in environmental science, food safety, and biomedical areas. However, the practical implementation of micro motors for sensing continues to face challenges, as many rely on toxic materials and corrosive fuels, raising concerns about potential contamination. The small size limits fuel and catalyst loading, impacting motion performance and lifespan.

Additionally, limited surface area hinders the immobilization of functional molecules, affecting detection sensitivity. Present micromotor-based sensing platforms are often specialized and lacking flexibility. Addressing these challenges requires further scientific efforts to make micromotor-based sensing platforms more adaptable for practical use.

Part I

3D-printed Electrodes for Sensing and Biosensing Applications

This page is left intentionally

Chapter 4.1

3D-printed nanocarbon sensors for the detection of chlorophenols and nitrophenols: Towards environmental applications of additive manufacturing

Published: Electrochemistry Communications 125 (**2021**) 106984

Presented: The 3rd Cross-Border Seminar on Electroanalytical Chemistry (CBSEC 2021)' & Ph.D. Retreat (2021)

4.1.1 Introduction

There is a substantial need to diagnose the phenolic compounds in industrial, environmental, or food samples because of the phenolic compound's toxic behaviour [314,315]. Conventional analytical methods used for detection, such as chromatography [316], capillary electrophoresis [317], and spectrophotometry [318], are time-consuming and not portable. Electrochemical methods have been proven suitable for rapid and mobile detection of phenols and their substituents [319,320]. Various electrochemical analytical techniques (such as voltammetry) can be used to to facilitate the electrochemical oxidation of the phenols at the solid electrode and, thus, enable their detection. Unfortunately, these phenolic compound's electro-oxidation produces phenoxy radicals, which combine to form a passivating layer at the electrode surface [314]. Considerable efforts have been made to identify new electrode materials and develop a surface pre-treatment that would effectively avoid surface fouling effects caused by the oxidation of the phenols [321–323]. 3D-printing to fabricate phenol sensing platforms represents a promising approach, as electrodes can be fabricated at low cost. 3D-printing, also known as additive manufacturing, is a recent technology that consists of a layer-by-layer deposition process guided by computer-aided design (CAD) software [11]. This novel technique has many advantages compared to traditional electrode manufacturing techniques, including the rapid production of devices with low waste generation, high accuracy, repeatability, high resolution, and high durability.

Furthermore, it offers the possibility of customizing the produced object shape and geometry through a highly automated system with minimal human intervention [8,9]. In particular, the fused deposition modelling (FDM) printing technique can be utilized for the fabrication of the 3D-printed nanocarbon electrodes (3DnCE), where a composite filament consisting of thermoplastic polymer (polylactic acid (PLA)) and nanocarbon is extruded down the nozzle, and the desired shape is printed. Inconsolably, these surfaces provide poor electrochemical activity due to the high amount of PLA needed for the successful extrusion and deposition of the materials. Hence, activation (post-treatment) is necessary to increase the electrochemical activity of the electrodes [324]. Thermal, electrochemical, and solvent treatment activations are the most used ones [325]. However, the solvent treatment activation using *N,N'*-dimethylformamide (DMF) represents one of the simplest and fastest approaches, providing improved electrochemical responses due to the removal of the PLA and the exposure of the nanocarbon on the electrode surface [326].

In this work, we demonstrate for the first time that the 3DnCEs significantly improve the sensing of phenolic compounds through voltammetric measurements. Such improvements promote the oxidation process by delaying the kinetics of polymeric film formation [327] on the electrode surface, as it is possible to sense the analytes at higher concentrations than glassy carbon electrodes. Cyclic voltammetry (CV) and differential pulse voltammetry (DPV) techniques have been used to investigate the oxidation behaviour of phenols. Furthermore, the pH conditions have been optimized for an enhanced electrochemical response of the phenolic compounds. 3DnCEs have been proven for the simultaneous detection of several compounds. These developments provide insight into the application of a 3DnCE for the voltammetric detection of phenolic compounds.

4.1.2 Experimental Section

Reagents

Phenol, 2,3-dichlorophenol, 2,4-dichlorophenol, 2,6-dichlorophenol, 3-chlorophenol, 4-chlorophenol, 2,4,6-trichlorophenol, 4-nitrophenol were purchased from Sigma-Aldrich (Czech Republic). Monobasic potassium phosphate (Sigma) and dibasic potassium phosphate (Merck), sodium chloride (Merck), and potassium chloride (Merck) were used for the preparation of phosphate buffer solution (PBS) were purchased. Deionized water having resistivity not less than 18.2 MΩ cm was used. Commercially available filament, conductive nanocarbon/ polylactic acid (PLA) filament (Graphene Laboratories Ink., New York, USA) was used for 3D-printing of the electrodes. pH measurements were carried out by Thermo Scientific Orion Star A111 pH meter.

Fabrication of 3DnCE using graphene/PLA filament

For the fabrication, fused deposition modelling is a method in which a spool of thermoplastic filament is melted inside a printing nozzle and laid down layer by layer according to the input program assigned to the printer (Prusai3 MK3s printer, Prusa Research, Czech Republic) with an Olsson Ruby ruby-tipped 0.6 mm nozzle (3DVerkstan, Sweden). Nanocarbon/PLA filament is evicted from the nozzle at a temperature of 220 °C and bed temperature of around 60 °C as the printing conditions [9,328,329]. The dimensions of the 3D-printed electrode were as follows: length: 1.6 cm, width: 0.6 cm (r = 0.3 cm) and 3mm thickness. Just the circular portion of the electrode was immersed in the electrolytic solution for the electrochemical estimations [330].

The as-printed electrode consists of a composition of conductive graphene and non-conductive PLA polymer. Solvent activation was carried out to improve the electrode's electrical conductivity by immersing the printed nanocarbon electrodes in DMF for six hours. After six hours, the electrodes were rinsed thoroughly with ethanol and then with ultrapure water and let dry for 24 hours [324].

Electrochemical Instruments

The electrochemical measurements were conducted at room temperature (25 ^{0}C) using a three electrodes configuration where Ag/AgCl (1 M KCl) was used as a reference electrode, a platinum wire was used as a counter electrode, and 3DnCE served as a working electrode, using Metrohm Autolab (PGSTAT 204) operated by Nova 2.14 software.

Material Characterization

The surface morphology of the 3DnCEs was evaluated with scanning electron microscopy (SEM) using the Verios 460L instrument (FEI, USA) to assess the changes before and after DMF treatment.

Electrochemical Detection

The influence of pH on the 4-chlorophenol voltammograms was investigated by CV using 50 µM 4-chlorophenol in 100 mM PBS as an electrolyte solution at different pH values (3,5,7,9,11). The scan rate of 10 mVs^{-1} was maintained for the various analytes.
5 mM stock solutions of (phenols, 2,3-dichlorophenol, 2,4-dichlorophenol, 2,6-dichlorophenol, 3-chlorophenol, 4-chlorophenol, 2,4,6-trichlorophenol, 4-nitrophenol) were prepared in 100 mM PBS solution, and DPV was performed at pH 11 by varying concentration (25-125 µM) of each analyte.

4.1.3 Results and Discussion

As described previously, we activated the nanocarbon/PLA electrodes (3DnCE) using a DMF activation method, which was mentioned earlier in [326]. Structural characterization of 3DnCE was performed using SEM to investigate the effect of the DMF treatment on the electrode morphology. The 3D-printed electrode surface is highly dominated by the presence of PLA,

which aggregated nanocarbons forming a composite with a dense structure **Figure 12(A)**. The SEM image of the DMF-treated 3DnCEs **Figure 12(B)** reveals that PLA has been partly removed from the electrode surface, and the nanocarbon forms a mesh-like structure [324].

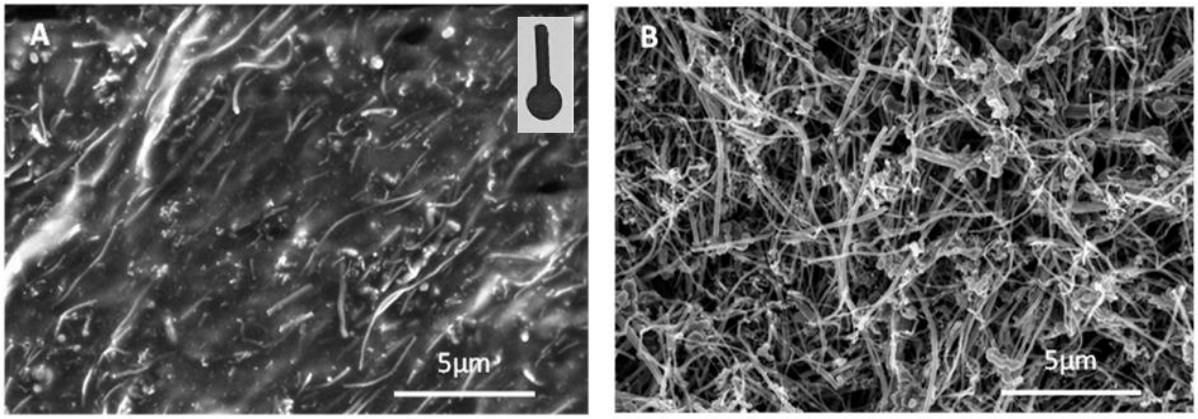

Figure 12. SEM of 3DnCE (A) PLA/nanocarbon electrode without activation (inset) photograph of the 3DnCE as/printed (B) PLA/nanocarbon electrode after DMF activation.

Subsequently, we employed the activated 3DnCE to detect 4-chlorophenol as an archedtypal compound. To evaluate the accuracy and precision of the 3DnCE, five different electrodes have been taken and measured their response value in 4-chlorophenol by keeping the concentration (100 µM) constant. The output response of all the different electrodes was consistent and obtained a mean peak current at 0.24 µA and a relative standard deviation of 8.81% (n=5). Since the pH value has a vital role in the electro-oxidation process of 4-chlorophenol, as a phenolic group dissociates, the electrochemical characterization was carried out at various pH values. CV **Figure 13(A)** shows the oxidation peak corresponding to the oxidation of 4-chlorophenol to the chloro-phenoxy radical, which appears during the positive scans. However, no reduction peak appears, suggesting that the process is chemically irreversible.

Interestingly, a reversible redox peak with 0.3 V oxidation and 0.2 V reduction value was observed at pH 3. This could be attributed to the presence of oxygenated functional groups (such as quinones) in nanocarbon electrodes [325]. When the pH is changed, electrochemical behaviour is affected in two ways. As the pH increases, the peak intensity also increases significantly, but the oxidation of the 4-chlorophenol is shifted to lower potential values. The rise in the peak intensity can be related to the availability of 4-chlorophenol in the anion form at higher pH values. Similarly, the peak shifts towards the lower potential values are associated

with the low pK_a value of the 4-chlorophenol as while shifting from the acidic medium to the alkaline solutions, the concentration of the H^+ ions decreases, which shifts the equilibrium towards the 4-chlorophenol anion species (see Eq. (3)).

$$C_6H_4ClOH \leftrightarrow C_6H_4ClO^- + H^+ \qquad \text{Eq.3}$$

Figure 13(B) shows oxidation potential values as a function of pH in PBS. The oxidation potential value decreases with the increase in the pH values following a linear trend, which is in close agreement with the Nernst equation (Eq. (4)):

$$E = E^0 + 0.059pH \qquad \text{Eq.4}$$

Where E^0 is the standard electrode potential, and E is the potential at 25 ^{0}C. The slope extracted from the fitted equation (y = -0.0487x + 1.0604) is 0.0487, shown in **Figure 13(B)**, corresponding approximately to n=1 from 0.059/n. Therefore, the oxidation of the 4-chlorophenol implies one electron and one proton have been transferred in the electrochemical reaction.

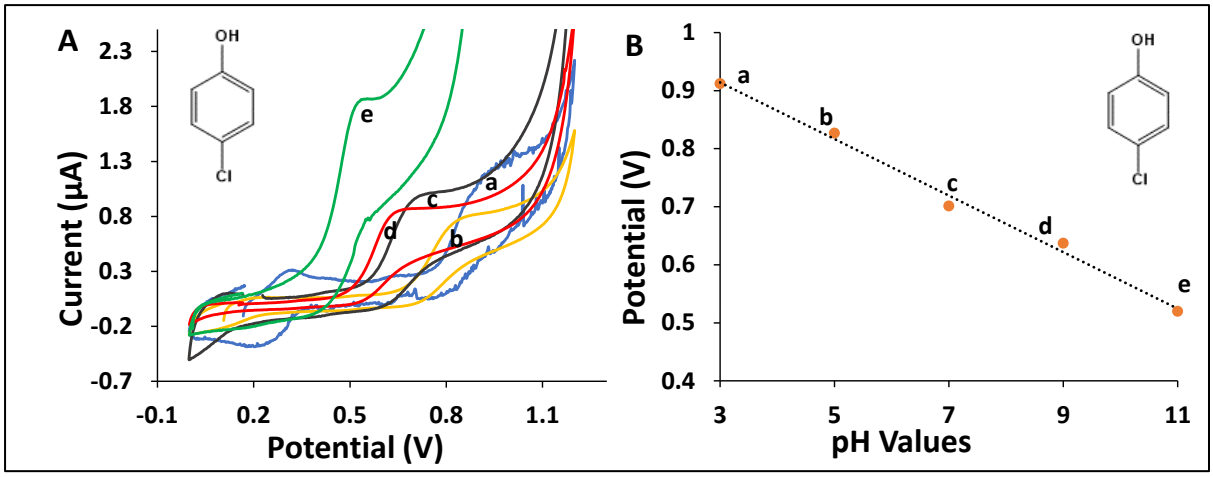

Figure 13. (A) Influence of pH on CV response of 50µM 4-chlorophenol in 100 mM PBS between +1.2 V and 0 V at a scan rate of 10 mVs^{-1} (a) pH 3 (b) pH 5 (c) pH 7 (d) pH 9 (e) pH 11. (B) Oxidation potential values of 50 µM 4-chlorophenol as a function of pH in PBS.

These results emphasize the influence of pH on the electro-oxidation process of 4-chlorophenol and conclude that the oxidation reaction would be favoured in the strong alkaline medium (pH 11). The oxidation reaction would be favoured because the current obtained at that pH is the

highest and the oxidation potential the lowest. Further studies were continued using this optimum pH value.

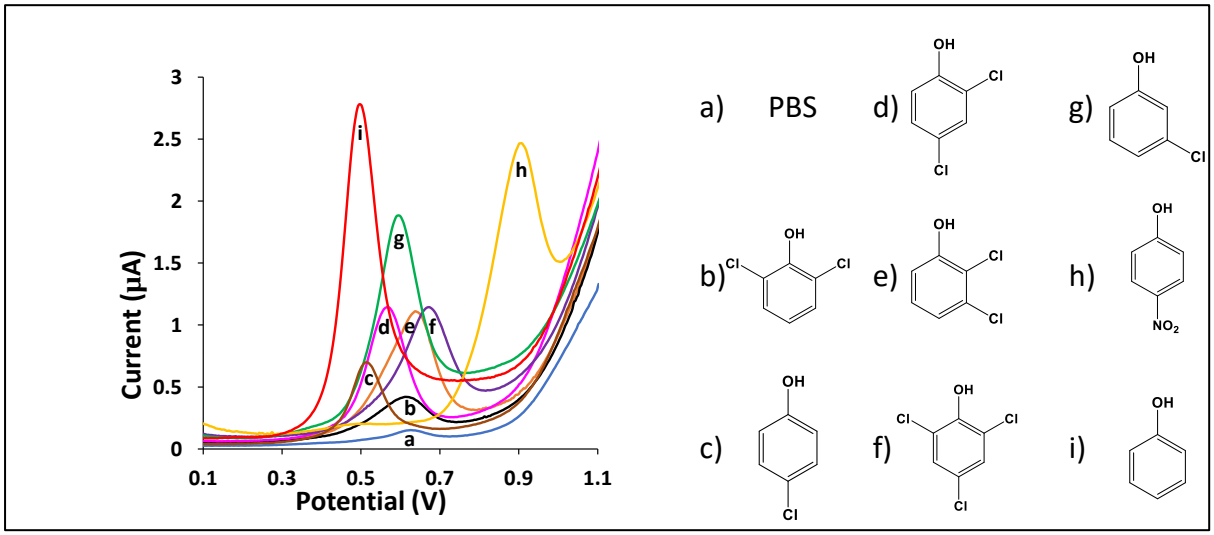

Figure 14. Influence of chemical structure of chlorophenols, nitrophenol and phenol on their voltammetric response (a) PBS (b) 2,6-dichlorophenol (c) 4-chlorophenol (d) 2,4-dichlorophenol (e) 2,3-dichlorophenol (f) 2,4,6-trichlorophenol (g) 3-chlorophenol (h) 4-nitrophenol (i) phenol, conc. 50 µM Conditions: DPV scan rate 10 mVs^{-1}, PBS buffer (100 mM, pH11)

The voltammetric behaviour of 2,3-dichlorophenol, 2,4-dichlorophenol, 2,6-dichlorophenol, 3-chlorophenol, 4-chlorophenol, 2,4,6-trichlorophenol, 4-nitrophenol, phenol, was studied using differential pulse voltammetry (DPV). **Figure 14** displays the typical voltammograms of various chlorophenols, 4-nitrophenol, and phenol in PBS (100 mM, pH 11) using 3DnCE. Each of these phenolic compounds shows an oxidation peak, attributed to the formation of the corresponding phenolate ions, which appear at different potentials and provide different currents. These differences in the electrochemical behaviour are correlated with the structural differences of the compounds.

It has been reported that the electrochemical oxidation of aromatic compounds may be impacted by the number of substituents, as well as their electronic nature and positioning at the aromatic ring [331]. Not only the ring substituents influence the reactivity of the phenolic compounds through steric, resonance (mesomeric, ±M), and field (inductive, ±I) effects, but also the electron-withdrawing substituents decrease the basicity (lower the pK_a) of phenol. On the other hand, electron-donating substituents increase the basicity and nucleophilicity of phenol [332]. The pK_a value of the phenol, 4-chlorophenol, 2,4-dichlorophenol, 3-chlorophenol, 2,6-dichlorophenol, 2,3-dichlorophenol, 2,4,6-trichlorophenol and 4-nitrophenol is 10.02,

9.38, 7.89, 9.02, 6.79, 7.45, 6.42, 7.15, respectively [333]. Corresponding, their oxidation potential vs Ag/AgCl is 498 mv, 513 mv, 568 mv, 593 mv, 612 mv, 637 mv, 670 mv, and 901 mv, respectively. There is an increase in the oxidation potential of disubstituted chlorophenols as compared to monosubstituted chlorophenols. The greater stability of the compound is directly correlated to the number of substituents, which favours the electronic delocalization, thus lowering the compound's acidic strength [334]. Therefore, phenolic compounds with electron-withdrawing substituents are more resistant to oxidation than the phenols with electron-donating substituents.

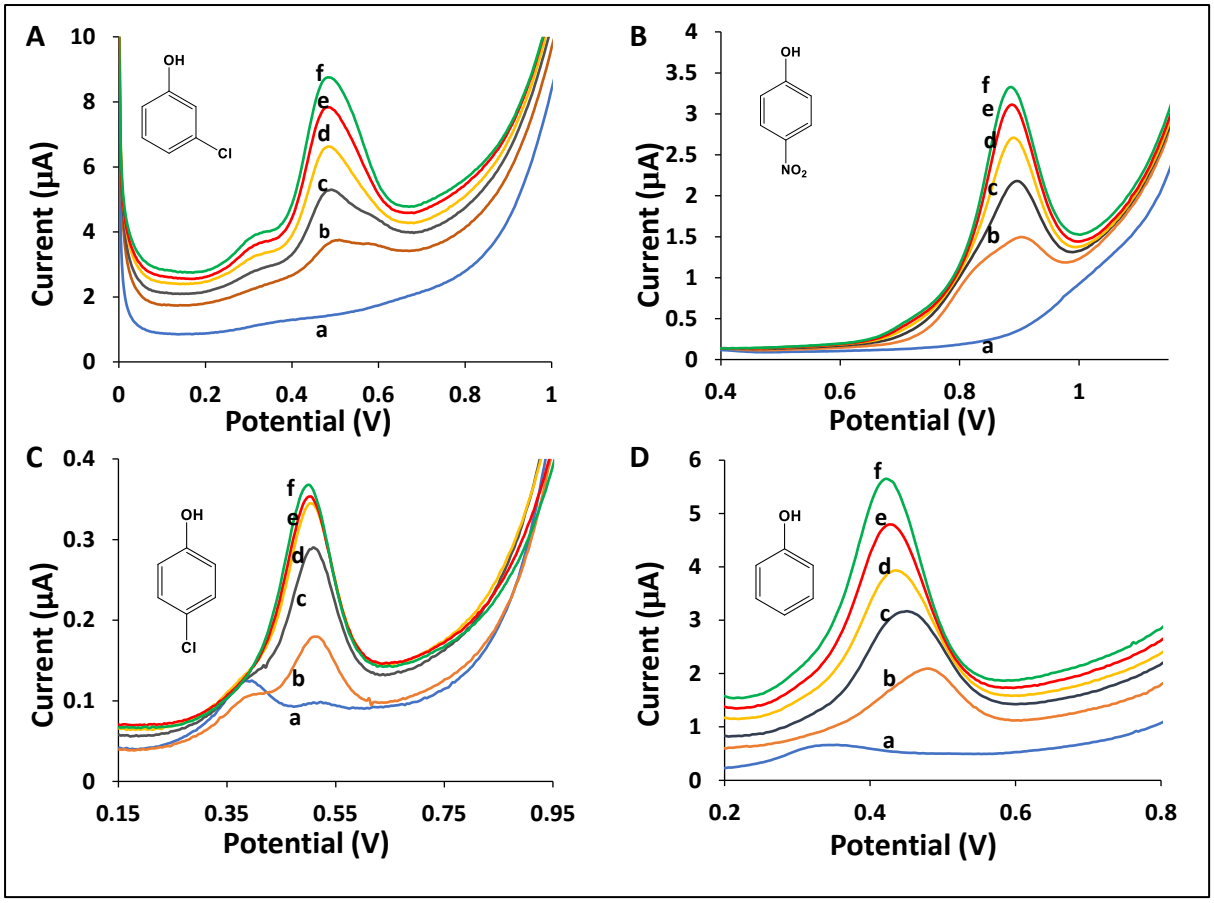

Figure 15. Effect of concentration of (A) 3-chlorophenol (B) 4-nitrophenol (C) 4-chlorophenol and (D) phenol on the DPV response, (a) in PBS, (b) 25 µM, (c) 50 µM, (d) 75 µM, (e) 100 µM and (f) 125 µM of each analyte, respectively, using a 100 mM PBS at pH 11.

Calibration curves were constructed for 3-chlorophenol, 4-nitrophenol, 4-chlorophenol, and phenol. **Figure 15(A–D)** shows the DPV responses of the 3DnCEs using different concentrations of 3-chlorophenol, 4-nitrophenol, 4-chlorophenol, and phenol in 100 mM PBS at pH 11. Comparing the DPVs obtained in the presence and absence of analytes illustrates the

successful electro-oxidation of the phenols, chlorophenols, and nitrophenols. These compounds show characteristic oxidation peaks using the 3DnCEs, and their intensity is proportional to

the concentration. To compare the analytical performance of a 3D-printed electrode with glassy carbon, a concentration calibration study of 4- nitrophenol was carried out **(Figures 16 and 17)** using a glassy carbon electrode. **Figure 16** shows the DPV response of the glassy carbon electrode as the concentration of 4-nitrophenol is varied.

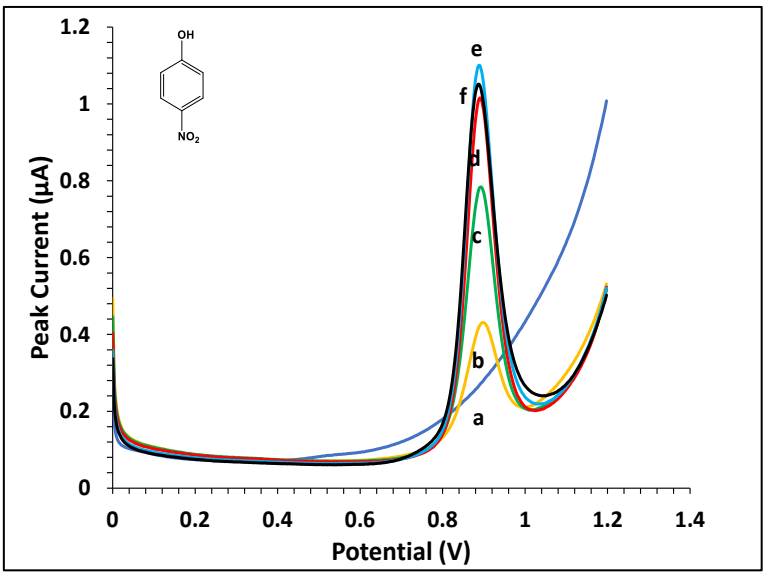

Figure 16. Effect of concentration of 4-nitrophenol on the DPV response using glassy carbon electrode (a) in PBS, (b) 25 µM, (c) 50 µM, (d) 75 µM, (e) 100 µM and (f) 125 µM, respectively, using a 100 mM PBS at pH 11.

Similarly, **Figure 17** shows the concentration calibration curve of 4-nitrophenol using a glassy carbon electrode. It is clear that after 100 µM concentration, passivation of the electrode occurs, as there is a decrease in the current intensity at 125 µM compared to 100 µM. By contrast, **Figure 15(B)** shows the same study carried out using a 3DnCE electrode, where no passivation is observed, and the peak intensity increased continuously as far as 125 µM concentration. Furthermore, the current peak intensities of the glassy carbon electrode were lower than those of the 3DnCE. However, the peak potential is observed at 0.88 V, which is similar to the value found with the 3DnCE.

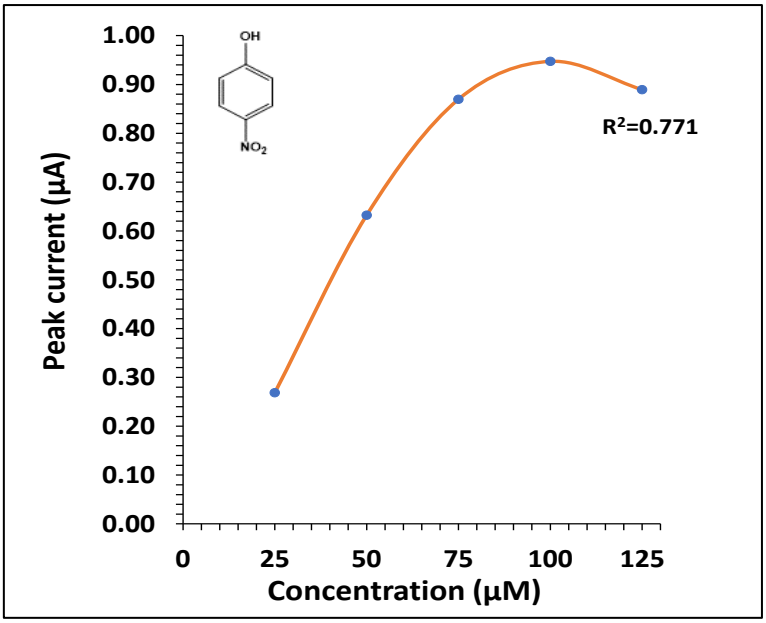

Figure 17. DPV Calibration curves of 4-nitrophenol by using a glassy carbon electrode. Between 25-125 µM of the analyte in 100 mM PBS at pH 11.

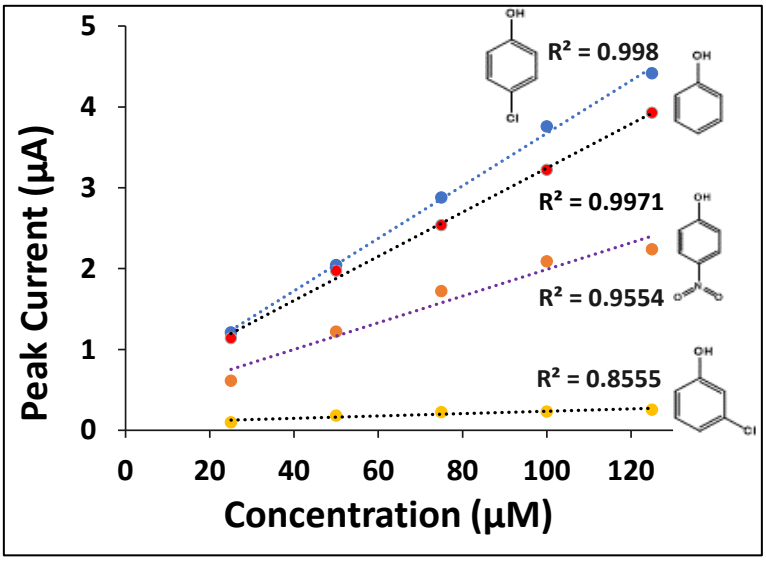

Figure 18. DPV Calibration curves of 3-chlorophenol, 4-nitrophenol, 4-chlorophenol and phenol. Between 25-125 µM of the analytes in 100 mM PBS at pH 11.

The calibration graphs of peak current density versus analyte concentration are plotted in **Figure 18** for different phenols, chlorophenols, and nitrophenols. Interestingly, the linear plots for all the analytes gave similar results, i.e., the peak current density increases with the increase in the concentration and reaches a maximum value of up to 125 µM. Whereas in glassy carbon

electrode, the maximum concentration is lower, only reaching to the 100 µM. Hence, 3D-printed electrodes show better response with lower rates of passivation with respect to glassy carbon electrode.

The calibration curves obtained for 3-chlorophenol, 4-nitrophenol, 4-chlorophenol, and phenol are y = 0.0325x + 0.4257, y = 0.0165x + 0.3408, y = 0.0014x + 0.0917 and y=0.0273x + 0.5152, respectively. It is clear that 3-chlorophenol and phenol detection is more sensitive than the remaining compounds [335].

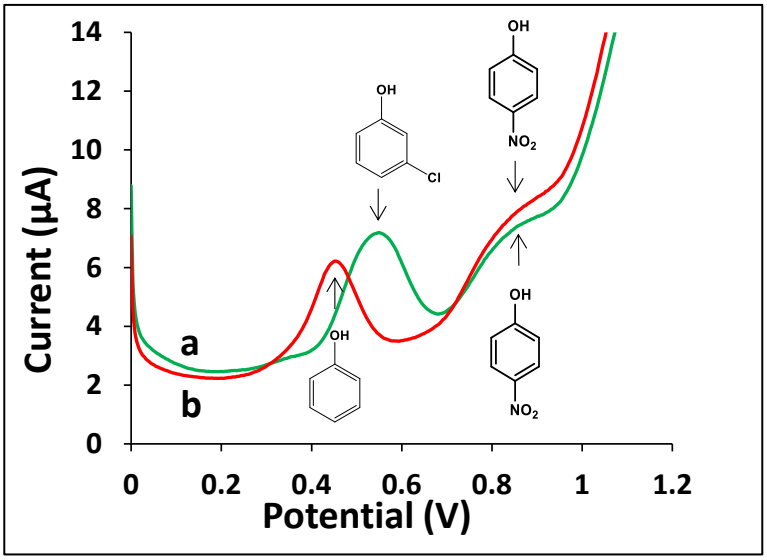

Figure 19. Determination of phenols mixtures. DPV for mixtures of phenolic compounds in 100 mM PBS at pH11: (a) 3-chlorophenol and 4-nitrophenol and (b) phenol and 4-nitrophenol at 50 µM concentrations of each compound.

We investigated the simultaneous detection of phenols. Two simultaneous detections of mixtures of 3-chlorophenol with 4-nitrophenol and phenol with 4-nitrophenol were carried out by DPV analysis (**Figure 19**) using 3DnCEs. This was performed simultaneously by keeping the same, i.e., 50 µM concentration of each compound. The results show well-defined independent anodic peaks at 0.545V and 0.823V and 0.450V and 0.805V, which correspond to the oxidation of the 3-chlorophenol and 4-nitrophenol; or phenol and 4-nitrophenol, respectively. This indicates that the simultaneous determination of 3-chlorophenol and 4-nitrophenol or phenol and 4-nitrophenol compounds is feasible with 3DnCEs [336].

4.1.4 Conclusion

In Chapter 4.1, we have demonstrated the utility of the 3D-printed nanocarbon electrodes as electrochemical detectors for the individual and simultaneous detection of phenolic compounds in aqueous solutions. The electrochemical behaviour of phenolic compounds was thoroughly studied by using voltammetry. The influence of pH on the oxidation of phenols was studied, and it was found that alkaline pH is the most suitable for the detection of these phenolic compounds. The chemical nature of the substituent plays a vital role in the oxidation potential of these phenolic compounds due to the inductive and mesomeric effects. Furthermore, the increase in the number of substituents also shifted the oxidation potential towards more positive values. The simultaneous analysis of various phenolic compounds in the mixture was also successfully carried out. Thus, 3D-printed electrode offers great promise for the environmental screening and industrial monitoring of toxic phenolic compounds.

List of Abbreviations

3D	Three dimensional
3DnCE	3D-printed nanocarbon electrodes
DMF	*N,N'*-dimethylformamide
SEM	Scanning Electron Microscopy
EDS	Energy Dispersive Spectroscopy
XPS	X-ray photoelectron spectroscopy
CAD	Computer-aided design
FDM	Fused Deposition Modelling
PLA	Polylactic acid
CV	Cyclic voltammetry
DPV	Differential Pulse Voltammetry
PBS	Phosphate Buffered Saline
±M	Mesomeric
±I	Inductive
µM	Micromolar
mM	Millimolar
mV s^{-1}	Mili volt per second

This page is left intentionally

Chapter 4.2

3D-printed Electrochemical Sensor for Organophosphate Nerve Agents

Published: Electroanalysis 2023, 35, 139 –144

4.2.1 Introduction

3D-printing has propelled the manufacturing of electrochemical sensors due to its enormous benefits, such as low price and fast prototyping. Its ability to produce autonomous fabrication with minimal human intervention and waste makes it an exceptional tool [8,9]. The manufacture of custom-made electrodes for particular capabilities with control over the dimensions, configuration, and morphology will be beneficial in electrochemistry [337]. Fused deposition modeling (FDM), which has gained popularity for 3D-printing, uses thermoplastic material for electrode fabrication [4]. Such electrodes have proven to be adaptable and useful in a variety of applications, including environmental measurements, energy storage, and bio-sensors [325,338,339]. This utilization of 3D-printed electrodes has encouraged the detection of different analytes with diverse electrochemical activity.

Organophosphate nerve agents act as precursors for chemical warfare agents and pesticides due to their rapid action and toxicity [323,340]. Many tons of these chemical bombs are claimed to have been disposed of in the oceans all over the world after World War II, presenting a threat to the whole of the biosphere [341,342]. The toxicity of these compounds is of great concern; hence, a detection method that is fast, compact, and reliable is required. Various analytical procedures, such as gas chromatography [343–345] and liquid chromatography [344–347], are used frequently for the detection of organophosphates and are shown to be sensitive and have high precision. However, these techniques require a tedious setup and complex procedures that are not suitable for field-based analysis. On the contrary, electroanalytical methods have great advantages such as high sensitivity, fast response, simplicity to operate and comparatively low cost [348,349].

The use of 3D-printed metal electrodes for the detection of nitroaromatic explosives and nerve agents has been reported [337]. However, these 3D metal electrodes have a few drawbacks, including cost and limited pH operating range [338]. Non-metal materials, such as graphene [67,350–353], carbon nanotubes [354–356], mesoporous carbon [357,358], etc. and their composites [359,360] have been used as alternatives to metals because they have good electrochemical performance as sensors and their surface properties can be tuned to desired responses. These methods require complex electrode surface modifications. To make the process facile and user-friendly, and to avoid complications such as surface modifications, 3D-printed can be used as an alternative. 3D-printed nano-carbon electrodes (3DnCEs) have proven to be efficient and cost-effective (2–3 Euro cents approx. per electrode) as sensors. The filament used in 3DnCEs

is a combination of nanocarbon and polylactic acid (PLA). The latter is a thermoplastic polymer and is responsible for the successful extrusion of the nanocarbon from the printer nozzle into the desired shape [361,362]. These filaments provide an encouraging platform for the electrochemical sensing of phenols [10,319]. Following the 3D-printing process, the electrochemical activity of the 3DnCEs is then activated for PLA removal [324]. Various post-treatment methods, such as chemical [324,326,363], electrochemical [324], and thermal treatment [325,364], are widely used. These treatments increase the electrode's electrochemical response by exposing the nanocarbon on the surface of the electrode after the significant removal of PLA. The use of *N*,*N'*-dimethylformamide (DMF) as a solvent activator is regarded as an easy and rapid approach [326]. These refinements also favor detection by delaying the surface passivation of the electrode [327].

Herein, we focused on an alternative sensing tool for the detection of organophosphates using 3D-printing technology. 3DnCEs were employed for the electrochemical investigation of organophosphate nerve agents (Scheme1) by displacing the 3D metal electrodes and the standard glassy carbon electrodes (GCEs). 3DnCEs significantly improved the sensing of organophosphate nerve agents through voltammetric measurements. As proof, a comparison was done between standard glassy carbon electrodes (GCEs) and the 3DnCEs using cyclic voltammetry (CV). 3DnCEs have also been tested for the detection of fenitrothion, methyl parathion, parathion, and paraoxon using differential pulse voltammetry (DPV).

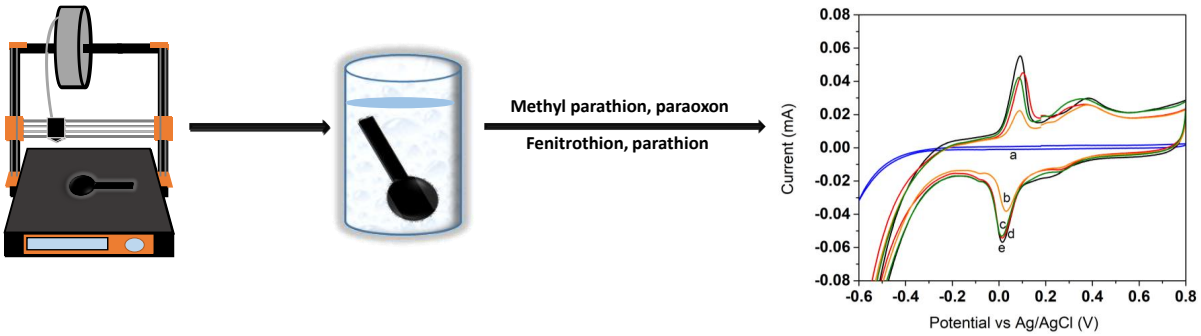

Scheme 1. Fabrication of 3DnCEs using fused deposition modeling and their activation by DMF for the detection of various organophosphates by means of cyclic voltammetry.

4.2.2 Experimental section

Reagents

Methyl parathion, paraoxon, parathion, and fenitrothion were purchased from Sigma-Aldrich (Czech Republic). Acetone (Merck) was used to make the stock solutions. Sodium acetate buffer (3M, pH 5.2±0.1) was obtained from Sigma-Aldrich. Deionized water was utilized with a resistivity of at least 18.2 MΩ cm. The electrodes were 3D-printed using available conductive nanocarbon/ PLA filament (Graphene Laboratories Ink., New York, USA). To prepare $[Fe(CN)_6]^{3-/4-}$ redox probe electrolyte, 1 mM of both $K_3Fe(CN)_6$ and $K_4Fe(CN)_6$ were mixed in a 0.1 M KCl aqueous solution.

3DnCE fabrication using graphene/PLA filament

Fused deposition modeling was utilized to create 3D printed electrodes using a 3D printer (Prusai3 MK3s printer, Prusa Research, Czech Republic) with an Olsson Ruby ruby-tipped 0.6 mm nozzle (3DVerkstan, Sweden). The printing parameters were 220 °C nozzle temperature and 60 °C bed temperature [9,328,329]. The specifications of the 3D-printed electrode were: length 1.6 cm, breadth 0.6 cm (r = 0.3 cm), and thickness 3 mm [362]. The rectangular section was 0.2 cm wide. For the measurements, only the circular section of the electrode was submerged in the electrolyte solution. However, the freshly printed electrodes contained a composite of an insulating PLA polymer and conducting graphene. To improve their electrical conductivity, the as-printed nanocarbon electrodes were immersed in DMF for six hours. Then, the electrodes were cleaned with ethanol and subsequently with ultrapure water and allowed to air-dry for 24 hours.

Electrochemical instruments

Analytical measurements were carried out using Metrohm Autolab (PGSTAT 204) and Nova 2.14 software at 25 °C (room temperature). They were performed in a three-electrode set-up cell filled with a redox marker aqueous solution consisting of 1 mM $K_3[Fe(CN)_6]/K_4[Fe(CN)_6]$ containing 0.1 M KCl as the electrolyte. The reference, counter, and working electrodes were Ag/AgCl, Pt wire, and activated 3DnCEs, respectively. CV measurements were performed at

a scan rate of 10 mV s^{-1}. The modified Randles-Ševčík equation was used to compute the electroactive area (*A*) of the 3DnCE (Eq. (5)) [324]:-

$$Ip = 3.01*10^5\, n^{3/2}\, (\alpha\, D_{red}\, v)^{1/2}\, A\, C^*red, \qquad \text{Eq. (5)}$$

Where I_p is peak current, *n* is the number of electrons ($n = 1$), α for symmetry factor ($\alpha = 0.5$), D_{red} for reduced species diffusion coefficient ($D_{red} = 6.32\ 10^{-6}$ cm ^{2} s $^{-1}$), *v* is the scan rate, and C*red is the bulk concentration of electroactive ions. 1.86 cm^2 was computed as the electrochemically active area *A*.

Materials characterization

To analyze the alterations before and after DMF treatment, the surface morphology of the 3DnCEs was examined using scanning electron microscopy (SEM) on the Verios 460L instrument (FEI, USA), having an electron beam accelerating voltage of 5 kV. X-ray photoelectron spectroscopy (XPS) was used to determine the atomic configuration of the 3DnCEs using an AXIS Supra instrument (Kratos Analytical, Japan) with monochromatic Al Ka (1486.7 eV) as excitation source and the data were plotted using Casa XPS software.

Electrochemical detection

Cyclic voltammetry (CV) and differential pulse voltammetry (DPV) were used to evaluate the electrochemical properties of the 3DnCEs. 1mM stock solutions of methyl parathion, parathion, fenitrothion, and paraoxon were prepared in 25 mL acetone. A buffer solution of 20 mM sodium acetate (pH 5.2) was made, and CV and DPV were performed at different analyte concentrations (2-72 µM). For the various analytes, a scan rate of 50 mV s^{-1} was maintained.

4.2.3 Results and Discussion

3DnCEs were activated using DMF, as reported previously [365]. The SEM images in **Figure 20** manifest the 3DnCE surface morphology before and after activation. **Figure 20(A)** depicts the dominance of the PLA, which formed a dense composite structure with nanocarbon filaments. The partial removal of PLA and disclosure of the nanocarbon filaments (mesh structures) on the electrode's surface is depicted in **Figure 20(B)**.

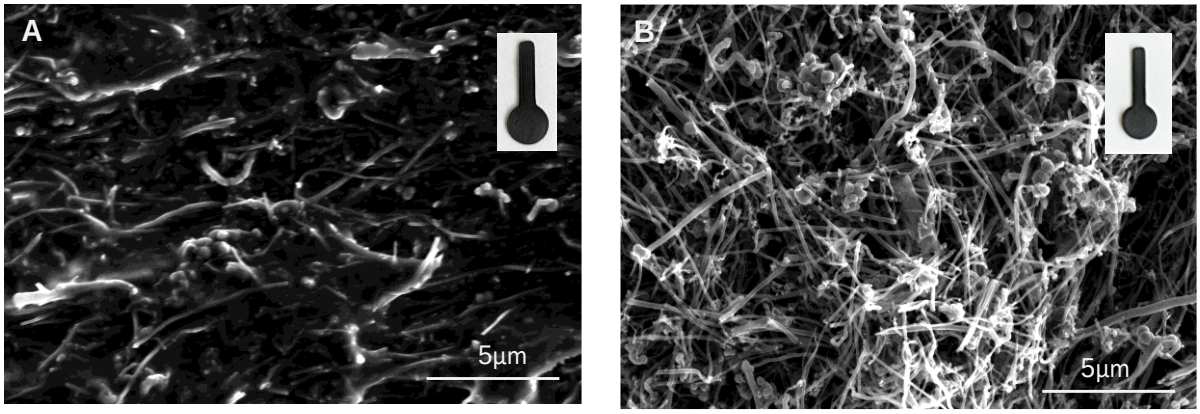

Figure 20. SEM image of a 3DnCE (A) PLA/nanocarbon electrode before activation. Inset image of the printed 3DnCE with a circular diameter 0.6 cm (B) 3DnCE after DMF activation.

Figure 21 presents the X-ray photoelectron spectroscopy (XPS) image of the 3DnCE before and after activation to reveal the chemical composition of the electrode surface. The wide-scan XPS spectra in **Figure 21** detect carbon and oxygen as the primary elements. The polymer matrix contained carbon and oxygen as significant elements, and the filament contained nanocarbon filler [325,366,367]. The peaks of the as-printed 3DnCE revealed that the PLA/nanocarbon electrodes largely contained PLA polymer (77% C *vs.* 23% O). After DMF activation, we observed a significant increase in carbon percentage (83% of C *vs.* 17% of O), indicating that the PLA had been partially removed, exposing the nanocarbon on the electrode's surface.

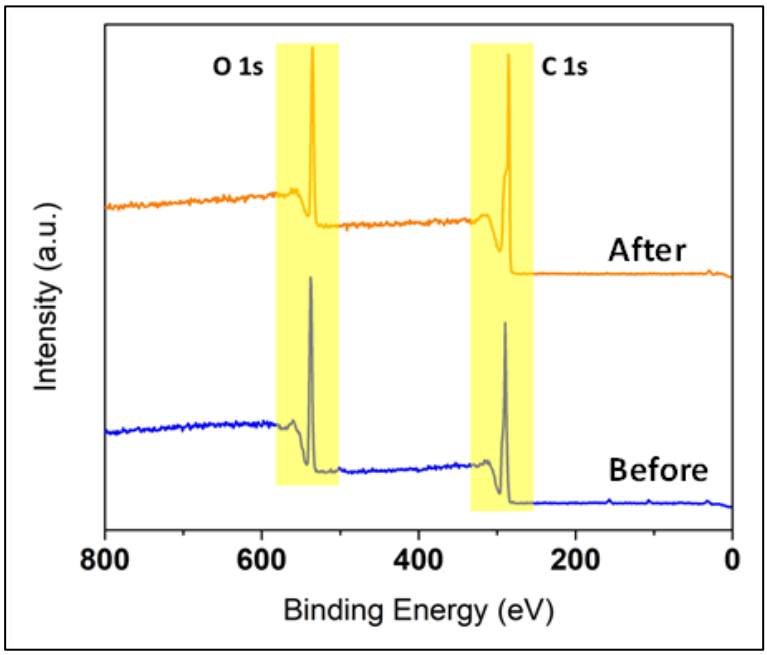

Fig 21. XPS spectra of 3DnCEs before and after activation.

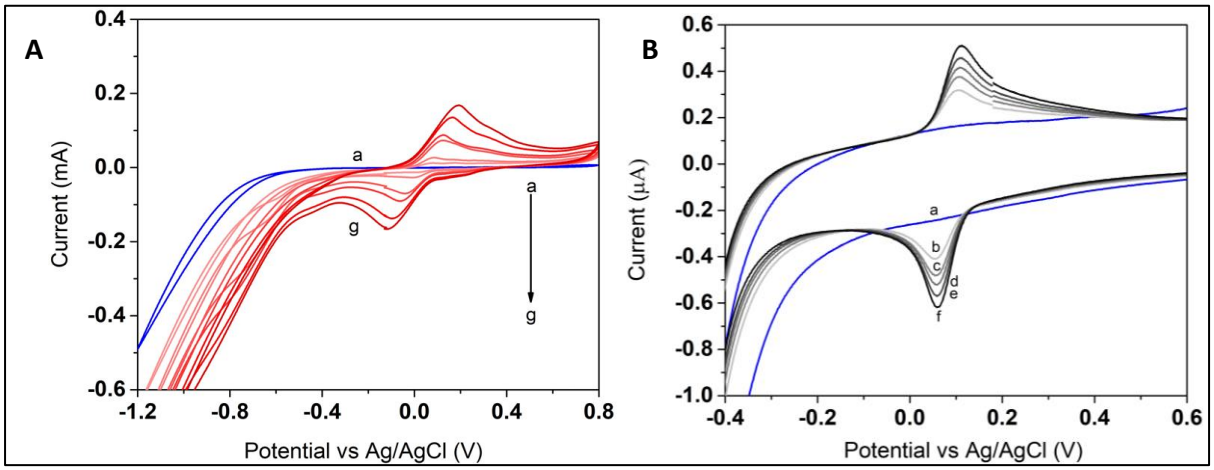

Figure 22. (A) Cyclic voltammograms showing response of methyl parathion at various concentrations of (a) 0 µM, (b) 2 µM, (c) 6 µM, (d) 20 µM, (e) 30 µM, (f) 56 µM, (g) 72 µM, using 3DnCE. **(B)** Cyclic voltammograms of methyl parathion at (a) 0 µM, (b) 6 µM, (c) 12 µM, (d) 20 µM, (e) 30 µM and (f) 56 µM, at glassy carbon electrode. Conditions: 20 sodium acetate buffer, pH 5.2.

Cyclic voltammetry was used to investigate the electrochemical activity of the 3DnCE toward methyl parathion. **Figure 22(A)** represents CVs of blank and various concentrations of the analyte (methyl parathion) from 2 µM to 72 µM in 20 mM sodium acetate buffer solution (pH 5.2) at a sweep rate of 50 mV s^{-1} [323]. Two primary electrochemical responses were observed while cycling the electrode in the potential range of -1.2 to 0.8 V. The first one displayed a couple of distinct redox peaks, having an oxidation potential (E_{pa}) of ~0.12 V and a reduction potential (E_{pc}) of ~0.0 V. The second response exhibited a peak at E_{pc} = −0.6 V (reduction potential) [368–373].

We utilized the current of the reduction peak as an analytical signal, as its current increased linearly as the concentration of the methyl parathion increased. The linear equation obtained from the linearly fitted curve between the cathodic current *vs* the methyl parathion concentration (2 µM to 72 µM) had a slope of -2.41 µA/µM with a correlation coefficient of 0.99. To evaluate the reproducibility of the 3DnCEs, the response of the electrodes (n = 5) was observed in 5 µM of methyl parathion, with RSD of 5%. The calculated limit of detection (LOD) was 0.5 µM. To compare the 3DnCE with the conventional glassy carbon electrode, CV was also performed using the glassy carbon electrode (GCE) for the methyl parathion while keeping the parameters constant (scan rate 50 mV s^{-1}) as shown in **Figure 22(B)**. A greater

reversibility was observed (anodic potential E_{pa} = 0.11 V and cathodic potential E_{pc} = 0.05 V), which could be attributed to the smooth surface of the GCE.

The advantage of 3D printed electrodes is demonstrated by the faster rate of passivation at the GCE compared to 3DnCE (not shown). The current response of the GCE was lower in comparison to 3DnCE with regression coefficient value, R^2 = 0.91. The electroactive area was calculated using the Randles-Ševčík equation (Eq. 1) for both 3DnCE and GCE, giving 1.86 cm^2 for the 3DnCE and 0.15 cm^2 for the GCE [374,375]. A control experiment was performed for the other organophosphates (paraoxon, fenitrothion, and parathion) under the same conditions.

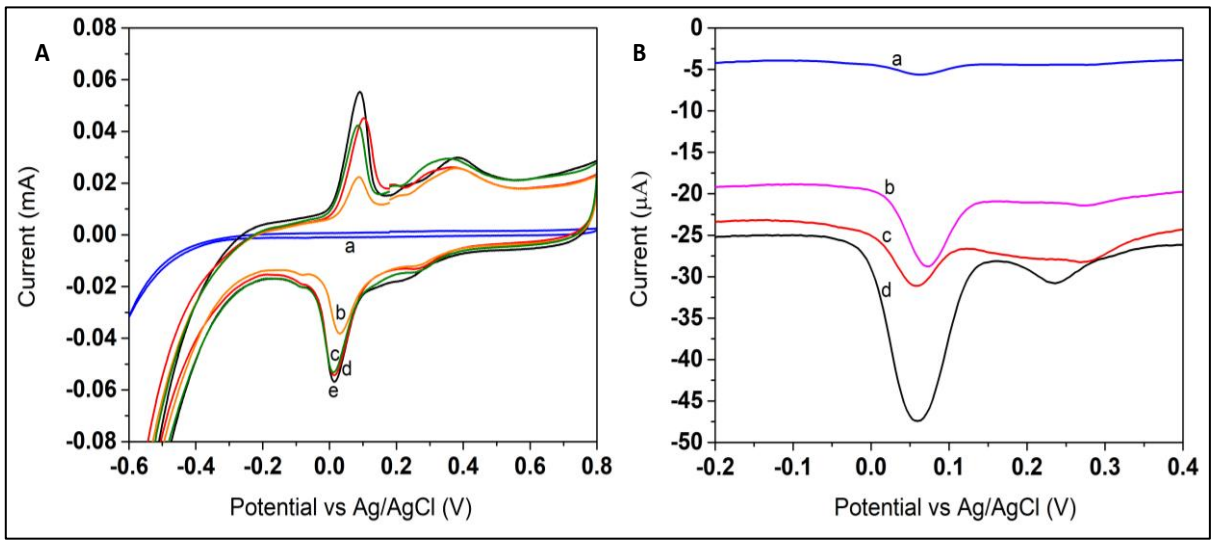

Figure 23. (A) Cyclic voltammetric responses of (a) blank buffer solution, (b) paraoxon ethyl, (c) parathion, (d) methyl parathion, (e) fenitrothion. **(B)** DPV responses of (a) methyl parathion, (b) paraoxon ethyl, (c) parathion, and (d) fenitrothion. Conditions: 5 µM concentration of each analyte, 20 mM acetate buffer (pH 5.2).

Figure 23(A) shows the electrochemical responses of parathion, paraoxon, fenitrothion and methyl parathion. As these organophosphates (OPs) possess a similar structure as methyl parathion, they also exhibit identical electrochemical characteristics [323,376,377]. It should be noted the peak current was different for different OPs, as shown in the DPVs in **Figure 23(B)**. This was because the response of the OPs was affected by their molecular structures [372,373]. **Figure 24** shows the DPV response of fenitrothion at different concentrations (15–75 µM) in 20 mM sodium acetate buffer solution (pH 5.2). The reduction peak appeared on the addition of the fenitrothion in the solution, and it increased with increased concentration of analyte [323,378]. Similarly to the previous example, fenitrothion followed the same reduction

mechanism. It showed a peak at around 0.07 V. A series of different concentrations were analyzed and the linear trend following the peak current and the concentration, with slope of -23.6 μA/mM (R^2 = 0.99).

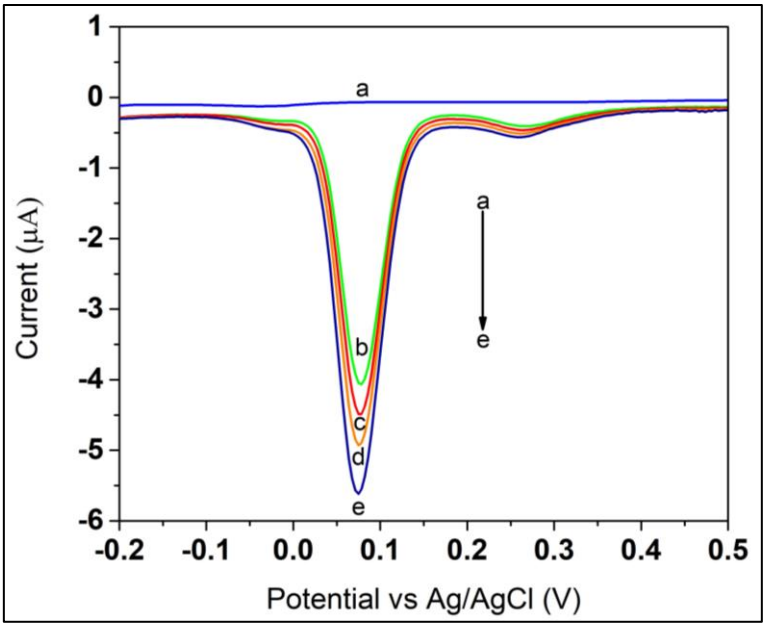

Figure 24. Concentration dependence of DPV signal of fenitrothion, (a) in blank sodium acetate, (b) 15 μM, (c) 30 μM, (d) 50 μM, (e) 75 μM. Conditions: 20 mM sodium acetate buffer solution (pH 5.2).

To evaluate the feasibility of the proposed electrochemical sensor, methyl parathion was measured in four different water samples. Real water samples (tap, river, pond, and lake water) were collected. Then, 1 mM methyl parathion was spiked in 1 mL of tap, river, pond, and lake water samples in 1:20 dilution. To perform the electrochemical measurement, the 1 mL spiked water samples containing the analyte were further mixed with 10 mL sodium acetate buffer solution. Therefore, the final concentration of the methyl parathion in the solution was 4.5 μM in each case. An intense peak was observed, as shown in **Figure 25**. These findings confirm the similar behavior to that previously reported data. Hence, the developed 3DnCE sensor has outstanding detection capabilities for organophosphates in real samples as well.

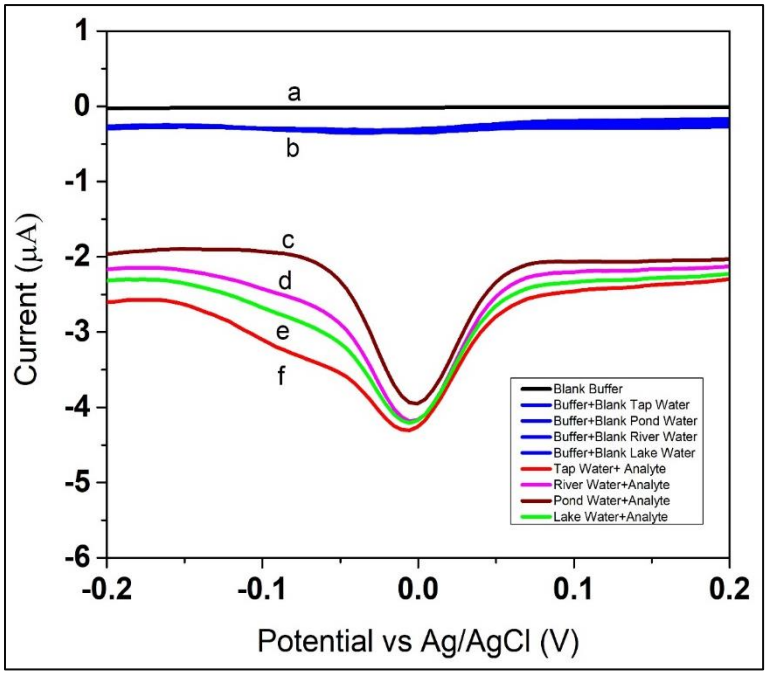

Fig. 25: Real sample analysis for 3DnCE in (a) blank sodium acetate buffer (black), (b) blank sodium acetate buffer with blank real water samples (tap, river, pond, lake) shown in blue colour. Whereas the buffer with real water sample (1 mL) containing 20x diluted methyl parathion is shown in different colours. (c) Buffer with 1ml pond water containing 20x analyte (maroon), (d) Buffer with 1ml river water containing 20x analyte (pink), (e) Buffer with 1ml lake water containing 20x analyte (green), (f) Buffer with 1ml tap water containing 20x analyte (red), respectively. Conditions: 20 mM sodium acetate buffer, pH 5.2, Methyl parathion stock solution concentration 1mM.

4.2.4 Conclusions

The viability of 3D-printed nanocarbon electrodes for the electrochemical reduction of methyl parathion, parathion, paraoxon and fenitrothion has been proved by utilizing cyclic voltammetry and differential pulse voltammetry. The projected technology provides new possibilities for sustainable, cost-effective, simple, rapid, and sensitive OPs analysis. Although the development of 3D-printed electrochemical sensors and their applications are in its early stages, it has a lot of potential for on-demand decentralized fabrication of such electrochemical detectors.

List of Abbreviations

3D	Three dimensional
3DnCE	3D-printed nanocarbon electrodes
DMF	*N,N'*-dimethylformamide
SEM	Scanning Electron Microscopy
EDS	Energy Dispersive Spectroscopy
XPS	X-ray photoelectron spectroscopy
CAD	Computer-aided design
FDM	Fused Deposition Modelling
PLA	Polylactic acid
CV	Cyclic voltammetry
DPV	Differential Pulse Voltammetry
PBS	Phosphate Buffered Saline
µM	Micromolar
mM	Millimolar
mV s^{-1}	Mili volt per second

This page is left intentionally

Chapter 4.3

Geno sensing on a 3D-printed Nanocarbon Electrode

Published: Electrochemistry Communications 151 (2023) 107508

Presented: Poster presentation: International Conference on Materials and Nanomaterials (MNs-22), Rome, 25-27 July 2022.

Project: Received Specific Research Internship (CEITEC VUT-J-22-8081)

4.3.1 Introduction

Over the past few years, 3D-printing, also referred to as additive manufacturing, has emerged as a powerful tool for fabricating a range of analytical devices and custom labware [8,379,380]. Technology has given rise to innovative applications in many fields. It provides practical solutions to scientific problems and has found a distinct segment in environmental protection [9,10]. The technology consists of layer-by-layer deposition of the appropriate material and instant formation of the required 3D object. In comparison to more traditional subtractive methods, 3D-printed devices can provide several advantages, including i) easy fabrication approach; ii) reduced waste output owing to fast production; iii) great precision, consistency, and resolution; iv) shape and geometries modification; v) little human interventions; vi) availability of a diverse variety of materials that may be treated, allowing for multifunctional qualities; and vii) excellent durability without loss of sensitivity and efficiency [8,11,361]. In response to those advantages, the scientific community has begun to employ 3D-printing technologies to provide analytical devices, particularly for electrochemical biosensing [381,382].

This work reports on enzyme-linked electrochemical detection of DNA hybridization using 3D-printed nanocarbon electrodes (3DnCes). Various electrochemical methods have been introduced that use enzyme-coupled detection based on enzymes such as alkaline phosphatase [383–392], peroxidase [393,394], or glucose oxidase [395] in combination with the respective substrates. As a result of enzymatic conversion of the substrate, electrochemically detectable products (such as electrochemically oxidizable 1-naphthol) are formed [248,277,396–399]; such an approach takes advantage of the signal amplification caused by the ability of the enzyme molecule to convert multiple substrate molecules into the electroactive indicator. In contrast to complex, time-consuming electrochemical enzyme-linked techniques requiring electrode surface modification, interfacing or various immobilization procedures, the DNA modification with a bio affinity tag (such as biotin) in connection with target DNA (t-DNA) adsorption at the carbon electrode surface enables the enzyme-linked detection to be performed in a very simple way [277,400–402].

In the following sections, we demonstrate the characterization of the 3DnCe and the development of a system for electrochemical detection of DNA hybridization (based on a facile adsorptive immobilization of the t-DNA on the 3DnCe surface and its hybridization with a complementary probe linked with alkaline phosphatase enzyme).

4.3.2 Experimental Methods

Materials and Chemicals Used

Sodium carbonate (Na_2CO_3), sodium bicarbonate ($NaHCO_3$), disodium phosphate (Na_2HPO_4), monopotassium phosphate (KH_2PO_4), bovine serum albumin (BSA), Tween®20, and 1-naphthyl phosphate were purchased from Sigma-Aldrich and streptavidin-alkaline phosphatase (SALP) from Promega. Commercially available filament (graphene/polylactic acid (PLA)) was collected from Graphene Laboratories, Inc., New York, NY, USA (commercial name of the product "Black Magic 3D"). By mixing 1 mM $K_3Fe(CN)_6$, 1 mM $K_4Fe(CN)_6$ and 0.1 M KCl, $[Fe(CN)_6]^{3-/4-}$ redox electrolyte was prepared. 1x sodium phosphate buffer (PBS) of pH 7.4 was prepared by mixing 10 mM Na_2HPO_4, 1.8 mM KH_2PO_4, 137 mM NaCl and 2.7 mM KCl in 1 liter of distilled water. Carbonate buffer (pH 9.5) consisted of 0.5 M Na_2CO_3 and 0.5 M $NaHCO_3$.

Oligodeoxynucleotides (ODN; with or without 5'-biotin modification) acquired from Sigma-Aldrich; their sequences were as follows:

Target (t-DNA): 5'-GGCACAAACACGCACCTC

Complementary biotinylated probe: 5'-Biotin-GAGGTGCGTGTTTGTGCC

Non-complementary control (NC): 5'-Biotin-CCCTAACCCTAACCCTAACCCTAA

3DnCes printing with nanocarbon/PLA filament

The electrode printing was done using the Fused Deposition Modeling (FDM) methodology. FDM is a rapid manufacturing technique that involves layer-by-layer coating of thermoplastic material in accordance with the printer's input program. The printer (Prusa i3 MK3s printer with an Olsson Ruby ruby-tipped 0.6 mm nozzle (3DVerkstan, Sweden) from Prusa Research, Czech Republic) was used for printing the electrodes. Printer settings included 220 °C as the extrusion temperature of nanocarbon/PLA filament from the nozzle and 60 °C as the bed temperature [361,395,403]. The 3D-printed electrode dimensions were 1.6 cm in length, 0.6 cm in breadth (r = 0.3 cm), and 3 mm in thickness. The rectangular section was 0.2 cm wide. Electrochemical measurements were carried out by immersing the circular section of the electrode into the background electrolyte solution [362].

In order to enhance the electrical conductivity of the 3DnCes, a previously developed solvent-activation procedure was used [327]. For activation, the as-printed electrodes were immersed in *N, N*-dimethylformamide (DMF) overnight to expose the graphene encapsulated within 3D-printed objects without disrupting their structural and mechanical properties, as shown in **Scheme 2**. After activation, ethanol was used to wash the electrodes, followed by ultrapure water and thermal drying for one hour at 120 °C [364].

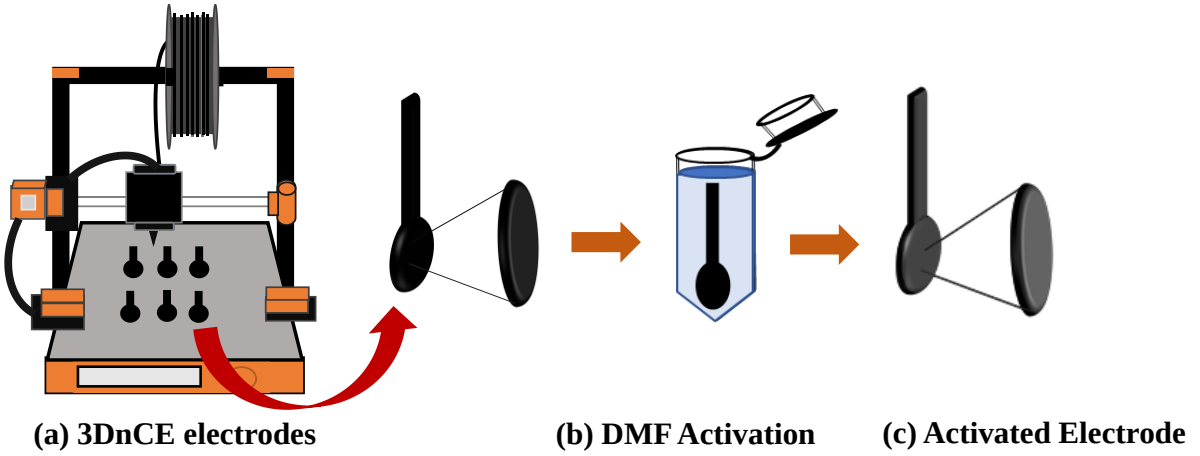

Scheme 1: Schematic representation of the fabrication and activation of 3DnCe: (**a**) printing of 3DnCe; (**b**) solvent activation (DMF); (**c**) 3DnCe after DMF activation.

Material characterization

Analysis of the 3DnCe surface morphology before and after DMF activation was carried out with scanning electron microscopy (SEM) using a TESCAN LYRA3 with an accelerating voltage of 10 kV. The atomic composition of 3DnCe was analyzed by X-ray photoelectron spectroscopy (XPS) using an AXIS Supra instrument (Kratos Analytical, Japan) with monochromatic Al Ka (1486.7 eV) excitation source and the spectra were fitted using Casa XPS software.

ODN hybridization on the electrode surface and electrochemical measurements

The t-DNA (50 µg/mL) was adsorbed at the 3DnCe electrode surface using a 10 µL drop containing 200mM NaCl for 120 seconds (s). The concentrations of ODNs varied according to the experiment while keeping the NaCl concentration at 200mM. The electrode with adsorbed

t-DNA was then washed with 1x sodium phosphate buffer (PBS), pH 7.4, for 60 s, followed by incubation in 5% bovine serum albumin (BSA) in PBS for 120 s to block the ODN-uncovered surface of the electrode. Afterwards, the electrode was rewashed in 1x PBS for 60 s. Then, the biotinylated probe of concentration 50 µg/mL (10 µL) was added on the electrode surface in order to hybridize with t-DNA for 120 s.

After the hybridization step, the electrode was rinsed with 1x PBS for 60 s and then incubated for 120 s in 1.5 mL 1x PBS solution containing 100-fold diluted streptavidin-alkaline phosphatase (SALP) and 2% BSA. In this step, the SALP conjugate was attached to the biotinylated DNA probe. After that, the electrode was rinsed in 1x PBS containing 0.05% Tween20 for 60 s, followed by 60 s washing with 1x PBS. After final rinsing, to carry out electrochemical measurements, the electrode was placed in a voltammetric cell containing 15 mL carbonate (0.5 M K_2CO_3 and 0.5 M $NaHCO_3$) buffer (pH 9.5), containing 0.5mM 1-naphthyl phosphate. For the enzymatic production of electroactive 1-naphthol from inactive 1-naphthyl phosphate, the electrode with immobilized SALP was incubated in the solution for 180 s before voltammetric measurements in the same solution (see **Scheme 3**). Subsequently, linear sweep voltammetry was used to detect the enzyme-produced 1-naphthol, with initial potential −0.5 V, end potential +0.9 V, scan rate 1 V/s, and potential step 5mV. The 3DnCes were used as working electrodes, Ag|AgCl|3 M KCl electrode as a reference, and platinum wire as an auxiliary electrode. Peak heights were measured relative to linear baseline in GPES4 software with all peak potentials indicated against Ag|AgCl|3 M KCl.

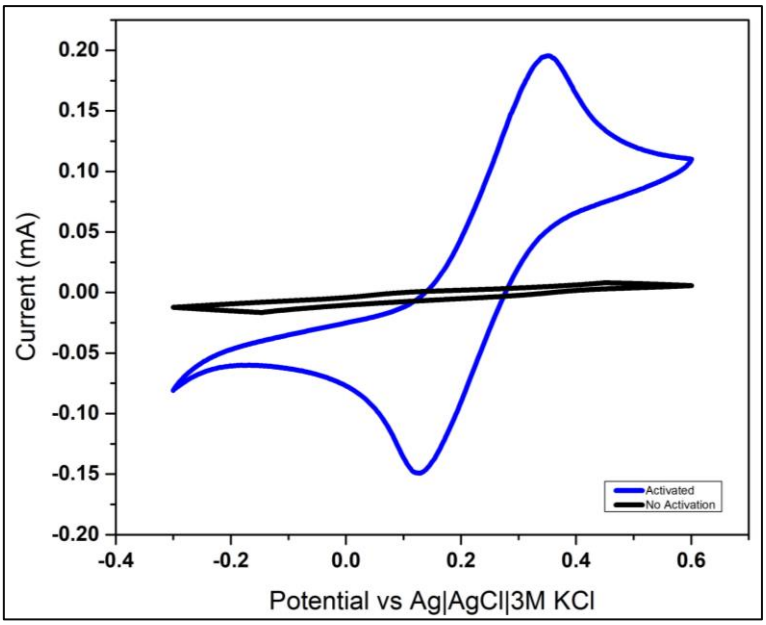

Figure 26: Evaluation of the electroactive area of the 3D-printed electrode. Voltammetric measurements were performed in a three-electrode cell containing a redox marker aqueous solution comprised of 1mM K_3[Fe

$(CN)_6]/K_4[Fe\ (CN)_6]$ containing 0.1M KCl. Cyclic voltammetric response of the 3D-printed electrode at a scan rate of 10 mV/s. (**Black**) as-printed and (**Blue**) DMF activated (for 15 hours).

To compute the electroactive area of the 3D-printed electrode, cyclic voltammetric (CV) measurements were performed at a scan rate of 10 mV/s in a three-electrode cell containing a redox marker aqueous solution of 1 mM $K_3[Fe\ (CN)_6]/K_4[Fe\ (CN)_6]$ containing 0.1 M KCl, using a CHI440 Electrochemical Workstation (CH Instruments, Inc., USA), at room temperature (25 °C) as shown in **Figure 26.**

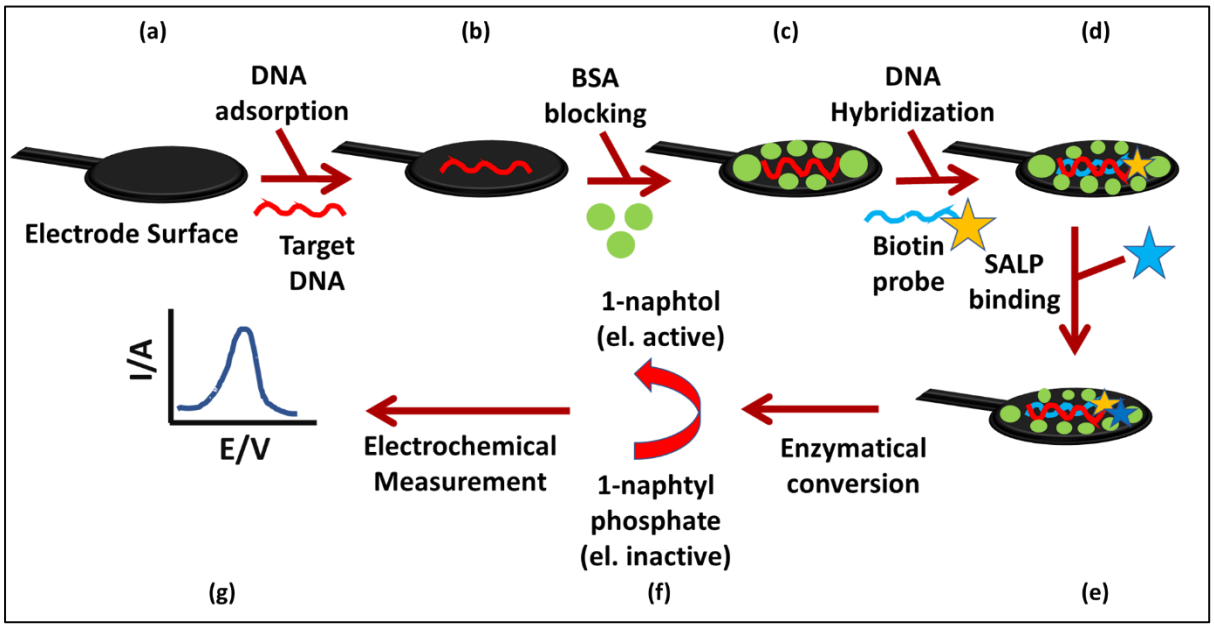

Scheme 3: Schematic representation of the analytical protocol: (**a**) introduction of the 3DnCe; (**b**) immobilization of the t-DNA on 3DnCe; (**c**) BSA blocking; (**d**) introduction of biotinylated probe and hybridization event; (**e**) binding of SALP; (**f**) conversion of 1-naphthyl phosphate to 1-naphthol; (**g**) electrochemical measurements.

4.3.3 Results and Discussion

Characterization of the 3DnCe

SEM characterization was done to explore the microstructure of the 3DnCe before and after DMF treatment **Figure 27**. A close examination revealed that the as-printed electrodes consisted of nano-carbon (nano-C) with a filament-like structure embedded in the polymer matrix, as shown in **Figure 27(A)**. However, there was a significant drop in the amount of the PLA after DMF activation while retaining the nano-C almost completely **Figure 27(B)**. As a

result, more conductive nano-C was exposed on the electrode surface, thus increasing its electro-active area [326].

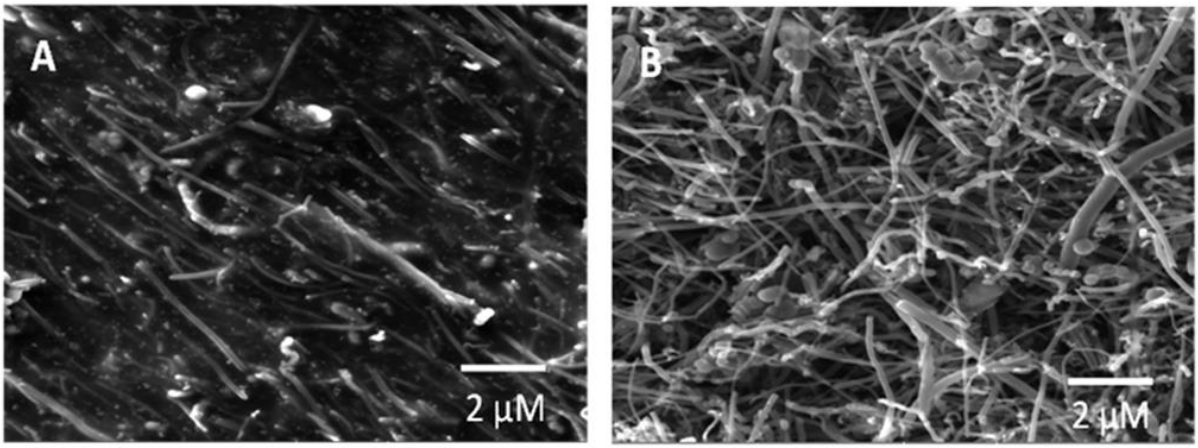

Figure 27: SEM of 3DnCe: (**A**) PLA/nano-carbon electrode as-printed (without DMF treatment); (**B**) PLA/nano-carbon electrode after overnight DMF treatment.

XPS spectroscopy was also performed to determine the elemental composition of the activated 3DnCe as shown in **Figure 28**. The wide scan XPS spectrum in **Figure 28(A)** identified carbon and oxygen as the primary components of each sample due to the presence of polymer matrix and nano-C filler [366,367]. The quantitative analysis of the peaks of the as printed 3DnCe confirmed that the electrode was mostly composed of PLA polymer (67% of C *vs*. 33% of O). Deconvolution of the C 1s spectrum **Figure 28(B)** showed that its peak distribution comprised three peaks at 285, 287, and 289 eV, which were ascribed to the C–C, C–O, and C=O functions that make up the PLA, respectively. A considerable increase in carbon content was detected after DMF activation of the 3DnCe, indicating a partial breakdown of the PLA. Moreover, a new carbon peak was observed at 285 eV, which was associated with the C=C of the nano-C embedded on the electrode surface, indicating the removal of an additional PLA (**Figure 28(C)**). In consequence, the percentage of C in nano-C fibers increased (92% of C *vs*. 8% of O) as shown in **Figure 28(A)**.

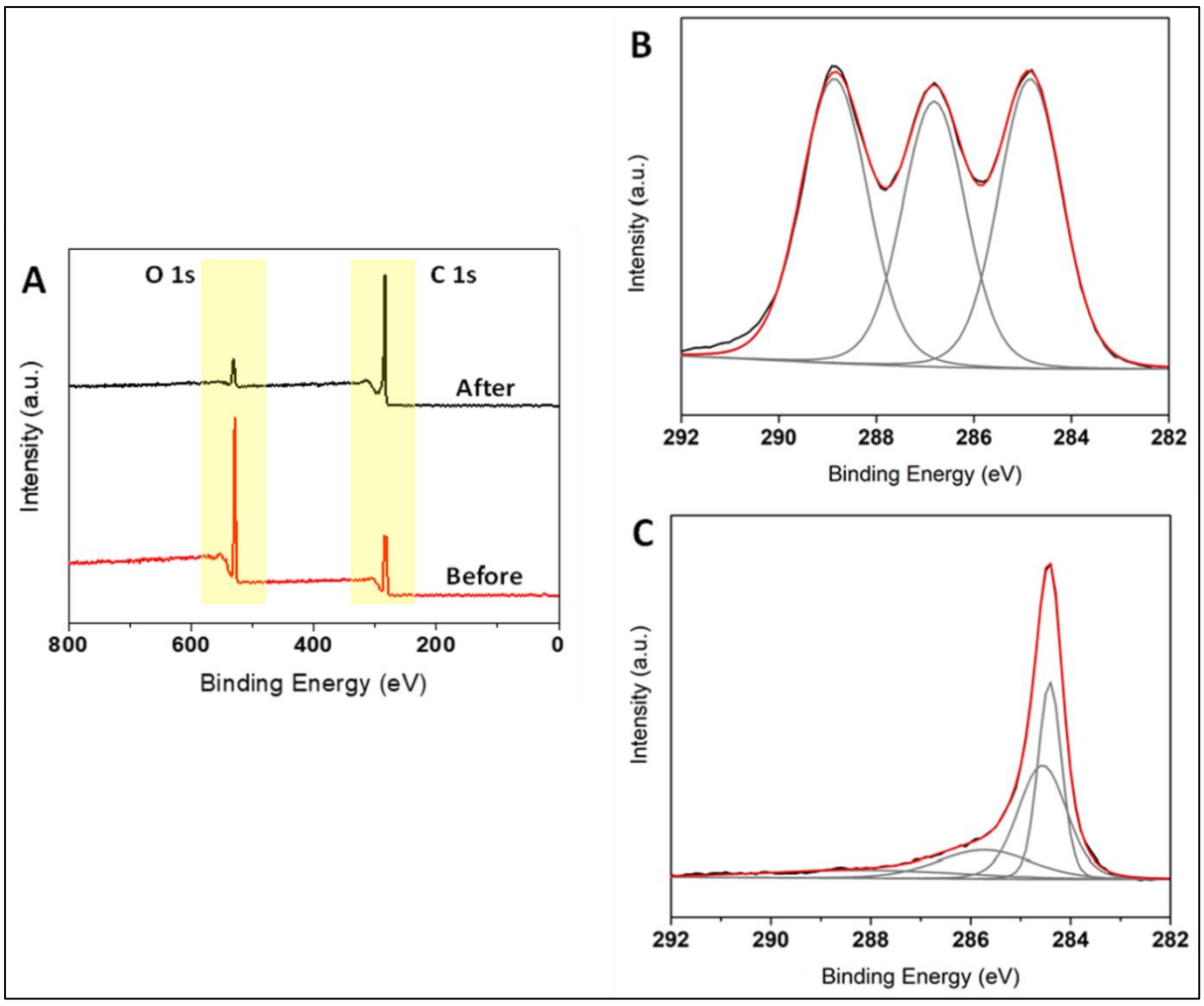

Figure 28: (A) XPS spectrum analysis of 3DnCes without and with DMF treatment. XPS C 1s core level spectrum of **(B)** the 3DnCe without DMF treatment and **(C)** the 3DnCe with DMF treatment.

DNA hybridization assay with enzyme-linked electrochemical detection

In this study, we evaluated the potential applications of 3DnCe for DNA biosensing. For the detection of DNA hybridization, a 3DnCe electrode was used as the transducing platform. As described in the previous section, the DNA duplex was formed by adsorptive immobilization of the target strand on a 3DnCe surface and its subsequent exposure to a complementary probe strand bearing a biotin tag at its end. An enzyme-labelling technique was employed to detect the hybrid duplex [386,404]. Streptavidin-ALP conjugate was used as the enzyme label and was attached to the biotinylated probe. As a result of the enzyme activity, 1-naphthyl phosphate was transformed into 1-naphthol. Consequently, its oxidation peak was measured as the sensor response to the DNA hybridization events. To test the feasibility of 3DnCe-based detection,

some preliminary optimization experiments were performed (such as conditions of surface blocking with BSA, hybridization time and SALP binding time, conditions of washing, etc.), which are described in the following section.

Conversion of 1-naphthyl phosphate to electroactive 1-naphthol catalyzed by the SALP is one of the important factors determining the performance of the sensor. Hence, the effects of enzyme conversion time on the voltammetric peak featuring the analytical signal (**Figure 29**) were studied. To perform the experiment, 1-naphthyl phosphate was spiked into the electrolyte solution together with 1.5 µl of SALP (directly into the electrolyte solution). Thus, 1-naphthyl phosphate was hydrolyzed to produce 1-naphthol, giving an oxidation peak around 0.3 V at the 3DnCe. **Figure 29(A)** shows the effect of the enzyme conversion time on the 1-naphthol oxidation peak, and **Figure 29(B)** demonstrates the peak intensity relationship with the enzyme conversion time. In agreement with expectations, the LSV signal increased with the incubation time as the 1-naphthol concentration was increasing, providing proof of electrochemical response to the produced indicator detectable at the 3DnCe. Further, BSA surface-blocking conditions, SALP binding conditions, and washing conditions were optimized (not shown). The results of hybridization control experiments are shown in **Figure 30**.

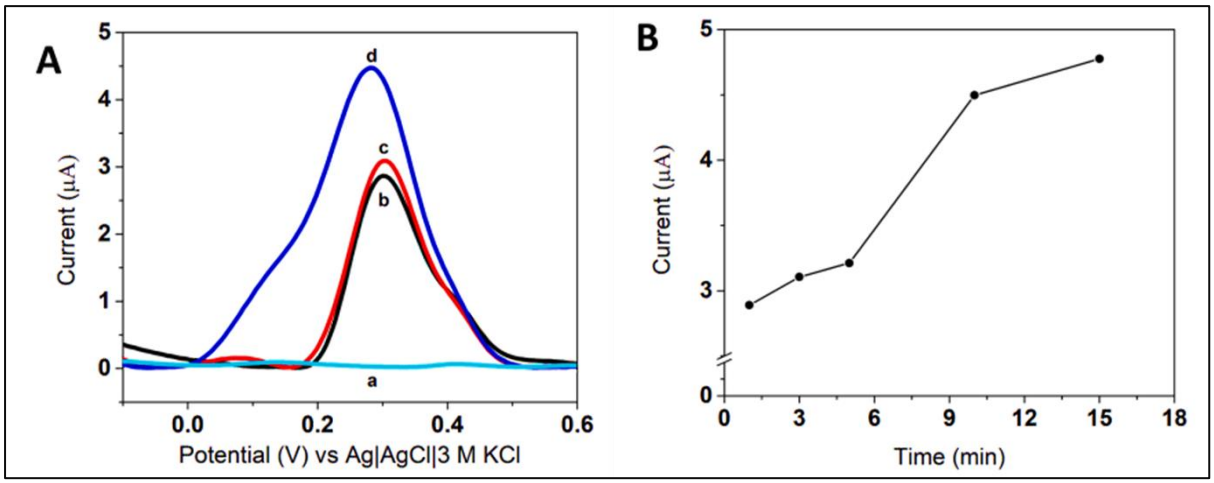

Figure 29: **(A)** Baseline-subtracted LSV responses of 1-naphthol enzymatically generated in the background electrolyte (carbonate buffer) solution measured on the 3DnCe (a) carbonate buffer; time after SALP addition: (b) 1 min; (c) 3 min; (d) 15 min. **(B)** Dependence of the peak current on the conversion time (1, 3, 5, 10, 15 minutes). 1-naphthyl phosphate concentration in the carbonate buffer: 0.5 mM, SALP addition: 1.5 µL of the stock solution into 15 mL of carbonate buffer. Measuring conditions: Carbonate buffer (0.5 M K_2CO_3 and 0.5 M $NaHCO_3$) pH 9.5, LSV: initial potential -0.5 V, end potential + 0.9 V, scan rate 1 V/s and step potential 5 mV.

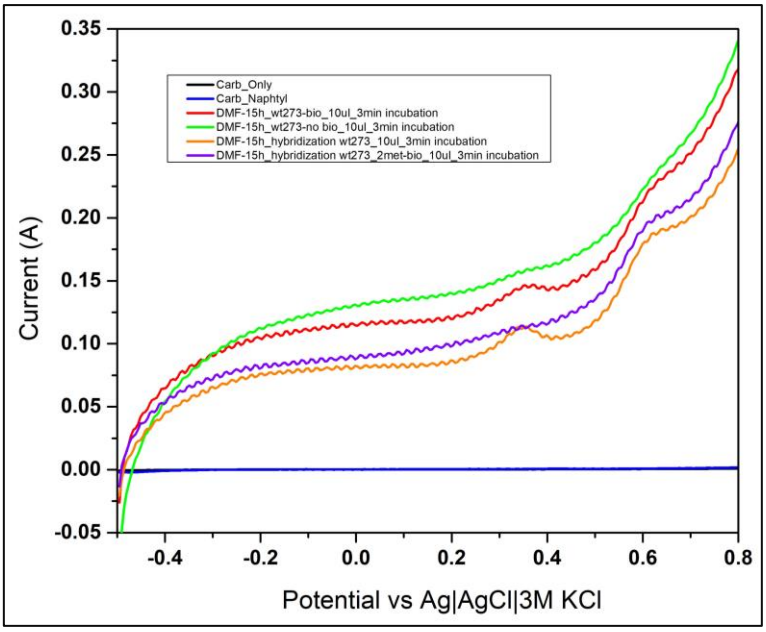

Figure 30: Hybridization optimization study for 3DnCE. **Blue**: the response of bare electrode (no DNA) in the carbonate buffer. **Black**: the response of the bare 3DnCE in the carbonate buffer with 0.5mM naphthyl phosphate. **Red**: The response of the electrode is only with a biotinylated probe. **Green**: response of the electrode with t-DNA only. **Orange**: response of the electrode after hybridization of t-DNA with complementary biotinylated probe. **Purple**: response of the electrode after hybridization of t-DNA with non-complementary DNA). Conversion time = 180 s, measurements conditions.

The DNA hybridization study was carried out subsequently using 3DnCes. Before DNA hybridization, each DNA strand was subjected to necessary experimental controls. **Figure 31** displays baseline-corrected sections of linear sweep voltammograms obtained at the 3DnCes after adsorption and/or hybridization (t-DNA with biotinylated probe) of the DNA. Control of the bare 3DnCe in the carbonate buffer can be seen in **Figure 31a**. The electrode surface was not modified with any DNA, and no indicator was added to the buffer, so we did not obtain any signal. **Figure 31b** shows an experiment with t-DNA alone adsorbed (from 50 µg/mL) at the 3DnCe followed by blocking with BSA. Then, 1x PBS washing (60 s) and incubation in BSA+SALP (120 s) was done. After 60 s, the electrode was rinsed in 1x PBS containing 0.05 % Tween20, followed by 60 s in 1x PBS and placed in a voltammetric cell with 15 mL of carbonate buffer pH 9.5 containing 0.5mM 1-naphthyl phosphate (see **Scheme 3**). No SALP binding to t-DNA occurred as there was no biotin attached to the t-DNA, and, accordingly, only a small signal was detected, which was probably due to some non-specific SALP binding to the electrode surface.

Further, a control experiment with the biotinylated probe alone (50 µg/mL, no t-DNA) adsorbed at the 3DnCe was performed, as shown in **Figure 31c**. After the adsorption of the biotinylated probe to the electrode, BSA was used to block the unoccupied electrode surface. As in the previous t-DNA control, 1x PBS washing (60 s) and incubation in BSA+SALP (120 s) was done. After 60 s of washing in 1x PBS containing 0.05 % Tween20, the electrode was washed in 1x PBS again for 60 s. A well-defined peak was observed because of the presence of the biotin on the probe (as SALP has an exceptional high binding affinity for biotin) [405]. **Figure 31d** shows a positive control experiment after the hybridization of the t-DNA with the biotinylated probe (both 50 µg/mL) following **Scheme 3**. A well-defined peak was observed after the hybridization reaction of the t-DNA with a complementary biotinylated probe, which allows strong binding of the SALP (which is responsible for the conversion of the 1-naphthyl phosphate into 1-naphthol). A similar response was observed with the conventional pyrolytic graphite electrode (PGE, **Figure 32**), implying that the 3DnCe is a potent alternative tool for DNA sensing. **Figure 31e** demonstrates the hybridization reaction experiment (following **Scheme 3**) of t-DNA with the non-complementary DNA (both 50 µg/mL). The signal greatly diminished in the presence of non-complementary DNA, which was expected since hybridization does not take place when the two DNA strands are not complementary. However, a small signal was observed, which could be ascribed to the non-specific SALP binding to the 3DnCe's surface [388,406].

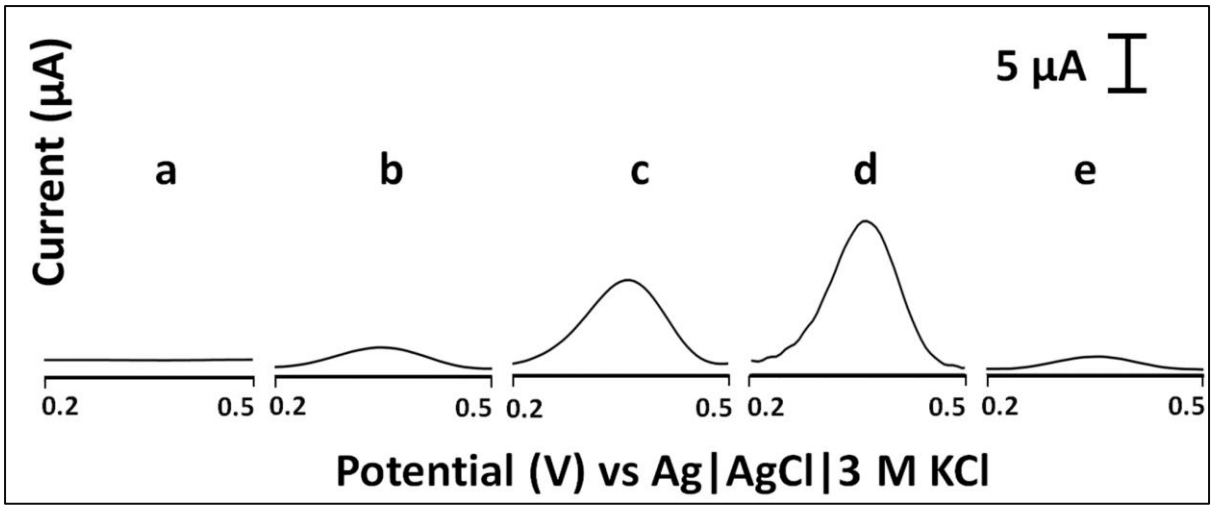

Figure 31: LSV responses at the 3DnCes: (**a**) bare electrode in background electrolyte (without DNA on the electrode and without 1-naphthyl phosphate in the buffer); (**b-e**) control experiments topped off by incubation of the electrode in SALP and 1-naphthyl phosphate solutions after (**b**) adsorption of 50 µg/mL t-DNA, no hybridization with the biotinylated probe; (**c**) no target DNA adsorption, adsorption of 50 µg/mL biotinylated probe only; (**d**) positive control hybridization experiment with target and complementary (biotinylated) probe; (**e**)

negative control hybridization experiment with target and non-complementary biotinylated probe. Conversion time, 180 s. Experimental conditions: carbonate buffer (0.5 M K_2CO_3 and 0.5 M $NaHCO_3$) pH 9.5, LSV: initial potential -0.5 V, end potential + 0.9 V, scan rate 1 V/s and step potential 5 mV.

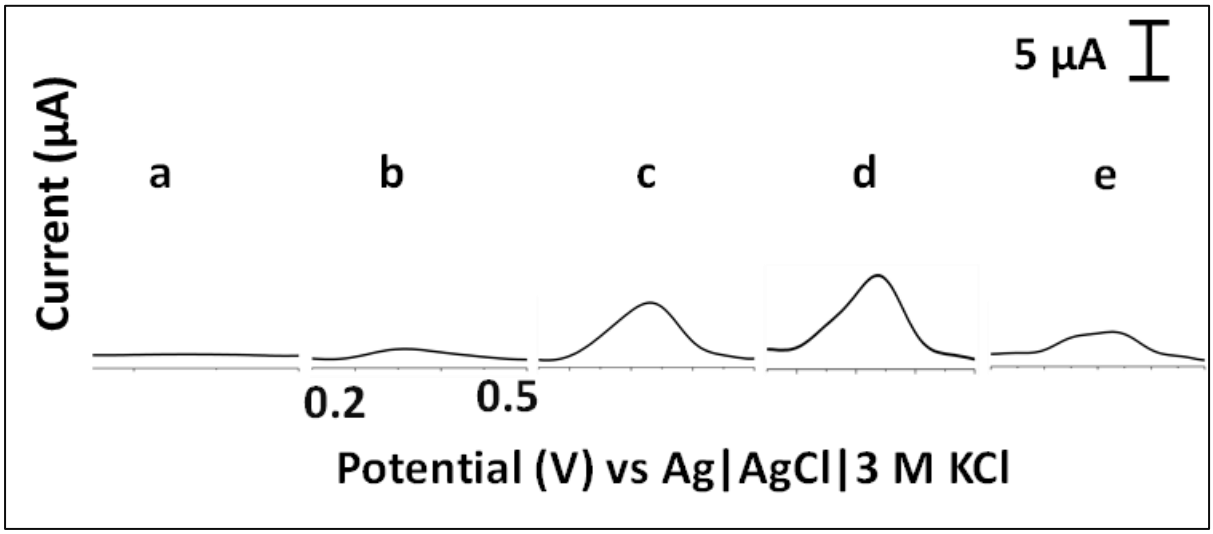

Figure 32: LSV response at the basal plane pyrolytic graphite electrode**:** (**a**) bare electrode in background electrolyte (without any DNA on the surface of the electrode, and without naphthyl phosphate in the background buffer); (**b-e**) control experiments topped off by incubation of the electrode in SALP (in 2% BSA) and 1-naphthyl-phosphate in background electrolyte after (**b**) adsorption of 50 µg/mL t-DNA, no hybridization with biotinylated probe; (**c**) adsorption of 50 µg/mL biotinylated probe only (no t-DNA adsorption); (**d**) positive control experiment: hybridization of t-DNA with complementary (biotinylated) probe; (**e**) negative control experiment: hybridization of t-DNA with non-complementary biotinylated probe. Conversion time, 180 s. Experimental conditions as in Figure 31.

Biotinylated DNA probe optimization

Following experiments were performed to examine the influence of biotinylated probe concentration on the indicator signal resulting from hybridization with t-DNA following **Scheme 3**. Some preliminary measurements had been made prior to this, such as the response of the 3DnCes in the carbonate buffer alone and the same buffer with 1-naphthyl phosphate as a control (not shown). **Figure 33(A)** illustrates data from 3DnCes with the fixed target DNA concentration (50 µg/mL) and varied biotinylated probe concentrations. As the biotinylated probe concentration increased from 0 to 50 µg/mL, we observed well-developed hybridization peaks following an increasing trend [400]. **Figure 33(B)** shows the data from a single measurement of various probe concentrations (with a 3-min enzymatic conversion time). The line of regression obtained for the biotinylated DNA probe was $y = 0.25x + 1.946$, having $R^2 = 0.99$, and it exhibited an almost linear response up to 50 µg/mL, as shown in Figure 6. Hence,

the biotinylated probe concentration of 50 µg/mL was used to evaluate the response of the t-DNA at various concentrations.

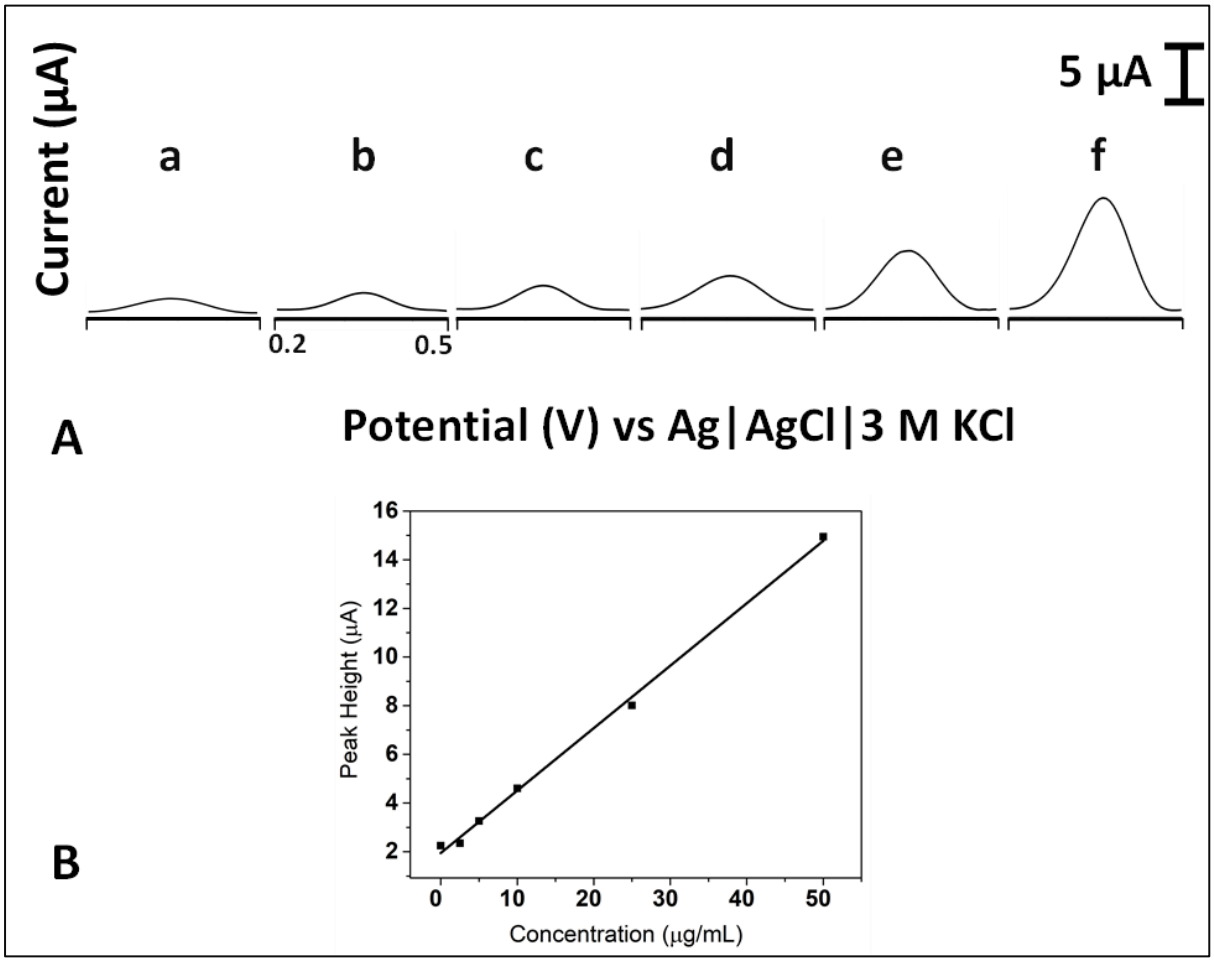

Figure 33(A): Effect of biotinylated probe concentration on the LSV hybridization response: (**a**) 0 µg/mL; (**b**) 2.5 µg/mL; (**c**) 5 µg/mL; (**d**) 10 µg/mL; (**e**) 25 µg/mL; (**f**) 50 µg/mL, respectively. Concentration of target DNA, 50 µg/mL; conversion time, 180 s; background electrolyte: 0.5 M carbonate buffer, pH 9.5. **Figure 33(B)** Dependence of the LSV peak height on biotinylated probe concentration. (0, 2.5, 5, 10, 25, and 50 µg/mL), whereas the concentration of target DNA is fixed to 50 µg/mL; conversion time 180 s. Measuring conditions as in Figure 31.

Influence of the target DNA concentration on the hybridization signal

To evaluate the influence of the target DNA concentration on the indicator peak height, we utilized the 3DnCe as the transducer, and we followed **Scheme 3**. To perform this experiment, the t-DNA was adsorbed on the 3DnCe. Then, the free surface of the electrode was blocked with 5 % BSA (120 s) to avoid unspecific binding of the biotinylated DNA to the electrode

surface. Afterwards, the biotinylated probe was added to the 3DnCe and hybridized with t-DNA for 120 s. Then, the 3DnCe was immersed into the BSA+SALP solution (120 s). After each step, the electrode was washed with 1xPBS (60 s). For electrochemical measurements, the electrode was fixed in a cell containing a carbonate buffer with 1-naphthyl phosphate. Concentration of the t-DNA varied from 0 to 50 µg/mL, whereas the concentration of the biotinylated probe was fixed to 50 µg/mL.

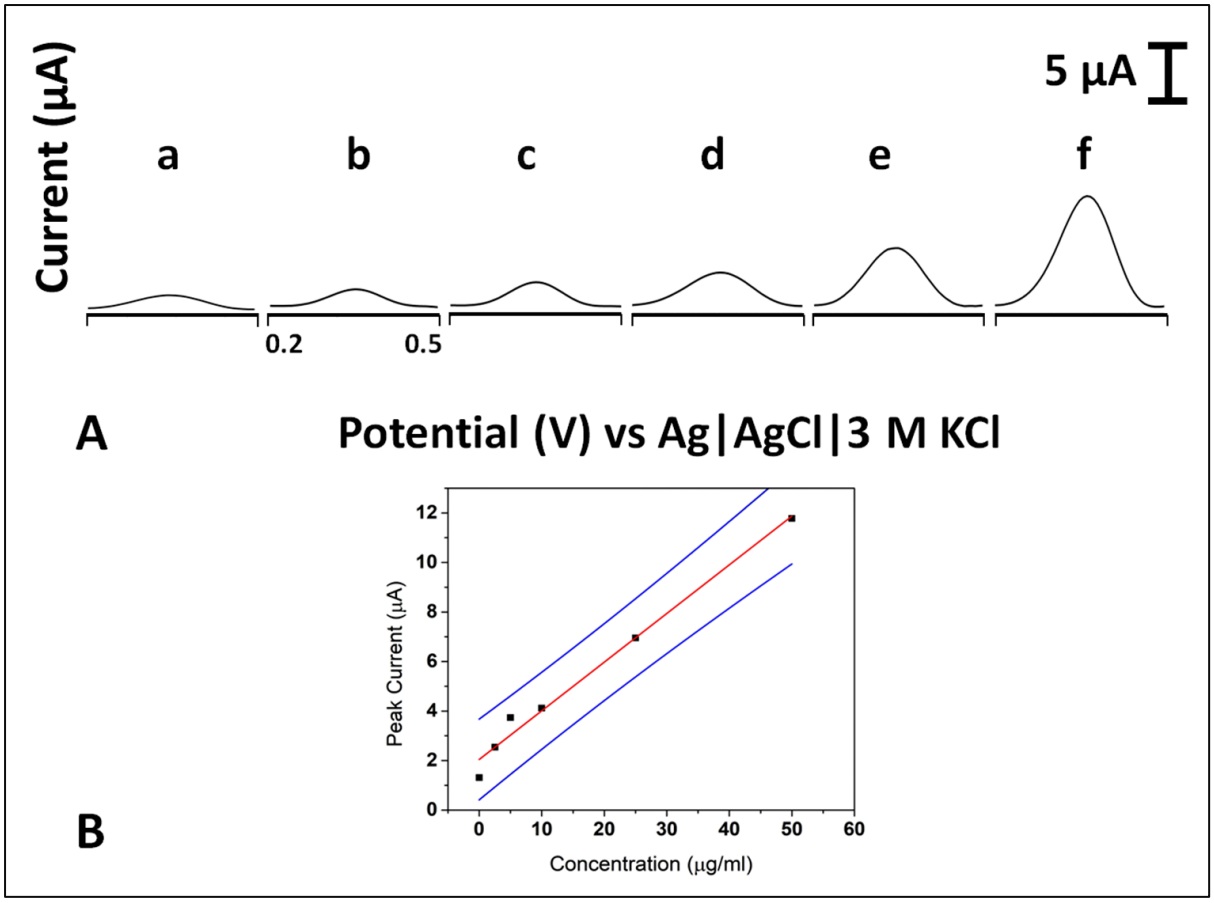

Figure 34(A): Effect of target DNA concentration on the LSV hybridization response by changing the target DNA concentration: (**a**) 0 µg/mL; (**b**) 2.5 µg/mL; (**c**) 5 µg/mL; (**d**) 10 µg/mL; (**e**) 25 µg/mL; (**f**) 50 µg/mL. **Figure 34(B)** calibration curve for the target DNA concentration on 3DnCes with 95% confidence limits. Conditions: concentration of biotinylated probe was fixed to 50 µg/mL; concentrations of the target DNA varied from 0 µg/mL; 2.5 µg/mL; 5 µg/mL; 10 µg/mL; 25 µg/mL; to 50 µg/mL with 180 s as optimum time of the enzymatic conversion of 1-naphthyl phosphate into 1-naphthol. Measuring conditions as in Figure 31.

The 1-naphthol oxidation peak height increased with increasing t-DNA concentration (from 0 to 50 µg/mL in solution), with 180 s as the enzyme conversion time (shown in **Figure 34(A)**. **Figure 35** shows histogram plots illustrating the mean and standard deviation obtained from

measurements with various t-DNA concentrations. The dependence of the peak height on t-DNA concentration with 95% confidence limits is depicted in **Figure 34(B)** and shows a nearly linear response. The peak currents linear regression equation is given as y = 0.1965x + 2.042 with R^2 = 0.98. The precision was estimated using a set of five different measurements of the concentration 10 µg/mL of t-DNA (180 s as conversion time, not shown). The mean peak height in this sample was calculated to be 3.81 µA, with 32 per cent as the relative standard deviation. Furthermore, using LOD = 3SD/Slope, the limit of detection was also computed and determined to be 0.95 µg/mL. Moreover, the electrode stability was assessed by storing the 3DnCe for 100 days under ambient conditions and measuring the t-DNA (conc. 50 µg/mL) response (by following the procedure mentioned above). The electrodes retained 81% of their original signal and demonstrated excellent signaling properties.

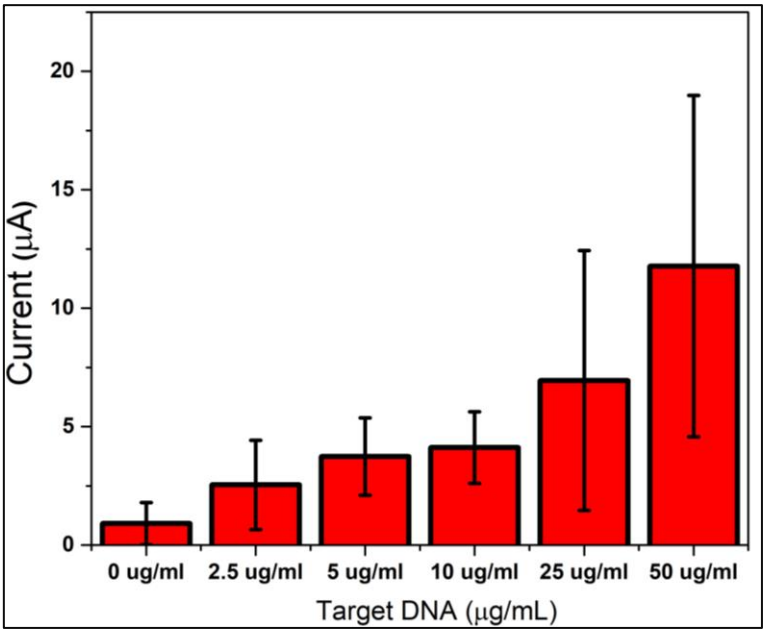

Figure 35: Dependence of the peak height on t-DNA concentration with 95% confidence limits. Histograms illustrate the mean and standard deviation obtained from three independent measurements. Concentrations of the t-DNA: 0 µg/mL; 2.5 µg/mL; 5 µg/mL; 10 µg/mL; 25 µg/mL; 50 µg/mL; concentration of biotinylated probe: 50 µg/mL, enzymatic conversion (transformation of 1-naphthyl phosphate into 1-naphthol) 180 s. Experimental conditions as in Figure 31.

4.3.4 Conclusion

Here, we demonstrated an enzyme-linked DNA hybridization assay using a 3D nanocarbon electrode as the transducing platform. In this method, the 3DnCe surface was modified with target DNA and its hybridization with biotinylated DNA probe was detected using enzymatic

conversion of the electro-inactive compound (1-naphthyl phosphate) to electro-active indicator (1-naphthol). The novelty of this work lies in the employment of the wide-scale use of 3D-printing technology to create custom-shaped devices on demand and in an environmentally benign manner. Using cost-effective, easily accessible 3DnCes, we demonstrated fast detection of the target DNA using a complementary biotinylated probe (50 µg/mL) within the concentration range from 0 to 50 µg/mL. This method has also proven to have good selectivity, as shown in the control experiment with non-complementary DNA strand. Based on the encouraging results of this study, it can be expected that 3D-printing might become an essential element of biosensor fabrication in the near future because of its custom-made property.

List of Abbreviations

3D	Three dimensional
3DnCes	3D-printed nanocarbon electrodes
DMF	*N,N'*-dimethylformamide
SEM	Scanning Electron Microscopy
EDS	Energy Dispersive Spectroscopy
XPS	X-ray photoelectron spectroscopy
CAD	Computer-aided design
FDM	Fused Deposition Modelling
PLA	Polylactic acid
CV	Cyclic voltammetry
LSV	Linear Sweep Voltammetry
PBS	Phosphate Buffered Saline
DNA	Deoxyribonucleic acid
t-DNA	Target Deoxyribonucleic acid
µg/mL	Microgram per milliliter
s	second

This page is left intentionally

Part II

Nano/micromotors for Biosensing Applications

This page is left intentionally

Chapter 5.1

Quantum Material-Based Self-Propelled Microrobots for the Optical “On-the-Fly” Monitoring of DNA

Published: ACS Applied Material. Interfaces 2023, 15, 58548−58555.

5.1.1 Introduction

In recent years, self-propelled microrobots (MRs) [407–410] —which can exhibit autonomous motion by harnessing chemical energy— have attracted great attention in different fields, including catalysis, environmental remediation, cancer therapy, and protein detection, among others.[112,411–415] In particular, self-propelled MRs are currently at the forefront of analytical chemistry owing to their unique capability to perform "on-the-fly" bio-recognition. The term "on-the-fly" refers to the capability of MRs to perform chemical pre-concentration or interactions with target analytes while in motion.[416,417] The main benefits of chemistry "on-the-fly" rely on the suitability of MRs to rapidly pre-concentrate targets on their surfaces (even in small volumes of complex biosamples), accelerating interactions while avoiding several samples post-treatments (*e.g.*, washing/mixing procedures).[300,380,409,418]

Graphene quantum dots (GQDs) are a type of 0D carbon nano allotrope that present excellent fluorescent features for optical analyses.[419,420] In addition, the high solubility, low toxicity and excellent water solubility of GQDs, together with their sp^2-like skeleton, make them ideal for processing carrier tasks in aqueous and/or physiological environments.[421–424] In particular, the sp^2-like skeleton of GQDs can behave as Fluorescence Resonance Energy Transfer (FRET) acceptors or donors by non-covalently absorbing (*e.g.*, π–stacking interactions or hydrophobic interactions) with biomaterials, like single strand DNA (ssDNA).[425,426] Although their aforementioned benefits, the exploration of GQDs as bulky material for MRs fabrication is almost an unexplored field, in which Escarpa's group is leading this field. In particular, they have demonstrated the advantages of using graphene quantum dots-based self-propelled microrobots (GQD–MRs) by means of rich surface chemistry and high surface area, favouring sensing activity.[427,428]

Detection methods involving optical readouts represent a pivotal strategy to evaluate DNA hybridization between a specific nucleic acid target and a complementary nucleic acid probe.[429–432] Optical DNA biosensing is primarily based on the FRET principle, which relies on the resonance energy transfer from an excited donor fluorophore to a corresponding acceptor fluorophore.[170] This donor–acceptor relationship helps to improve the analytical performance of the biosensor effectively, resulting in a highly sensitive technique.[433] Otherwise, the water solubility of GQDs is known to facilitate homogeneous assays, which are vital to DNA detection.[434–436] The driving force of any DNA hybridization process relies on an adequate close proximity of the complementary strands of DNA for proper interactions, in which

diffusion and transport are the main kinetic limiting steps.[437] In order to overcome this drawback, microrobots have provided new insight into the field of analytical chemistry by improving fluid mixing and localized convection. Compared to conventional methods, the implementation of microrobots can dramatically improve probe interaction for lower samples and reagent usage without the implementation of an external mixing source, the fact that can improve kinetic processes by reducing incubation times by 'on-the-fly' reactions.[416,438–441] Although few types of self-propelled MRs have already been proposed as DNA biosensing platforms employing different readouts,[441–444] to the best of our knowledge, the exploration of GQD–MRs for this aim is nowadays an unexplored field.

Herein, dynamic biocarriers made of GQD–MRs have been synthesized and evaluated towards the "on-the-fly" determination of DNA. For this aim, tubular GQD–MRs were fabricated *via* a membrane-assisted electrodeposition method [445–447] by electrochemically depositing GQDs (chemically active surface, outer layer), Ni (magnetic core, middle layer) and Pt (motion inducer, inner layer); see **Scheme 4A** for illustration. The inner walls of GQD-MRs with deposited platinum were responsible for inducing motion by the catalytic disproportionation of H_2O_2 into H_2O and O_2.[448] The formation of O_2 molecules triggers a nucleation process, leading to the subsequent growth of oxygen bubbles. These bubbles can then diffuse and ultimately pop out from an open end of the asymmetric tubular form of GQD-MRs. As a result, when a bubble is expelled from one end of the tube, a movement takes place in the opposite direction.[448–450] Afterwards, the resulting GQD–MRs were biofunctionalized with a biomarker probe (*i.e.*, Fluorescein Amidites Labelled, FAM-L). According to the FRET phenomena, the FAM-L probe acted as a fluorophore, while the GQD–MRs served as the fluorescence quenching platform. The non-covalent π-π stacking interactions between *i)* the structures of the nucleobases of the FAM-L probe and *ii)* the sp^2-rich skeleton of GQDs leads to the adsorption of the FAM-L probe on GQD–MRs,[425] resulting in the FAM-L@GQD–MR dynamic biocarriers. Such π-π stacking interactions are the ones responsible of fluorescent quenching. Nonetheless, it is important to note that the interactions between the FAM-L and GQD–MRs involve a continuous competition between electrostatic repulsion and hydrophobic interactions.[451] For the optical analytical assay, the resulting dynamic biocarriers were propel-induced by utilizing a 1% v/*v* H_2O_2 *buffered* medium containing different concentrations of a complementary DNA sequence (DNA target). The changes in the fluorescence (FL) emission of the FAM-L probe with increasing concentrations of DNA target —owing to the hybridization process— (*inputs*) were used as the optical *output* signals (see **Scheme 4B**).[426]

Further, the selectivity of the devised dynamic biocarriers was also interrogated by using both mismatch and non-complementary DNA sequences.

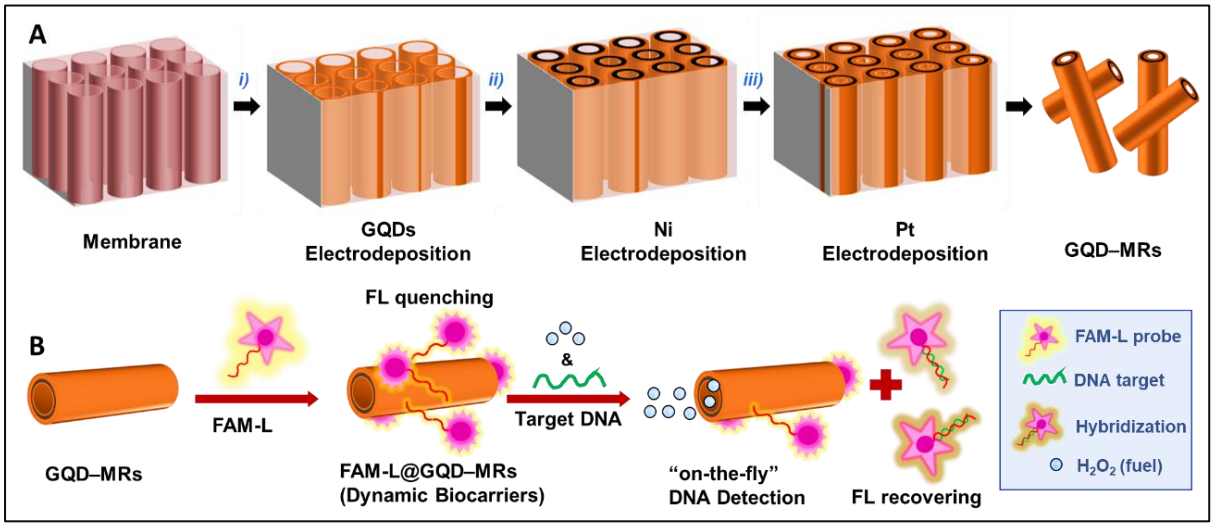

Scheme 4. Fabrication of self-propelled GQD–MRs and their exploitation as dynamic biocarriers for the optical "on-the-fly" DNA determination. (A) GQD–MRs were synthesized *via* membrane-assisted electrodeposition of *i)* GQDs (outer layer), *ii)* Ni (middle layer) and *iii)* Pt (inner layer). **(B)** Biofunctionalization of GQD–MRs with a biomarker (*i.e.*, FAM-L probe) *via* π-stacking interactions, where the resulting FAM-L@GQD-MRs (dynamic biocarriers) promotes a quenching in the fluorescence activity of the probe. The optical analytical assay relies on "on-the-fly" DNA determination using different concentrations of a complementary DNA target under fuel-induced motion (1% v/*v* in H_2O_2), where the DNA hybridization process between probe and target derives in an FL recovery.

5.1.2 Experimental Methods

Materials, Chemicals and DNA Sequences

GQDs, H_2O_2 and sodium dodecyl sulfate (SDS) were provided by Sigma-Aldrich. Commercial Ni and Pt plating solutions were purchased from Singapore. DNA sequences were obtained from the Sigma-Aldrich (Czech Republic), which are given as follows: FAM-L DNA probe: 5′ [6FAM] ACC AGG CGG CCG CAC ACG TCC TCC AT 3′; DNA target: 5′ATG GAG GAC GTG TGC GGC CGC CTG GT 3′; Mismatch DNA: 5′ ATG GAG GAC GTG CGC GGC CGC CTG GT 3′; Non-Complementary DNA target: 5′ A-AAA GTG TTT TTC ATA AAC CCA TTA TCC AGG ACT GTT TAT AGC TGT TGG AAG GAC TAG GTC 3′. Biological fluids (*i.e.*, sigmatrix urine diluent (mimics human urine) and plasma from humans) for the implementation experiments were obtained from Sigma-Aldrich.

Synthesis of self-propelled GQD–MRs

GQD–MRs were prepared by using our established membrane-assisted electrodeposition method (see **Scheme 4A**)[446,447,452]. Briefly, a 100 nm thick Au layer was sputtered on a Whatman Cyclopore polycarbonate membrane (3 μm pore size) *via* electron-beam evaporation and subsequently affixed on a piece of Cu tape as the electrical contact to fabricate a working electrode. Then, it was placed in a three-electrode configuration cell using a Pt wire and an Ag/AgCl (1 M KCl) electrode as the counter and reference electrodes, respectively. Electrochemical depositions were run in an AUTOLAB potentiostat (Metrohm). Firstly, *i)* the outer layer was made by depositing GQDs employing a 0.1 $mg \cdot mL^{-1}$ dispersion (support electrolyte: 0.1 M H_2SO_4 containing 0.5 M Na_2SO_4) *via* cyclic voltammetry (CV): potential window: +0.3 to –1.5 V *vs.* Ag/AgCl; scan rate: 50 $mV \cdot s^{-1}$; number of cycles: 40 cycles. Afterwards, *ii)* Ni middle layer deposition was carried out by chronoamperometry (bias potential: +1 V *vs.* Ag/AgCl; time: 60 s), while chronopotentiometry (current: –20 mA; time: 500 s) was utilized for *iii)* the Pt inner layer electrodeposition. Once the electrodeposition was done, the membrane was detached from the copper tape, carefully washed with deionized water and hand polished with an alumina slurry (0.5 μm) in order to remove the Au layer. Then, the membrane was thoroughly washed (3 times) with deionized, dissolved in dichloromethane and finally washed with isopropanol, ethanol and deionized water thrice under ultrasounds. Finally, the resulting self-propelled GQD–MRs were magnetically collected and air-dried.

Preparation of dynamic biocarriers

1 mL of a GQD–MRs dispersion (0.1 $mg \cdot mL^{-1}$ in 100 mM Tris-HCl buffer solution, pH 7.0) was mixed with 40 nM of the FAM-L probe for 5 min at room temperature to induce supramolecular π-stacking interactions.[431] The resulting dynamic biocarriers (FAM-L/GQD–MRs) were then properly washed with Tris-HCl buffer by collecting them magnetically. According to the FRET phenomena, the quenching observed at the FL emission band of the FAM-L was indicative of the proper biofunctionalization.[433,148,453]

Optical assay for DNA determination

The optical assay for DNA determination was carried out by adding different concentrations (0.05 –100 nM) of DNA target into a fluorescence cell containing a 0.1 $mg \cdot mL^{-1}$ aqueous solution of dynamic biocarriers under H_2O_2-induced motion (1% v/*v*). The mixture was aged

for 5 min at room temperature to promote the hybridization between the FAM-L probe and the DNA target. The recovery of the FL emission band of the FAM-L probe confirmed the hybridization process. It is important to point out that the "on-the-fly" hybridization assay was optimized by studying different experimental conditions, such as pH and concentration of the buffered medium and incubation time, as shown in **Figure 36**.

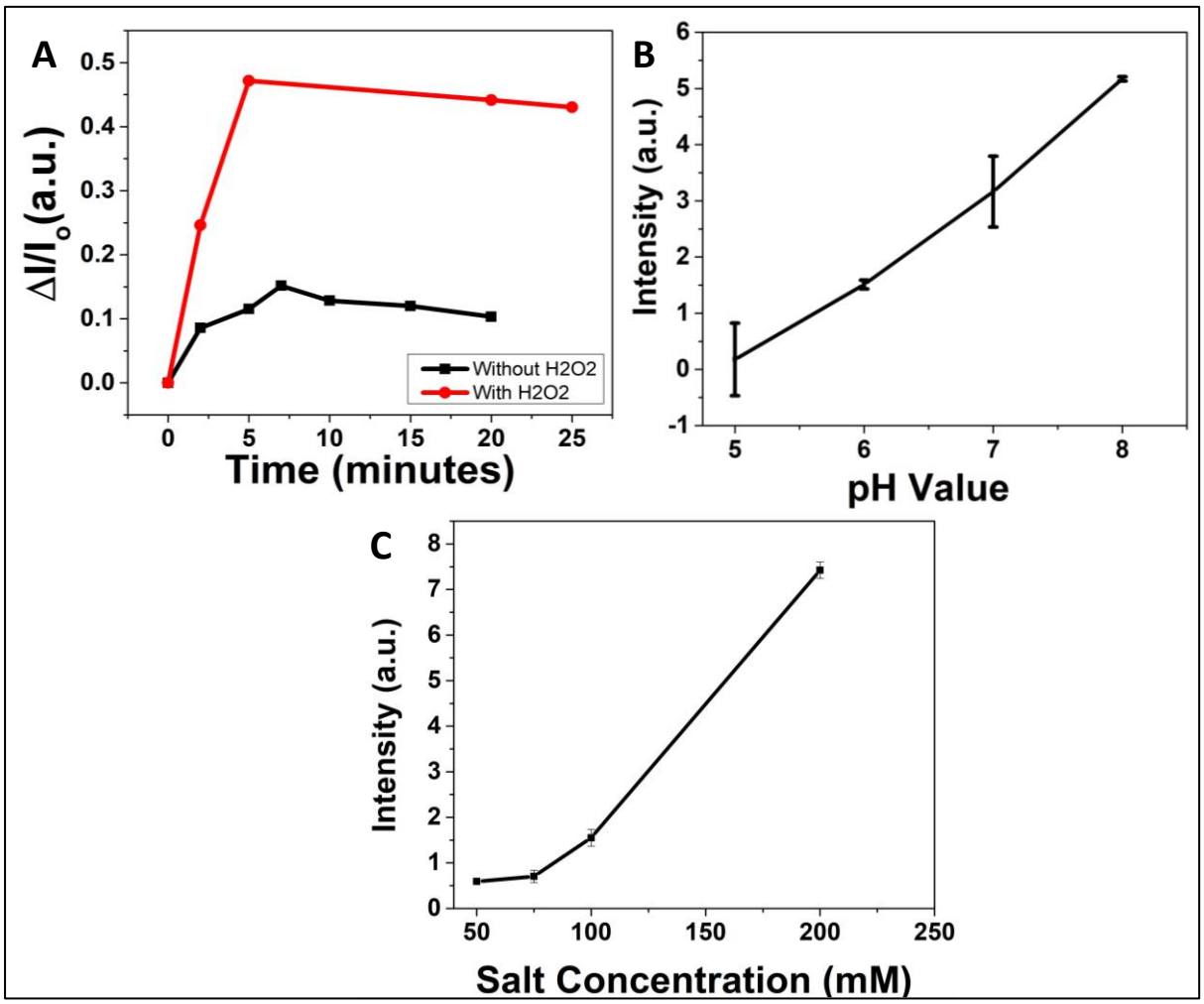

Figure 36. **(A)** Hybridization time optimization study (target DNA hybridization (1 nM) with FAM-L probe (40 nM)) (red) GQDs-MRs in motion by using1% H_2O_2 (black) GQDs-MRs without motion. During the time optimization study, the fluorescence intensity increased with the increase in time up to 7 minutes (in case no H_2O_2) whereas up to 5 minutes (in case H_2O_2). **(B)** Effect of pH study (5, 6, 7, 8) on DNA hybridization using GQD–MRs. While pH 5 exhibited poor signals due to partial protonation of ssDNA's phosphate backbone, resulting in weak hybridization, at pH 6 protonation and deprotonation led to a slightly higher signal. A significant signal increase occurred at pH 7, peaking at pH 8, indicating pH strongly influences hybridization efficiency.[160,454,455] **(C)** Effect of the salt concentration (50, 75, 100, 200 mM) on the DNA hybridization process. Increasing Tris-HCl concentration (50 to 200 mM) enhanced the peak, possibly due to Tris molecules forming hydrogen bonds with DNA backbones and binding to solid surfaces via $-NH_3^+$ groups. Additionally, $-NH_3^+$ groups attached to

DNA phosphate groups, while -OH groups formed hydrogen bonds with the adsorbent surface, contributing to the observed increase.[456,457] Conditions: Excitation wavelength 490 nm.

Finally, experiments with biological samples (urine and human serum) were performed as follows: GQD–MRs were dispersed in the biological fluids (0.1 $mg \cdot mL^{-1}$) and then mixed with 40 nM of the FAM-L probe for 5 min at room temperature to induce supramolecular π-stacking interactions. After washing steps by magnetic collection, the motors were incubated with 1 nM of DNA target in the corresponding biological fluids and self-propelled by adding 1% of H_2O_2 as fuel. The experiments were carried out in triplicate (*n=3*).

Equipment and Procedures

The surface morphology and atomic distribution of GQD–MRs were characterized by using a scanning electron microscopy coupled to an energy-dispersive X-rays detector (SEM-EDX, TESCAN LYRA 3 XMH). The charge distribution of the microrobots was determined *via* Z-potential by using a Malvern Zetasizer. For the optical measurements, FL measurements were performed using a Jasco FP-8300 spectrofluorometer at room temperature. The FL emission spectra of GQD–MRs was recorded from 370 to 550 nm using a λ_{ex} = 350 nm, while the spectra of dynamic biocarriers were conducted from 500 to 700 nm at an excitation wavelength, and for the GQDs-MRs coupled with FAM-L probe was recorded at λ_{ex} = 490 nm. In order to avoid the effect of the fuel, optical measurements were carried out by subtracting the background employing the solvent (water containing either 1% v/*v* in H_2O_2 or pure water blank experiments). Furthermore, UV-vis absorption spectroscopy (Jasco V-750 spectrophotometer) and VERTEX 70v FT-IR Spectrometer were employed to confirm the interactions between GQD–MRs and the biomolecules. A Nikon ECLIPSE TS2R inverted microscope integrated with a Basler digital camera (acA1920-155uc) was utilized to record the autonomous motion behaviour of the microrobots. In detail, 10 μL of microrobots was added on a glass slide. Subsequently, a drop of both 1% H_2O_2 and 0.1% SDS (v/*v*) were added to induce the motion while improving the viscosity of the solution thanks to the presence of the SDS surfactant.[111] Videos were recorded using the NIS Elements Advanced Research software at 25 fps to record the motion of the bubble-propelled microrobots. Fiji software was used to treat the videos in order to calculate the speed and trajectories of the MR-based materials. Fluorescence microscopy measurements of FAM-L@GQD–MRs were performed using a Nikon Eclipse Ti2

fluorescence microscopy employing different excitation wavelengths (green excitation/red emission for GQDs and blue excitation/green emission for FAM-L).

5.1.3 Results and Discussion

Material characterization of GQD–MRs

GQD–MRs were synthesized by following our previously reported membrane-assisted method. To confirm their successful fabrication, a material characterization by means of SEM, EDX and FL analyses was carried out (**Figure 37**). **Figure 37(A)** displayed the lateral SEM image of the GQD–MMs, indicating a microrocket-like structure with a tubular length of around 10 μm and a cross-sectional diameter of around 1 μm (see inset image). A magnified longitudinal view of the microrobot (**Figure 37(B)**) was utilized for EDX analyses. The elemental mapping composition of the material shown in **Figure 37(C-D)** revealed the presence of main elements, such as Pt and Ni, respectively. According to this characterization data, results suggest that the self-propelled GQD–MRs made of three layers (GQDs, Ni and Pt as outer, middle, and inner layers, respectively) were successfully synthesized. Further, the inherent fluorescent features of GQDs [458,459] were also explored in the resulting GQD–MMs. **Figure 37(E)** depicts the emission spectrum of GQD–MMs, with a maximum intensity at 430 nm (excitation light: λ_{ex} = 350 nm). This result clearly confirms that the optical properties of the pristine GQDs were properly transferred to the micromachine.

Following this, the bubble-induced self-propulsion behaviour of GQD–MRs *via* H_2O_2 decomposition was explored, where the Pt inner layer is the one in charge of catalysing the fuel.[460–462] For this aim, the speed of GQD–MRs was monitored by using 1% (v/*v)* of H_2O_2. The bubble propulsion of the GQD–MRs was clearly visualized in the micrographs of **Figure 38(A)**, with an average speed as fast as 233 ± 36 μm·s^{-1} (**Figure 38(B)**). Taking into account the biotoxicity of H_2O_2 at high concentrations, such a low concentration of fuel (1% H_2O_2) was chosen in order not to disrupt the following biological purpose: the optical "on-the-fly" DNA determination. It is important to highlight that the amount of fuel used in this work is in line with the concentrations of H_2O_2 reported by another research groups for biosensing approaches since, in all cases, the experiments are carried out *ex vivo*.[417,443,463,464]

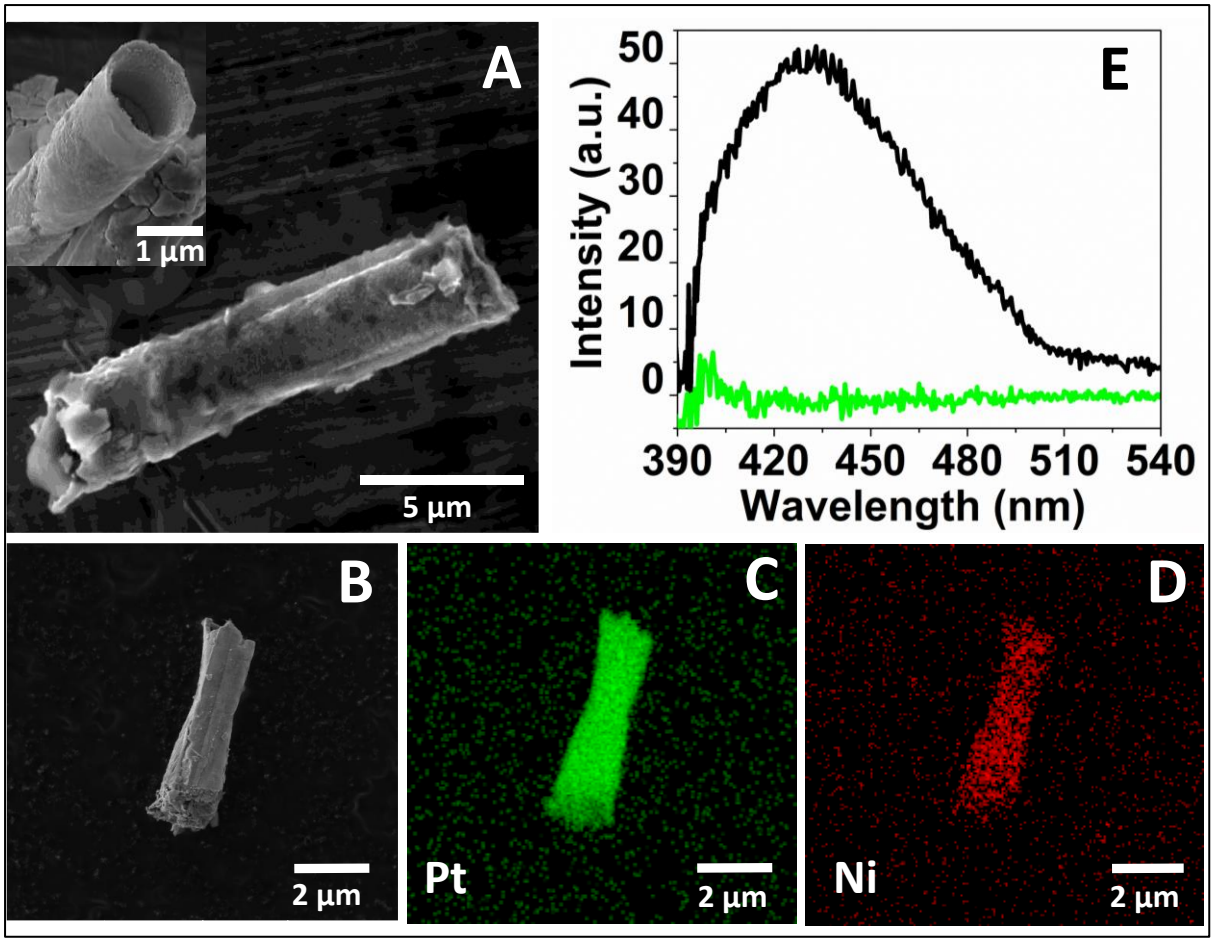

Figure 37: Material characterization of self-propelled GQD–MRs. (A) SEM image (inset: cross-sectional view at higher magnification) and **(B)** SEM-EDX image of GQD–MRs with its corresponding elemental mapping composition for **(C)** Pt, **(D)** Ni. **(E)** Fluorescence emission spectra of GQD–MRs at λ_{ex} = 350 nm (green line: control emission spectra utilizing the aqueous media without the presence of GQD–MMs).

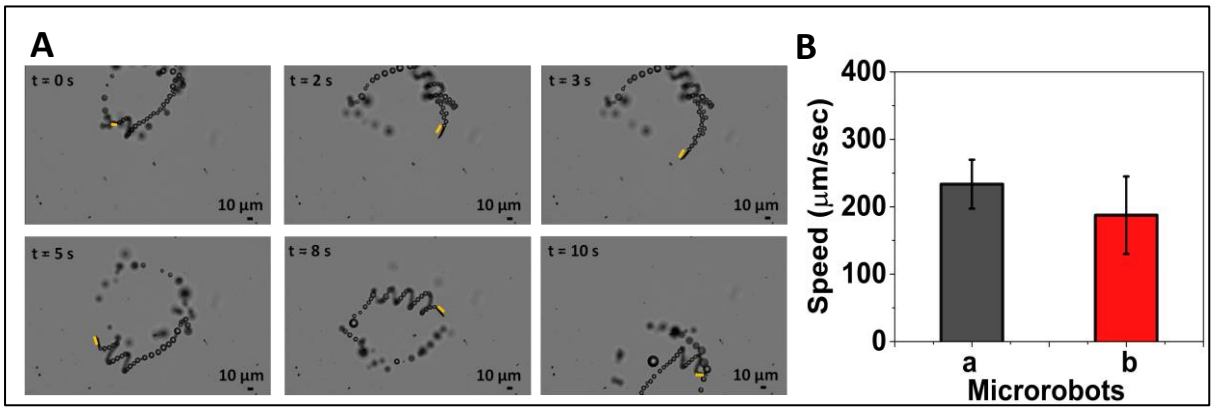

Figure 38: Motion behaviour of microrobots. (A) Optical microscope images showing the trajectory of GQD–MRs at different intervals of times (0 s, 2 s, 3 s, 5 s, 8 s, 10 s, respectively); Scale bar: 10 µm. A yellow bar is added to guide the eye to follow the microrobot; **(B)** Histograms depicting the average speed data of GQD–MRs

(a) before and **(b)** after biofunctionalization with the FAM-L probe. Experimental conditions: Motion tracking was done in 1% H_2O_2 (v/*v*) for 5 different microrobots (*n=5*).

Exploration of dynamic biocarriers made of GQD–MRs

Having verified the successful synthesis and motion of GQD–MRs, the next step focused on their exploration of biological applications. As a proof-of-principle, the "on-the-fly" DNA determination was considered. For this aim, GQD–MRs were biofunctionalized with the FAM-L probe *via* π-stacking interactions.

Firstly, both GQD–MRs and FAM-L@GQD–MRs were characterized *via* FTIR spectroscopy. As shown in **Figure 39**, both spectra present the characteristic absorption bands corresponding to the stretching and bending vibration of the aromatic C–H group at 3385 cm^{-1}, C=C stretching at 1637 cm^{-1}, C–H aromatic at 2000 cm^{-1}, and epoxy stretching vibration of C–O–C groups at 1049 cm^{-1}. Unfortunately, after conjugation, the peaks that could be attributed to the amino groups from FAM-L (*i.e.*, located around 654 cm^{-1}, 1620 cm^{-1} and 3310-3350 cm^{-1} corresponding to NH_2/N–H, N–H and N–H amines, respectively) [465–467] clearly overlapped with the weak peaks from the bare GQD-MRs. Consequently, the FTIR analysis does not reveal the proper decoration of GQD–MRs with the FAM-L probe. Thus, further characterization was carried out by means of UV-vis spectroscopy.

Figure 40 shows the UV-vis spectra of bare GQD–MRs and FAM-L@GQD–MRs (before and after hybridization with the DNA target). While the absorption spectrum of bare GQD–MRs exhibited the typical bands at 240 nm and 270 nm —assigned to π–π* transition of C=C in aromatics [468], a red shift was observed after functionalization with the FAM-L probe, demonstrating a significant change in the optical properties as compared to unmodified GQD–MRs.

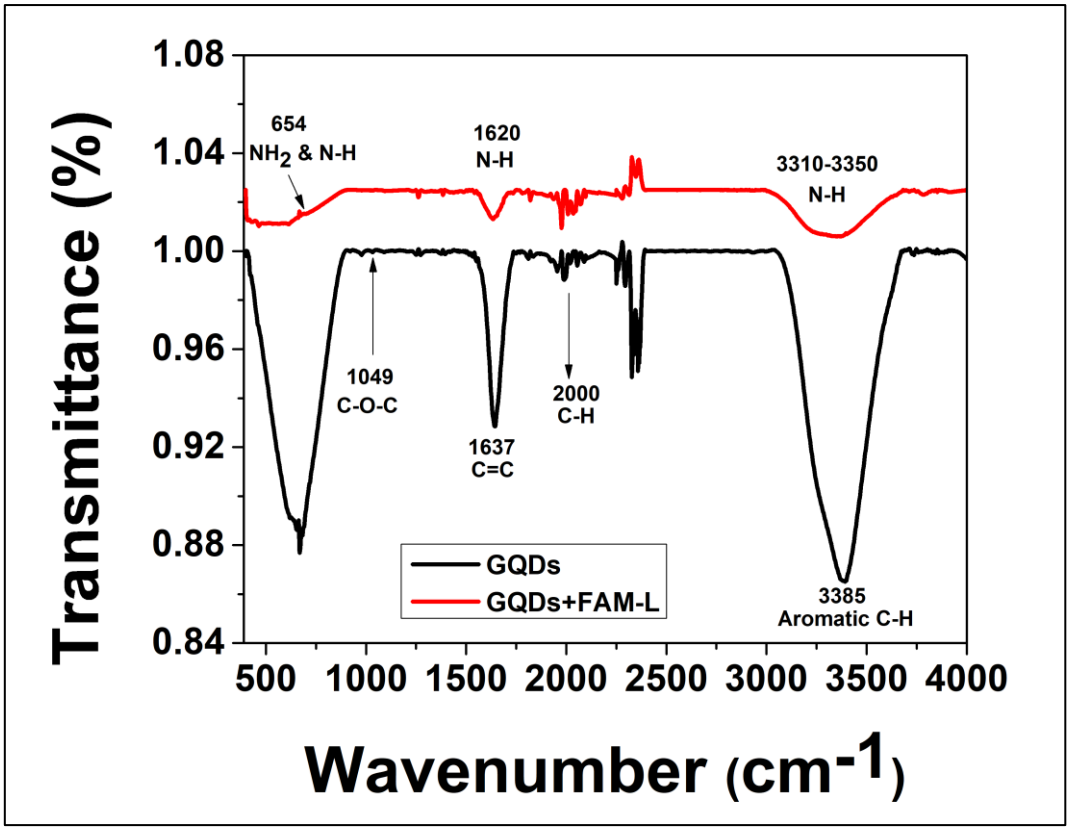

Figure 39: The FTIR spectra of the bare GQD–MRs (black), FAM-L@GQD–MRs (red).

This fact can be ascribed to the biofunctionalization of GQD–MRs with FAM-L probe *via* π-stacking interactions. Importantly, an additional optical change was reached after material hybridization with the DNA target, resulting in a band at 262 nm, suggesting the proper desorption of the FAM-L probe.[469,470] Additional optical characterization was run by means of fluorescence microscopy.

The optical images shown in **Figure 41** evidenced the fluorescence features of both GQDs and FAM-L probe in the dynamic biocarriers, indicating a proper material biofunctionalization. In addition, the speed of the resulting FAM-L@GQD-MR dynamic biocarriers was also monitored, displaying a significant speed decrease from 233 ± 36 $\mu m \cdot s^{-1}$ to 187 ± 57 $\mu m \cdot s^{-1}$ when compared with the non-biofunctionalized counterpart (**Figure 38(B)**). This is also an indication that the biomarker might be immobilized on the microrobot surface since the speed of MRs is influenced by the nature of the surface exposed on the medium. Finally, the charge distribution of GQD–MRs before and after biofunctionalization was recorded by Z-potential under various conditions (bare GQD–MRs, and FAM-L@GQD–MRs before and after hybridization with the target DNA).

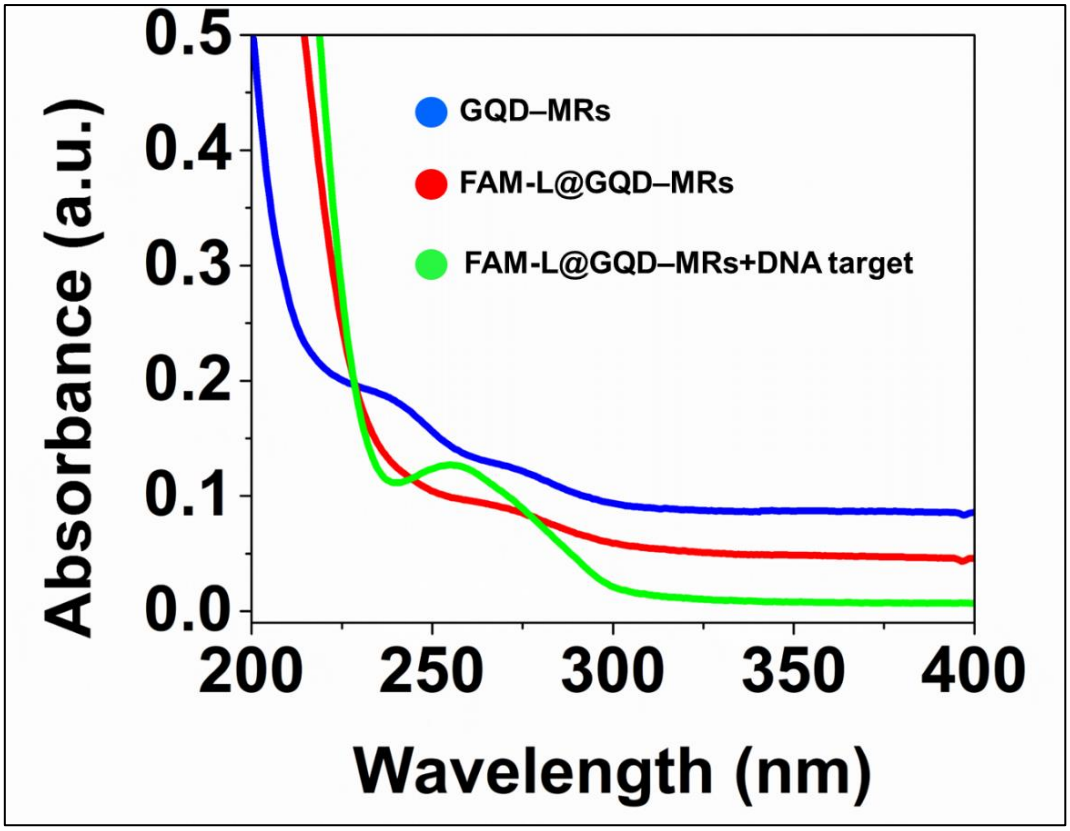

Figure 40: The UV-vis absorption spectrum of the bare GQD–MRs (blue), FAM-L@GQD–MRs before (red) and after hybridization with the target DNA (green).

As shown in **Figure 42(A)**, the Z-potential value of GQD–MRs decreased from –49 ± 5 mV to –65 ± 1 mV after biofunctionalization with the FAM-L probe. This Z-potential decrease is in agreement with the negative phosphodiester backbone of the FAM-L probe.[431] To demonstrate the suitability of the dynamic biocarriers to interact with a complementary DNA target, they were firstly incubated with an aliquot of DNA target (40 nM) for 5 min to promote the DNA hybridization process. As expected, the Z-potential value was completely recovered after DNA hybridization, yielding to a Z-potential value of –42 ± 6 mV. This data fully demonstrates that the dynamic biocarriers can properly interact with the DNA target, resulting in a release of the biomarker from the GQD–MRs's walls. It is important to point out that these experiments were run under static conditions (considering the microrobots as passive particles).

Further, these results are also in line with the ones obtained by FL measurements (**Figure 42(B)**), in which a quenching on the emission band of the FAM-L probe (control) at 527 nm (λ_{ex} = 490) was clearly observed after immobilization on GQD–MRs *via* π-stacking interactions, while the intensity of the emission band remarkably increased when the dynamic biocarriers were exposed to a fixed concentration of DNA target driven by the DNA

hybridization process. All in all, it is safe to conclude that the FAM-L probe was successfully immobilized on the GQD–MRs' walls *via* π–stacking interactions, as well as the DNA target provides a proper environment to release such interactions after hybridization. Thus, motivated by these promising results obtained under static conditions, the last step was focused on exploiting the devised dynamic biocarriers towards the "on-the-fly" determination of DNA.

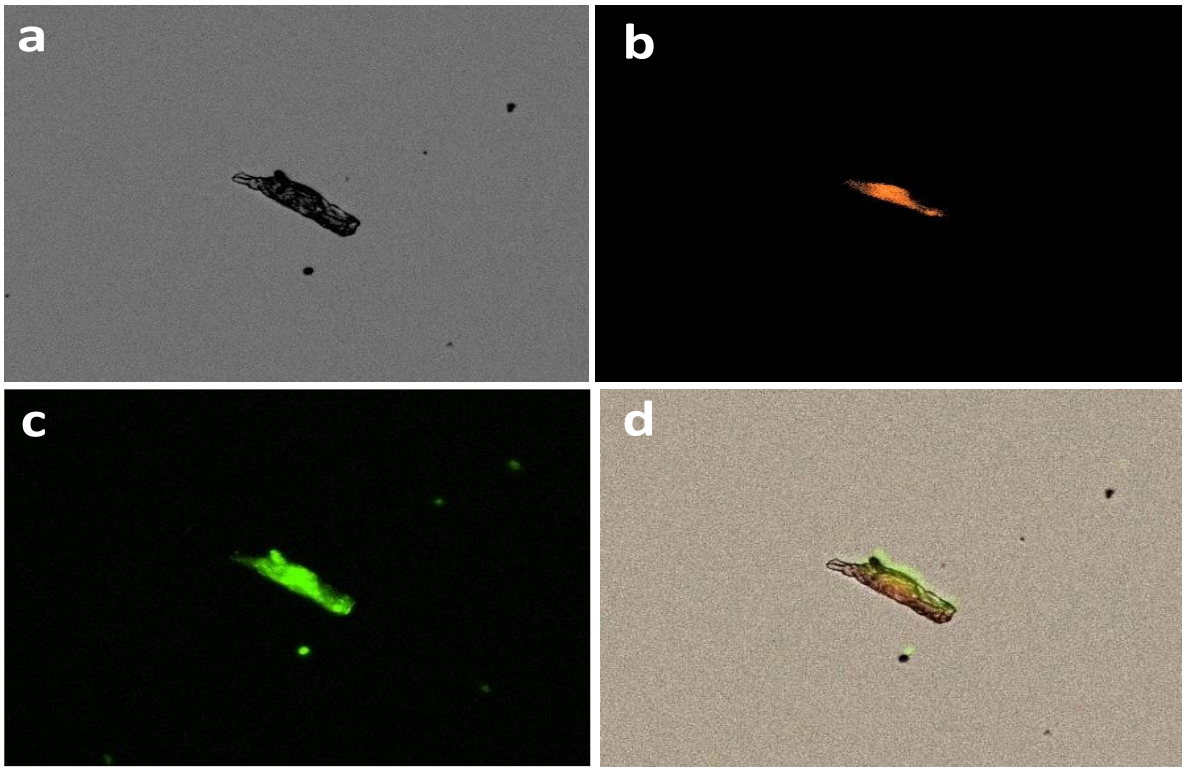

Figure 41. (a) is depicting the control of the GQD–MR in the bright field mode. (b) fluorescence due to the GQDs embedded on the surface of the microrobots. (c) fluorescence of FAM-L probe present on the surface of the GQD–MRs. (d) is depicting the multichannel image of the GQD–MR with DNA probe on its surface.

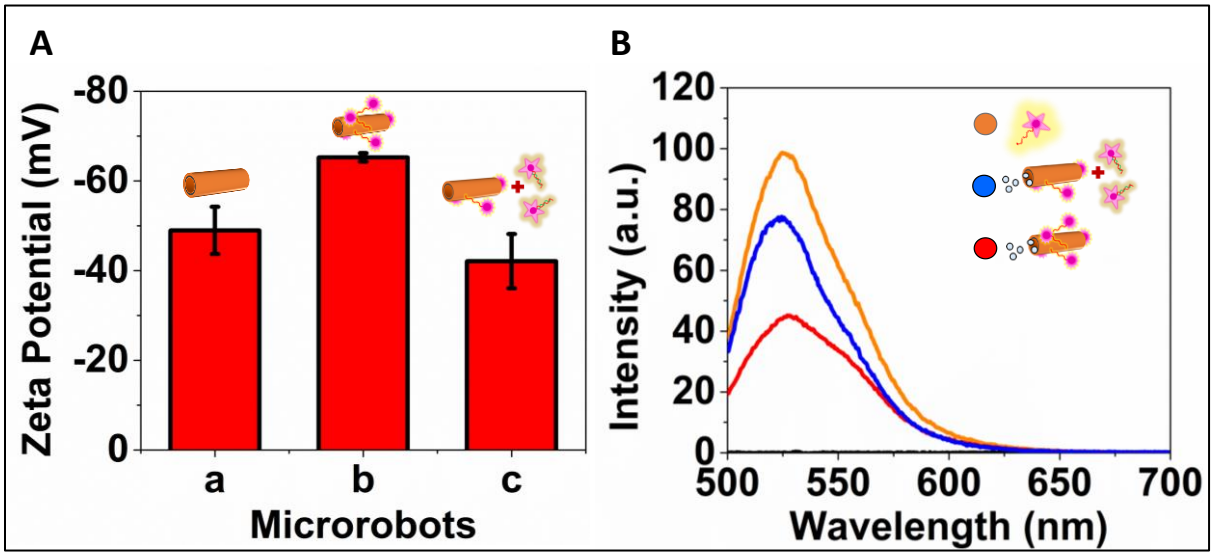

Figure 42. Characterization of microrobots at the different biofunctionalization stages under static conditions. (A) Z-potential values of GQD–MRs and dynamic biocarriers before and after DNA target interactions. **(B)** Emission spectra of FAM-L probe (control, orange line) and dynamic biocarriers before (red line) and after DNA target interactions (blue line). Experimental conditions: λ_{ex} = 490 nm; [FAM-L probe] = 40 nM; Hybridization time: 5 minutes.

Optical "on-the-fly" DNA determination using dynamic biocarriers

Once verified the formation of the dynamic biocarriers and their feasibility towards DNA determination *via* a DNA hybridization process, the optimization of the "on-the-fly" detection conditions was first studied. This includes optimizing pH, salt concentration, and incubation time (**Figure 36**). From this optimization study, it can be concluded that the best experimental conditions are: *i)* pH: 7, salt concentration: 200 nM, and incubation time: 5 min.

As demonstrated by Zeta potential, UV-vis spectroscopy and FL analyses, the reported conditions successfully reached the DNA hybridization, which was monitored via FRET effect by employing different concentrations of DNA target. During all the processes, the temperature was fixed to room temperature to make the experiments simpler in the cuvette.

After optimizing these factors, the last stage was focused on exploring their optical "on-the-fly" biorecognition capabilities. For this aim, a fluorometric assay was run by adding a fixed amount of dynamic biocarriers containing different concentrations of DNA target at the nM range to a quartz cuvette. Further, the solution was filled with a drop of H_2O_2 to reach 1% H_2O_2 (v/v) to induce the "on-the-fly" DNA determination. Thus, the intensity changes on the emission band of the FAM-L probe were monitored after 5 min of incubation time and represented as $\Delta_{FL} = I_x - I_0$, where I_x and I_0 are the fluorescence intensity obtained before and after adding different *x* concentrations of DNA target, respectively (**Figure 43**). Herein, the optical detection principle relies on monitoring the fluorescence recovery of the quenched FAM-L probe presented in the dynamic biocarriers after incubation with different concentrations of DNA target (complementary to the FAM-L probe sequence).[160-472] Thus, the addition of the DNA target promotes the hybridization between the FAM-L probe immobilized on the GQD–MRs and the target, leading to a double-stranded DNA (ds-DNA) formation. Since the resulting ds-DNA has a poor binding affinity to the GQD–MRs,[473,474] it releases from the surface of the dynamic biocarriers, resulting in a fluorescence intensity recovery. Hence, the changes in the fluorescence intensity band of the FAM-L probe with regarding different concentrations of DNA target (optical readouts) were the key to the "on-the-fly" DNA determination.

As shown in **Figure 44**, the "on-the-fly" DNA determination study was conducted *via* FL analyses, where the emission band intensity increases with increasing concentration of DNA target ranging from 0.05 to 100 nM. In contrast, linear range was obtained from 1 to 100 nM (**Figure 43(A)**). **Figure 43(A)** (inset) displays a linear plot of [DNA target] *vs.* Δ_{FL} with its corresponding error bars (*n=3*). An excellent calibration curve —Δ_{FL} = 1.70 + 0.04 [DNA target] (nM), R^2 = 0.99 at the 1.0–100 nM range was yielded, with a detection limit as low as 0.05 nM. Importantly, a control calibration plot under static conditions (without H_2O_2-induced motion) was also run in order to demonstrate the benefits of the dynamic biocarriers (**Figure 45**). As shown in **Figure 43(B)**, the sensitivity of the method was 3 times enhanced under motion conditions. In addition, while the dynamic biocarriers obtained an excellent linear trend with increasing the [DNA target] through the "on-the-fly" analysis, a non-linear trend was observed during the static control (**Figure 46**). Principally, the continuous motion of the microrobots enhanced the mass transport within the solution. Further, due to the propulsion of the microrobots, the rate of diffusion increases, which amplifies the homogeneous dispersion of desired materials.

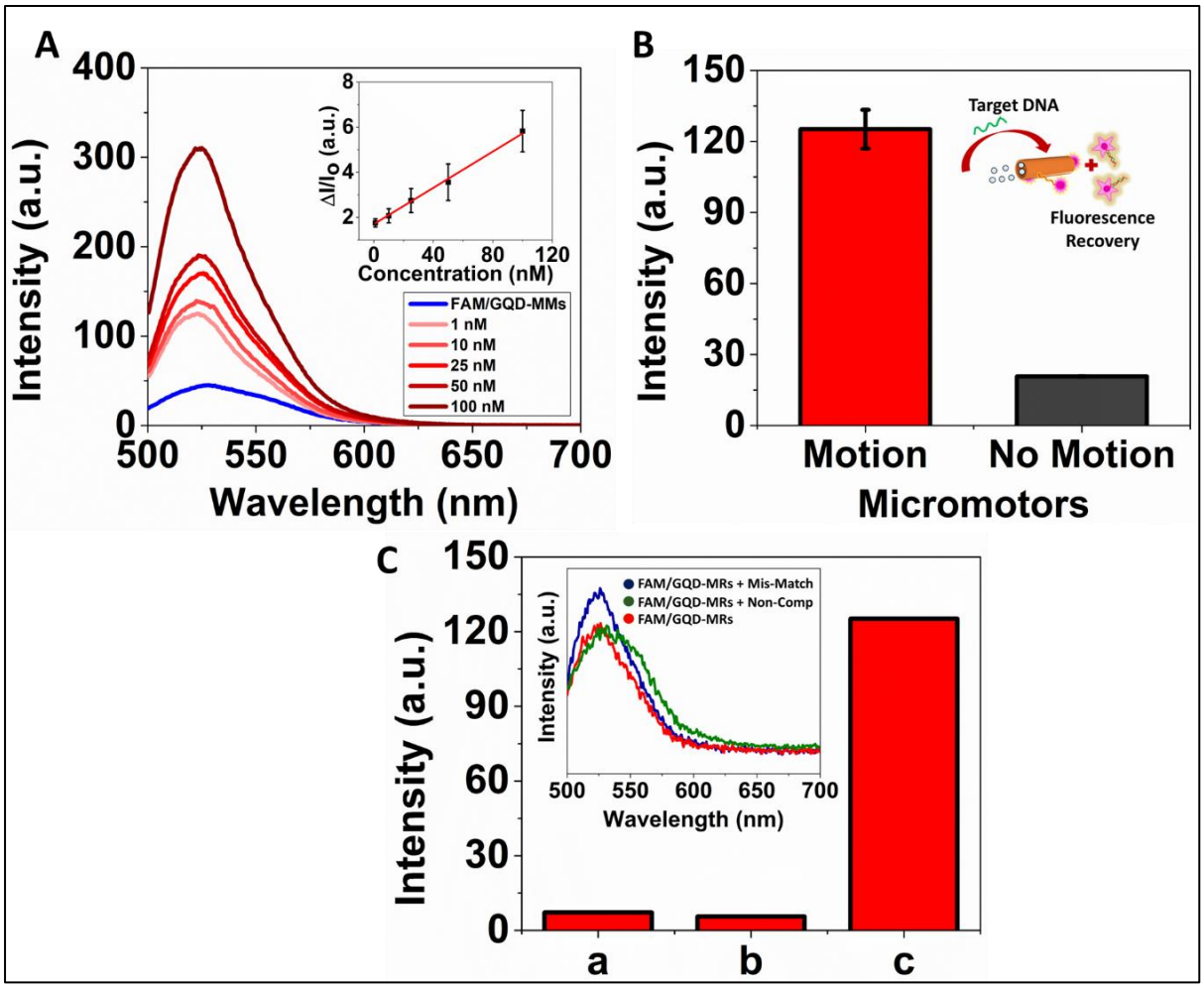

Figure 43. Benefits of exploiting dynamic biocarriers towards the optical "on-the-fly" DNA determination. **(A)** Emission spectrum of dynamic biocarriers before and after adding different [DNA target], demonstrating how the FL of the FAM-L probe is progressively recovered after "on-the-fly" DNA hybridization (*n=3*). Inset: calibration plot under motion conditions represented as $\Delta I/I_0$ *vs.* [DNA target]. **(B)** Histogram depicting the FL intensities achieved by the FM/GQD–MRs towards a fixed concentration of DNA target (1 nM) under motion (1% H_2O_2) or non-motion (no fuel) conditions (inset: schematic representation of microrobots with motion). **(C)** FL intensities achieved by the dynamic biocarriers towards different targets (1% H_2O_2) (*i.e.*, mis-match **(a)** and non-complementary DNA **(b)** DNA target **(c)**; target concentration: 1 nM) (inset: emission spectrum of the dynamic biocarriers (1% H_2O_2) *i.e.*, FAM/GQD-MRs (red), FAM/GQD-MRs with non-complementary DNA (green) and FAM/GQD-MRs with mis-match DNA (blue). Experimental conditions: λ_{ex} = 490 nm, hybridization time: 5 min, concentration (mis-match, non-complementary DNA): 1 nM.

Thus, enabling them to enhance the efficiency, velocity, and yield of their processes. Hence, it demonstrates the pivotal role of "on-the-fly" analyses in rapidly interacting/being intimate with the target of interest, making it possible to reach better sensitivities.

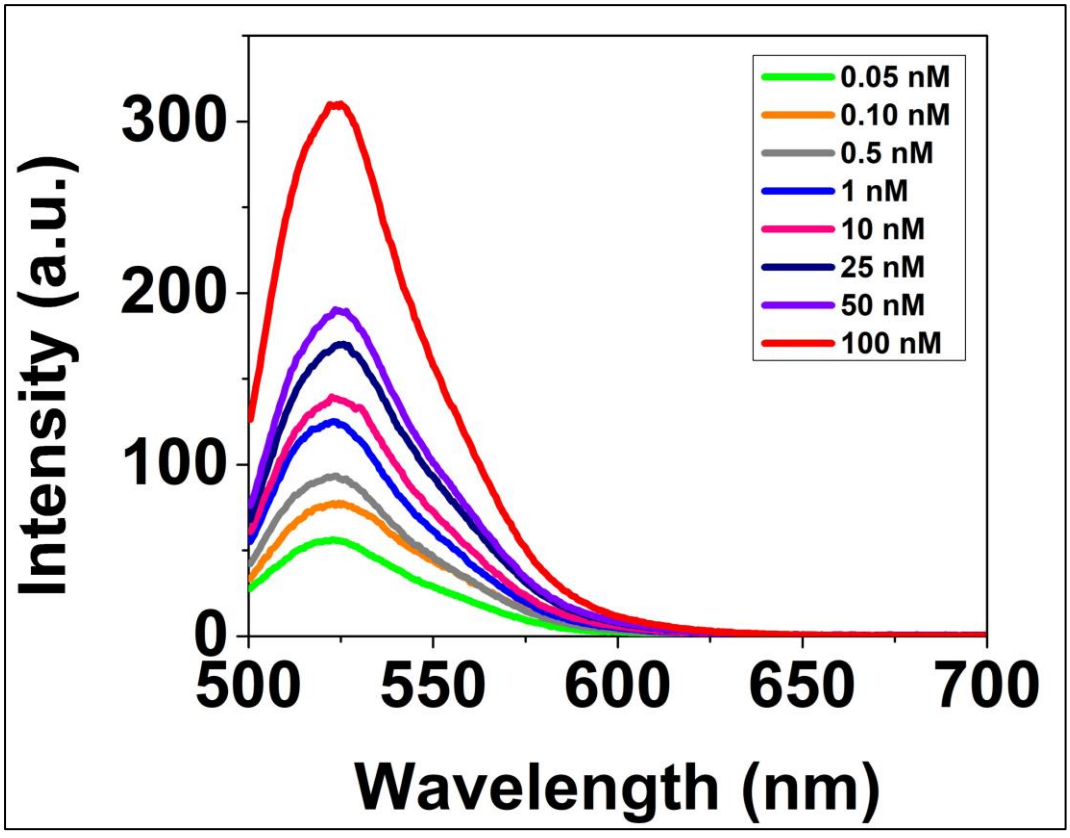

Figure 44: Effect of the different concentrations (0.05, 0.10, 0.5, 1, 10, 25, 50, 100 nM) of the target DNA on the fluorescence emission spectra of the GQDs-MRs (with motion). Conditions: Excitation wavelength 490 nm, FAM-L probe concentration 40 nM, hybridization time 5 minutes.

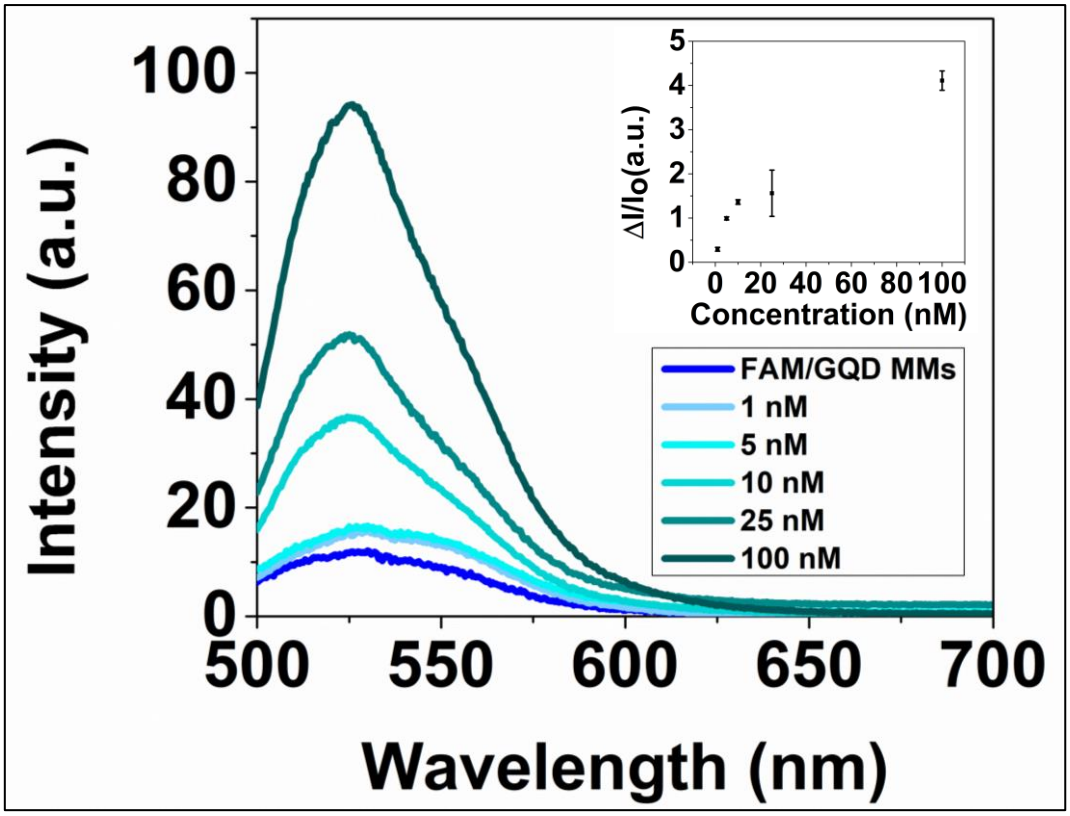

Figure 45. Effect of the different concentrations (1, 10, 25, 100 nM) of the target DNA on the fluorescence emission spectra of the GQDs-MRs (no motion). An inset shows the concentration calibration curve for the target DNA hybridization based on the performance of GQDs-MRs in the absence of motion. Conditions: Excitation wavelength 490 nm, FAM-L probe concentration 40 nM, hybridization time 5 minutes.

Compared to the state-of-the-art DNA-based MRs utilized so far for the optical "on-the-fly" determination of DNA (see **Table S1**),[441,442,444,475] to the best of our knowledge, this supposes the first GQD-based MRs for optically monitoring DNA, presenting one of the lowest detection limits (0.05 nM *vs.* 10–1300 nM). Only the work carried out by Wu *et al.* surpassed the presented GQD–based MRs, where a detection limit of 0.01 nM was yielded using Au-Pt bimetallic nanomotors.[442]

The selectivity of the dynamic biocarriers towards the complementary DNA target was evaluated by exploring alternative DNA targets, such as mis-match and non-complementary DNA sequences. As shown in **Figure 43(C)**, a significant decrease in the emission band intensity was observed after the mis-match DNA hybridized with the FAM-L probe anchored to the GQD–MRs**.** Nonetheless, such intensity was 15 times lower than the one achieved by the complementary DNA target. Otherwise, almost no fluorescence response was evidenced when the dynamic biocarriers were exposed to the non-complementary DNA target. This

suggests that the devised GQD–MR-based dynamic biocarriers preferably interact with the complementary DNA target, validating the selectivity of the microrobots.

Finally, in order to validate its applicability in biological samples, the "on-the-fly" determination of DNA was also monitored employing biological fluids (urine and human plasma). To perform this study, 1 nM of the DNA target was spiked to urine and human plasma samples in the presence of dynamic biocarriers under motion conditions (fuel concentration: 1% H_2O_2), and the recovered concentration was optically quantified per triplicate ($n=3$) by extrapolation in the calibration curve from **Figure 43(A)** (inset). The average concentration of DNA target found in both urine and human plasma was 1.27 ± 0.34 nM and 1.31 ± 0.07 nM, respectively. These results evidenced a nonsignificant interfering effect from the complex matrices, demonstrating that the dynamic biocarriers can also be utilized for the "on-the-fly" monitoring of DNA in biological fluids.

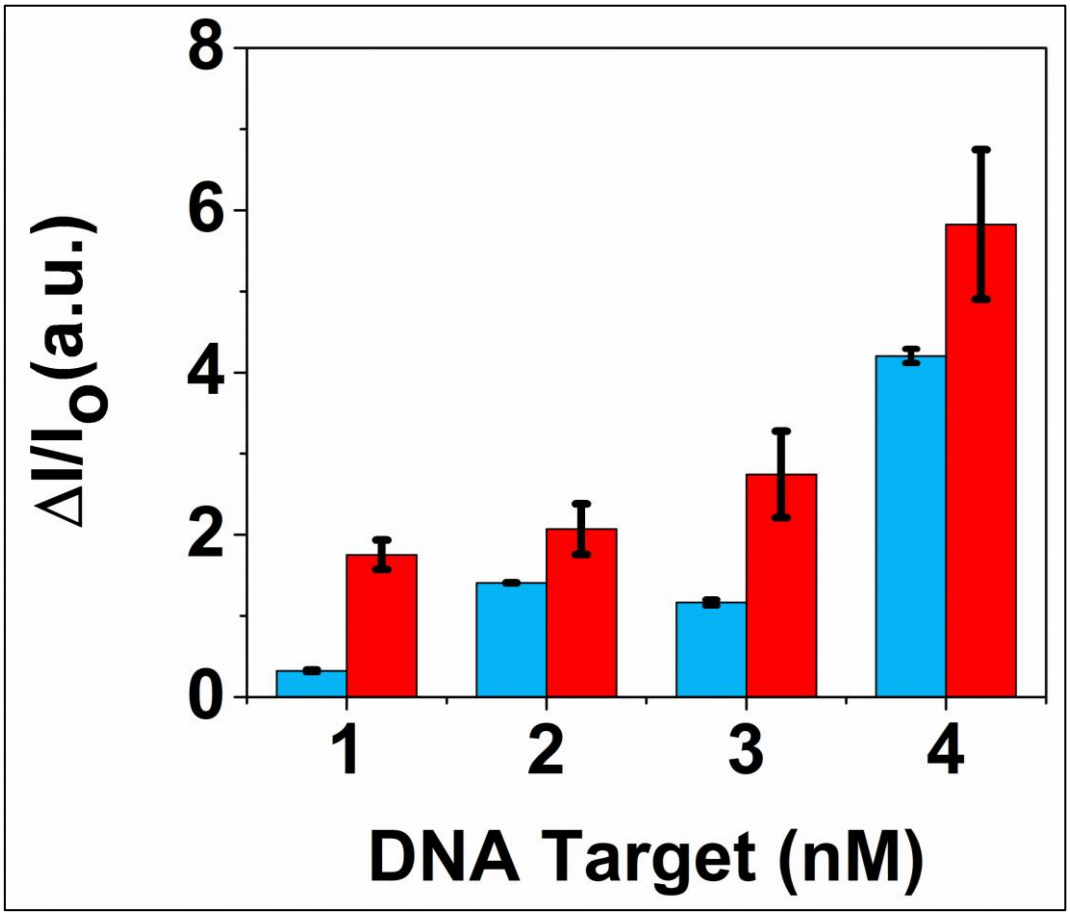

Figure 46. Comparison between the fluorescence intensity of the FAM-L probe (40 nM) hybridized with the target DNA (variable concentration). **Red** depicting the fluorescence response of the FAM-L probe, when GQDs-MRs were in motion while **blue** represents the micromotors without motion. Conditions: Excitation wavelength 490 nm, FAM-L probe concentration 40 nM, hybridization time 5 minutes.

5.1.4 Conclusion

Herein, a facile and cost-effective fabrication of dynamic biocarriers made of GQD-based self-propelled microrobots carrying a biological marker is presented for their exploration as unconventional optical platforms for enhancing analytical assays *via* "on-the-fly" interactions. As a proof-of-concept, the "on-the-fly" determination of DNA has been considered by immobilizing a DNA probe (*viz.* FAM-L probe) *via* supramolecular π–π interactions, obtaining excellent detection limits and selectivity when comparing with non-specific/mis-match DNA targets. Remarkably, this method was 3 times enhanced when the microrobots were in motion mode; in other words, it was enhanced when the biocarriers were in dynamic mode by taking advantage of the fuel (1% H_2O_2). In addition, the feasibility of the developed dynamic biocarriers was also explored by spiking the DNA target in two different biological fluids (*i.e.*, urine and plasma), demonstrating promising recoveries in both cases. Consequently, the preparation of hybrid MRs by combining different materials exhibiting different features (*i.e.*, GQD with fluorescence and π-stacking interactions, Pt with self-propelling capabilities and Ni responding to an external magnetic field) provides multifunctional microrobots capable of performing analytical tasks in a rapid, sensitive and selective way. This work opens a way for rapid DNA optical assays, which are dramatically enhanced by the presence of micromachines.

Type of Micromotors	Target detected	Detection Range	Environment	Detection Limit	Reference
Catalytic Nanomotors (Au-Pt bimetallic nanowire)	DNA sensing	0.01 -100 nM	In-vitro	0.01 nM	[442]
Enzyme-powered micromotor	DNA detection	10 nM to 1000 nM	In-vitro	10 nM	[441]
Catalytic, magnetic and hybrid micromotors	Gastric cancer biomarker detection	1000 to 10000 nM	In-vitro	1300 nM	[444]
Helical hydrogel micromotor	Tumor DNA detection	2500–25,000 nM	In-vitro	250 nM	[475]
GQD-MRs- based dynamic biocarriers	DNA detection	1–100 nM	In-vitro	0.05 nM	Present work

Table S1. Table showing different microrobots exploited towards the optical "on-the-fly" determination of DNA.

List of Abbreviations

0D	Zero dimensional
GQDs	Graphene Quantum Dots
Ni	Nickel
Pt	Platinum
SEM	Scanning Electron Microscopy
EDS	Energy Dispersive Spectroscopy
UV-vis	Ultraviolet–visible spectroscopy
MRs	Microrobots
FRET	Fluorescence Resonance Energy Transfer
DNA	Deoxyribonucleic acid
ss DNA	Single-stranded DNA
FAM-L	Fluorescein Amidites Labelled
H_2O_2	Hydrogen Peroxide
FL	Fluorescence Intensity
nM	Nano Molar
FTIR	Fourier-transform infrared spectroscopy

This page is left intentionally

Chapter 5.2

Active Quantum Materials Enhanced Microrobots for Food Safety

Publication: Manuscript under revision

5.2.1 Introduction

Food safety is a paramount concern in today's world, with an increasing global population and the globalization of food supply chains. The proliferation of foodborne pathogens is a growing matter for public health and the food industry. *Salmonella* is an anaerobic, gram-negative, rod-shaped bacterium that readily spreads among humans and animals, leading to food and waterborne diseases.[476] *S. enterica* serovar Typhimurium (*S. typhimurium*) is the principal representative among a cluster of bacterial species responsible for numerous cases of foodborne illnesses (diarrhoea, abdominal pain, nausea) each year, leading to hospitalizations and millions of dollars in annual economic losses worldwide.[477,478] In 2022, the World Health Organization (WHO) reported 34 instances of food safety incidents related to Salmonella across member states and territories.[479] Among Salmonella infections, *S. typhimurium* had the highest incidence rate, which was linked to nosocomial infections and severe food poisoning with a substantial fatality rate.[480] This data underscores the significance of addressing *Salmonella*-related risks to public health. To combat such risks, the European Union has implemented strict standards to ensure *Salmonella*-free food.[481,482] However, this underscores the importance of addressing Salmonella-related risks to public health and emphasizes the need for innovative and rapid methods of identifying and mitigating *Salmonella* contamination in food products. Traditional culture-based methods are time-consuming and prevent fast action.[483] Alternatives such as polymerase chain reaction (PCR)[484] and enzyme-linked immunosorbent assays (ELISA)[485,486] methods offer high reliability and low limits of detection. Still, they are laborious, time-consuming and require specialized equipment and personnel. Therefore, it is crucial to develop prompt, robust, and cost-effective novel methods for real-time detection of *Salmonella* contamination and other food-related pathogens.

Over the past decade, there has been significant progress in biosensing technologies and the development of new biomaterials.[487–490] These advancements have been effectively applied for the detection of biomarkers associated with major foodborne pathogens in a myriad of biodefense, food safety, and public health settings.[439,491–493] Quantum materials (QMs) have paved the way for groundbreaking developments in food safety. In this context, particularly the emerging field of 'active quantum materials' is revolutionizing the way we approach food safety. Quantum dots are zero-dimensional carbon nanostructures that exhibit quantum confinement effects, leading to size-dependent electronic properties[494], making them ideal carriers for optical biosensors. Furthermore, these QMs can significantly enhance the

capabilities of biosensors due to their unique physicochemical properties and diverse surface chemistry.[420–423,495]

Chemically propelled microrobots, powered by chemical energy sources, are micro- and nanomachines capable of manoeuvring through complex environments. This enables them to reach predetermined locations for targeted sensing. Particularly noteworthy is their proficiency in "*on-the-fly*" bio-recognition, enabling rapid interaction with target substances. It eliminates the need for additional steps in the detection process. Thus resulting in a significant reduction overall costs. Owing to these exceptional benefits, microrobots are employed in various fields such as catalysis, environmental remediation, cancer therapy, biosensing, among other applications.[441,443,496–498]

In view of the potential of QMs for biosensing, our research group explored the integration of such materials as active elements in polycaprolactone/Pt catalytic Janus microrobots for fluorescence detection of *Escherichia coli* (*E. coli*) endotoxins in clinical samples, including human serum and urine,[428] as well as *S. enterica* endotoxins in milk, eggs, and mayonnaise.[499] A notable drawback of this method lies in its constrained selectivity and specificity. This approach predominantly depends on recognizing the oligosaccharide core, a shared fragment present in endotoxins across most gram-negative bacteria. Later, the strategies were implemented by our research group for the use of selective affinity peptides in OFF-ON approaches but using chalcogenides as active materials for encapsulation into the micromotors,[500,501]. Quantum materials can also be used as the external layer of catalytic tubular microrobots prepared by template-assisted electrodeposition. The resulting quantum materials enhanced microrobots (QEMRs) have a high density of active functional groups for probe immobilization, combining at the same time the enhanced fluid mixing and motion in microvolume samples.[427] The "moving biosensors" with optimal analytical features, as already illustrated by our research group for the detection of DNA. The outer QMs layer allows for the incorporation of fluorescein amidite-labelled DNA probe by π- π interactions. In the presence of the target DNA, the probe is released, increasing the fluorescence of the solution for OFF-ON detection and allowing detection at the nM range.[502] In all these strategies, only a few microliters of sample are required, achieving detection in a few minutes. This study aims to demonstrate the huge potential of quantum materials enhanced microrobots for food safety applications related to the detection of *S. typhimurium* endotoxin by limiting the required sample volumes.

5.2.2 Experimental Methods

Chemicals

Citric acid (cat. 251275), nickel tetrahydrate (cat. 262277), nickel chloride hexahydrate (cat. N6136), boric acid (cat. 15665), chloroplatinic acid hydrate (cat. 520896), sodium dodecyl sulphate (cat. 71727) (SDS), polyethylene glycol (cat. 89510) (PEG), Tween 20 (cat. P9416), hydrogen peroxide (30%, cat. 216763) (H_2O_2), Triton X-100 and endotoxins from *S. enterica* Typhimurium (cat. L6143) and *S. enterica* Enteritidis (cat. L7770) were purchased from Merck (Madrid, Spain). Rhodamine (RhO)-labeled affinity peptide (RhO-NFMESLPRLGMH) was custom-made by Quimigen (Madrid, Spain).

Equipment Used

Scanning electron microscopy with energy-dispersive X-ray detection (SEM-EDX) characterization was performed using a TESCAN LYRA 3 XMH instrument. Further, VERTEX 70v FT-IR Spectrometer were used to validate the interactions between the microrobots and the affinity peptide. To evaluate the charge distribution of the microrobots, Z-potential measurements were conducted with a Malvern Zetasizer. Fluorescence measurements were performed with a Biotek Cytation 5 imaging reader at room temperature. Nikon ECLIPSE Ti-S/L100 inverted microscope equipped with a multi-LED light illumination source (CoolLED's pE-4000), a zyla sCMOS camera and a G-2A epifluorescence filter (510-560 nm) was used to capture the autonomous motion behaviour of the microrobots and to capture fluorescence images.

Synthesis of Graphene Quantum Dots (GQDs)

QDs were produced *via* direct pyrolysis using 2 g of citric acid (CA). CA was heated to 200°C in a 5 mL beaker on a heating mantle. Within 30 minutes, the liquid transformed from colourless to pale yellow to orange, indicating the generation of the QDs, which were subsequently dispersed in alkaline solution. For more details on the synthesis, see the previous procedure followed.[503]

Synthesis of GQMs/Ni/Pt microrobots

Microrobots were synthesized by using the previously established membrane-assisted electrodeposition method, following **Scheme 5**.[427,446,447,452] In brief, a 100 nm-thick layer of gold (Au) was sputtered onto a Whatman Cyclopore polycarbonate membrane (cat. WHA70602513, purchased from Merck) with 5 μm pore size using electron-beam evaporation (1.4 kV, 1.8 mA). This modified membrane was assembled in a custom-made Teflon cell, using aluminium foil as the electrical contact for the working electrode. A platinum wire was used as a counter electrode, while an Ag/AgCl electrode in a 1 M KCl solution acted as the reference electrode. The membrane-based electrode was then integrated into a three-electrode cell configuration, employing electrochemical depositions that were carried out using an AUTOLAB potentiostat (Metrohm). The electrodeposition process involved the following steps: (i) Formation of the outer GQD layer: GQDs were deposited from a 0.1 $mg \cdot mL^{-1}$ dispersion in a supporting electrolyte of 0.1 M H_2SO_4 containing 0.5 M Na_2SO_4 using cyclic voltammetry. The potential window ranged from +0.3 to –1.5 V vs. Ag/AgCl, with a scan rate of 50 $mV \cdot s^{-1}$ and a total of 40 cycles. ii) Deposition of the Ni middle layer: The Ni middle layer was deposited from a solution containing 2M of nickel sulfamate, 82mM of nickel chloride and 485mM of boric acid (pH, 4) through chronopotentiometry, maintaining a bias potential of +1 V vs. Ag/AgCl for 350 seconds. iii) Electrodeposition of the Pt inner layer: The Pt inner layer was electrodeposited using a 4 mM H_2PtCl_6 solution in 0.5 M boric acid by chronoamperometry with a current set to –20 mA for 2000 seconds.

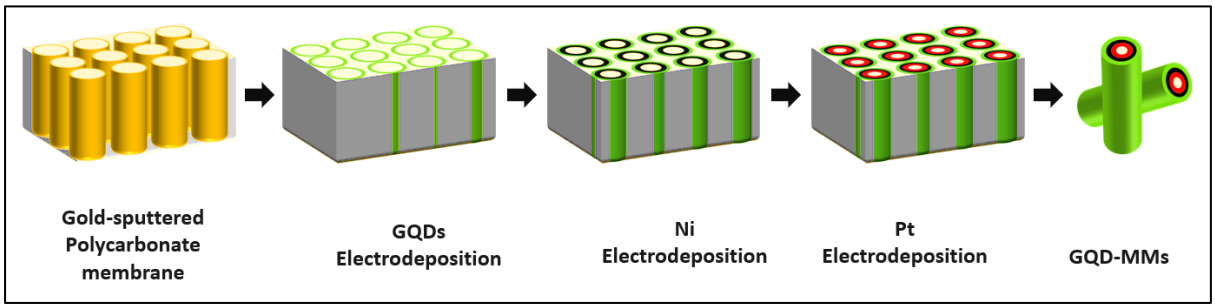

Scheme 5. Synthesis of QMs/Ni/Pt microrobots: Template-assisted method was used to incorporate *i)* QMs (outer layer), *ii)* Ni (middle layer) and *iii)* Pt (inner layer) *via* electrodeposition.

Following electrodeposition, the membrane was carefully detached from the Teflon cell and thoroughly rinsed with deionized water. Subsequently, it underwent a hand-polishing process with an alumina slurry (0.5 μm) to remove the Au layer. The membrane was then subjected to

a series of washes, including 2x dichloromethane (30 min vortex, 3 min centrifuge at 7000 rpm) followed by 2x washing in isopropanol (15 min vortex, 3 min centrifuge at 8000 rpm) and at last, it was subjected to 3x deionized water (15 min vortex, 10000 rpm). The resulting microrobots, were stored in 1 mL of deionized water for further use and remained stable for 4 weeks without any changes in their properties.

Functionalization of the GQMs/Ni/Pt microrobots with affinity peptide

After the synthesis, the microrobots underwent modification by combining 100 μL of the as-synthesized microrobots with 50 μg mL^{-1} of peptide (100 μL), and allowing them to incubate at 25 °C for 10 minutes at 950 rpm to initiate the electrostatic interactions between the two which led to the quenching of the fluorescence of the affinity peptide (*OFF* state) as shown in **Scheme 6**. The resulting active quantum carriers were then properly washed with deionized water by centrifuging twice for 5 min at 5000 rpm and finally resuspended in 90 μL of solution containing 1% PEG.

Microrobots motion study and endotoxin detection assay

Microrobots motion and speed was studied by placing a 1 μL of microrobot solution in a glass slide, 1 μL of H_2O_2 solution (final concentration, 9%) and 1 μL of PEG solution (final concentration, 1 % v/v). The videos were recorded, and the speed was tracked using NIS Elements Advanced Research software (Nikon).

The detection assay involved mixing 90 μL of the microrobots at a final concentration of 10 microrobots μL^{-1} with 15 μL of *S. enterica* endotoxin solutions to get a final concentration ranging from 0 to 300 μg mL^{-1}, along with 45 μL of 30% H_2O_2 (final concentration, 9%) in a 96-well microplate. The mixture was allowed to sit undisturbed for 5 minutes to allow microrobot motion in the solution. Subsequently, fluorescence was measured at 560 nm (excitation) and 601 nm (emission) (*ON* state) (**Scheme 6**). Each experiment was conducted in triplicate.

Bacteria culture

E. Coli strain B or *Staphylococcus aureus* bacteria were cultivated in Luria-Bertani medium incubated at 100 rpm and 37 °C for 16 h. The culture media was then collected and used to test the performance of the procedure. All the experiments followed UAH regulations, and all biosafety measurements were taken.

5.2.3 Results and Discussion

An *OFF–ON* fluorescence detection strategy is employed for the sensitive detection of low levels of endotoxins by functionalization of the surface of the microrobots with a fluorescence-labelled affinity peptide, as described in **Scheme 6**. The presence of sp^2 groups in the outer QEMRs surface facilitates the immobilization by π stacking. In the presence of the target endotoxin, the peptides are released from the microrobots surface, increasing the fluorescence of the solution in a concentration-dependent manner. The strategy is implemented in a microplate reader for future routine analysis. By harnessing the properties of quantum materials and the agility of microrobots, these innovative systems promise precision, speed, and versatility.

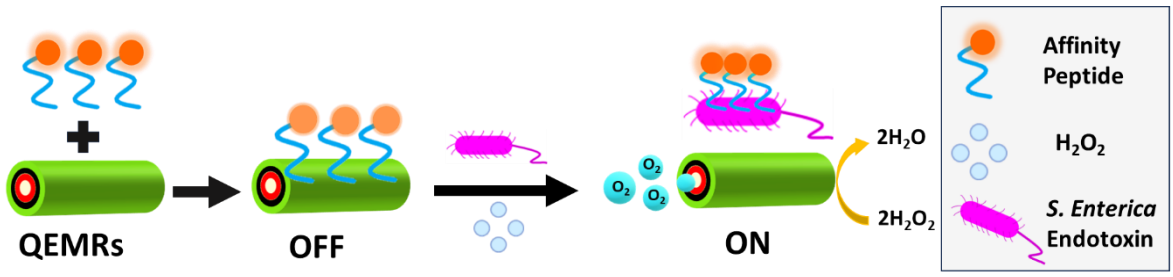

Scheme 6. Self-Propelled GQDs microrobots as active biocarriers for '*On-the-fly*' detection of *S. Enterica* Endotoxin Biofunctionalization of QEMRs with Rhodamine labelled affinity peptide, resulting in peptide@QEMRs, acting as active biocarriers inducing peptide's fluorescence quenching. The analytical assay relied on the real-time *on-the-fly* detection of *S. Enterica* endotoxin using 9% v/v in H_2O_2 as fuel. This initiated the release and interaction of the affinity peptide with the *S. Enterica* endotoxin, resulting in fluorescence recovery.

QEMRs synthesis, functionalization, and characterization

We prepared microrobots by electrodeposition technique. To confirm the successful synthesis of microrobots and to elucidate its surface morphology and composition, SEM-EDX was conducted. **Figure 47(A) (a)** showcases the SEM images of the microrobots, revealing a tubular structure with an approximate length of 5 µm and a cross-sectional diameter of 2.5 µm. The elemental mapping in **Figure 47(A),** such as **(b) (c) (d)** —indicates the presence of key elements, notably C, Ni and Pt. These findings suggest the successful synthesis of self-propelled microrobots and the presence of three distinct layers: QMs, Ni, and Pt as the outer, middle, and inner layers, respectively.

The outer QMs-based layer serves as the chemically active surface. Due to its exceptional chemical reactivity and unique electronic properties, it is a suitable choice for facilitating various chemical reactions and interactions at the material's surface.[504,505] Hence, after the addition of the fluorescence-labelled affinity peptide (acting as fluorophore), due to the electrostatic interactions between the GQMs and the peptide, it led to the quenching of the fluorescence of the solution (according to the FRET phenomenon).[439,506] Nickel (Ni), on the other hand, forms the magnetic core, constituting the middle layer of this composite structure. The presence of nickel in this configuration likely imparts magnetic properties to the material, potentially enabling it to respond to magnetic fields and exhibit magnetic behaviour, facilitating the washing steps, and holding considerable promise to explore alternative propulsion schemes desirable in labile samples.[507,508] Pt serves as the innermost layer in this composite material, functioning as a motion inducer. It is strategically placed within the inner wall of the tubular configuration to initiate motion. This placement allows for a precise and controlled mechanism for inducing motion. Within this tube, Pt undergoes nucleation, maturation, and diffusion, ultimately expelling oxygen from one of the micromotor's openings and propelling it in the opposite direction, which triggers the dynamic motion of the microtube, as required for specific applications.[14,448]

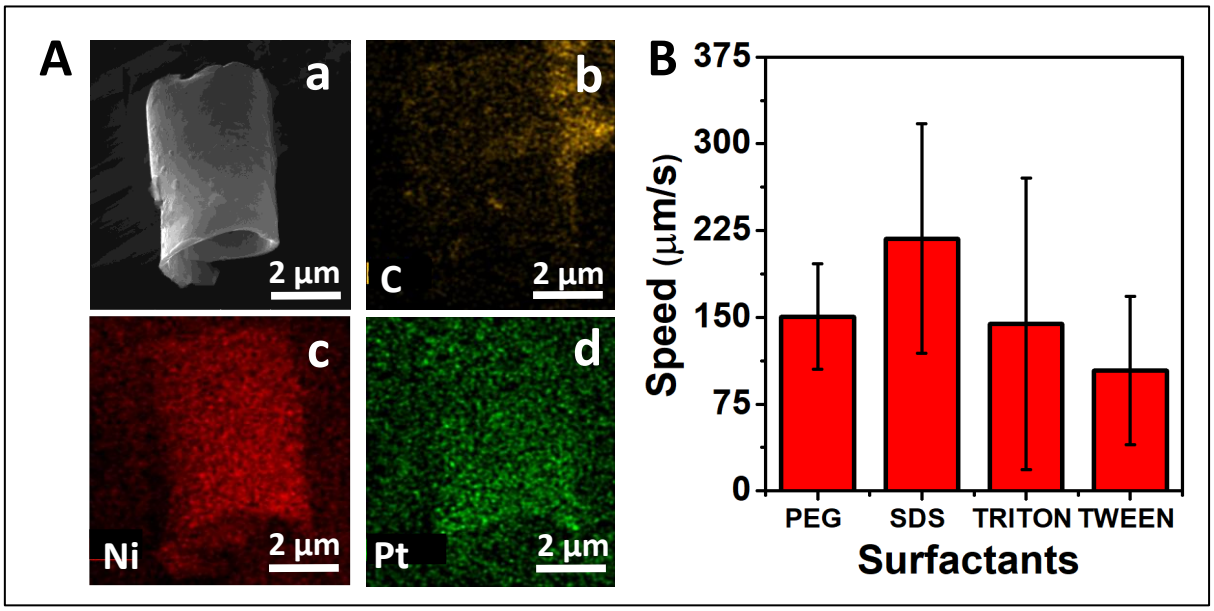

Figure 47 (A). (a) SEM and EDX (b-d) images of the QEMRs. **(B)** Effect of the surfactants on the speed of the QEMRs at 9% H_2O_2 levels and 1% of each surfactant. Errors bars represent the standard deviation of 3 measurements.

Before employing these microrobots for analyte detection, we investigated the impact of various surfactants on the speed, as depicted in **Figure 47(B)**. It was observed that in the absence of surfactants, microrobots were unable to achieve self-propulsion, especially at lower concentrations of H_2O_2. This highlights the essential role of surfactants in lowering the surface tension of the microrobots and stabilizing the generation of bubbles, which ultimately improves the micromotor speed.[509–511] Hence, to optimize the concentration of H_2O_2, we explored various surfactants, specifically anionic (SDS) and non-ionic (PEG, Tween 20, Triton X-100) surfactants at 1% concentration. Notably, we found that the use of 1% SDS resulted in significantly higher microrobots speed. In contrast, the use of non-ionic surfactants such as PEG, Tween 20, and Triton X-100 resulted in a significant decrease in micromotor speed. This reduction in speed can be attributed to the non-ionic surfactants with larger molecular mass, which is approximately four times that of the other surfactants used, and it substantially slowed down the microrobots.[510–512] Yet, for further studies, 1% PEG solution to block the potential non-specific binding of fluorescent biomolecules to the microrobots, minimizing the background noise and thus enhancing the performance in the analytical detection step.[513]

Once the synthesis and motion of QEMRs were confirmed, we studied the presence of surface functional groups and successful functionalization by FTIR spectroscopy. The FTIR spectra of the microrobots revealed the characteristic absorption bands corresponding to the stretching and bending vibration of the aromatic C–H group at 3385 cm^{-1}, C=C stretching at 1637 cm^{-1}, C–H aromatic at 2000 cm^{-1}, and epoxy stretching vibration of C–O–C groups at 1049 cm^{-1} (as shown in **Figure 48)**. Whereas the peaks (*i.e.*, located around 654 cm^{-1}, and 3400 cm^{-1} corresponding to N–H amines, respectively) were attributed to the presence of amino groups from peptide.[465–467] Additionally, the presence of C=O stretching at 1650 cm^{-1} and C-N group at 1250-1020 cm^{-1}, confirmed the conjugation (peptide@QEMRs). Moreover, the slight shift of the peptide@ QEMRs spectra towards the lower wavenumbers also confirmed the conjugation.

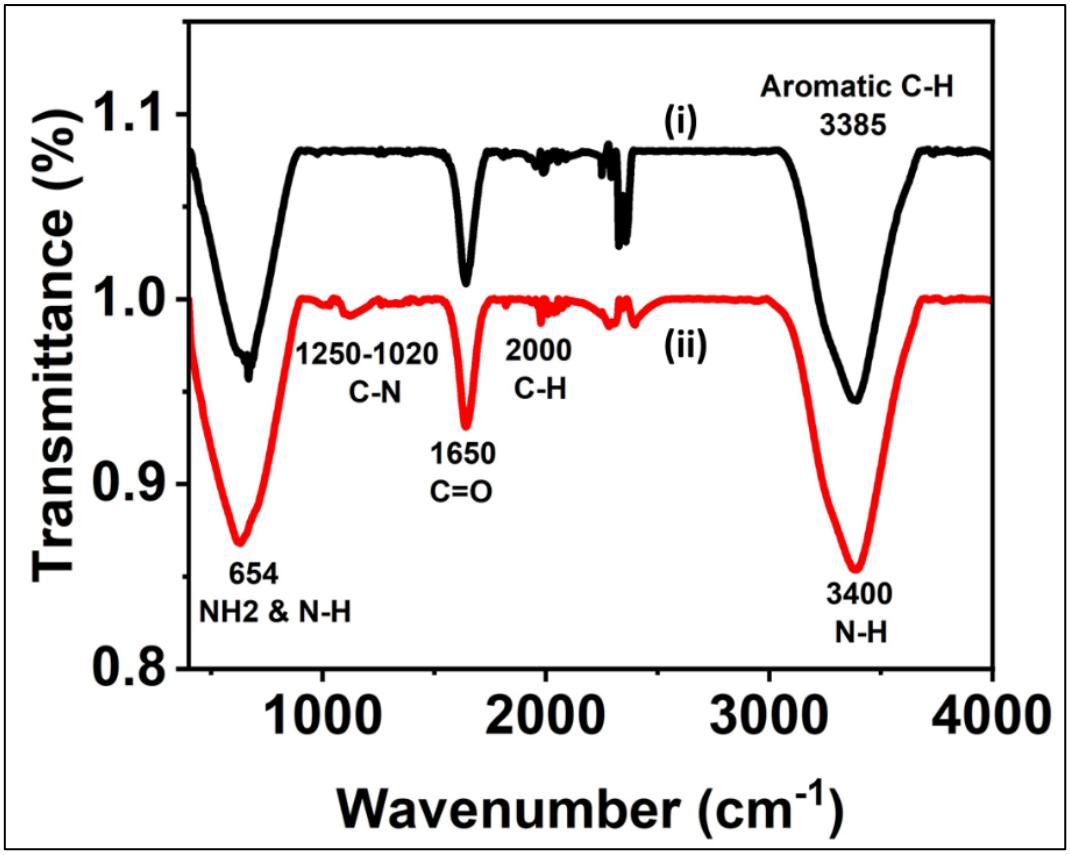

Figure 48. FTIR spectra of the **(i)** bare QBEMRs micromotors (black), **(ii)** peptide@QBEMRs micromotors (red).

Next, we investigated the charge distribution of QEMRs at two key stages: *before* and *after* the biofunctionalization. This was accomplished through Z-potential measurements conducted under various conditions, which included examination of the bare QEMRs and the peptide@ QEMRs along with affinity peptide and endotoxin, as shown in **Figure 49(A)**. It was observed that the zeta potential of the peptide@QEMRs decreased to –5.12 ± 2.37 mV following the successful functionalization of the positively charged QEMRs (+8.38 ± 3.18 mV) and the affinity peptide, which carried a negative charge of –16.04 ± 2.02 mV. This shift in Z-potential aligns with the anticipated electrostatic interactions between the microrobot's surface and the affinity peptide. Subsequently, upon the introduction of the negatively charged endotoxin (–38.79 ± 6.33 mV), the overall charge of the sample containing these dynamic bio carriers increased to –30.07 ± 3.81 mV. This confirmed the detachment of the affinity peptide from the surface of the QEMRs, thus demonstrating the effective '*ON-OFF'* interactions of the affinity peptide with the microrobot's surface. It's noteworthy that these tests were conducted with the microrobots in a stationary state (*no fuel*, H_2O_2).

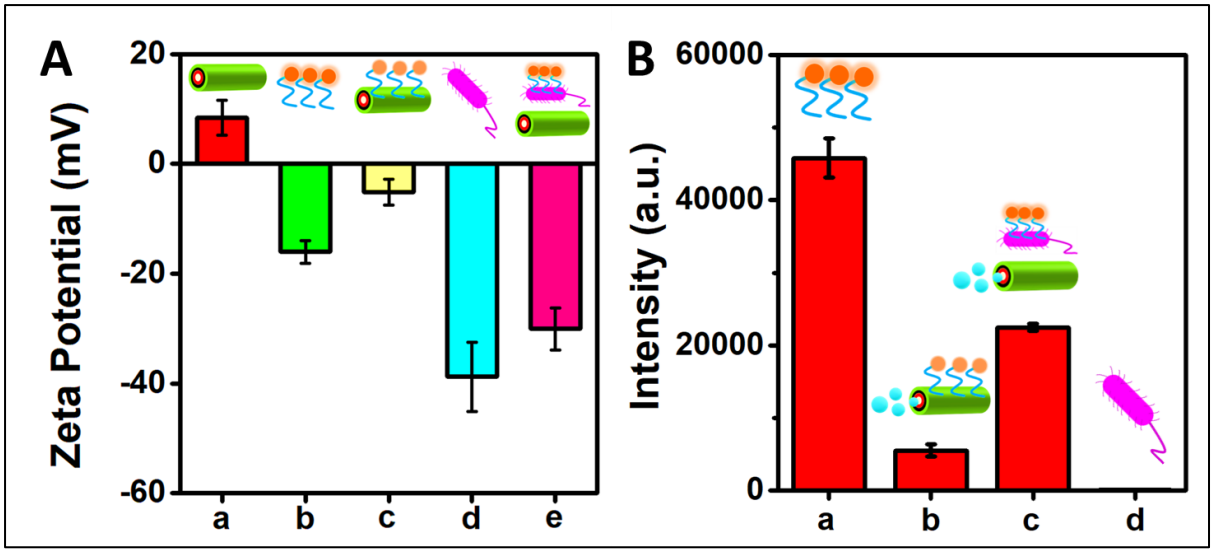

Figure 49. (A) Z-potential measurements of GQDs and peptide@QEMRs biocarriers before and after *S. enterica* endotoxin interactions (a) QEMRs (b) Rho labelled affinity peptide (c) peptide@QEMRs (d) *S. typhimurium* endotoxins (e) peptide@QEMRs interacting with *S. typhimurium* endotoxins **(B)** Histogram illustrating fluorescence intensities controls for (a) Rho labelled affinity peptide, (b) peptide@QEMRs, (c) peptide@ QEMRs interacting with *S. typhimurium* endotoxins (d) *S. typhimurium* endotoxins. Experimental conditions: λ_{ex} = 560 nm; [peptide, *S. enterica* endotoxin] = 50 µg/mL; incubation time: 10 minutes; recovery time: 5 minutes; 1% PEG; 9 % v/v in H_2O_2. Errors bars represent the standard deviation (n=3).

Consequently, an optical measurement was conducted to characterize the observed 'ON-OFF' behaviour of the affinity peptide after the introduction of the *S. typhimurium* endotoxin. Figure 49(B)illustrates the fluorescence measurement controls. **Figure 49(B) (a)** depicts the fluorescence intensity of the affinity peptide only**.** Following the incubation of the affinity peptide with the QEMRs, there was a significant decrease in fluorescence intensity (**Figure 49 (B) (b))**. This decrement in the fluorescence can be related to the interaction of the affinity peptide with the microrobot's surface, thus causing fluorescence quenching (*OFF state*). Whereas on the introduction of the definite endotoxin, the high binding affinity of the affinity peptide to the *S. typhimurium* endotoxins caused the peptide to dissociate from the QEMRs surface. As follows, it leads to the restoration of fluorescence of the fluorophore, depicted in **Figure 49(B)(c)**. And almost no fluorescence was observed from the separate *S. typhimurium* endotoxins control (**Figure 49(B)(d)**. Thus, motivated by these promising results, we further exploited these active quantum carriers for the detection of such endotoxins in real food samples.

Optical '*ON-OFF*' determination of endotoxin using QEMRs

Before moving to the analyte concentration calibration study, it's important to highlight that several essential optimization studies have been conducted. It included the peptide loading efficiency of the QEMRs and the incubation time optimization study for peptide@QEMRs complexes, illustrated in **Figure 50.** Certainly, the Eq. (6):

$$\eta\% = ([Fo - Fx] / Fo) * 100 \qquad \text{Eq. (6)}$$

Used to calculate the loading efficiency, expressed as a percentage of a substance, typically a peptide, onto QEMRs. *Fo* is the initial fluorescence of the affinity peptide, serving as a reference. *Fx* is the fluorescence of the peptide following incubation with QEMRs, reflecting the effectiveness of the substance loading onto the carrier. A higher η% indicates more efficient loading of affinity peptide onto the active biocarriers, as shown in **Table 2.**

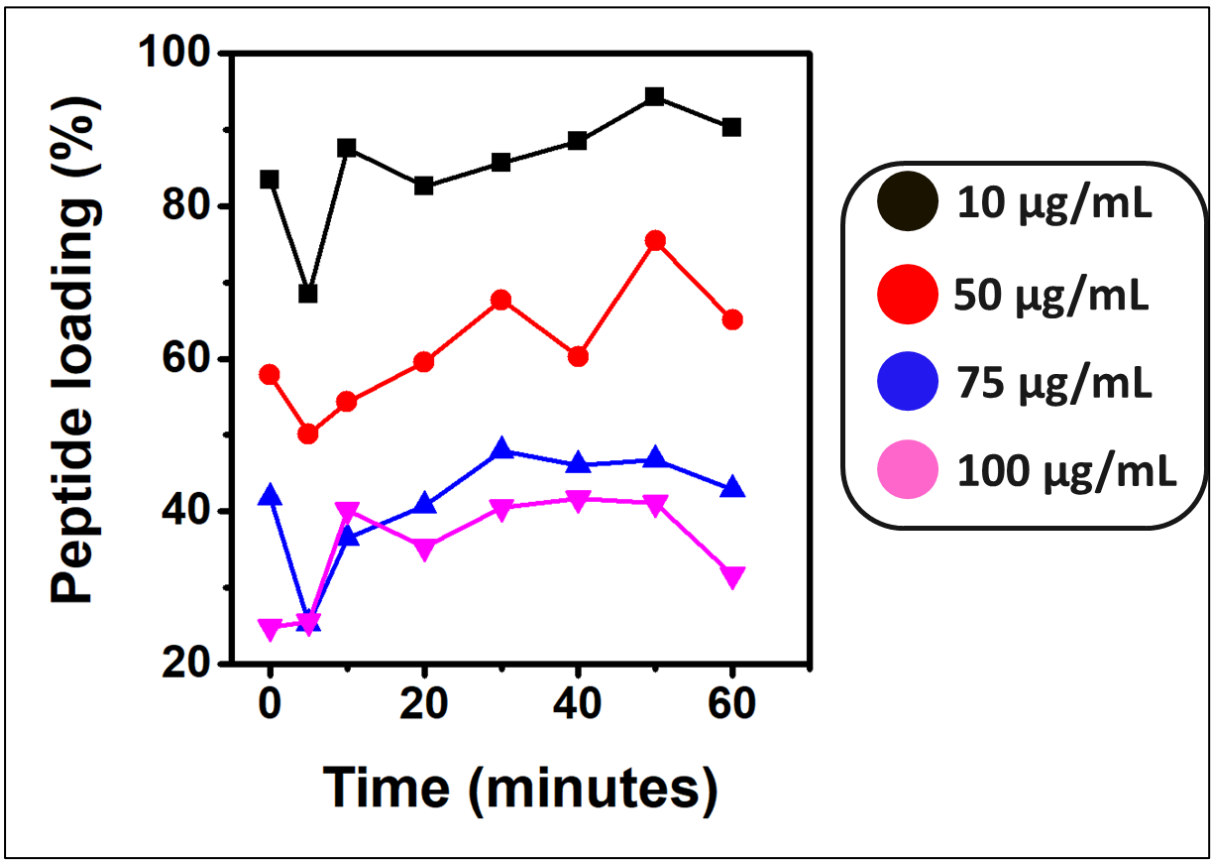

Figure 50. Optimization of the peptide loading capacity. Solutions containing different concentrations of the peptide (10-100 µg/mL) were incubated with the QBEMRs. The loading capacity was calculated by comparing the fluorescence of the solution prior and after micromotor incubation.

Concentration (µg/ml)	F_o (Affinity Peptide)	F_t (Average (n=3))	$(F_o-F_t)/F_o$ *100
10	37294	4641	90
50	314204	143631	54
75	343346	218216	36
100	324165	258278	20

Table 2. Peptide loading efficiency at 10 minutes.

Based on the study results, we conclude that incubating QEMRs with a 50 µg mL^{-1} peptide concentration for 10 minutes was the optimum time to carry out the subsequent studies. Furthermore, we performed a comprehensive investigation into the analyte detection time (0, 2, 5, 7, 10, 15, 18 min), *i.e.*, for *S. typhimurium* endotoxin (as presented in **Figure 51**), concluding 5 minutes as optimized duration. As longer times did not increase the signal significantly.

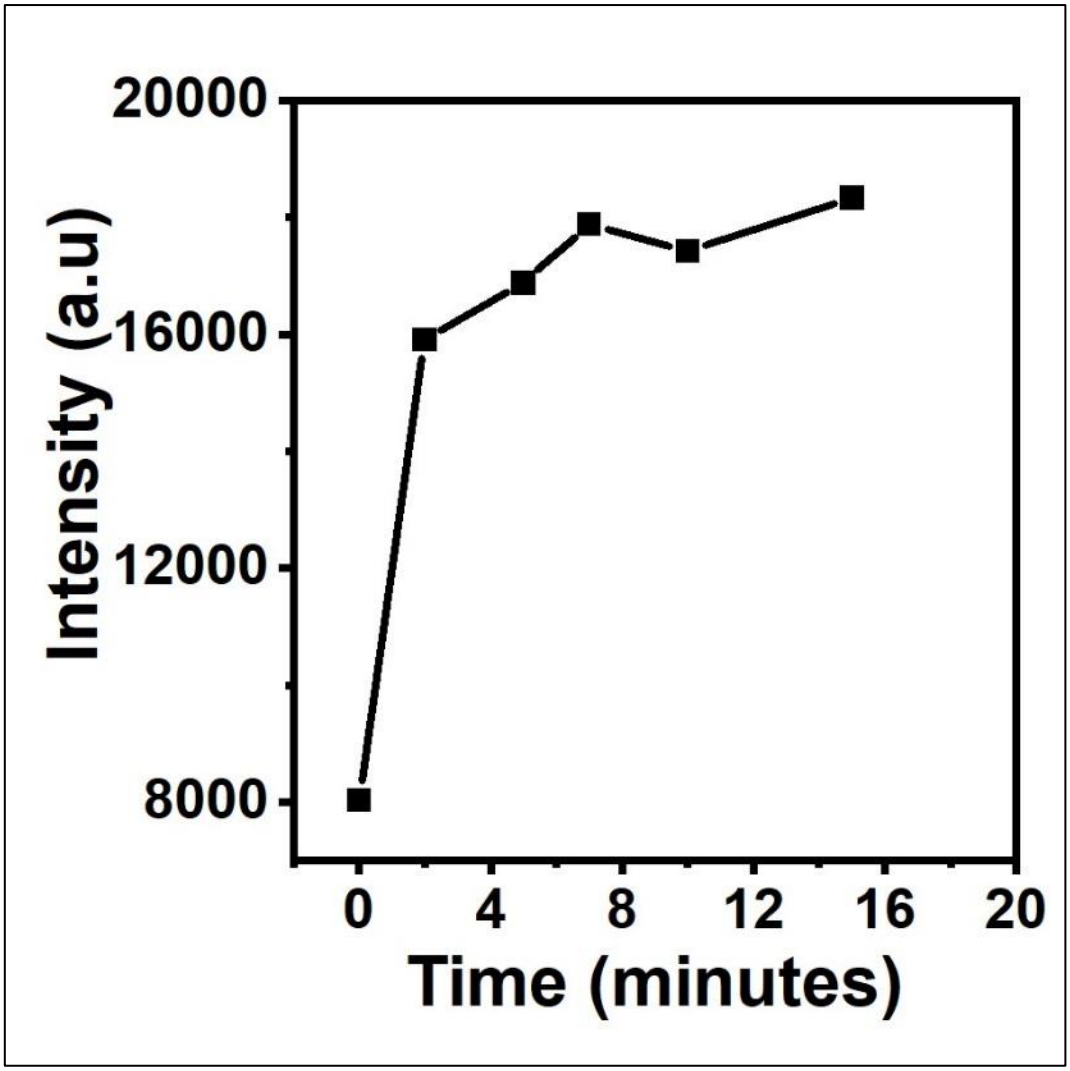

Figure 51. Optimization of the detection time. Fluorescence intensity of the solution after micromotor navigation in the *S. enterica endotoxin* (50 μg/mL) solution at different times.

Once these parameters were established, the results from these studies were utilized to utilize the QEMRs for the concentration calibration study of the *S. typhimurium* endotoxins. To achieve this, we performed a fluorometric assay within a 96-well plate. This involved the introduction of incubated peptide@QEMRs (90 μL) containing 1% PEG (1.5 μL). Subsequently, *S. typhimurium* endotoxin was added (45 μL) and allowed to incubate for 5 minutes. Followed by the introduction of H_2O_2 (13.5 μL) to reach a 9% H_2O_2 (v/v) concentration, activating real-time detection of *S. enterica* Typhimurium. In this context, detection approach relies on monitoring the fluorescence recovery of a quenched fluorophore (peptide@QEMRs) as it binds to different concentrations of *S. typhimurium* endotoxin.[478] Therefore, the introduction of the endotoxin induces the detachment of the affinity peptide from

the QEMRs surface. This detachment enables the peptide to bind to the endotoxin, resulting in the recovery of fluorescence in the fluorophore in a concentration-dependent manner. **Figure 52(A)** displays a linear plot between the logarithmic (log) values of the concentration of the analyte [endotoxin] *vs.* log [Fluorescence Intensity] with its corresponding error bars (*n=3*). This calibration curve exhibited —y = 0.2893x + 3.8369, linearity with R = 0.99 at the 10–300 μg mL^{-1} range, boasting a remarkably low detection limit of 1.8 μg mL^{-1}. And the detection range extended from 6 to 300 μg $mL.^{-1}$ **Figure 52(B)** depicts a sensitivity comparative study of the microrobots in both motion and stationary states. Notably, there was a significant reduction in the fluorescence recovery when the microrobots were stationary (—*no fuel*) as shown in **Figure 52(B) (a)**, in contrast to their motion (—*fuel used*) in **Figure 52(B) (b)**. This discrepancy can be attributed to the higher rate of diffusion observed when the microrobots are actively moving. Interestingly, almost no fluorescence was detected with blank microrobots, indicating their lack of inherent fluorescence, as evident in **Figure 52(B) (c)**. Furthermore, an intermediate response was observed when microrobots were blended (—*fuel, —no fuel*), reaffirming their high sensitivity to the surrounding matrix **Figure 52(B) (d)**. It was further validated by the microscopic fluorescence images as shown in **Figure 53.** Next, the selectivity of the active biocarriers was evaluated by exposing them to a range of gram-negative bacteria, including *E. coli*, *S. enterica* serovar Enteriditis (*S. Enterid*.), *vs. S. enterica* serovar Typhimurium, as depicted in **Figure 52(C)**. Notably, *S. enterica* Typhimurium showed stronger fluorescence recovery compared to *E. coli* and *S. enterica* serovar Enteriditis. This difference in response can be attributed to variations in the structural characteristics of the endotoxin's antigen O segment, thus enabling the distinction between 50 μg mL^{-1} S. *enterica* serovar Typhimurium endotoxins *vs. S. enterica* serovar Enteriditis. Hence, the strategy demonstrates a robust selectivity by employing specific affinity peptides to discriminate between bacterial types.

Subsequently, to confirm its utility in food samples such as orange juice, milk, and bacterial cultures, we conducted real-time '*on-the-fly*' monitoring of *S. enterica* serovar Typhimurium endotoxin detection. For this investigation, the actual samples (orange juice, milk, and bacterial culture) were fortified with 15 μg mL^{-1} of the target endotoxin. The results, as presented in **Figure 52(D)**, showcased varying recovery percentages for each sample. However,, a significant reduction in microrobots speed was observed, approximately around 51 ± 34; 44 ± 25, and 38 ± 24 μm s^{-1} upon the introduction of real samples like orange juice, milk, and bacterial culture. This decrease in speed was likely due to the higher viscosity of these real

samples, as depicted in **Figure 54**. It's worth noting that this speed reduction did not impede the practical use of microrobots, as they still achieved good recoveries in both situations. Thus, this confirms the successful implication of these active biocarriers for the detection of *S. enterica serovar typhimurium* endotoxins.

Furthermore, **Table 3** provides a comprehensive comparison of methods developed for the detection of *S. enterica* endotoxins. Firstly, Deby Choi *et.al.,* reported the detection of the lipopolysaccharide (LPS) antigens from *S. enterica* Typhimurium by using ELISA by taking 4 h.[514] S. Sannigrahi, *et al.,* (2020)[515] & X. Wang *et al.,* (2016)[516] reported magnetic methods for the *S. enterica* Typhimurium detection by taking longer times (30 min, 3 h, respectively). M. Pacheco. *et. al*.,[499] reported the detection by using GQDs Janus micromotors as sensing probe with lower limit of detection but the analysis time around 15 minutes. Although M. Pacheco *et. al*, also reported the optical detection of *S. typhimurium* endotoxins by using transition metal dichalcogenides (TMDs).[500] While TMDs like WS_2 and MoS_2 have shown promising results but the TMD-based micromotors be sensitive to changes in environmental conditions, such as pH and temperature, thus posing the stability issue.[517] Food samples often contain a diverse range of compounds, and some of them might interfere with the detection process.[518–521] TMD-based micromotors may exhibit issues related to long-term stability, affecting their shelf life and reliability over extended periods.[522,523] Whereas in the reported work, QEMRs offer high biocompatibility, ease of functionalization, and demonstrate excellent stability under various conditions, contributing to the reliability of detection methods over time[307,412]. Hence, this approach possesses essential bioanalytical characteristics, such as high sensitivity and selectivity, rapidity, simplicity, and cost-effectiveness, which effectively render it an efficient method for detecting *S. typhimurium* in food and environmental samples.

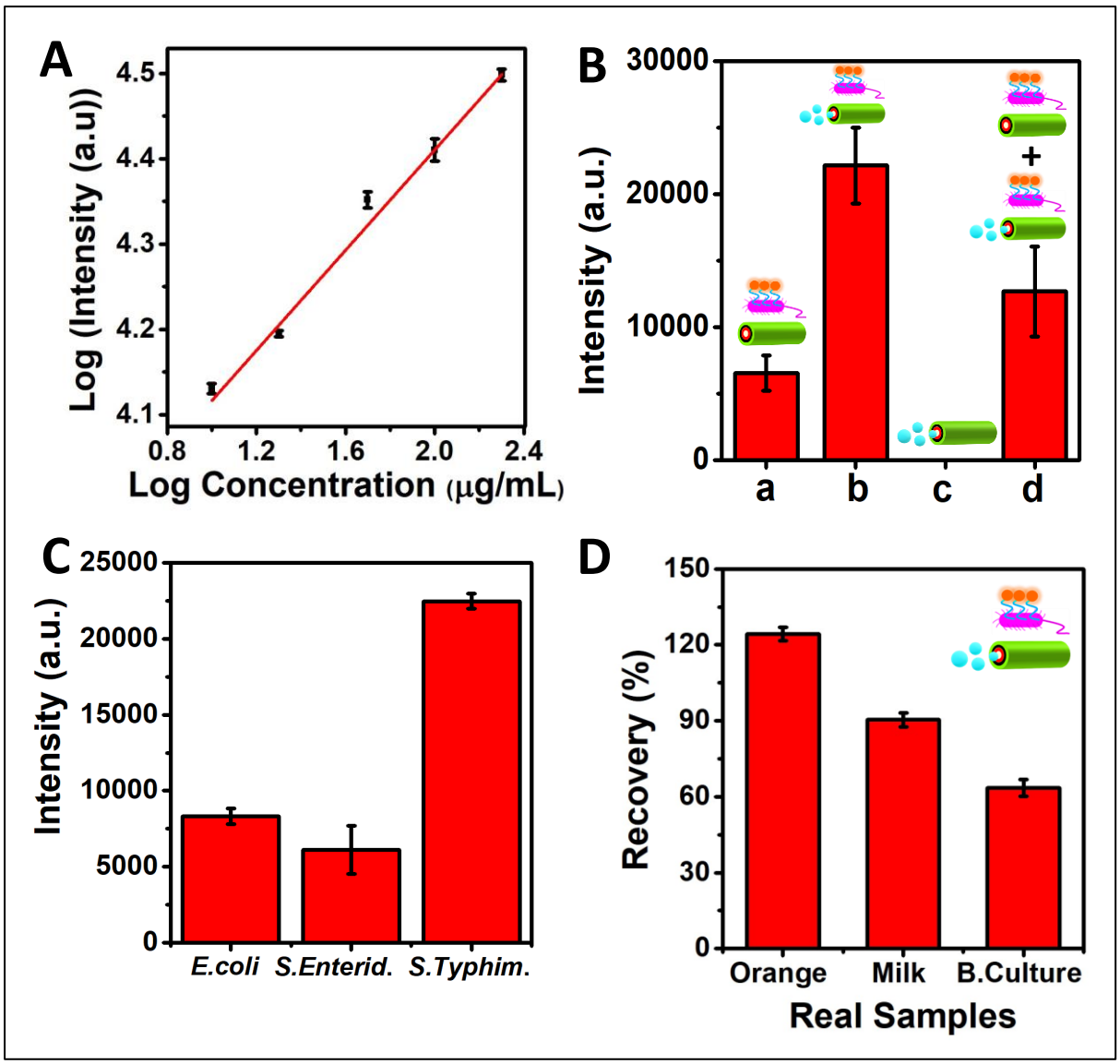

Figure 52: Implementation of the active biocarriers towards the optical "on-the-fly" *S. enterica* endotoxins determination. (A) Calibration plot between the logarithmic (log) values of the concentration of the analyte [endotoxin] *vs.* log [Fluorescence Intensity] under motion, with its corresponding error bars (*n=3*). **(B)** Histogram illustrating the recovery in the fluorescence intensities achieved by the peptide@QEMRs towards a fixed concentration of *S. enterica* endotoxins (50 µg mL^{-1}) under motion (9% H_2O_2) or static (no fuel) conditions. **(C)** Histogram depicting the fluorescence intensities achieved by the peptide@QEMRs biocarriers towards different targets (9% H_2O_2) (*such as, E. coli*, *S. Enterid* and *S. Typhim.*: (50 µg mL^{-1}). **(D)** Histogram showing the recovery average % recovery obtained through the peptide@QEMRs in various real samples (Orange, Milk, Bacteria culture) fortified with 15 µg mL^{-1} of endotoxin (*n=3*). Experimental conditions: λ_{ex} = 560 nm, incubation time: 10 min, recovery time: 5 min; 1% PEG; 9 % v/v in H_2O_2.

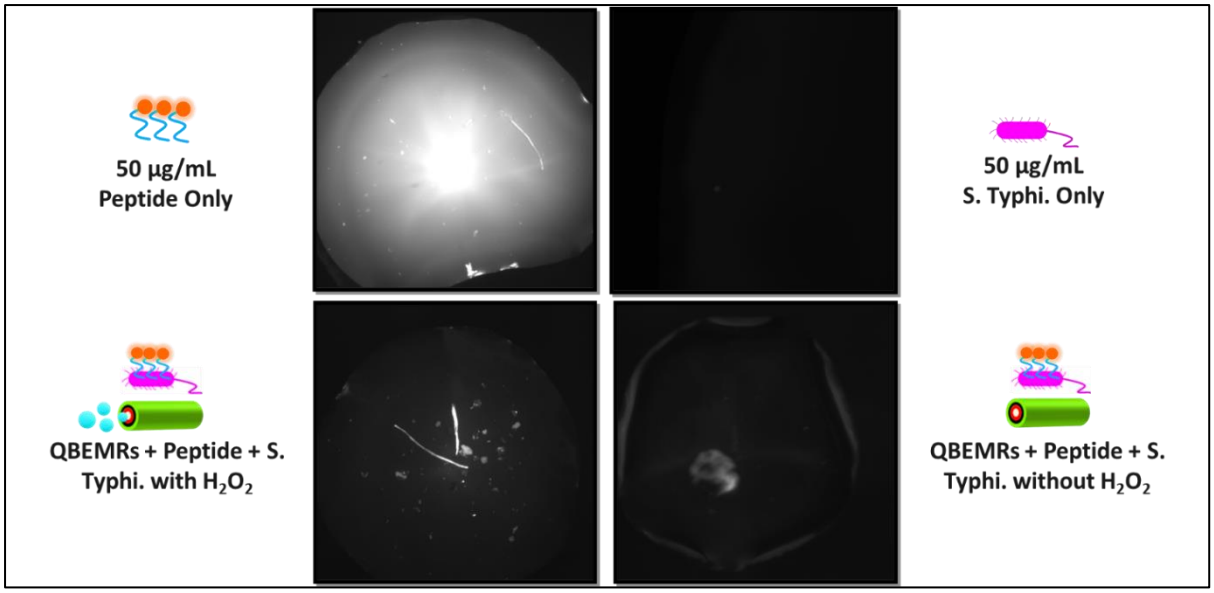

Figure 53: Validation by Fluorescence Images.

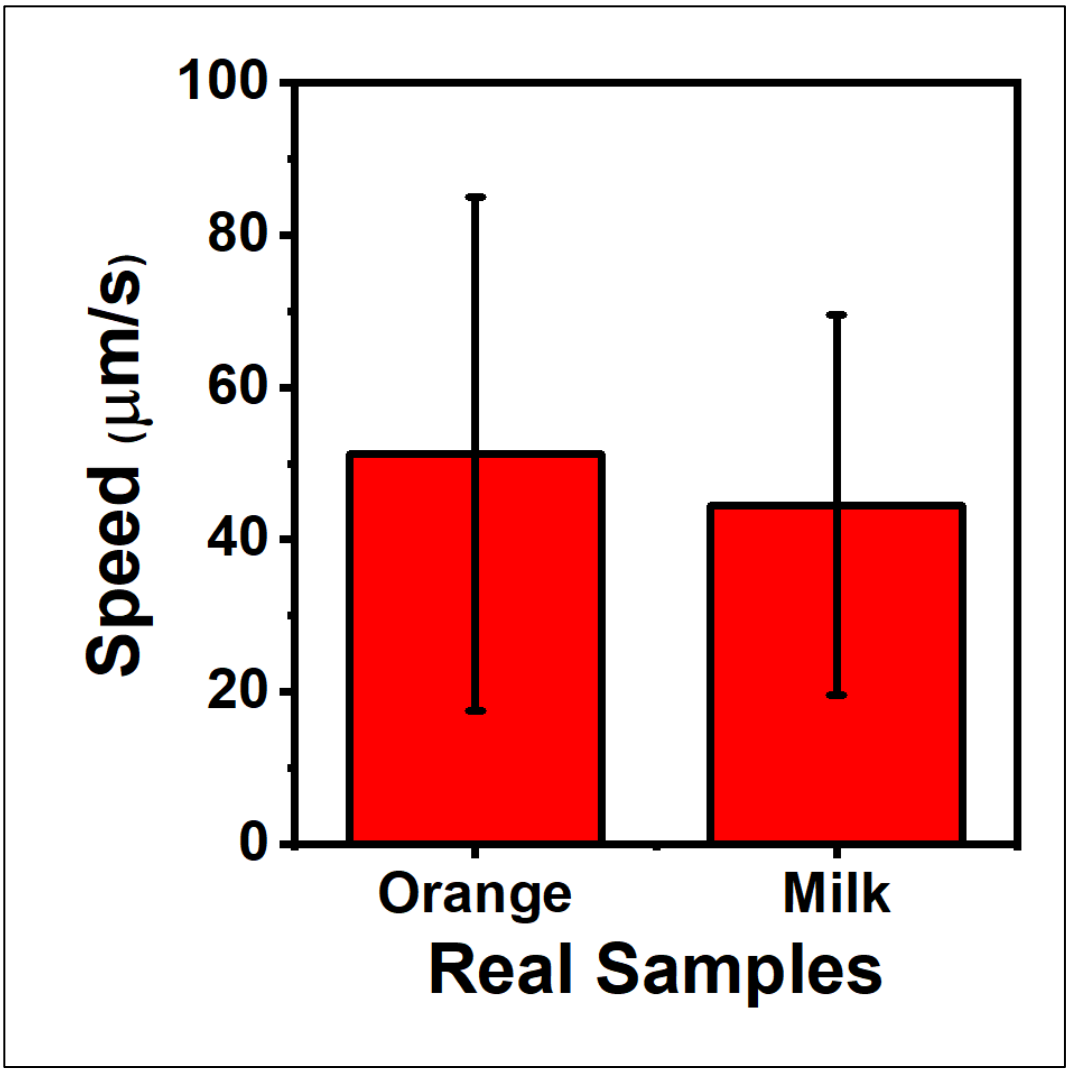

Figure 54. Speed of micromotors in real samples.

Detection	**Sensing Probe**	**LOD**	**Linear range**	**Advantages/ disadvantages**	**Analysis time**	**Ref.**
ELISA	Murine monoclonal Antibody	1 ng mL^{-1}	NR	Highly sensitive /time consuming	4 h	[514]
Electrochemical (impedance)	Magnetosome-antibody complex	0.001 µg mL^{-1}	NR	Significantly faster than traditional culture methods/delayed intervention	30 min	[515]
Electrochemical (impedance)	Magnetic nanoparticles, macrophage	0.15 µg mL^{-1}	1–50 µg mL^{-1}	Label-free detection/time taking	3 h	[516]
Fluorescent (ON–OFF)	GQDs Janus micromotors	0.07 ng mL^{-1}	0.2–3.5 ng mL^{-1}	Reduced Sample Preparation/ time consuming	15 min	[499]
Fluorescence (OFF-ON)	WS2 Janus micromotors MoS2 Janus micromotors	1.2 µg mL^{-1} 2.0 µg mL^{-1}	4–333.3 µg mL^{-1} 9.8–333.3 µg mL^{-1}	Fast and Efficient/ stability and toxicity can be an issue	5 min	[500]
Fluorescence (OFF-ON)	QEMRs	1.8 µg mL^{-1}	3–300 µg mL^{-1}	Fast, Efficient and Highly stable	5 min	This work

Table 3. *S. enterica* endotoxin previous literature data.

5.2.4 Conclusion

Our study highlights the potential of quantum materials enhanced microrobots in connection with self-propelled behaviour to enhance sensitivity and signal stability, particularly for in-field *S. enterica* contamination and detection in the context of food safety. Quantum materials enhanced microrobots combined with the use of affinity peptides, eliminate the need for lengthy incubation and expensive antibodies, thus improving efficiency and cost-effectiveness. This method achieves a low detection limit, with a rapid detection time and low sample volumes. Furthermore, this method demonstrates remarkable specificity, surpassing prior techniques and displaying heightened selectivity for *S. enterica* endotoxins. We demonstrate the application of these emerging quantum materials enhanced microrobots in detection of toxins in real food samples. This quantum-enhanced technology paves new ways for on-demand, point-of-care detection of food toxins for greater food safety and security.

List of Abbreviations

0D	Zero dimensional
GQDs	Graphene Quantum Dots
Ni	Nickel
Pt	Platinum
SEM	Scanning Electron Microscopy
EDS	Energy Dispersive Spectroscopy
UV-vis	Ultraviolet–visible spectroscopy
QMs	Quantum Materials
QEMRs	Quantum Enhanced Microrobots
FRET	Fluorescence Resonance Energy Transfer
PEG	Polyethylene glycol
SDS	Sodium dodecyl sulfate
S.typh/ *S. typhimurium*	*Salmonella enterica* serovar Typhimurium
FAM-L	Fluorescein Amidites Labelled
H_2O_2	Hydrogen Peroxide
FL	Flourescence Intensity
nM	Nano Molar
FTIR	Fourier-transform infrared spectroscopy
E. coli	*Escherichia coli*

Chapter 6

Conclusion and Future Aspects

In conclusion, this thesis has embarked on a comprehensive exploration of novel materials, with a specific focus on 2D material-based 3D printed electrodes and nano/micromotors, to advance the field of chemical sensing and biosensing applications. The primary objective has been to contribute valuable insights in sensing and biosensing applications through systematic experimentation and analysis of the analytes that are aimed at elevating the performance and capabilities of chemical and biosensor technologies.

For instance, **Chapters 4.1 and 4.2** address critical challenges associated with the widespread use of analytes in diverse industries, especially those characterized by rapid action and potential toxicity. By researching advanced detection methodologies and incorporating cutting-edge technologies such as 3D-printing, these studies have provided innovative solutions for the problems. These solutions are designed to enhance sensitivity, precision, and diagnostic capabilities in both environmental monitoring and medical applications.

Chapter 4.3 shows that the application of 3D printed electrodes for DNA detection holds significant promise in revolutionizing the field of genetic analysis. The integration of 3D-printing technology allows for the precise fabrication of electrodes with tailored structures, enhancing surface area and electrochemical performance. This, in turn, leads to improved sensitivity and specificity in DNA detection assays. The versatility and cost-effectiveness of 3D-printing further contribute to its potential widespread adoption in laboratories, offering a scalable and accessible solution for advancing genetic diagnostics and research. As the

technology continues to mature, 3D-printed electrodes are poised to play a pivotal role in shaping the future landscape of DNA detection methodologies.

Furthermore, **Chapters 5.1 and 5.2** show the utilization of nano/micromotors in DNA and Salmonella bacteria detection marks a significant leap forward in the field of biosensing.
The autonomous movement of nano/micromotors facilitates rapid and thorough mixing, ensuring efficient interactions between DNA targets and sensing elements. This technology not only accelerates the detection process due to its autonomous movement but also allows for the exploration of diverse biofunctionalization strategies, contributing to the development of highly selective and sensitive DNA detection platforms. Additionally, in Salmonella detection, the ability of nano/micromotors to navigate complex environments enhances their capability to reach and interact with bacteria, improving the overall sensitivity and specificity of detection platforms.
The incorporation of nano/micromotors in biosensing strategies not only accelerates detection processes but also enables the exploration of various biofunctionalization techniques. This versatility contributes to the development of highly selective and sensitive detection platforms for both DNA and Salmonella bacteria. Furthermore, the application of diverse propulsion mechanisms, including magnetic, ultrasonic, and electric fields, ensures adaptability to different operational conditions, offering a versatile solution for various biosensing applications. The amalgamation of nano/micromotors with DNA and Salmonella detection methodologies holds immense promise for advancing point-of-care diagnostics, environmental monitoring, and food safety. Continued research and innovation in this field are expected to open new frontiers in the realm of DNA and pathogens detection, contributing to more efficient, accessible, and reliable diagnostic tools.
Through the rigorous investigation of 2D material-based 3D printed electrodes and nano/micromotors, this thesis seeks to lay the groundwork for significant advancements in chemical and biosensing. The knowledge and methods revealed in this research endeavour are intended to encourage continued discovery and advancement, playing a crucial role in driving the development of new technologies necessary for addressing pressing issues in analytical chemistry and biomedical sciences.

Chapter 7

References

(1) Terry, A. V. Functional Consequences of Repeated Organophosphate Exposure: Potential Non-Cholinergic Mechanisms. *Pharmacology and Therapeutics* **2012**. https://doi.org/10.1016/j.pharmthera.2012.03.001.

(2) Loza, E. Treatment of Postmenopausal Osteoporosis. *Anales del Sistema Sanitario de Navarra* **2003**. https://doi.org/10.4264/numa.80.

(3) Kyselova, Z. Toxicological Aspects of the Use of Phenolic Compounds in Disease Prevention. *Interdisciplinary Toxicology* **2011**. https://doi.org/10.2478/v10102-011-0027-5.

(4) Mie, A.; Andersen, H. R.; Gunnarsson, S.; Kahl, J.; Kesse-Guyot, E.; Rembiałkowska, E.; Quaglio, G.; Grandjean, P. Human Health Implications of Organic Food and Organic Agriculture: A Comprehensive Review. *Environmental Health: A Global Access Science Source* **2017**. https://doi.org/10.1186/s12940-017-0315-4.

(5) Arfin, T.; Sonawane ; Arshiya Tarannum, K. Review on Detection of Phenol in Water. *Advanced Materials Letters* **2019**. https://doi.org/10.5185/amlett.2019.0036.

(6) Delfino, I.; Diano, N.; Lepore, M. Advanced Optical Sensing of Phenolic Compounds for Environmental Applications. *Sensors* **2021**. https://doi.org/10.3390/s21227563.

(7) Asif, M.; Xiao, F.; Govindasamy, M.; Sun, Y. 2D Nanoarchitectures for Sensing/Biosensing Applications. *Frontiers in Chemistry* **2022**. https://doi.org/10.3389/fchem.2022.992793.

(8) Manzanares Palenzuela, C. L.; Pumera, M. (Bio)Analytical Chemistry Enabled by 3D Printing: Sensors and Biosensors. *TrAC - Trends in Analytical Chemistry* **2018**. https://doi.org/10.1016/j.trac.2018.03.016.

(9) Ambrosi, A.; Pumera, M. 3D-Printing Technologies for Electrochemical Applications. *Chemical Society Reviews* **2016**. https://doi.org/10.1039/c5cs00714c.

(10) Jyoti; Redondo, E.; Alduhaish, O.; Pumera, M. 3D-Printed Nanocarbon Sensors for the Detection of Chlorophenols and Nitrophenols: Towards Environmental Applications of Additive Manufacturing. *Electrochemistry Communications* **2021**. https://doi.org/10.1016/j.elecom.2021.106984.

(11) Muñoz, J.; Pumera, M. Accounts in 3D-Printed Electrochemical Sensors: Towards Monitoring of Environmental Pollutants. *ChemElectroChem* **2020**. https://doi.org/10.1002/celc.202000601.

(12) Gómez, I. J.; Alegret, N.; Dominguez-Alfaro, A.; Sulleiro, M. V. Recent Advances on 2D Materials towards 3D Printing. *Chemistry (Switzerland)* **2021**. https://doi.org/10.3390/chemistry3040095.

(13) Wang, H.; Pumera, M. Fabrication of Micro/Nanoscale Motors. *Chemical Reviews* **2015**. https://doi.org/10.1021/acs.chemrev.5b00047.

(14) Xu, B.; Zhang, B.; Wang, L.; Huang, G.; Mei, Y. Tubular Micro/Nanomachines: From the Basics to Recent Advances. *Advanced Functional Materials* **2018**. https://doi.org/10.1002/adfm.201705872.

(15) Campuzano, S.; Kagan, D.; Orozco, J.; Wang, J. Motion-Driven Sensing and Biosensing Using Electrochemically Propelled Nanomotors. *Analyst* **2011**. https://doi.org/10.1039/c1an15599g.

(16) Kagan, D.; Campuzano, S.; Balasubramanian, S.; Kuralay, F.; Flechsig, G. U.; Wang, J. Functionalized Micromachines for Selective and Rapid Isolation of Nucleic Acid Targets from Complex Samples. *Nano Letters* **2011**. https://doi.org/10.1021/nl2005687.

(17) Restrepo-Pérez, L.; Soler, L.; Martínez-Cisneros, C.; Sánchez, S.; Schmidt, O. G. Biofunctionalized Self-Propelled Micromotors as an Alternative on-Chip Concentrating System. *Lab on a Chip* **2014**. https://doi.org/10.1039/c4lc00439f.

(18) Li, J.; Ávila, B. E. F. De; Gao, W.; Zhang, L.; Wang, J. Micro/Nanorobots for Biomedicine: Delivery, Surgery, Sensing, and Detoxification. *Science Robotics* **2017**. https://doi.org/10.1126/scirobotics.aam6431.

(19) Guix, M.; Mayorga-Martinez, C. C.; Merkoçi, A. Nano/Micromotors in (Bio)Chemical Science Applications. *Chemical Reviews* **2014**. https://doi.org/10.1021/cr400273r.

(20) Gao, W.; Wang, J. The Environmental Impact of Micro/Nanomachines: A Review. *American Chemical Society Nano* **2014**. https://doi.org/10.1021/nn500077a.

(21) Eskandarloo, H.; Kierulf, A.; Abbaspourrad, A. Nano- and Micromotors for Cleaning Polluted Waters: Focused Review on Pollutant Removal Mechanisms. *Nanoscale* **2017**. https://doi.org/10.1039/c7nr05494g.

(22) Kim, S.; Qiu, F.; Kim, S.; Ghanbari, A.; Moon, C.; Zhang, L.; Nelson, B. J.; Choi, H. Fabrication and Characterization of Magnetic Microrobots for Three-Dimensional Cell Culture and Targeted Transportation. *Advanced Materials* **2013**. https://doi.org/10.1002/adma.201301484.

(23) Credi, A. Book Review "Nanomachines: Fundamentals and Applications." *Angewandte*

Chemie International Edition **2014**. https://doi.org/10.1002/anie.201311274.

(24) Zhang, L.; Petit, T.; Lu, Y.; Kratochvil, B. E.; Peyer, K. E.; Pei, R.; Lou, J.; Nelson, B. J. Controlled Propulsion and Cargo Transport of Rotating Nickel Nanowires near a Patterned Solid Surface. *American Chemical Society Nano* **2010**. https://doi.org/10.1021/nn101861n.

(25) Peng, F.; Tu, Y.; Wilson, D. A. Micro/Nanomotors towards: In Vivo Application: Cell, Tissue and Biofluid. *Chemical Society Reviews* **2017**. https://doi.org/10.1039/c6cs00885b.

(26) Suter, M.; Zhang, L.; Siringil, E. C.; Peters, C.; Luehmann, T.; Ergeneman, O.; Peyer, K. E.; Nelson, B. J.; Hierold, C. Superparamagnetic Microrobots: Fabrication by Two-Photon Polymerization and Biocompatibility. *Biomedical Microdevices* **2013**. https://doi.org/10.1007/s10544-013-9791-7.

(27) Singh, V. V.; Wang, J. Nano/Micromotors for Security/Defense Applications. A Review. *Nanoscale* **2015**. https://doi.org/10.1039/c5nr06254c.

(28) Zhang, Y.; Yuan, K.; Zhang, L. Micro/Nanomachines: From Functionalization to Sensing and Removal. *Advanced Materials Technologies* **2019**. https://doi.org/10.1002/admt.201800636.

(29) Wang, J. Self-Propelled Affinity Biosensors: Moving the Receptor around the Sample. *Biosensors and Bioelectronics* **2016**. https://doi.org/10.1016/j.bios.2015.04.095.

(30) Tan, C.; Cao, X.; Wu, X. J.; He, Q.; Yang, J.; Zhang, X.; Chen, J.; Zhao, W.; Han, S.; Nam, G. H.; Sindoro, M.; Zhang, H. Recent Advances in Ultrathin Two-Dimensional Nanomaterials. *Chemical Reviews* **2017**. https://doi.org/10.1021/acs.chemrev.6b00558.

(31) Chimene, D.; Alge, D. L.; Gaharwar, A. K. Two-Dimensional Nanomaterials for Biomedical Applications: Emerging Trends and Future Prospects. *Advanced Materials* **2015**. https://doi.org/10.1002/adma.201502422.

(32) Ferrari, A. C.; Meyer, J. C.; Scardaci, V.; Casiraghi, C.; Lazzeri, M.; Mauri, F.; Piscanec, S.; Jiang, D.; Novoselov, K. S.; Roth, S.; Geim, A. K. Raman Spectrum of Graphene and Graphene Layers. *Physical Review Letters* **2006**. https://doi.org/10.1103/PhysRevLett.97.187401.

(33) Naumis, G. G.; Barraza-Lopez, S.; Oliva-Leyva, M.; Terrones, H. Electronic and Optical Properties of Strained Graphene and Other Strained 2D Materials: A Review. *Reports on Progress in Physics* **2017**. https://doi.org/10.1088/1361-6633/aa74ef.

(34) Huo, C.; Yan, Z.; Song, X.; Zeng, H. 2D Materials via Liquid Exfoliation: A Review on Fabrication and Applications. *Science Bulletin* **2015**. https://doi.org/10.1007/s11434-015-0936-3.

(35) Mas-Ballesté, R.; Gómez-Navarro, C.; Gómez-Herrero, J.; Zamora, F. 2D Materials: To Graphene and Beyond. *Nanoscale* **2011**. https://doi.org/10.1039/c0nr00323a.

(36) Glavin, N. R.; Rao, R.; Varshney, V.; Bianco, E.; Apte, A.; Roy, A.; Ringe, E.; Ajayan, P. M. Emerging Applications of Elemental 2D Materials. *Advanced Materials* **2020**.

https://doi.org/10.1002/adma.201904302.

(37) Iqbal, A.; Sambyal, P.; Koo, C. M. 2D MXenes for Electromagnetic Shielding: A Review. *Advanced Functional Materials* **2020**. https://doi.org/10.1002/adfm.202000883.

(38) Tahir, M. B.; Fatima, N.; Fatima, U.; Sagir, M. A Review on the 2D Black Phosphorus Materials for Energy Applications. *Inorganic Chemistry Communications* **2021**. https://doi.org/10.1016/j.inoche.2020.108242.

(39) Chhowalla, M.; Liu, Z.; Zhang, H. Two-Dimensional Transition Metal Dichalcogenide (TMD) Nanosheets. *Chemical Society Reviews* **2015**. https://doi.org/10.1039/c5cs90037a.

(40) Bie, C.; Cheng, B.; Fan, J.; Ho, W.; Yu, J. Enhanced Solar-to-Chemical Energy Conversion of Graphitic Carbon Nitride by Two-Dimensional Cocatalysts. *Energy Chemistry* **2021**. https://doi.org/10.1016/j.enchem.2021.100051.

(41) Zhang, C.; Tan, J.; Pan, Y.; Cai, X.; Zou, X.; Cheng, H. M.; Liu, B. Mass Production of 2D Materials by Intermediate-Assisted Grinding Exfoliation. *National Science Review* **2020**. https://doi.org/10.1093/nsr/nwz156.

(42) Yao, J. D.; Zheng, Z. Q.; Yang, G. W. Production of Large-Area 2D Materials for High-Performance Photodetectors by Pulsed-Laser Deposition. *Progress in Materials Science* **2019**. https://doi.org/10.1016/j.pmatsci.2019.100573.

(43) Yang, S.; Zhang, P.; Nia, A. S.; Feng, X. Emerging 2D Materials Produced via Electrochemistry. *Advanced Materials* **2020**. https://doi.org/10.1002/adma.201907857.

(44) Chacham, H.; Santos, J. C. C.; Pacheco, F. G.; Silva, D. L.; Martins, R. M.; Del'boccio, J. P.; Soares, E. M.; Altoé, R.; Furtado, C. A.; Plentz, F.; Neves, B. R. A.; Cançado, L. G. Controlling the Morphology of Nanoflakes Obtained by Liquid-Phase Exfoliation: Implications for the Mass Production of 2D Materials. *American Chemical Society Applied Nano Materials* **2020**. https://doi.org/10.1021/acsanm.0c02598.

(45) Park, S.; Ruoff, R. S. Chemical Methods for the Production of Graphenes. *Nature Nanotechnology* **2009**. https://doi.org/10.1038/nnano.2009.58.

(46) Hernandez, Y.; Nicolosi, V.; Lotya, M.; Blighe, F. M.; Sun, Z.; De, S.; McGovern, I. T.; Holland, B.; Byrne, M.; Gun'ko, Y. K.; Boland, J. J.; Niraj, P.; Duesberg, G.; Krishnamurthy, S.; Goodhue, R.; Hutchison, J.; Scardaci, V.; Ferrari, A. C.; Coleman, J. N. High-Yield Production of Graphene by Liquid-Phase Exfoliation of Graphite. *Nature Nanotechnology* **2008**. https://doi.org/10.1038/nnano.2008.215.

(47) Zhang, D.; Chi, B.; Li, B.; Gao, Z.; Du, Y.; Guo, J.; Wei, J. Fabrication of Highly Conductive Graphene Flexible Circuits by 3D Printing. *Synthetic Metals* **2016**. https://doi.org/10.1016/j.synthmet.2016.03.014.

(48) Ye, J.; Craciun, M. F.; Koshino, M.; Russo, S.; Inouea, S.; Yuan, H.; Shimotani, H.; Morpurgo, A. F.; Iwasa, Y. Accessing the Transport Properties of Graphene and Its Multilayers at High Carrier Density. *Proceedings of the National Academy of Sciences of the United States of America* **2011**. https://doi.org/10.1073/pnas.1018388108.

(49) Lee, G. H.; Cooper, R. C.; An, S. J.; Lee, S.; Van Der Zande, A.; Petrone, N.; Hammerberg, A. G.; Lee, C.; Crawford, B.; Oliver, W.; Kysar, J. W.; Hone, J. High-Strength Chemical-Vapor-Deposited Graphene and Grain Boundaries. *Science* **2013**. https://doi.org/10.1126/science.1235126.

(50) Gómez, I. J.; Sulleiro, M. V.; Mantione, D.; Alegret, N. Carbon Nanomaterials Embedded in Conductive Polymers: A State of the Art. *Polymers*. **2021**. https://doi.org/10.3390/polym13050745.

(51) Sulleiro, M. V.; Quiroga, S.; Peña, D.; Pérez, D.; Guitián, E.; Criado, A.; Prato, M. Microwave-Induced Covalent Functionalization of Few-Layer Graphene with Arynes under Solvent-Free Conditions. *Chemical Communications* **2018**. https://doi.org/10.1039/c7cc08676h.

(52) Nine, M. J.; Cole, M. A.; Tran, D. N. H.; Losic, D. Graphene: A Multipurpose Material for Protective Coatings. *Journal of Materials Chemistry A* **2015**. https://doi.org/10.1039/c5ta01010a.

(53) Novoselov, K. S.; Fal'Ko, V. I.; Colombo, L.; Gellert, P. R.; Schwab, M. G.; Kim, K. A Roadmap for Graphene. *Nature* **2012**. https://doi.org/10.1038/nature11458.

(54) Nicolosi, V.; Chhowalla, M.; Kanatzidis, M. G.; Strano, M. S.; Coleman, J. N. Liquid Exfoliation of Layered Materials. *Science* **2013**. https://doi.org/10.1126/science.1226419.

(55) Sarno, M.; Scarpa, D.; Senatore, A.; Mustafa, W. A. A. RGO/GO Nanosheets in Tribology: From the State of the Art to the Future Prospective. *Lubricants* **2020**. https://doi.org/10.3390/lubricants8030031.

(56) Agarwal, V.; Zetterlund, P. B. Strategies for Reduction of Graphene Oxide – A Comprehensive Review. *Chemical Engineering Journal* **2021**. https://doi.org/10.1016/j.cej.2020.127018.

(57) Nurunnabi, M.; Parvez, K.; Nafiujjaman, M.; Revuri, V.; Khan, H. A.; Feng, X.; Lee, Y. K. Bioapplication of Graphene Oxide Derivatives: Drug/Gene Delivery, Imaging, Polymeric Modification, Toxicology, Therapeutics and Challenges. *Royal Society Chemistry Advances* **2015**. https://doi.org/10.1039/c5ra04756k.

(58) Guex, L. G.; Sacchi, B.; Peuvot, K. F.; Andersson, R. L.; Pourrahimi, A. M.; Ström, V.; Farris, S.; Olsson, R. T. Experimental Review: Chemical Reduction of Graphene Oxide (GO) to Reduced Graphene Oxide (RGO) by Aqueous Chemistry. *Nanoscale* **2017**. https://doi.org/10.1039/c7nr02943h.

(59) Additive Manufacturing — General Principles — Part 1 : Terminology. ASTM *International* **2015**. https://edisciplinas.usp.br/pluginfile.php/5341680/mod_resource/content/1/ISOASTM 52900.11961.pdf

(60) Holzmann, P.; Breitenecker, R. J.; Soomro, A. A.; Schwarz, E. J. User Entrepreneur Business Models in 3D Printing. *Journal of Manufacturing Technology Management*. **2017**. https://doi.org/10.1108/JMTM-12-2015-0115.

(61) Indian Jewelry Brand {Isharya} Unveils '{Infinite} {Petals}' {3D} Printed Jewelry Collection. *3D printer and 3D printing news* **2017**. https://www.3ders.org/articles/20170412-indian-jewelry-brand-isharya-unveils-infinite-petals-3d-printed-kewelry-collection.html

(62) Paul {G}. {Allen}'s {Stratolaunch} Space Venture Uses {3D} Printing to Develop {PGA} Rocket Engine. *3D printer and 3D printing news* **2018**. https://spacenews.com/rocket-engine-startup-ursa-major-to-venture-into-solid-propulsion/

(63) Sparkes, M. World's first 3D-printed steel bridge opens in Amsterdam. *New Scientist* **2021**. https://www.newscientist.com/article/2283934-worlds-first-3d-printed-steel-bridge-opens-in-amsterdam

(64) Shahrubudin, N.; Lee, T. C.; Ramlan, R. An Overview on 3D Printing Technology: Technological, Materials, and Applications. In *Procedia Manufacturing* **2019**. https://doi.org/10.1016/j.promfg.2019.06.089.

(65) Browne, M. P.; Redondo, E.; Pumera, M. 3D Printing for Electrochemical Energy Applications. *Chemical Reviews* **2020**. https://doi.org/10.1021/acs.chemrev.9b00783.

(66) Hashim, H. S.; Fen, Y. W.; Omar, N. A. S.; Fauzi, N. I. M. Sensing Methods for Hazardous Phenolic Compounds Based on Graphene and Conducting Polymers-Based Materials. *Chemosensors* **2021**. https://doi.org/10.3390/chemosensors9100291.

(67) Govindasamy, M.; Mani, V.; Chen, S. M.; Chen, T. W.; Sundramoorthy, A. K. Methyl Parathion Detection in Vegetables and Fruits Using Silver@graphene Nanoribbons Nanocomposite Modified Screen Printed Electrode. *Scientific Reports* **2017**, *7*, 46471. https://doi.org/10.1038/srep46471.

(68) Girdhar, A.; Sathe, C.; Schulten, K.; Leburton, J. P. Graphene Quantum Point Contact Transistor for DNA Sensing. *Proceedings of the National Academy of Sciences of the United States of America* **2013**. https://doi.org/10.1073/pnas.1308885110.

(69) Tang, X.; Bansaruntip, S.; Nakayama, N.; Yenilmez, E.; Chang, Y. I.; Wang, Q. Carbon Nanotube DNA Sensor and Sensing Mechanism. *Nano Letters* **2006**. https://doi.org/10.1021/nl060613v.

(70) Rahman, M. M.; Balkhoyor, H. B.; Asiri, A. M. Phenolic Sensor Development Based on Chromium Oxide-Decorated Carbon Nanotubes for Environmental Safety. *Journal of Environmental Management* **2017**. https://doi.org/10.1016/j.jenvman.2016.12.008.

(71) Zhang, Y.; Kang, T. F.; Wan, Y. W.; Chen, S. Y. Gold Nanoparticles-Carbon Nanotubes Modified Sensor for Electrochemical Determination of Organophosphate Pesticides. *Microchimica Acta* **2009**. https://doi.org/10.1007/s00604-008-0134-y.

(72) Lee, J. H.; Park, J. Y.; Min, K.; Cha, H. J.; Choi, S. S.; Yoo, Y. J. A Novel Organophosphorus Hydrolase-Based Biosensor Using Mesoporous Carbons and Carbon Black for the Detection of Organophosphate Nerve Agents. *Biosensors and Bioelectronics* **2010**. https://doi.org/10.1016/j.bios.2009.10.013.

(73) Fu, S.; Zhu, Y.; Zhang, Y.; Zhang, M.; Zhang, Y.; Qiao, L.; Yin, N.; Song, K.; Liu, M.;

Wang, D. Recent Advances in Carbon Nanomaterials-Based Electrochemical Sensors for Phenolic Compounds Detection. *Microchemical Journal*. **2021**. https://doi.org/10.1016/j.microc.2021.106776.

(74) Wang, Y.; Blache, R.; Xu, X. Selection of Additive Manufacturing Processes. *Rapid Prototyping Journal* **2017**. https://doi.org/10.1108/RPJ-09-2015-0123.

(75) Stansbury, J. W.; Idacavage, M. J. 3D Printing with Polymers: Challenges among Expanding Options and Opportunities. In *Dental Materials* **2016**. https://doi.org/10.1016/j.dental.2015.09.018.

(76) Yap, Y. L.; Tan, Y. S. E.; Tan, H. K. J.; Peh, Z. K.; Low, X. Y.; Yeong, W. Y.; Tan, C. S. H.; Laude, A. 3D Printed Bio-Models for Medical Applications. *Rapid Prototyping Journal* **2017**. https://doi.org/10.1108/RPJ-08-2015-0102.

(77) Tofail, S. A. M.; Koumoulos, E. P.; Bandyopadhyay, A.; Bose, S.; O'Donoghue, L.; Charitidis, C. Additive Manufacturing: Scientific and Technological Challenges, Market Uptake and Opportunities. *Materials Today* **2018**. https://doi.org/10.1016/j.mattod.2017.07.001.

(78) Caminero, M. A.; Chacón, J. M.; García-Moreno, I.; Rodríguez, G. P. Impact Damage Resistance of 3D Printed Continuous Fibre Reinforced Thermoplastic Composites Using Fused Deposition Modelling. *Composites Part B: Engineering* **2018**. https://doi.org/10.1016/j.compositesb.2018.04.054.

(79) Dizon, J. R. C.; Espera, A. H.; Chen, Q.; Advincula, R. C. Mechanical Characterization of 3D-Printed Polymers. *Additive Manufacturing* **2018**. https://doi.org/10.1016/j.addma.2017.12.002.

(80) Hitzler, L.; Alifui-Segbaya, F.; Williams, P.; Heine, B.; Heitzmann, M.; Hall, W.; Merkel, M.; Öchsner, A. Additive Manufacturing of Cobalt-Based Dental Alloys: Analysis of Microstructure and Physicomechanical Properties. *Advances in Materials Science and Engineering* **2018**. https://doi.org/10.1155/2018/8213023.

(81) Srivastava, P.; Sahlot, P. Additive Manufacturing in Industry 4.0: A Review. In *Lecture Notes in Mechanical Engineering* **2023**. https://doi.org/10.1007/978-981-19-7709-1_29.

(82) Martin, J. H.; Yahata, B. D.; Hundley, J. M.; Mayer, J. A.; Schaedler, T. A.; Pollock, T. M. 3D Printing of High-Strength Aluminium Alloys. *Nature* **2017**. https://doi.org/10.1038/nature23894.

(83) Murr, L. E. Frontiers of 3D Printing/Additive Manufacturing: From Human Organs to Aircraft Fabrication. *Journal of Materials Science and Technology* **2016**. https://doi.org/10.1016/j.jmst.2016.08.011.

(84) DebRoy, T.; Wei, H. L.; Zuback, J. S.; Mukherjee, T.; Elmer, J. W.; Milewski, J. O.; Beese, A. M.; Wilson-Heid, A.; De, A.; Zhang, W. Additive Manufacturing of Metallic Components – Process, Structure and Properties. *Progress in Materials Science* **2018**. https://doi.org/10.1016/j.pmatsci.2017.10.001.

(85) Uhlmann, E.; Kersting, R.; Klein, T. B.; Cruz, M. F.; Borille, A. V. Additive Manufacturing of Titanium Alloy for Aircraft Components. In *Procedia CIRP* **2015**.

https://doi.org/10.1016/j.procir.2015.08.061.

(86) Trevisan, F.; Calignano, F.; Aversa, A.; Marchese, G.; Lombardi, M.; Biamino, S.; Ugues, D.; Manfredi, D. Additive Manufacturing of Titanium Alloys in the Biomedical Field: Processes, Properties and Applications. *Journal of Applied Biomaterials and Functional Materials* **2018**. https://doi.org/10.5301/jabfm.5000371.

(87) Chen, Y.; Zhao, H.; Mao, J.; Chirarattananon, P.; Helbling, E. F.; Hyun, N. seung P.; Clarke, D. R.; Wood, R. J. Controlled Flight of a Microrobot Powered by Soft Artificial Muscles. *Nature* **2019**. https://doi.org/10.1038/s41586-019-1737-7.

(88) Guo, Z.; Wu, Y.; Xie, Z.; Shao, J.; Liu., J.; Yao, Y.; Wang, J.; Shen, Y.; Gooding, J. J.; Liang, K. Self-Propelled Initiative Collision at Microelectrodes with Vertically Mobile Micromotors. *Angewandte Chemie* **2022**. https://doi.org/10.1002/ange.202209747.

(89) Erbas-Cakmak, S.; Fielden, S. D. P.; Karaca, U.; Leigh, D. A.; McTernan, C. T.; Tetlow, D. J.; Wilson, M. R. Rotary and Linear Molecular Motors Driven by Pulses of a Chemical Fuel. *Science* **2017**. https://doi.org/10.1126/science.aao1377.

(90) Vaghasiya, J. V.; Mayorga-Martinez, C. C.; Matějková, S.; Pumera, M. Pick up and Dispose of Pollutants from Water via Temperature-Responsive Micellar Copolymers on Magnetite Nanorobots. *Nature Communications* **2022**. https://doi.org/10.1038/s41467-022-28406-5.

(91) Yang, H.; Pang, Y.; Bu, T.; Liu, W.; Luo, J.; Jiang, D.; Zhang, C.; Wang, Z. L. Triboelectric Micromotors Actuated by Ultralow Frequency Mechanical Stimuli. *Nature Communications* **2019**. https://doi.org/10.1038/s41467-019-10298-7.

(92) Wang, D.; Han, X.; Dong, B.; Shi, F. Stimuli Responsiveness, Propulsion and Application of the Stimuli-Responsive Polymer Based Micromotor. *Applied Materials Today* **202**1. https://doi.org/10.1016/j.apmt.2021.101250.

(93) Nourhani, A.; Karshalev, E.; Soto, F.; Wang, J. Multigear Bubble Propulsion of Transient Micromotors. *Research* **2020**. https://doi.org/10.34133/2020/7823615.

(94) Zhao, Y.; Lo, C. Y.; Ruan, L.; Pi, C. H.; Kim, C.; Alsaid, Y.; Frenkel, I.; Rico, R.; Tsao, T. C.; He, X. Somatosensory Actuator Based on Stretchable Conductive Photothermally Responsive Hydrogel. *Science Robotics* **2021**. https://doi.org/10.1126/SCIROBOTICS.ABD5483.

(95) Lin, Z.; Gao, C.; Wang, D.; He, Q. Bubble-Propelled Janus Gallium/Zinc Micromotors for the Active Treatment of Bacterial Infections. *Angewandte Chemie - International Edition* **2021**. https://doi.org/10.1002/anie.202016260.

(96) Zhang, J.; Zeng, L.; Qiao, Z.; Wang, J.; Jiang, X.; Zhang, Y. S.; Yang, H. Functionalizing Double-Network Hydrogels for Applications in Remote Actuation and in Low-Temperature Strain Sensing. *American Chemical Society Applied Materials & Interfaces* **2020**. https://doi.org/10.1021/acsami.0c10430.

(97) Wu, Y.; Liu, Y.; Wang, T.; Jiang, Q.; Xu, F.; Liu, Z. Living Cell for Drug Delivery. *Engineered Regeneration* **2022**. https://doi.org/10.1016/j.engreg.2022.03.001.

(98) Yuan, K.; Jurado-Sánchez, B.; Escarpa, A. Dual-Propelled Lanbiotic Based Janus Micromotors for Selective Inactivation of Bacterial Biofilms. *Angewandte Chemie - International Edition* **2021**. https://doi.org/10.1002/anie.202011617.

(99) Li, Z.; Yi, X.; Yang, J.; Bian, L.; Yu, Z.; Dong, S. Designing Artificial Vibration Modes of Piezoelectric Devices Using Programmable, 3D Ordered Structure with Piezoceramic Strain Units. *Advanced Materials* **2022**. https://doi.org/10.1002/adma.202107236.

(100) Zhang, Y.; Yang, F.; Wei, W.; Wang, Y.; Yang, S.; Li, J.; Xing, Y.; Zhou, L.; Dai, W.; Dong, H. Self-Propelled Janus Mesoporous Micromotor for Enhanced MicroRNA Capture and Amplified Detection in Complex Biological Samples. *American Chemical Society Nano* **2022**. https://doi.org/10.1021/acsnano.1c10437.

(101) Yuan, K.; Cuntín-Abal, C.; Jurado-Sánchez, B.; Escarpa, A. Smartphone-Based Janus Micromotors Strategy for Motion-Based Detection of Glutathione. *Analytical Chemistry* **2021**. https://doi.org/10.1021/acs.analchem.1c02947.

(102) Cai, L.; Xu, D.; Chen, H.; Wang, L.; Zhao, Y. Designing Bioactive Micro-/Nanomotors for Engineered Regeneration. *Engineered Regeneration* **2021**. https://doi.org/10.1016/j.engreg.2021.09.003.

(103) Su, Y.; Ge, Y.; Liu, L.; Zhang, L.; Liu, M.; Sun, Y.; Zhang, H.; Dong, B. Motion-Based PH Sensing Based on the Cartridge-Case-like Micromotor. *American Chemical Society Applied Materials & Interfaces* **2016**. https://doi.org/10.1021/acsami.6b00012.

(104) Gao, W.; de Ávila, B. E. F.; Zhang, L.; Wang, J. Targeting and Isolation of Cancer Cells Using Micro/Nanomotors. *Advanced Drug Delivery Reviews* **2018**. https://doi.org/10.1016/j.addr.2017.09.002.

(105) Parmar, J.; Vilela, D.; Villa, K.; Wang, J.; Sánchez, S. Micro- and Nanomotors as Active Environmental Microcleaners and Sensors. *Journal of the American Chemical Society* **2018**. https://doi.org/10.1021/jacs.8b05762.

(106) Jurado-Sánchez, B. Nanoscale Biosensors Based on Self-Propelled Objects. *Biosensors* **2018**. https://doi.org/10.3390/bios8030059.

(107) Pacheco, M.; Jurado-Sánchez, B.; Escarpa, A. Functional Coatings Enable Navigation of Light-Propelled Micromotors in Blood for Effective Biodetoxification. *Nanoscale* **2021**. https://doi.org/10.1039/d1nr04842b.

(108) Kim, K.; Guo, J.; Liang, Z.; Fan, D. Artificial Micro/Nanomachines for Bioapplications: Biochemical Delivery and Diagnostic Sensing. *Advanced Functional Materials* **2018**. https://doi.org/10.1002/adfm.201705867.

(109) María Hormigos, R.; Jurado Sánchez, B.; Escarpa, A. Multi-Light-Responsive Quantum Dot Sensitized Hybrid Micromotors with Dual-Mode Propulsion. *Angewandte Chemie - International Edition* **2019**. https://doi.org/10.1002/anie.201811050.

(110) Wang, H.; Cai, L.; Zhang, D.; Shang, L.; Zhao, Y. Responsive Janus Structural Color Hydrogel Micromotors for Label-Free Multiplex Assays. *Research* **2021**. https://doi.org/10.34133/2021/9829068.

(111) Zhao, G.; Nguyen, N. T.; Pumera, M. Reynolds Numbers Influence the Directionality of Self-Propelled Microjet Engines in the 10-4 Regime. *Nanoscale* **2013**. https://doi.org/10.1039/c3nr01891a.

(112) Zhou, H.; Mayorga-Martinez, C. C.; Pané, S.; Zhang, L.; Pumera, M. Magnetically Driven Micro and Nanorobots. *Chemical Reviews* **2021**. https://doi.org/10.1021/acs.chemrev.0c01234.

(113) Nagle, S. F.; Livermore, C.; Frechette, L. G.; Ghodssi, R.; Lang, J. H. An Electric Induction Micromotor. *Journal of Microelectromechanical Systems* **2005**. https://doi.org/10.1109/JMEMS.2005.851816.

(114) Das, S. S.; Pedireddi, V. M.; Bandopadhyay, A.; Saha, P.; Chakraborty, S. Electrical Power Generation from Wet Textile Mediated by Spontaneous Nanoscale Evaporation. *Nano Letters* **2019**. https://doi.org/10.1021/acs.nanolett.9b02783.

(115) Xiao, Z.; Wei, M.; Wang, W. A Review of Micromotors in Confinements: Pores, Channels, Grooves, Steps, Interfaces, Chains, and Swimming in the Bulk. *ACS Applied Materials & Interfaces* **2019**. https://doi.org/10.1021/acsami.8b13103.

(116) Molinero-Fernández, Á.; Moreno-Guzmán, M.; Arruza, L.; López, M. Á.; Escarpa, A. Polymer-Based Micromotor Fluorescence Immunoassay for On-the-Move Sensitive Procalcitonin Determination in Very Low Birth Weight Infants' Plasma. *ACS Sensors* **2020**. https://doi.org/10.1021/acssensors.9b02515.

(117) Zhang, Y. S.; Khademhosseini, A. Advances in Engineering Hydrogels. *Science* **2017**. https://doi.org/10.1126/science.aaf3627.

(118) Wang, J.; Li, X.; Zhang, R.; Fu, B.; Chen, M.; Ye, M.; Liu, W.; Xu, J.; Pan, G.; Zhang, H. A Molecularly Imprinted Antibiotic Receptor on Magnetic Nanotubes for the Detection and Removal of Environmental Oxytetracycline. *Journal of Materials Chemistry B* **2022**. https://doi.org/10.1039/d2tb00497f.

(119) Rojas, D.; Jurado-Sánchez, B.; Escarpa, A. "Shoot and Sense" Janus Micromotors-Based Strategy for the Simultaneous Degradation and Detection of Persistent Organic Pollutants in Food and Biological Samples. *Analytical Chemistry* **2016**. https://doi.org/10.1021/acs.analchem.6b00574.

(120) Molinero-Fernández, Á.; Moreno-Guzmán, M.; López, M. Á.; Escarpa, A. Biosensing Strategy for Simultaneous and Accurate Quantitative Analysis of Mycotoxins in Food Samples Using Unmodified Graphene Micromotors. *Analytical Chemistry* **2017**. https://doi.org/10.1021/acs.analchem.7b02440.

(121) Yu, X.; Li, Y.; Wu, J.; Ju, H. Motor-Based Autonomous Microsensor for Motion and Counting Immunoassay of Cancer Biomarker. *Analytical Chemistry* **2014**. https://doi.org/10.1021/ac500912c.

(122) de Ávila, B. E. F.; Zhao, M.; Campuzano, S.; Ricci, F.; Pingarrón, J. M.; Mascini, M.; Wang, J. Rapid Micromotor-Based Naked-Eye Immunoassay. *Talanta* **2017**. https://doi.org/10.1016/j.talanta.2017.02.068.

(123) Ensafi, A. A. An Introduction to Sensors and Biosensors. In *Electrochemical Biosensors*

2019. https://doi.org/10.1016/B978-0-12-816491-4.00001-2.

(124) Ohashi, T.; Dai, L. C60 and Carbon Nanotube Sensors. In *Carbon Nanotechnology: Recent Developments in Chemistry, Physics, Materials Science and Device Applications* **2006**. https://doi.org/10.1016/B978-044451855-2/50018-8.

(125) Pelle, F. Della; Compagnone, D. Nanomaterial-Based Sensing and Biosensing of Phenolic Compounds and Related Antioxidant Capacity in Food. *Sensors (Switzerland)* **2018**. https://doi.org/10.3390/s18020462.

(126) Saha, K.; Agasti, S. S.; Kim, C.; Li, X.; Rotello, V. M. Gold Nanoparticles in Chemical and Biological Sensing. *Chemical Reviews* **2012**. https://doi.org/10.1021/cr2001178.

(127) Hu, S.; Hu, C. Carbon Nanotube-Based Electrochemical Sensors: Principles and Applications in Biomedical Systems. *Journal of Sensors* **2009**. https://doi.org/10.1155/2009/187615.

(128) Patel, P. D. (Bio)Sensors for Measurement of Analytes Implicated in Food Safety: A Review. *TrAC - Trends in Analytical Chemistry* **2002**. https://doi.org/10.1016/S0165-9936(01)00136-4.

(129) Dai, L. *Intelligent Macromolecules for Smart Devices: From Materials Synthesis to Device Applications* **2003**. https://link.springer.com/book/10.1007/b97517

(130) Vasilescu, A.; Sharpe, E.; Andreescu, S. Nanoparticle-Based Technologies for the Detection of Food Antioxidants. *Current Analytical Chemistry* **2012**. https://doi.org/10.2174/157341112803216780.

(131) Wang, Y. H.; He, L. L.; Huang, K. J.; Chen, Y. X.; Wang, S. Y.; Liu, Z. H.; Li, D. Recent Advances in Nanomaterial-Based Electrochemical and Optical Sensing Platforms for MicroRNA Assays. *Journal of Combinatorial Mathematics and Combinatorial Computing* **2019**. https://doi.org/10.1039/c9an00081j.

(132) Zhu, C.; Yang, G.; Li, H.; Du, D.; Lin, Y. Electrochemical Sensors and Biosensors Based on Nanomaterials and Nanostructures. *Analytical Chemistry* **2015**. https://doi.org/10.1021/ac5039863.

(133) Dobes, J.; Zitka, O.; Sochor, J.; Ruttkay-Nedecky, B.; Babula, P.; Beklova, M.; Kynicky, J.; Hubalek, J.; Klejdus, B.; Kizek, R.; Adam, V. Electrochemical Tools for Determination of Phenolic Compounds in Plants. A Review. *International Journal of Electrochemical Science* **2013**. https://doi.org/10.1016/s1452-3981(23)14619-0.

(134) Liu, L.; Anwar, S.; Ding, H.; Xu, M.; Yin, Q.; Xiao, Y.; Yang, X.; Yan, M.; Bi, H. Electrochemical Sensor Based on F,N-Doped Carbon Dots Decorated Laccase for Detection of Catechol. *Journal of Electroanalytical Chemistry* **2019**. https://doi.org/10.1016/j.jelechem.2019.03.071.

(135) Hart, J. P.; Crew, A.; Crouch, E.; Honeychurch, K. C.; Pemberton, R. M. Some Recent Designs and Developments of Screen-Printed Carbon Electrochemical Sensors/Biosensors for Biomedical, Environmental, and Industrial Analyses. *Analytical Letters* **2004**. https://doi.org/10.1081/AL-120030682.

(136) Chen, A.; Chatterjee, S. Nanomaterials Based Electrochemical Sensors for Biomedical Applications. *Chemical Society Reviews* **2013**. https://doi.org/10.1039/c3cs35518g.

(137) Justino, C. I. L.; Duarte, A. C.; Rocha-Santos, T. A. P. Recent Progress in Biosensors for Environmental Monitoring: A Review. *Sensors (Switzerland)* **2017**. https://doi.org/10.3390/s17122918.

(138) Scott, A. O. Biosensors: Theory and Applications. *Trends in Food Science & Technology* **1994**. https://doi.org/10.1016/0924-2244(94)90110-4.

(139) Ivnitski, D.; Abdel-Hamid, I.; Atanasov, P.; Wilkins, E. Biosensors for Detection of Pathogenic Bacteria. *Biosensors and Bioelectronics* **1999**. https://doi.org/10.1016/S0956-5663(99)00039-1.

(140) Singh, A. K.; Mittal, S.; Das, M.; Saharia, A.; Tiwari, M. Optical Biosensors: A Decade in Review. *Alexandria Engineering Journal* **2023**. https://doi.org/10.1016/j.aej.2022.12.040.

(141) Wilberforce, T.; Baroutaji, A.; Alaswad, A.; Abdelkareem, M. A.; Ramadan, M.; Olabi, A. G.; Sayed, E. T.; Elsaid, K.; Maghrabie, H. M. Piezoelectric Sensors. In *Encyclopedia of Smart Materials* **2021**. https://doi.org/10.1016/B978-0-12-815732-9.00110-8.

(142) Zhou, S.; Zhao, Y.; Mecklenburg, M.; Yang, D.; Xie, B. A Novel Thermometric Biosensor for Fast Surveillance of β-Lactamase Activity in Milk. *Biosensors and Bioelectronics* **2013**. https://doi.org/10.1016/j.bios.2013.05.005.

(143) Thévenot, D. R.; Toth, K.; Durst, R. A.; Wilson, G. S. Electrochemical Biosensors: Recommended Definitions and Classification. *Biosensors and Bioelectronics* **2001**. https://doi.org/10.1016/S0956-5663(01)00115-4.

(144) Naresh, V.; Lee, N. A Review on Biosensors and Recent Development of Nanostructured Materials-Enabled Biosensors. *Sensors (Switzerland)* **2021**. https://doi.org/10.3390/s21041109.

(145) Liu, L.; He, F.; Yu, Y.; Wang, Y. Application of FRET Biosensors in Mechanobiology and Mechanopharmacological Screening. *Frontiers in Bioengineering and Biotechnology* **2020**. https://doi.org/10.3389/fbioe.2020.595497.

(146) Schneider, R.; Lamien-Meda, A.; Auer, H.; Wiedermann-Schmidt, U.; Chiodini, P. L.; Walochnik, J. Validation of a Novel FRET Real-Time PCR Assay for Simultaneous Quantitative Detection and Discrimination of Human Plasmodium Parasites. *Public Library of Science ONE* **2021**. https://doi.org/10.1371/journal.pone.0252887.

(147) Zhu, H.; Zhang, H.; Xu, Y.; Laššáková, S.; Korabečná, M.; Neužil, P. PCR Past, Present and Future. *BioTechniques* **2020**. https://doi.org/10.2144/BTN-2020-0057.

(148) Didenko, V. V. Dna Probes Using Fluorescence Resonance Energy Transfer (Fret): Designs and Applications. *BioTechniques* **2001**. https://doi.org/10.2144/01315rv02.

(149) Heid, C. A.; Stevens, J.; Livak, K. J.; Williams, P. M. Real Time Quantitative PCR. *Genome Research* **1996**. https://doi.org/10.1101/gr.6.10.986.

(150) Ahmad, A. I.; Ghasemi, J. B. New FRET Primers for Quantitative Real-Time PCR. *Analytical and Bioanalytical Chemistry* **2007**. https://doi.org/10.1007/s00216-007-1123-4.

(151) Nath-Chowdhury, M.; Sangaralingam, M.; Bastien, P.; Ravel, C.; Pratlong, F.; Mendez, J.; Libman, M.; Ndao, M. Real-Time PCR Using FRET Technology for Old World Cutaneous Leishmaniasis Species Differentiation. *Parasites and Vectors* **2016**. https://doi.org/10.1186/s13071-016-1531-4.

(152) Corman, V. M.; Landt, O.; Kaiser, M.; Molenkamp, R.; Meijer, A.; Chu, D. K. W.; Bleicker, T.; Brünink, S.; Schneider, J.; Schmidt, M. L.; Mulders, D. G. J. C.; Haagmans, B. L.; Van Der Veer, B.; Van Den Brink, S.; Wijsman, L.; Goderski, G.; Romette, J. L.; Ellis, J.; Zambon, M.; Peiris, M.; Goossens, H.; Reusken, C.; Koopmans, M. P. G.; Drosten, C. Detection of 2019 Novel Coronavirus (2019-NCoV) by Real-Time RT-PCR. *Eurosurveillance* **2020**. https://doi.org/10.2807/1560-7917.ES.2020.25.3.2000045.

(153) Zhang, Q.; Yin, B.; Hao, J.; Ma, L.; Huang, Y.; Shao, X.; Li, C.; Chu, Z.; Yi, C.; Wong, S. H. D.; Yang, M. An AIEgen/Graphene Oxide Nanocomposite (AIEgen@GO)-Based Two-Stage "Turn-on" Nucleic Acid Biosensor for Rapid Detection of SARS-CoV-2 Viral Sequence. *Aggregate* **2023**. https://doi.org/10.1002/agt2.195.

(154) Rudkouskaya, A.; Sinsuebphon, N.; Ochoa, M.; Chen, S. J.; Mazurkiewicz, J. E.; Intes, X.; Barroso, M. Multiplexed Non-Invasive Tumor Imaging of Glucose Metabolism and Receptor-Ligand Engagement Using Dark Quencher FRET Acceptor. *Theranostics* **2020**. https://doi.org/10.7150/thno.45825.

(155) Szalai, A. M.; Siarry, B.; Lukin, J.; Giusti, S.; Unsain, N.; Cáceres, A.; Steiner, F.; Tinnefeld, P.; Refojo, D.; Jovin, T. M.; Stefani, F. D. Super-Resolution Imaging of Energy Transfer by Intensity-Based STED-FRET. *Nano Letters* **2021**. https://doi.org/10.1021/acs.nanolett.1c00158.

(156) Verma, A. K.; Ansari, Z. A. Fluorescent ZnO Quantum Dot Probe to Study Glucose–Glucose Oxidase Interaction via Fluorescence Resonance Energy Transfer. *Sensor Letters* **2020**. https://doi.org/10.1166/sl.2020.4232.

(157) Rasnik, I.; McKinney, S. A.; Ha, T. Surfaces and Orientations: Much to FRET About? *Accounts of Chemical Research* **2005**. https://doi.org/10.1021/ar040138c.

(158) Grüber, G.; Börsch, M.; Sielaff, H.; Singh, D. Analyzing Conformational Changes in Single FRET-Labeled A1 Parts of Archaeal A1AO-ATP Synthase. *Nanyang Technological University, Singapore* **2018.** https://doi.org/10.1117/12.2286785.

(159) Calleja, V.; Ameer-Beg, S. M.; Vojnovic, B.; Woscholski, R.; Downward, J.; Larijani, B. Erratum: Monitoring Conformational Changes of Proteins in Cells by Fluorescence Lifetime Imaging Microscopy (Biochemical Journal (2003)). *Biochemical Journal* **2003**. https://doi.org/10.1042/bj3730999v.

(160) Lee, J.; Kim, J.; Kim, S.; Min, D. H. Biosensors Based on Graphene Oxide and Its Biomedical Application. *Advanced Drug Delivery Reviews* **2016**. https://doi.org/10.1016/j.addr.2016.06.001.

(161) Chen, C.; Hildebrandt, N. Resonance Energy Transfer to Gold Nanoparticles: NSET Defeats FRET. *TrAC - Trends in Analytical Chemistry* **2020**. https://doi.org/10.1016/j.trac.2019.115748.

(162) Forster, T. Energiewanderung Und Fluoreszenz. *Die Naturwissenschaften* **1946**. https://doi.org/10.1007/BF00585226.

(163) Andrews, D. L.; Bradshaw, D. S. Virtual Photons, Dipole Fields and Energy Transfer: A Quantum Electrodynamical Approach. *European Journal of Physics* **2004**. https://doi.org/10.1088/0143-0807/25/6/017.

(164) Van Munster, E. B.; Kremers, G. J.; Adjobo-Hermans, M. J. W.; Gadella, T. W. J. Fluorescence Resonance Energy Transfer (FRET) Measurement by Gradual Acceptor Photobleaching. *Journal of Microscopy* **2005**. https://doi.org/10.1111/j.1365-2818.2005.01483.x.

(165) Cano-Raya, C.; Fernández-Ramos, M. D.; Capitán-Vallvey, L. F. Fluorescence Resonance Energy Transfer Disposable Sensor for Copper(II). *Analytica Chimica Acta* **2006**. https://doi.org/10.1016/j.aca.2005.09.011.

(166) Sekar, R. B.; Periasamy, A. Fluorescence Resonance Energy Transfer (FRET) Microscopy Imaging of Live Cell Protein Localizations. *Journal of Cell Biology* **2003**. https://doi.org/10.1083/jcb.200210140.

(167) JR, L. *Introduction to Fluorescence. In: Principles of Fluorescence Spectroscopy* **2006**. https://link.springer.com/chapter/10.1007/978-0-387-46312-4_1

(168) Stryer, L. Fluorescence Energy Transfer as a Spectroscopic Ruler. *Annual review of biochemistry* **1978**. https://doi.org/10.1146/annurev.bi.47.070178.004131.

(169) Chirio-Lebrun, M. C.; Prats, M. Fluorescence Resonance Energy Transfer (FRET): Theory and Experiments. *Biochemical Education* **1998**. https://doi.org/10.1016/S0307-4412(98)80010-1.

(170) Jares-Erijman, E. A.; Jovin, T. M. FRET Imaging. *Nature Biotechnology* **2003**. https://doi.org/10.1038/nbt896.

(171) Andrews, D. L. A Unified Theory of Radiative and Radiationless Molecular Energy Transfer. *Chemical Physics* **1989**. https://doi.org/10.1016/0301-0104(89)87019-3.

(172) Schobel, U.; Egelhaaf, H. J.; Brecht, A.; Oelkrug, D.; Gauglitz, G. New Donor Acceptor Pair for Fluorescent Immunoassays by Energy Transfer. *Bioconjugate Chemistry* **1999**. https://doi.org/10.1021/bc990073b.

(173) Mohammed, A.; Abdullah, A. Scanning Electron Microscopy (SEM): A Review PhD Courses View Project Construction and Building Materials View Project Scanning Electron Microscopy (SEM): A Review. *Proceedings of International Conference on Hydraulics and Pneumatics - HERVEX* **2019**. https://fluidas.ro/hervex/proceedings2018/77-85.pdf

(174) Zhou, W.; Apkarian, R.; Wang, Z. L.; Joy, D. Fundamentals of Scanning Electron Microscopy (SEM). In *Scanning Microscopy for Nanotechnology: Techniques and*

Applications **2007**. https://doi.org/10.1007/978-0-387-39620-0_1.

(175) Frahm, E. Scanning Electron Microscopy (SEM): Applications in Archaeology. In *Encyclopedia of Global Archaeology* **2020**. https://doi.org/10.1007/978-3-030-30018-0_341.

(176) Abd Mutalib, M.; Rahman, M. A.; Othman, M. H. D.; Ismail, A. F.; Jaafar, J. Scanning Electron Microscopy (SEM) and Energy-Dispersive X-Ray (EDX) Spectroscopy. In *Membrane Characterization* **2017**. https://doi.org/10.1016/B978-0-444-63776-5.00009-7.

(177) Western, S. S. Scanning Electron Microscopy Coupled with Energy Dispersive X-Ray (SEM/EDX) Spectroscopy. *Western University* **2017**. https://www.surfacesciencewestern.com/analytical-services/scanning-electron-microscopy-coupled-with-energy-dispersive-x-ray-semedx-spectroscopy.

(178) Konno, H. X-Ray Photoelectron Spectroscopy (XPS). *Zairyo-to-Kankyo* **1993**. https://doi.org/10.3323/jcorr1991.42.27.

(179) Stevie, F. A.; Donley, C. L. Introduction to X-Ray Photoelectron Spectroscopy. *Journal of Vacuum Science & Technology A: Vacuum, Surfaces, and Films* **2020**. https://doi.org/10.1116/6.0000412.

(180) Shinde, K. N.; Dhoble, S. J.; Swart, H. C.; Park, K. Basic Mechanisms of Photoluminescence **2012**. https://doi.org/10.1007/978-3-642-34312-4_2.

(181) Lefebvre, J.; Maruyama, S.; Finnie, P. Photoluminescence: Science and Applications. In *Topics in Applied Physics* **2008**. https://doi.org/10.1007/978-3-540-72865-8_9.

(182) Bebb, H. B.; Williams, E. W. Photoluminescence I: Theory. *Semiconductors and Semimetals* **1972**. https://doi.org/10.1016/S0080-8784(08)62345-5.

(183) Wu, R.; Liu, Y.; Tang, J.; Xiao, Z. Excited-State Dopant-Host Energy-Level Alignment: Toward a Better Understanding of the Photoluminescence Behaviors of Doped Phosphors. *Journal of Physical Chemistry Letters* **2023**. https://doi.org/10.1021/acs.jpclett.3c00722.

(184) Ehrat, F.; Bhattacharyya, S.; Schneider, J.; Löf, A.; Wyrwich, R.; Rogach, A. L.; Stolarczyk, J. K.; Urban, A. S.; Feldmann, J. Tracking the Source of Carbon Dot Photoluminescence: Aromatic Domains versus Molecular Fluorophores. *Nano Letters* **2017**. https://doi.org/10.1021/acs.nanolett.7b03863.

(185) Gami, A. A.; Shukor, M. Y.; Khalil, K. A.; Dahalan, F. A.; Khalid, A.; Ahmad, S. A. Phenol and Its Toxicity. *Journal of Environmental Microbiology and Toxicology* **2014**. https://doi.org/10.54987/jemat.v2i1.89.

(186) Kafi, A. K. M.; Chen, A. A Novel Amperometric Biosensor for the Detection of Nitrophenol. *Talanta* **2009**. https://doi.org/10.1016/j.talanta.2009.03.015.

(187) Belekbir, S.; El Azzouzi, M.; El Hamidi, A.; Rodríguez-Lorenzo, L.; Santaballa, J. A.; Canle, M. Improved Photocatalyzed Degradation of Phenol, as a Model Pollutant, over Metal-Impregnated Nanosized Tio2. *Nanomaterials* **2020**.

https://doi.org/10.3390/nano10050996.

(188) Guan, H.; Liu, X.; Wang, W. Encapsulation of Tyrosinase within Liposome Bioreactors for Developing an Amperometric Phenolic Compounds Biosensor. *Journal of Solid State Electrochemistry* **2013**. https://doi.org/10.1007/s10008-013-2181-5.

(189) Abdullah, J.; Ahmad, M.; Karuppiah, N.; Heng, L. Y.; Sidek, H. Immobilization of Tyrosinase in Chitosan Film for an Optical Detection of Phenol. *Sensors and Actuators, B: Chemical* **2006**. https://doi.org/10.1016/j.snb.2005.06.019.

(190) Wen, Y.; Li, R.; Liu, J.; Zhang, X.; Wang, P.; Zhang, X.; Zhou, B.; Li, H.; Wang, J.; Li, Z.; Sun, B. Promotion Effect of Zn on 2D Bimetallic NiZn Metal Organic Framework Nanosheets for Tyrosinase Immobilization and Ultrasensitive Detection of Phenol. *Analytica Chimica Acta* **2020**. https://doi.org/10.1016/j.aca.2020.06.062.

(191) Jiang, L.; Santiago, I.; Foord, J. Nanocarbon and Nanodiamond for High Performance Phenolics Sensing. *Communications Chemistry* **2018**. https://doi.org/10.1038/s42004-018-0045-8.

(192) ATSDR, U. S. Agency for Toxic Substances and Disease Registry. *Case Studies in Environmental Medicine **1997**.http://www. atsdr. cdc. gov/HEC/CSEM/csem. html* 1997.

(193) Mu'azu, N. D.; Jarrah, N.; Zubair, M.; Alagha, O. Removal of Phenolic Compounds from Water Using Sewage Sludge-Based Activated Carbon Adsorption: A Review. *International Journal of Environmental Research and Public Health* **2017**. https://doi.org/10.3390/ijerph14101094.

(194) St. John, P. M.; Kienzle, S. D.; Flood, B. M.; Moody, T. V.; Depaola, N. F.; Mass, S. Extracting and Quantifying Deuterated Bisphenol A from Planaria Using Gas Chromatography/Mass Spectrometry: An Integrative Laboratory Experiment. *Journal of Chemical Education* **2021**. https://doi.org/10.1021/acs.jchemed.0c01088.

(195) Ge, K.; Li, Y.; Wu, Q.; Gu, Y. Simultaneous and Rapid Detection of Polychlorinated Phenols in Water Samples by Surface-Enhanced Raman Spectroscopy Combined with Principal Component Analysis. *Analytical and Bioanalytical Chemistry* **2022**. https://doi.org/10.1007/s00216-022-03876-0.

(196) Al-Shaalan, N. H.; Ali, I.; ALOthman, Z. A.; Al-Wahaibi, L. H.; Alabdulmonem, H. Application of Composite NanoMaterial to Determine Phenols in Wastewater by Solid Phase Micro Membrane Tip Extraction and Capillary Electrophoresis. *Molecules* **2019**. https://doi.org/10.3390/molecules24193443.

(197) Chi, X.; Liu, J.; Yu, M.; Xie, Z.; Jiang, G. Analysis of Bromophenols in Various Aqueous Samples Using Solid Phase Extraction Followed by HPLC-MS/MS. *Talanta* **2017**. https://doi.org/10.1016/j.talanta.2016.11.010.

(198) Li, N.; Chen, H.; Zhang, M.; Zha, Y.; Mu, Z.; Ma, Y.; Chen, P. A Universal Ultrasensitive Platform for Enzyme-Linked Immunoassay Based on Responsive Surface-Enhanced Raman Scattering. *Sensors and Actuators, B: Chemical* **2020**. https://doi.org/10.1016/j.snb.2020.128135.

(199) ALOthman, Z. A.; Badjah, A. Y.; Locatelli, M.; Ali, I. Multi-Walled Carbon Nanotubes Solid-Phase Extraction and Capillary Electrophoresis Methods for the Analysis of 4-Cyanophenol and 3-Nitrophenol in Water. *Molecules* **2020**. https://doi.org/10.3390/molecules25173893.

(200) Lazarević-Pašti, T. Carbon Materials for Organophosphate Pesticide Sensing. *Chemosensors* **2023**. https://doi.org/10.3390/chemosensors11020093.

(201) Boruah, P. K.; Sharma, B.; Karbhal, I.; Shelke, M. V.; Das, M. R. Ammonia-Modified Graphene Sheets Decorated with Magnetic Fe3O4 Nanoparticles for the Photocatalytic and Photo-Fenton Degradation of Phenolic Compounds under Sunlight Irradiation. *Journal of Hazardous Materials* **2017**. https://doi.org/10.1016/j.jhazmat.2016.11.023.

(202) Shandilya, P.; Mittal, D.; Soni, M.; Raizada, P.; Lim, J. H.; Jeong, D. Y.; Dewedi, R. P.; Saini, A. K.; Singh, P. Islanding of EuVO4 on High-Dispersed Fluorine Doped Few Layered Graphene Sheets for Efficient Photocatalytic Mineralization of Phenolic Compounds and Bacterial Disinfection. *Journal of the Taiwan Institute of Chemical Engineers* **2018**. https://doi.org/10.1016/j.jtice.2018.08.034.

(203) Lü, M. J.; Li, J.; Yang, X. Y.; Zhang, C. A.; Yang, J.; Hu, H.; Wang, X. B. Applications of Graphene-Based Materials in Environmental Protection and Detection. *Chinese Science Bulletin* **2013**. https://doi.org/10.1007/s11434-013-5887-y.

(204) Park, J. M.; Kim, C. M.; Jhung, S. H. Melamine/Polyaniline-Derived Carbons with Record-High Adsorption Capacities for Effective Removal of Phenolic Compounds from Water. *Chemical Engineering Journal* **2021**. https://doi.org/10.1016/j.cej.2020.127627.

(205) Majumdar, S.; Nath, J.; Mahanta, D. Surface Modified Polypyrrole for the Efficient Removal of Phenolic Compounds from Aqueous Medium. *Journal of Environmental Chemical Engineering* **2018**. https://doi.org/10.1016/j.jece.2018.04.002.

(206) Tuncagil, S.; Varis, S.; Toppare, L. Design of a Biosensor Based on 1-(4-Nitrophenyl)-2,5-Di(2-Thienyl)-1H Pyrrole. *Journal of Molecular Catalysis B: Enzymatic* **2010**. https://doi.org/10.1016/j.molcatb.2009.06.002.

(207) Abdi, M. M.; Abdullah, L. C.; Sadrolhosseini, A. R.; Yunus, W. M.; Moksin, M. M.; Tahir, P. M. Surface Plasmon Resonance Sensing Detection of Mercury and Lead Ions Based on Conducting Polymer Composite. *Public Library of Science ONE* **2011**. https://doi.org/10.1371/journal.pone.0024578.

(208) Ramanavicius, S.; Ramanavicius, A. Charge Transfer and Biocompatibility Aspects in Conducting Polymer-Based Enzymatic Biosensors and Biofuel Cells. *Nanomaterials* **2021**. https://doi.org/10.3390/nano11020371.

(209) Naveen, M. H.; Gurudatt, N. G.; Shim, Y. B. Applications of Conducting Polymer Composites to Electrochemical Sensors: A Review. *Applied Materials Today* **2017**. https://doi.org/10.1016/j.apmt.2017.09.001.

(210) Sulak, M. T.; Erhan, E.; Keskinler, B.; Yilmaz, F.; Celik, A. Development of Amperometric Biosensor for Phenolic Compounds Using a Modified Electrode with Poly(GMA-Co-MTM) and Laccase. *Sensor Letters* **2010**.

https://doi.org/10.1166/sl.2010.1260.

(211) Zhao, Y.; Cao, L.; Li, L.; Cheng, W.; Xu, L.; Ping, X.; Pan, L.; Shi, Y. Conducting Polymers and Their Applications in Diabetes Management. *Sensors (Switzerland)* **2016**. https://doi.org/10.3390/s16111787.

(212) Gurunathan, K.; Amalnerkar, D. P.; Trivedi, D. C. Synthesis and Characterization of Conducting Polymer Composite (PAn/TiO2) for Cathode Material in Rechargeable Battery. *Materials Letters* **2003**. https://doi.org/10.1016/S0167-577X(02)01045-5.

(213) Coskun, Y.; Cirpan, A.; Toppare, L. Conducting Polymers of Terepthalic Acid Bis-(2-Thiophen-3-Yl-Ethyl) Ester and Their Electrochromic Properties. *Polymer* **2004**. https://doi.org/10.1016/j.polymer.2004.05.038.

(214) Lee, A. S.; Peteu, S. F.; Ly, J. V.; Requicha, A. A. G.; Thompson, M. E.; Zhou, C. Actuation of Polypyrrole Nanowires. *Nanotechnology* **2008**. https://doi.org/10.1088/0957-4484/19/16/165501.

(215) Otero, T. F.; Sanchez, J. J.; Martinez, J. G. Biomimetic Dual Sensing-Actuators Based on Conducting Polymers. Galvanostatic Theoretical Model for Actuators Sensing Temperature. *Journal of Physical Chemistry B* **2012**. https://doi.org/10.1021/jp300290s.

(216) Mi, H.; Zhang, X.; Ye, X.; Yang, S. Preparation and Enhanced Capacitance of Core-Shell Polypyrrole/Polyaniline Composite Electrode for Supercapacitors. *Journal of Power Sources* **2008**. https://doi.org/10.1016/j.jpowsour.2007.10.070.

(217) Omar, N. A. S.; Fen, Y. W.; Saleviter, S.; Daniyal, W. M. E. M. M.; Anas, N. A. A.; Ramdzan, N. S. M.; Roshidi, M. D. A. Development of a Graphene-Based Surface Plasmon Resonance Optical Sensor Chip for Potential Biomedical Application. *Materials* **2019**. https://doi.org/10.3390/ma12121928.

(218) Daniyal, W. M. E. M. M.; Fen, Y. W.; Abdullah, J.; Sadrolhosseini, A. R.; Saleviter, S.; Omar, N. A. S. Label-Free Optical Spectroscopy for Characterizing Binding Properties of Highly Sensitive Nanocrystalline Cellulose-Graphene Oxide Based Nanocomposite towards Nickel Ion. *Spectrochimica Acta - Part A: Molecular and Biomolecular Spectroscopy* **2019**. https://doi.org/10.1016/j.saa.2018.12.031.

(219) Ramdzan, N. S. M.; Fen, Y. W.; Omar, N. A. S.; Anas, N. A. A.; Liew, J. Y. C.; Daniyal, W. M. E. M. M.; Hashim, H. S. Detection of Mercury Ion Using Surface Plasmon Resonance Spectroscopy Based on Nanocrystalline Cellulose/Poly(3,4-Ethylenedioxythiophene) Thin Film. *Measurement: Journal of the International Measurement Confederation* **2021**. https://doi.org/10.1016/j.measurement.2021.109728.

(220) Zhang, Y.; Wu, L.; Lei, W.; Xia, X.; Xia, M.; Hao, Q. Electrochemical Determination of 4-Nitrophenol at Polycarbazole/N-Doped Graphene Modified Glassy Carbon Electrode. *Electrochimica Acta* **2014**. https://doi.org/10.1016/j.electacta.2014.08.153.

(221) Saadati, F.; Ghahramani, F.; Shayani-jam, H.; Piri, F.; Yaftian, M. R. Synthesis and Characterization of Nanostructure Molecularly Imprinted Polyaniline/Graphene Oxide Composite as Highly Selective Electrochemical Sensor for Detection of p-Nitrophenol. *Journal of the Taiwan Institute of Chemical Engineers* **2018**.

https://doi.org/10.1016/j.jtice.2018.02.019.

(222) Hashemi, S. A.; Mousavi, S. M.; Bahrani, S.; Ramakrishna, S. Integrated Polyaniline with Graphene Oxide-Iron Tungsten Nitride Nanoflakes as Ultrasensitive Electrochemical Sensor for Precise Detection of 4-Nitrophenol within Aquatic Media. *Journal of Electroanalytical Chemistry* **2020**. https://doi.org/10.1016/j.jelechem.2020.114406.

(223) Zhu, G.; Tang, Q.; Dou, J.; Li, X.; Yang, J.; Xu, R.; Liu, J. Partially Reduced Graphene Oxide Sheet-Covered Polyaniline Nanotubes for the Simultaneous Determination of Bisphenol A and Phenol. *Journal of The Electrochemical Society* **2019**. https://doi.org/10.1149/2.1381915jes.

(224) Peleyeju, M. G.; Idris, A. O.; Umukoro, E. H.; Babalola, J. O.; Arotiba, O. A. Electrochemical Detection of 2,4-Dichlorophenol on a Ternary Composite Electrode of Diamond, Graphene, and Polyaniline. *ChemElectroChem* **2017**. https://doi.org/10.1002/celc.201600621.

(225) Khan, A.; Khan, A. A. P.; Rahman, M. M.; Asiri, A. M.; Inamuddin; Alamry, K. A.; Hameed, S. A. Preparation and Characterization of PANI@G/CWO Nanocomposite for Enhanced 2-Nitrophenol Sensing. *Applied Surface Science* **2018**. https://doi.org/10.1016/j.apsusc.2017.09.219.

(226) Aragay, G.; Pino, F.; Merkoçi, A. Nanomaterials for Sensing and Destroying Pesticides. *Chemical Reviews* **2012**. https://doi.org/10.1021/cr300020c.

(227) Thanos, C. A. A.; Tomuka, D.; Mallo, N. T. S. Livor Mortis Pada Keracunan Insektisida Golongan Organofosfat Di Kelinci. *e-CliniC* **2016**. https://doi.org/10.35790/ecl.4.1.2016.10827.

(228) Carvalho, F. P. Pesticides, Environment, and Food Safety. *Food and Energy Security* **2017**. https://doi.org/10.1002/fes3.108.

(229) Saiya, A. Analisis Residu Klorpirifos Dalam Sayuran Kubis Dengan Metode Hplc Di Beberapa Pasar Tradisional Di Sulawesi Utara. *EKSAKTA: Berkala Ilmiah Bidang MIPA* **2017**. https://doi.org/10.24036/eksakta/vol18-iss02/57.

(230) Saiya, A.; Gumolung, D.; Caroles, J. D. S. Analisis Residu Pestisida Dalam Tomat, Cabai Rawit Dan Wortel Dari Beberapa Pasar Tradisional Di Sulawesi Utara. *Fullerene Journal of Chemistry* **2018**. https://doi.org/10.37033/fjc.v3i2.40.

(231) Harsojo, H.; M Chairul, S. Kandungan Mikroba Patogen, Residu Insektisida Organofosfat Dan Logam Berat Dalam Sayuran. *Jurnal Ecolab* **2011**. https://doi.org/10.20886/jklh.2011.5.2.89-95.

(232) Zhang, W.; Asiri, A. M.; Liu, D.; Du, D.; Lin, Y. Nanomaterial-Based Biosensors for Environmental and Biological Monitoring of Organophosphorus Pesticides and Nerve Agents. *TrAC - Trends in Analytical Chemistry* **2014**. https://doi.org/10.1016/j.trac.2013.10.007.

(233) Tang, Q.; Wang, X.; Yu, F.; Qiao, X.; Xu, Z. Simultaneous Determination of Ten Organophosphate Pesticide Residues in Fruits by Gas Chromatography Coupled with

Magnetic Separation. *Journal of Separation Science* **2014**. https://doi.org/10.1002/jssc.201301161.

(234) Jin, M.; Zhu, G.; Jin, R.; Liu, S.; Shao, H.; Jin, F.; Guo, Y.; Wang, J. A Sensitive Chemiluminescent Enzyme Immunoassay for Carbofuran Residue in Vegetable, Fruit and Environmental Samples. *Food and Agricultural Immunology* **2013**. https://doi.org/10.1080/09540105.2012.694096.

(235) Mubarok, A. Z.; Mani, V.; Huang, C. H.; Chang, P. C.; Huang, S. T. Label-Free Electrochemical Detection of Neuraminidase Activity: A Facile Whole Blood Diagnostic Probe for Infectious Diseases. *Sensors and Actuators, B: Chemical* **2017**. https://doi.org/10.1016/j.snb.2017.06.061.

(236) Arduini, F.; Cinti, S.; Scognamiglio, V.; Moscone, D. Nanomaterials in Electrochemical Biosensors for Pesticide Detection: Advances and Challenges in Food Analysis. *Microchimica Acta* **2016**. https://doi.org/10.1007/s00604-016-1858-8.

(237) Mahmoudi, E.; Fakhri, H.; Hajian, A.; Afkhami, A.; Bagheri, H. High-Performance Electrochemical Enzyme Sensor for Organophosphate Pesticide Detection Using Modified Metal-Organic Framework Sensing Platforms. *Bioelectrochemistry* **2019**. https://doi.org/10.1016/j.bioelechem.2019.107348.

(238) Xu, G.; Huo, D.; Hou, C.; Zhao, Y.; Bao, J.; Yang, M.; Fa, H. A Regenerative and Selective Electrochemical Aptasensor Based on Copper Oxide Nanoflowers-Single Walled Carbon Nanotubes Nanocomposite for Chlorpyrifos Detection. *Talanta* **2018**. https://doi.org/10.1016/j.talanta.2017.08.086.

(239) Mishra, R. K.; Hubble, L. J.; Martín, A.; Kumar, R.; Barfidokht, A.; Kim, J.; Musameh, M. M.; Kyratzis, I. L.; Wang, J. Wearable Flexible and Stretchable Glove Biosensor for On-Site Detection of Organophosphorus Chemical Threats. *ACS Sensors* **2017**. https://doi.org/10.1021/acssensors.7b00051.

(240) Surucu, O.; Bolat, G.; Abaci, S. Electrochemical Behavior and Voltammetric Detection of Fenitrothion Based on a Pencil Graphite Electrode Modified with Reduced Graphene Oxide (RGO)/Poly(E)-1-(4-((4 (Phenylamino)Phenyl)Diazenyl)Phenyl)Ethanone (DPA) Composite Film. *Talanta* **2017**. https://doi.org/10.1016/j.talanta.2017.03.033.

(241) Xu, J.; Yu, C.; Feng, T.; Liu, M.; Li, F.; Wang, Y.; Xu, J. N -Carbamoylmaleimide-Treated Carbon Dots: Stabilizing the Electrochemical Intermediate and Extending It for the Ultrasensitive Detection of Organophosphate Pesticides. *Nanoscale* **2018**. https://doi.org/10.1039/c8nr05098h.

(242) Mehta, J.; Bhardwaj, N.; Bhardwaj, S. K.; Tuteja, S. K.; Vinayak, P.; Paul, A. K.; Kim, K. H.; Deep, A. Graphene Quantum Dot Modified Screen Printed Immunosensor for the Determination of Parathion. *Analytical Biochemistry* **2017**. https://doi.org/10.1016/j.ab.2017.01.026.

(243) Bolat, G.; Abaci, S.; Vural, T.; Bozdogan, B.; Denkbas, E. B. Sensitive Electrochemical Detection of Fenitrothion Pesticide Based on Self-Assembled Peptide-Nanotubes Modified Disposable Pencil Graphite Electrode. *Journal of Electroanalytical Chemistry* **2018**. https://doi.org/10.1016/j.jelechem.2017.12.060.

(244) Zhang, J.; Hu, H.; Wang, P.; Zhang, C.; Wu, M.; Yang, L. A Stable Biosensor for Organophosphorus Pesticide Detection Based on Chitosan Modified Graphene. *Biotechnology and Applied Biochemistry* **2022**. https://doi.org/10.1002/bab.2133.

(245) Ho, K. C.; Chen, C. Y.; Hsu, H. C.; Chen, L. C.; Shiesh, S. C.; Lin, X. Z. Amperometric Detection of Morphine at a Prussian Blue-Modified Indium Tin Oxide Electrode. In *Biosensors and Bioelectronics* **2004**. https://doi.org/10.1016/j.bios.2003.11.027.

(246) Bunde, R. L.; Jarvi, E. J.; Rosentreter, J. J. Piezoelectric Quartz Crystal Biosensors. *Talanta* **1998**. https://doi.org/10.1016/S0039-9140(97)00392-5.

(247) Mehrvar, M.; Bis, C.; Scharer, J. M.; Moo-Young, M.; Luong, J. H. Fiber-Optic Biosensors - Trends and Advances. *Analytical Sciences* **2000**. https://doi.org/10.2116/analsci.16.677.

(248) Kumar, N.; Hu, Y.; Singh, S.; Mizaikoff, B. Emerging Biosensor Platforms for the Assessment of Water-Borne Pathogens. *Analyst* **2018**, *143*, 359–373. https://doi.org/10.1039/c7an00983f.

(249) Cheng, V. C. C.; Wong, S. C.; Chen, J. H. K.; Yip, C. C. Y.; Chuang, V. W. M.; Tsang, O. T. Y.; Sridhar, S.; Chan, J. F. W.; Ho, P. L.; Yuen, K. Y. Escalating Infection Control Response to the Rapidly Evolving Epidemiology of the Coronavirus Disease 2019 (COVID-19) Due to SARS-CoV-2 in Hong Kong. *Infection Control and Hospital Epidemiology* **2020**. https://doi.org/10.1017/ice.2020.58.

(250) Fritsch, A.; Schweiger, B.; Biere, B. Influenza c Virus in Pre-School Children with Respiratory Infections: Retrospective Analysis of Data from the National Influenza Surveillance System in Germany, 2012 to 2014. *Eurosurveillance* **2019**. https://doi.org/10.2807/1560-7917.ES.2019.24.10.1800174.

(251) A.A., S.; J., S.; S.B., B. Respiratory Pathogens in Infants Diagnosed with Acute Lower Respiratory Tract Infection in a Tertiary Care Hospital of Western India Using Multiplex Real Time PCR. *Indian Journal of Pediatrics* **2019**.

(252) Deghmane, A. E.; Hong, E.; Taha, M. K. Diagnosis of Meningococcal Infection Using Internally Controlled Multiplex Real-Time PCR. In *Methods in Molecular Biology*; **2019**. https://doi.org/10.1007/978-1-4939-9202-7_2.

(253) Wlassow, M.; Poiteau, L.; Roudot-Thoraval, F.; Rosa, I.; Soulier, A.; Hézode, C.; Ortonne, V.; Pawlotsky, J. M.; Chevaliez, S. The New Xpert HCV Viral Load Real-Time PCR Assay Accurately Quantifies Hepatitis C Virus RNA in Serum and Whole-Blood Specimens. *Journal of Clinical Virology* **2019**. https://doi.org/10.1016/j.jcv.2019.06.007.

(254) Zhang, C.; Zheng, X.; Zhao, C.; Li, Y.; Chen, S.; Liu, G.; Wang, C.; Lv, Q.; Liu, P.; Zheng, Y.; Kong, D.; Jiang, H.; Jiang, Y. Detection of Pathogenic Microorganisms from Bloodstream Infection Specimens Using TaqMan Array Card Technology. *Scientific Reports* **2018**. https://doi.org/10.1038/s41598-018-31200-3.

(255) Loonen, A. J. M.; Bos, M. P.; van Meerbergen, B.; Neerken, S.; Catsburg, A.; Dobbelaer, I.; Penterman, R.; Maertens, G.; van de Wiel, P.; Savelkoul, P.; van den Brule, A. J. C. Comparison of Pathogen DNA Isolation Methods from Large Volumes

of Whole Blood to Improve Molecular Diagnosis of Bloodstream Infections. *Public Library of Science ONE* **2013**. https://doi.org/10.1371/journal.pone.0072349.

(256) Teengam, P.; Siangproh, W.; Tuantranont, A.; Vilaivan, T.; Chailapakul, O.; Henry, C. S. Multiplex Paper-Based Colorimetric DNA Sensor Using Pyrrolidinyl Peptide Nucleic Acid-Induced AgNPs Aggregation for Detecting MERS-CoV, MTB, and HPV Oligonucleotides. *Analytical Chemistry* **2017**. https://doi.org/10.1021/acs.analchem.7b00255.

(257) Myers, F. B.; Lee, L. P. Innovations in Optical Microfluidic Technologies for Point-of-Care Diagnostics. *Lab on a Chip* **2008**. https://doi.org/10.1039/b812343h.

(258) Xu, J.; Jiang, B.; Xie, J.; Xiang, Y.; Yuan, R.; Chai, Y. Sensitive Point-of-Care Monitoring of HIV Related DNA Sequences with a Personal Glucometer. *Chemical Communications* **2012**. https://doi.org/10.1039/c2cc35941c.

(259) Trotter, M.; Borst, N.; Thewes, R.; von Stetten, F. Review: Electrochemical DNA Sensing – Principles, Commercial Systems, and Applications. *Biosensors and Bioelectronics* **2020**. https://doi.org/10.1016/j.bios.2020.112069.

(260) Liu, G.; Wan, Y.; Gau, V.; Zhang, J.; Wang, L.; Song, S.; Fan, C. An Enzyme-Based E-DNA Sensor for Sequence-Specific Detection of Femtomolar DNA Targets. *Journal of the American Chemical Society* **2008**. https://doi.org/10.1021/ja800554t.

(261) Zhang, D. Y.; Chen, S. X.; Yin, P. Optimizing the Specificity of Nucleic Acid Hybridization. *Nature Chemistry* **2012**. https://doi.org/10.1038/nchem.1246.

(262) Wang, J. Nanomaterial-Based Amplified Transduction of Biomolecular Interactions. *Small* **2005**. https://doi.org/10.1002/smll.200500214.

(263) Blair, E. O.; Corrigan, D. K. A Review of Microfabricated Electrochemical Biosensors for DNA Detection. *Biosensors and Bioelectronics* **2019**. https://doi.org/10.1016/j.bios.2019.03.055.

(264) Hoilett, O. S.; Walker, J. F.; Balash, B. M.; Jaras, N. J.; Boppana, S.; Linnes, J. C. Kickstat: A Coin-Sized Potentiostat for High-Resolution Electrochemical Analysis. *Sensors (Switzerland)* **2020**. https://doi.org/10.3390/s20082407.

(265) Taleat, Z.; Khoshroo, A.; Mazloum-Ardakani, M. Screen-Printed Electrodes for Biosensing: A Review (2008-2013). *Microchimica Acta* **2014**. https://doi.org/10.1007/s00604-014-1181-1.

(266) Berney, H.; West, J.; Haefele, E.; Alderman, J.; Lane, W.; Collins, J. K. DNA Diagnostic Biosensor: Development, Characterisation and Performance. *Sensors and Actuators, B: Chemical* **2000**. https://doi.org/10.1016/S0925-4005(00)00468-8.

(267) Erdem, A.; Kerman, K.; Meric, B.; Akarca, U. S.; Ozsoz, M. Novel Hybridization Indicator Methylene Blue for the Electrochemical Detection of Short DNA Sequences Related to the Hepatitis B Virus. *Analytica Chimica Acta* **2000**. https://doi.org/10.1016/S0003-2670(00)01058-8.

(268) Millan, K. M.; Mikkelsen, S. R. Sequence-Selective Biosensor for DNA Based on

Electroactive Hybridization Indicators. *Analytical Chemistry* **1993**. https://doi.org/10.1021/ac00065a025.

(269) Prabhakar, N.; Arora, K.; Singh, S. P.; Singh, H.; Malhotra, B. D. DNA Entrapped Polypyrrole-Polyvinyl Sulfonate Film for Application to Electrochemical Biosensor. *Analytical Biochemistry* **2007**. https://doi.org/10.1016/j.ab.2007.03.009.

(270) Arora, K.; Prabhakar, N.; Chand, S.; Malhotra, B. D. Escherichia Coli Genosensor Based on Polyaniline. *Analytical Chemistry* **2007**. https://doi.org/10.1021/ac070403i.

(271) Arora, K.; Prabhakar, N.; Chand, S.; Malhotra, B. D. Immobilization of Single Stranded DNA Probe onto Polypyrrole-Polyvinyl Sulfonate for Application to DNA Hybridization Biosensor. *Sensors and Actuators, B: Chemical* **2007**. https://doi.org/10.1016/j.snb.2007.04.029.

(272) Yau, H. C. M.; Chan, H. L.; Yang, M. Electrochemical Properties of DNA-Intercalating Doxorubicin and Methylene Blue on n-Hexadecyl Mercaptan-Doped 5′-Thiol-Labeled DNA-Modified Gold Electrodes. *Biosensors and Bioelectronics* **2003**. https://doi.org/10.1016/S0956-5663(02)00161-6.

(273) Gu, J.; Lu, X.; Ju, H. DNA Sensor for Recognition of Native Yeast DNA Sequence with Methylene Blue as an Electrochemical Hybridization Indicator. *Electroanalysis* **2002**. https://doi.org/10.1002/1521-4109(200207)14:13

(274) Reddy, R. R. K.; Chadha, A.; Bhattacharya, E. Porous Silicon Based Potentiometric Triglyceride Biosensor. *Biosensors and Bioelectronics* **2001**. https://doi.org/10.1016/S0956-5663(01)00129-4.

(275) Kara, P.; Kerman, K.; Ozkan, D.; Meric, B.; Erdem, A.; Ozkan, Z.; Ozsoz, M. Electrochemical Genosensor for the Detection of Interaction between Methylene Blue and DNA. *Electrochemistry Communications* **2002**. https://doi.org/10.1016/S1388-2481(02)00428-9.

(276) Lucarelli, F.; Tombelli, S.; Minunni, M.; Marrazza, G.; Mascini, M. Electrochemical and Piezoelectric DNA Biosensors for Hybridisation Detection. *Analytica Chimica Acta* **2008**. https://doi.org/10.1016/j.aca.2007.12.035.

(277) Wang, J. Electrochemical Nucleic Acid Biosensors. *Analytica Chimica Acta* **2002**, *469*, 63–71. https://doi.org/10.1016/S0003-2670(01)01399-X.

(278) Chrisey, L. A.; Lee, G. U.; O'Ferrall, C. E. Covalent Attachment of Synthetic DNA to Self-Assembled Monolayer Films. *Nucleic Acids Research* **1996**. https://doi.org/10.1093/nar/24.15.3031.

(279) Wang, J. From DNA Biosensors to Gene Chips. *Nucleic Acids Research* **2000**. https://doi.org/10.1093/nar/28.16.3011

(280) Marrazza, G.; Chianella, I.; Mascini, M. Disposable DNA Electrochemical Sensor for Hybridization Detection. *Biosensors and Bioelectronics* **1999**. https://doi.org/10.1016/S0956-5663(98)00102-X.

(281) Lee, J.; Morita, M.; Takemura, K.; Park, E. Y. A Multi-Functional Gold/Iron-Oxide

Nanoparticle-CNT Hybrid Nanomaterial as Virus DNA Sensing Platform. *Biosensors and Bioelectronics* **2018**. https://doi.org/10.1016/j.bios.2017.11.052.

(282) Shariati, M.; Ghorbani, M.; Sasanpour, P.; Karimizefreh, A. An Ultrasensitive Label Free Human Papilloma Virus DNA Biosensor Using Gold Nanotubes Based on Nanoporous Polycarbonate in Electrical Alignment. *Analytica Chimica Acta* **2019**. https://doi.org/10.1016/j.aca.2018.09.062.

(283) Xu, J.; Jiang, B.; Su, J.; Xiang, Y.; Yuan, R.; Chai, Y. Background Current Reduction and Biobarcode Amplification for Label-Free, Highly Sensitive Electrochemical Detection of Pathogenic DNA. *Chemical Communications* **2012**. https://doi.org/10.1039/c2cc18107j.

(284) Khater, M.; de la Escosura-Muñiz, A.; Quesada-González, D.; Merkoçi, A. Electrochemical Detection of Plant Virus Using Gold Nanoparticle-Modified Electrodes. *Analytica Chimica Acta* **2019**. https://doi.org/10.1016/j.aca.2018.09.031.

(285) Singhal, C.; Dubey, A.; Mathur, A.; Pundir, C. S.; Narang, J. Paper Based DNA Biosensor for Detection of Chikungunya Virus Using Gold Shells Coated Magnetic Nanocubes. *Process Biochemistry* **2018**. https://doi.org/10.1016/j.procbio.2018.08.020.

(286) Xiang, Y.; Zhang, H.; Jiang, B.; Chai, Y.; Yuan, R. Quantum Dot Layer-by-Layer Assemblies as Signal Amplification Labels for Ultrasensitive Electronic Detection of Uropathogens. *Analytical Chemistry* **2011**. https://doi.org/10.1021/ac200564r.

(287) Iftikhar, T.; Asif, M.; Aziz, A.; Ashraf, G.; Jun, S.; Li, G.; Liu, H. Topical Advances in Nanomaterials Based Electrochemical Sensors for Resorcinol Detection. *Trends in Environmental Analytical Chemistry*. **2021**. https://doi.org/10.1016/j.teac.2021.e00138.

(288) Aziz, A.; Asif, M.; Ashraf, G.; Azeem, M.; Majeed, I.; Ajmal, M.; Wang, J.; Liu, H. Advancements in Electrochemical Sensing of Hydrogen Peroxide, Glucose and Dopamine by Using 2D Nanoarchitectures of Layered Double Hydroxides or Metal Dichalcogenides. A Review. *Microchimica Acta*. **2019**. https://doi.org/10.1007/s00604-019-3776-z.

(289) Dral, A. P.; ten Elshof, J. E. 2D Metal Oxide Nanoflakes for Sensing Applications: Review and Perspective. *Sensors and Actuators, B: Chemical*. **2018**. https://doi.org/10.1016/j.snb.2018.05.157.

(290) Asamoah, B. O.; Uurasjärvi, E.; Räty, J.; Koistinen, A.; Roussey, M.; Peiponen, K. E. Towards the Development of Portable and in Situ Optical Devices for Detection of Micro and Nanoplastics in Water: A Review on the Current Status. *Polymers* **2021**. https://doi.org/10.3390/polym13050730.

(291) Xu, K.; Lu, Y.; Takei, K. Multifunctional Skin-Inspired Flexible Sensor Systems for Wearable Electronics. *Advanced Materials Technologies* **2019**. https://doi.org/10.1002/admt.201800628.

(292) Asif, M.; Xu, Y.; Xiao, F.; Sun, Y. Diagnosis of COVID-19, Vitality of Emerging Technologies and Preventive Measures. *Chemical Engineering Journal* **2021**. https://doi.org/10.1016/j.cej.2021.130189.

(293) Zhang, Z.; Pan, P.; Liu, X.; Yang, Z.; Wei, J.; Wei, Z. 3D-Copper Oxide and Copper Oxide/Few-Layer Graphene with Screen Printed Nanosheet Assembly for Ultrasensitive Non-Enzymatic Glucose Sensing. *Materials Chemistry and Physics* **2017**. https://doi.org/10.1016/j.matchemphys.2016.11.032.

(294) Guo, Y.; Zhong, M.; Fang, Z.; Wan, P.; Yu, G. A Wearable Transient Pressure Sensor Made with MXene Nanosheets for Sensitive Broad-Range Human-Machine Interfacing. *Nano Letters* **2019**. https://doi.org/10.1021/acs.nanolett.8b04514.

(295) Cheng, Y.; Ma, Y.; Li, L.; Zhu, M.; Yue, Y.; Liu, W.; Wang, L.; Jia, S.; Li, C.; Qi, T.; Wang, J.; Gao, Y. Bioinspired Microspines for a High-Performance Spray Ti3C2Tx MXene-Based Piezoresistive Sensor. *American Chemical Society Nano* **2020**. https://doi.org/10.1021/acsnano.9b08952.

(296) Wang, Z.; Gao, W.; Zhang, Q.; Zheng, K.; Xu, J.; Xu, W.; Shang, E.; Jiang, J.; Zhang, J.; Liu, Y. 3D-Printed Graphene/Polydimethylsiloxane Composites for Stretchable and Strain-Insensitive Temperature Sensors. *American Chemical Society Applied Materials & Interfaces* **2019**. https://doi.org/10.1021/acsami.8b16139.

(297) Credi, A. Nanomachines. Fundamentals and Applications. By Joseph Wang. *Angewandte Chemie International Edition* **2014**. https://doi.org/10.1002/anie.201311274.

(298) Wang, J.; Gao, W. Nano/Microscale Motors: Biomedical Opportunities and Challenges. *American Chemical Society Nano* **2012**. https://doi.org/10.1021/nn3028997.

(299) Gao, W.; Kagan, D.; Pak, O. S.; Clawson, C.; Campuzano, S.; Chuluun-Erdene, E.; Shipton, E.; Fullerton, E. E.; Zhang, L.; Lauga, E.; Wang, J. Cargo-Towing Fuel-Free Magnetic Nanoswimmers for Targeted Drug Delivery. *Small* **2012**. https://doi.org/10.1002/smll.201101909.

(300) Jurado-Sánchez, B.; Escarpa, A. Milli, Micro and Nanomotors: Novel Analytical Tools for Real-World Applications. *TrAC - Trends in Analytical Chemistry* **2016**. https://doi.org/10.1016/j.trac.2016.03.009.

(301) Jurado-Sánchez, B.; Escarpa, A. Janus Micromotors for Electrochemical Sensing and Biosensing Applications: A Review. *Electroanalysis* **2017**. https://doi.org/10.1002/elan.201600567.

(302) Jurado-Sánchez, B.; Pacheco, M.; Maria-Hormigos, R.; Escarpa, A. Perspectives on Janus Micromotors: Materials and Applications. *Applied Materials Today* **2017**. https://doi.org/10.1016/j.apmt.2017.09.005.

(303) Orozco, J.; García-Gradilla, V.; D'Agostino, M.; Gao, W.; Cortés, A.; Wang, J. Artificial Enzyme-Powered Microfish for Water-Quality Testing. *American Chemical Society Nano* **2013**. https://doi.org/10.1021/nn305372n.

(304) Singh, V. V.; Kaufmann, K.; Orozco, J.; Li, J.; Galarnyk, M.; Arya, G.; Wang, J. Micromotor-Based on-off Fluorescence Detection of Sarin and Soman Simulants. *Chemical Communications* **2015**. https://doi.org/10.1039/c5cc04120a.

(305) Yuan, Y.; Gao, C.; Wang, D.; Zhou, C.; Zhu, B.; He, Q. Janus-Micromotor-Based on-

off Luminescence Sensor for Active TNT Detection. *Beilstein Journal of Nanotechnology* **2019**. https://doi.org/10.3762/BJNANO.10.131.

(306) Yang, W.; Li, J.; Xu, Z.; Yang, J.; Liu, Y.; Liu, L. A Eu-MOF/EDTA-NiAl-CLDH Fluorescent Micromotor for Sensing and Removal of Fe3+ from Water. *Journal of Materials Chemistry C* **2019**. https://doi.org/10.1039/c9tc03328a.

(307) Cai, L.; Xu, D.; Zhang, Z.; Li, N.; Zhao, Y. Tailoring Functional Micromotors for Sensing. *Research* **2023**. https://doi.org/10.34133/research.0044.

(308) Liu, M.; Sun, Y.; Wang, T.; Ye, Z.; Zhang, H.; Dong, B.; Li, C. Y. A Biodegradable, All-Polymer Micromotor for Gas Sensing Applications. *Journal of Materials Chemistry C* **2016**. https://doi.org/10.1039/c6tc00971a.

(309) Solovev, A. A.; Sanchez, S.; Pumera, M.; Mei, Y. F.; Schmidt, O. C. Magnetic Control of Tubular Catalytic Microbots for the Transport, Assembly, and Delivery of Micro-Objects. *Advanced Functional Materials* **2010**. https://doi.org/10.1002/adfm.200902376.

(310) Solovev, A. A.; Mei, Y.; Schmidt, O. G. Catalytic Microstrider at the Air-Liquid Interface. *Advanced Materials* **2010**. https://doi.org/10.1002/adma.201001468.

(311) Sanchez, S.; Solovev, A. A.; Harazim, S. M.; Schmidt, O. G. Microbots Swimming in the Flowing Streams of Microfluidic Channels. *Journal of the American Chemical Society* **2011**. https://doi.org/10.1021/ja109627w.

(312) Orozco, J.; Cortés, A.; Cheng, G.; Sattayasamitsathit, S.; Gao, W.; Feng, X.; Shen, Y.; Wang, J. Molecularly Imprinted Polymer-Based Catalytic Micromotors for Selective Protein Transport. *Journal of the American Chemical Society* **2013**. https://doi.org/10.1021/ja4018545.

(313) Orozco, J.; Pan, G.; Sattayasamitsathit, S.; Galarnyk, M.; Wang, J. Micromotors to Capture and Destroy Anthrax Simulant Spores. *Analyst* **2015**. https://doi.org/10.1039/c4an02169j.

(314) Wang, J.; Deo, R. P.; Musameh, M. Stable and Sensitive Electrochemical Detection of Phenolic Compounds at Carbon Nanotube Modified Glassy Carbon Electrodes. *Electroanalysis* **2003**. https://doi.org/10.1002/elan.200302772.

(315) Rohaizad, N.; Mayorga-Martinez, C. C.; Fojtů, M.; Latiff, N. M.; Pumera, M. Two-Dimensional Materials in Biomedical, Biosensing and Sensing Applications. *Chemical Society Reviews* **2020**. https://doi.org/10.1039/d0cs00150c.

(316) Achilli, G.; Piero Cellerino, G.; Melzi d'Eril, G.; Bird, S. Simultaneous Determination of 27 Phenols and Herbicides in Water by High-Performance Liquid Chromatography with Multielectrode Electrochemical Detection. *Journal of Chromatography A* **1995**. https://doi.org/10.1016/0021-9673(94)00791-7.

(317) Hilmi, A.; Luong, J. H. T.; Nguyen, A. L. Applicability of Capillary Electrophoresis with Amperometric Detection to Study Degradation of Chlorophenols in Contaminated Soil. *Environmental Science and Technology* **1997**. https://doi.org/10.1021/es9608914.

(318) Crespín, M. A.; Gallego, M.; Valcarcel, M. Solid-Phase Extraction Method for the Determination of Free and Conjugated Phenol Compounds in Human Urine. *Journal of Chromatography B: Analytical Technologies in the Biomedical and Life Sciences* **2002**. https://doi.org/10.1016/S1570-0232(02)00012-0.

(319) Singh, S.; Kumar, N.; Kumar, M.; Jyoti; Agarwal, A.; Mizaikoff, B. Electrochemical Sensing and Remediation of 4-Nitrophenol Using Bio-Synthesized Copper Oxide Nanoparticles. *Chemical Engineering Journal* **2017**. https://doi.org/10.1016/j.cej.2016.12.049.

(320) Singh, S.; Kumar, N.; Meena, V. K.; Kranz, C.; Mishra, S. Impedometric Phenol Sensing Using Graphenated Electrochip. *Sensors and Actuators, B: Chemical* **2016**. https://doi.org/10.1016/j.snb.2016.06.079.

(321) Terashima, C.; Rao, T. N.; Sarada, B. V.; Tryk, D. A.; Fujishima, A. Electrochemical Oxidation of Chlorophenols at a Boron-Doped Diamond Electrode and Their Determination by High-Performance Liquid Chromatography with Amperometric Detection. *Analytical Chemistry* **2002**. https://doi.org/10.1021/ac010681w.

(322) Wang, J.; Lin, M. S. In Situ Electrochemical Renewal of Glassy Carbon Electrodes. *Analytical Chemistry* **1988**. https://doi.org/10.1021/ac00156a026.

(323) Wang, J.; Chatrathi, M. P.; Mulchandani, A.; Chen, W. Capillary Electrophoresis Microchips for Separation and Detection of Organophosphate Nerve Agents. *Analytical Chemistry* **2001**. https://doi.org/10.1021/ac001424e.

(324) Browne, M. P.; Novotný, F.; Sofer, Z.; Pumera, M. 3D Printed Graphene Electrodes' Electrochemical Activation. *American Chemical Society Applied Materials & Interfaces* **2018**. https://doi.org/10.1021/acsami.8b14701.

(325) Redondo, E.; Ng, S.; Muñoz, J.; Pumera, M. Tailoring Capacitance of 3D-Printed Graphene Electrodes by Carbonisation Temperature. *Nanoscale* **2020**. https://doi.org/10.1039/d0nr04864j.

(326) Manzanares Palenzuela, C. L.; Novotný, F.; Krupička, P.; Sofer, Z.; Pumera, M. 3D-Printed Graphene/Polylactic Acid Electrodes Promise High Sensitivity in Electroanalysis. *Analytical Chemistry* **2018**. https://doi.org/10.1021/acs.analchem.8b00083.

(327) Manzanares-Palenzuela, C. L.; Hermanova, S.; Sofer, Z.; Pumera, M. Proteinase-Sculptured 3D-Printed Graphene/Polylactic Acid Electrodes as Potential Biosensing Platforms: Towards Enzymatic Modeling of 3D-Printed Structures. *Nanoscale* **2019**, *11*, 12124–12131. https://doi.org/10.1039/c9nr02754h.

(328) Singh, R.; Garg, H. K. Fused Deposition Modeling – A State of Art Review and Future Applications. In Reference Module in *Materials Science and Materials Engineering* **2016**. https://doi.org/10.1016/b978-0-12-803581-8.04037-6.

(329) Daminabo, S. C.; Goel, S.; Grammatikos, S. A.; Nezhad, H. Y.; Thakur, V. K. Fused Deposition Modeling-Based Additive Manufacturing (3D Printing): Techniques for Polymer Material Systems. *Materials Today Chemistry* **2020**. https://doi.org/10.1016/j.mtchem.2020.100248.

(330) Muñoz, J.; Redondo, E.; Pumera, M. Bistable (Supra)Molecular Switches on 3D-Printed Responsive Interfaces with Electrical Readout. *American Chemical Society Applied Materials & Interfaces* **2020**. https://doi.org/10.1021/acsami.0c14487.

(331) Tian, M.; Thind, S. S.; Dondapati, J. S.; Li, X.; Chen, A. Electrochemical Oxidation of 4-Chlorophenol for Wastewater Treatment Using Highly Active UV Treated TiO2 Nanotubes. *Chemosphere* **2018**. https://doi.org/10.1016/j.chemosphere.2018.06.042.

(332) Pintar, A.; Levec, J. Catalytic Oxidation of Aqueous P-Chlorophenol and p-Nitrophenol Solutions. *Chemical Engineering Science* **1994**. https://doi.org/10.1016/S0009-2509(05)80029-6.

(333) Hanai, T.; Koizumi, K.; Kinoshita, T.; Arora, R.; Ahmed, F. Prediction of PK(a) Values of Phenolic and Nitrogen-Containing Compounds by Computational Chemical Analysis Compared to Those Measured by Liquid Chromatography. In *Journal of Chromatography A* **1997**. https://doi.org/10.1016/S0021-9673(96)01009-6.

(334) Ureta-Zaartu, S. S.; Bustos, P.; Diez, M. C.; Mora, M. L.; Gutiérrez, C. Electro-Oxidation of Chlorophenols at a Gold Electrode. *Electrochimica Acta* **2001**. https://doi.org/10.1016/S0013-4686(01)00448-0.

(335) Cheng, T. S.; Nasir, M. Z. M.; Ambrosi, A.; Pumera, M. 3D-Printed Metal Electrodes for Electrochemical Detection of Phenols. *Applied Materials Today* **2017**. https://doi.org/10.1016/j.apmt.2017.07.005.

(336) Ensafi, A. A.; Heydari-Bafrooei, E.; Rezaei, B. Simultaneous Detection of Hydroxylamine and Phenol Using P-Aminophenol-Modified Carbon Nanotube Paste Electrode. *Cuihua Xuebao/Chinese Journal of Catalysis* **2013**. https://doi.org/10.1016/s1872-2067(12)60652-4.

(337) Tan, C.; Nasir, M. Z. M.; Ambrosi, A.; Pumera, M. 3D Printed Electrodes for Detection of Nitroaromatic Explosives and Nerve Agents. *Analytical Chemistry* **2017**. https://doi.org/10.1021/acs.analchem.7b01614.

(338) Wang, L.; Gao, W.; Ng, S.; Pumera, M. Chiral Protein-Covalent Organic Framework 3D-Printed Structures as Chiral Biosensors. *Analytical Chemistry* **2021**. https://doi.org/10.1021/acs.analchem.1c00322.

(339) Gao, W.; Pumera, M. 3D Printed Nanocarbon Frameworks for Li-Ion Battery Cathodes. *Advanced Functional Materials* **2021**. https://doi.org/10.1002/adfm.202007285.

(340) Wang, J.; Pumera, M.; Chatrathi, M. P.; Escarpa, A.; Musameh, M.; Collins, G.; Mulchandani, A.; Lin, Y.; Olsen, K. Single-Channel Microchip for Fast Screening and Detailed Identification of Nitroaromatic Explosives or Organophosphate Nerve Agents. *Analytical Chemistry* **2002**. https://doi.org/10.1021/ac0111356.

(341) Vucinic, S.; Antonijevic, B.; Tsatsakis, A. M.; Vassilopoulou, L.; Docea, A. O.; Nosyrev, A. E.; Izotov, B. N.; Thiermann, H.; Drakoulis, N.; Brkic, D. Environmental Exposure to Organophosphorus Nerve Agents. *Environmental Toxicology and Pharmacology* **2017**. https://doi.org/10.1016/j.etap.2017.09.004.

(342) Gupta, R. Toxicology of Organophosphate & Carbamate Compounds. In *Toxicology of*

Organophosphate & Carbamate Compounds; **2006**. https://doi.org/10.1016/B978-0-12-088523-7.X5000-5.

(343) Rossi, S.; Dalpero, A. P.; Ghini, S.; Colombo, R.; Sabatini, A. G.; Girotti, S. Multiresidual Method for the Gas Chromatographic Analysis of Pesticides in Honeybees Cleaned by Gel Permeation Chromatography. *Journal of Chromatography A* **2001**. https://doi.org/10.1016/S0021-9673(00)00928-6.

(344) Diagne, R. G.; Foster, G. D.; Khan, S. U. Comparison of Soxhlet and Microwave-Assisted Extractions for the Determination of Fenitrothion Residues in Beans. *Journal of Agricultural and Food Chemistry* **2002**. https://doi.org/10.1021/jf011469w.

(345) Tuan, S. J.; Tsai, H. M.; Hsu, S. M.; Li, H. P. Multiresidue Analysis of 176 Pesticides and Metabolites in Pre-Harvested Fruits and Vegetables for Ensuring Food Safety by Gas Chromatography and High Performance Liquid Chromatography. *Journal of Food and Drug Analysis* **2009**. https://doi.org/10.38212/2224-6614.2611.

(346) Fernández, M.; Picó, Y.; Girotti, S.; Mañes, J. Analysis of Organophosphorus Pesticides in Honeybee by Liquid Chromatography-Atmospheric Pressure Chemical Ionization-Mass Spectrometry. *Journal of Agricultural and Food Chemistry* **2001**. https://doi.org/10.1021/jf010238m.

(347) Mol, H. G. J.; Van Dam, R. C. J.; Steijger, O. M. Determination of Polar Organophosphorus Pesticides in Vegetables and Fruits Using Liquid Chromatography with Tandem Mass Spectrometry: Selection of Extraction Solvent. *Journal of Chromatography A* **2003**. https://doi.org/10.1016/S0021-9673(03)01209-3.

(348) Geremedhin, W.; Amare, M.; Admassie, S. Electrochemically Pretreated Glassy Carbon Electrode for Electrochemical Detection of Fenitrothion in Tap Water and Human Urine. *Electrochimica Acta* **2013**. https://doi.org/10.1016/j.electacta.2012.09.046.

(349) Nasir, M. Z. M.; Mayorga-Martinez, C. C.; Sofer, Z.; Pumera, M. Two-Dimensional 1T-Phase Transition Metal Dichalcogenides as Nanocarriers to Enhance and Stabilize Enzyme Activity for Electrochemical Pesticide Detection. *American Chemical Society Nano* **2017**. https://doi.org/10.1021/acsnano.7b01364.

(350) Gong, J.; Miao, X.; Wan, H.; Song, D. Facile Synthesis of Zirconia Nanoparticles-Decorated Graphene Hybrid Nanosheets for an Enzymeless Methyl Parathion Sensor. *Sensors and Actuators, B: Chemical* **2012**. https://doi.org/10.1016/j.snb.2011.12.094.

(351) Gao, N.; He, C.; Ma, M.; Cai, Z.; Zhou, Y.; Chang, G.; Wang, X.; He, Y. Electrochemical Co-Deposition Synthesis of Au-ZrO2-Graphene Nanocomposite for a Nonenzymatic Methyl Parathion Sensor. *Analytica Chimica Acta* **2019**. https://doi.org/10.1016/j.aca.2019.04.043.

(352) Zhu, W.; Liu, W.; Li, T.; Yue, X.; Liu, T.; Zhang, W.; Yu, S.; Zhang, D.; Wang, J. Facile Green Synthesis of Graphene-Au Nanorod Nanoassembly for on-Line Extraction and Sensitive Stripping Analysis of Methyl Parathion. *Electrochimica Acta* **2014**. https://doi.org/10.1016/j.electacta.2014.09.085.

(353) Wu, S.; Lan, X.; Cui, L.; Zhang, L.; Tao, S.; Wang, H.; Han, M.; Liu, Z.; Meng, C. Application of Graphene for Preconcentration and Highly Sensitive Stripping

Voltammetric Analysis of Organophosphate Pesticide. *Analytica Chimica Acta* **2011**. https://doi.org/10.1016/j.aca.2011.05.032.

(354) Du, D.; Chen, W.; Zhang, W.; Liu, D.; Li, H.; Lin, Y. Covalent Coupling of Organophosphorus Hydrolase Loaded Quantum Dots to Carbon Nanotube/Au Nanocomposite for Enhanced Detection of Methyl Parathion. *Biosensors and Bioelectronics* **2010**. https://doi.org/10.1016/j.bios.2009.10.032.

(355) Saleh Ahammad, A. J.; Lee, J. J.; Rahman, M. A. Electrochemical Sensors Based on Carbon Nanotubes. *Sensors* **2009**. https://doi.org/10.3390/s90402289.

(356) Dong, J.; Wang, X.; Qiao, F.; Liu, P.; Ai, S. Highly Sensitive Electrochemical Stripping Analysis of Methyl Parathion at MWCNTs-CeO2-Au Nanocomposite Modified Electrode. *Sensors and Actuators, B: Chemical* **2013**. https://doi.org/10.1016/j.snb.2013.06.068.

(357) de Oliveira, P. R.; Kalinke, C.; Gogola, J. L.; Mangrich, A. S.; Junior, L. H. M.; Bergamini, M. F. The Use of Activated Biochar for Development of a Sensitive Electrochemical Sensor for Determination of Methyl Parathion. *Journal of Electroanalytical Chemistry* **2017**. https://doi.org/10.1016/j.jelechem.2017.06.020.

(358) Bazuła, P. A.; Lu, A. H.; Nitz, J. J.; Schüth, F. Surface and Pore Structure Modification of Ordered Mesoporous Carbons via a Chemical Oxidation Approach. *Microporous and Mesoporous Materials* **2008**. https://doi.org/10.1016/j.micromeso.2007.04.008.

(359) Liu, R.; Wang, Y.; Li, B.; Liu, B.; Ma, H.; Li, D.; Dong, L.; Li, F.; Chen, X.; Yin, X. VXC-72R/ZrO2/GCE-Based Electrochemical Sensor for the High-Sensitivity Detection of Methyl Parathion. *Materials* **2019**. https://doi.org/10.3390/ma12213637.

(360) Gannavarapu, K. P.; Ganesh, V.; Thakkar, M.; Mitra, S.; Dandamudi, R. B. Nanostructured Diatom-ZrO2 Composite as a Selective and Highly Sensitive Enzyme Free Electrochemical Sensor for Detection of Methyl Parathion. *Sensors and Actuators, B: Chemical* **2019**. https://doi.org/10.1016/j.snb.2019.03.036.

(361) Ng, S.; Iffelsberger, C.; Michalička, J.; Pumera, M. Atomic Layer Deposition of Electrocatalytic Insulator Al2O3on Three-Dimensional Printed Nanocarbons. *American Chemical Society Nano* **2021**. https://doi.org/10.1021/acsnano.0c06961.

(362) Redondo, E.; Muñoz, J.; Pumera, M. Green Activation Using Reducing Agents of Carbon-Based 3D Printed Electrodes: Turning Good Electrodes to Great. *Carbon* **2021**. https://doi.org/10.1016/j.carbon.2021.01.107.

(363) Wirth, D. M.; Sheaff, M. J.; Waldman, J. V.; Symcox, M. P.; Whitehead, H. D.; Sharp, J. D.; Doerfler, J. R.; Lamar, A. A.; Leblanc, G. Electrolysis Activation of Fused-Filament-Fabrication 3D-Printed Electrodes for Electrochemical and Spectroelectrochemical Analysis. *Analytical Chemistry* **2019**. https://doi.org/10.1021/acs.analchem.9b01331.

(364) Novotný, F.; Urbanová, V.; Plutnar, J.; Pumera, M. Preserving Fine Structure Details and Dramatically Enhancing Electron Transfer Rates in Graphene 3D-Printed Electrodes via Thermal Annealing: Toward Nitroaromatic Explosives Sensing. *American Chemical Society Applied Materials & Interfaces* **2019**.

https://doi.org/10.1021/acsami.9b06683.

(365) Browne, M. P.; Novotný, F.; Sofer, Z.; Pumera, M. 3D Printed Graphene Electrodes' Electrochemical Activation. *American Chemical Society Applied Materials & Interfaces* **2018**. https://doi.org/10.1021/acsami.8b14701.

(366) Browne, M. P.; Urbanova, V.; Plutnar, J.; Novotný, F.; Pumera, M. Inherent Impurities in 3D-Printed Electrodes Are Responsible for Catalysis towards Water Splitting. *Journal of Materials Chemistry A* **2020**. https://doi.org/10.1039/c9ta11949c.

(367) Browne, M. P.; Pumera, M. Impurities in Graphene/PLA 3D-Printing Filaments Dramatically Influence the Electrochemical Properties of the Devices. *Chemical Communications* **2019**. https://doi.org/10.1039/c9cc03774h.

(368) Tan, X.; Liu, Y.; Zhang, T.; Luo, S.; Liu, X.; Tian, H.; Yang, Y.; Chen, C. Ultrasensitive Electrochemical Detection of Methyl Parathion Pesticide Based on Cationic Water-Soluble Pillar[5]Arene and Reduced Graphene Nanocomposite. *Royal Society of Chemistry Advances* **2019**. https://doi.org/10.1039/C8RA08555B.

(369) Ma, B.; Cheong, L. Z.; Weng, X.; Tan, C. P.; Shen, C. Lipase@ZIF-8 Nanoparticles-Based Biosensor for Direct and Sensitive Detection of Methyl Parathion. *Electrochimica Acta* **2018**. https://doi.org/10.1016/j.electacta.2018.06.176.

(370) Pan, D.; Ma, S.; Bo, X.; Guo, L. Electrochemical Behavior of Methyl Parathion and Its Sensitive Determination at a Glassy Carbon Electrode Modified with Ordered Mesoporous Carbon. *Microchimica Acta* **2011**. https://doi.org/10.1007/s00604-011-0551-1.

(371) Thota, R.; Ganesh, V. Selective and Sensitive Electrochemical Detection of Methyl Parathion Using Chemically Modified Overhead Projector Sheets as Flexible Electrodes. *Sensors and Actuators, B: Chemical* **2016**. https://doi.org/10.1016/j.snb.2015.12.008.

(372) Chua, C. K.; Pumera, M. Influence of Methyl Substituent Position on Redox Properties of Nitroaromatics Related to 2,4,6-Trinitrotoluene. *Electroanalysis* **2011**. https://doi.org/10.1002/elan.201100359.

(373) Chua, C. K.; Pumera, M.; Rulíšek, L. Reduction Pathways of 2,4,6-Trinitrotoluene: An Electrochemical and Theoretical Study. *Journal of Physical Chemistry C* **2012**. https://doi.org/10.1021/jp209631x.

(374) Shams, N.; Lim, H. N.; Hajian, R.; Yusof, N. A.; Abdullah, J.; Sulaiman, Y.; Ibrahim, I.; Huang, N. M. Electrochemical Sensor Based on Gold Nanoparticles/Ethylenediamine-Reduced Graphene Oxide for Trace Determination of Fenitrothion in Water. *Royal Society of Chemistry Advances* **2016**. https://doi.org/10.1039/c6ra13384c.

(375) Chowdhury, D. R.; Spiccia, L.; Amritphale, S. S.; Paul, A.; Singh, A. A Robust Iron Oxyhydroxide Water Oxidation Catalyst Operating under near Neutral and Alkaline Conditions. *Journal of Materials Chemistry A* **2016**. https://doi.org/10.1039/c6ta00313c.

(376) Lin, Y.; Zhang, R. Liquid Chromatography Series Dual-electrode Amperometric Detection for Aromatic Nitro Compounds. *Electroanalysis* **1994**. https://doi.org/10.1002/elan.1140061135.

(377) Liu, G.; Lin, Y. Electrochemical Stripping Analysis of Organophosphate Pesticides and Nerve Agents. *Electrochemistry Communications* **2005**. https://doi.org/10.1016/j.elecom.2005.02.002.

(378) Wang, L.; Dong, J.; Wang, Y.; Cheng, Q.; Yang, M.; Cai, J.; Liu, F. Novel Signal-Amplified Fenitrothion Electrochemical Assay, Based on Glassy Carbon Electrode Modified with Dispersed Graphene Oxide. *Scientific Reports* **2016** https://doi.org/10.1038/srep23409.

(379) Zhang, C.; Bills, B. J.; Manicke, N. E. Rapid Prototyping Using 3D Printing in Bioanalytical Research. *Bioanalysis* **2017**. https://doi.org/10.4155/bio-2016-0293.

(380) Li, J.; Pumera, M. 3D Printing of Functional Microrobots. *Chemical Society Reviews* **2021**. https://doi.org/10.1039/d0cs01062f.

(381) Loo, A. H.; Chua, C. K.; Pumera, M. DNA Biosensing with 3D Printing Technology. *Analyst* **2017**. https://doi.org/10.1039/c6an02038k.

(382) Abdalla, A.; Patel, B. A. 3D-Printed Electrochemical Sensors: A New Horizon for Measurement of Biomolecules. *Current Opinion in Electrochemistry* **2020**. https://doi.org/10.1016/j.coelec.2020.04.009.

(383) Walter, A.; Wu, J.; Flechsig, G. U.; Haake, D. A.; Wang, J. Redox Cycling Amplified Electrochemical Detection of DNA Hybridization: Application to Pathogen E. Coli Bacterial RNA. *Analytica Chimica Acta* **2011**. https://doi.org/10.1016/j.aca.2011.01.014.

(384) Berti, F.; Laschi, S.; Palchetti, I.; Rossier, J. S.; Reymond, F.; Mascini, M.; Marrazza, G. Microfluidic-Based Electrochemical Genosensor Coupled to Magnetic Beads for Hybridization Detection. *Talanta* **2009**. https://doi.org/10.1016/j.talanta.2008.07.064.

(385) Erdem, A.; Congur, G.; Eksin, E. Multi Channel Screen Printed Array of Electrodes for Enzyme-Linked Voltammetric Detection of MicroRNAs. *Sensors and Actuators, B: Chemical* **2013**. https://doi.org/10.1016/j.snb.2013.07.114.

(386) Fojta, M.; Brázdilová, P.; Cahová, K.; Pečinka, P. A Single-Surface Electrochemical Biosensor for the Detection of DNA Triplet Repeat Expansion. *Electroanalysis* **2006**. https://doi.org/10.1002/elan.200503379.

(387) Horáková, P.; Šimková, E.; Vychodilová, Z.; Brázdová, M.; Fojta, M. Detection of Single Nucleotide Polymorphisms in P53 Mutation Hotspots and Expression of Mutant P53 in Human Cell Lines Using an Enzyme-Linked Electrochemical Assay. *Electroanalysis* **2009**. https://doi.org/10.1002/elan.200904656.

(388) Horakova-Brazdilova, P.; Fojtova, M.; Vytras, K.; Fojta, M. Enzyme-Linked Electrochemical Detection of PCR-Amplified Nucleotide Sequences Using Disposable Screen-Printed Sensors. Applications in Gene Expression Monitoring. *Sensors* **2008**. https://doi.org/10.3390/s8010193.

(389) Li, Q.; Cheng, W.; Zhang, D.; Yu, T.; Yin, Y.; Ju, H.; Ding, S. Rapid and Sensitive Strategy for Salmonella Detection Using an InvA Gene-Based Electrochemical DNA Sensor. *International Journal of Electrochemical Science* **2012**.

(390) Rochelet-Dequaire, M.; Djellouli, N.; Limoges, B.; Brossier, P. Bienzymatic-Based Electrochemical DNA Biosensors: A Way to Lower the Detection Limit of Hybridization Assays. *Analyst* **2009**. https://doi.org/10.1039/b816220d.

(391) Stejskalová, E.; Horáková, P.; Vacek, J.; Bowater, R. P.; Fojta, M. Enzyme-Linked Electrochemical DNA Ligation Assay Using Magnetic Beads. *Analytical and Bioanalytical Chemistry* **2014**. https://doi.org/10.1007/s00216-014-7811-y.

(392) Liu, G.; Lao, R.; Xu, L.; Xu, Q.; Li, L.; Zhang, M.; Shen, H.; Mathur, S.; Fan, C.; Song, S. Detection of Single-Nucleotide Polymorphism on UidA Gene of Escherichia Coli by a Multiplexed Electrochemical DNA Biosensor with Oligonucleotide-Incorporated Nonfouling Surface. *Sensors* **2011**. https://doi.org/10.3390/s110808018.

(393) Rochelet, M.; Solanas, S.; Grossiord, C.; Maréchal, P.; Résa, C.; Vienney, F.; Barranger, C.; Joannes, M. A Thin Layer-Based Amperometric Enzyme Immunoassay for the Rapid and Sensitive Diagnosis of Respiratory Syncytial Virus Infections. *Talanta* **2012**. https://doi.org/10.1016/j.talanta.2012.07.088.

(394) Hajdukiewicz, J.; Boland, S.; Kavanagh, P.; Leech, D. An Enzyme-Amplified Amperometric DNA Hybridisation Assay Using DNA Immobilised in a Carboxymethylated Dextran Film Anchored to a Graphite Surface. *Biosensors and Bioelectronics* **2010**. https://doi.org/10.1016/j.bios.2009.09.020.

(395) Carneiro, O. S.; Silva, A. F.; Gomes, R. Fused Deposition Modeling with Polypropylene. *Materials and Design* **2015**. https://doi.org/10.1016/j.matdes.2015.06.053.

(396) Wang, J.; Kawde, A. N.; Musameh, M. Carbon-Nanotube-Modified Glassy Carbon Electrodes for Amplified Label-Free Electrochemical Detection of DNA Hybridization. *Analyst* **2003**. https://doi.org/10.1039/b303282e.

(397) Paleček, E.; Fojta, M.; Jelen, F. New Approaches in the Development of DNA Sensors: Hybridization and Electrochemical Detection of DNA and RNA at Two Different Surfaces. In *Bioelectrochemistry* **2002**. https://doi.org/10.1016/S1567-5394(02)00025-7.

(398) Wang, J.; Kawde, A. N.; Erdem, A.; Salazar, M. Magnetic Bead-Based Label-Free Electrochemical Detection of DNA Hybridization. *Analyst* **2001**. https://doi.org/10.1039/b106343j.

(399) Wang, J.; Kawde, A. N. Amplified Label-Free Electrical Detection of DNA Hybridization. *Analyst* **2002**. https://doi.org/10.1039/b110821m.

(400) Špaček, J.; Eksin, E.; Havran, L.; Erdem, A.; Fojta, M. Fast Enzyme-Linked Electrochemical Sensing of DNA Hybridization at Pencil Graphite Electrodes. Application to Detect Gene Deletion in a Human Cell Culture. *Journal of Electroanalytical Chemistry* **2020**. https://doi.org/10.1016/j.jelechem.2020.113951.

(401) Palek, E.; Fojta, M. Peer Reviewed: Detecting DNA Hybridization and Damage. *Analytical Chemistry* **2001**. https://doi.org/10.1021/ac0123936.

(402) Hasoň, S.; Pivoňková, H.; Vetterl, V.; Fojta, M. Label-Free Sequence-Specific DNA Sensing Using Copper-Enhanced Anodic Stripping of Purine Bases at Boron-Doped Diamond Electrodes. *Analytical Chemistry* **2008**. https://doi.org/10.1021/ac7019305.

(403) Thrimurthulu, K.; Pandey, P. M.; Reddy, N. V. Optimum Part Deposition Orientation in Fused Deposition Modeling. *International Journal of Machine Tools and Manufacture* **2004**. https://doi.org/10.1016/j.ijmachtools.2003.12.004.

(404) Azek, F.; Grossiord, C.; Joannes, M.; Limoges, B.; Brossier, P. Hybridization Assay at a Disposable Electrochemical Biosensor for the Attomole Detection of Amplified Human Cytomegalovirus DNA. *Analytical Biochemistry* **2000**. https://doi.org/10.1006/abio.2000.4692.

(405) Pazy, Y.; Kulik, T.; Bayer, E. A.; Wilchek, M.; Livnah, O. Ligand Exchange between Proteins: Exchange of Biotin and Biotin Derivatives between Avidin and Streptavidin. *Journal of Biological Chemistry* **2002**. https://doi.org/10.1074/jbc.M202874200.

(406) Plucnara, M.; Eksin, E.; Erdem, A.; Fojta, M. Electrochemical Detection of SNP in Human Mitochondrial DNA Using Cyclic Primer Extension with Biotinylated Nucletides and Enzymatic Labeling at Disposable Pencil Graphite Electrodes. *Electroanalysis* **2018**. https://doi.org/10.1002/elan.201800314.

(407) Soler, L.; Magdanz, V.; Fomin, V. M.; Sanchez, S.; Schmidt, O. G. Self-Propelled Micromotors for Cleaning Polluted Water. *American Chemical Society Nano* **2013**. https://doi.org/10.1021/nn405075d.

(408) Maria-Hormigos, R.; Jurado-Sánchez, B.; Escarpa, A. Labs-on-a-Chip Meet Self-Propelled Micromotors. *Lab on a Chip* **2016**. https://doi.org/10.1039/c6lc00467a.

(409) Karshalev, E.; Esteban-Fernández De Ávila, B.; Wang, J. Micromotors for "Chemistry-on-the-Fly." *Journal of the American Chemical Society* **2018**. https://doi.org/10.1021/jacs.8b00088.

(410) Muñoz, J.; Urso, M.; Pumera, M. Self-Propelled Multifunctional Microrobots Harboring Chiral Supramolecular Selectors for "Enantiorecognition-on-the-Fly." *Angewandte Chemie - International Edition* **2022**. https://doi.org/10.1002/anie.202116090.

(411) Liu, W.; Ge, H.; Gu, Z.; Lu, X.; Li, J.; Wang, J. Electrochemical Deposition Tailors the Catalytic Performance of MnO2-Based Micromotors. *Small* **2018**. https://doi.org/10.1002/smll.201802771.

(412) Yuan, K.; Jiang, Z.; Jurado-Sánchez, B.; Escarpa, A. Nano/Micromotors for Diagnosis and Therapy of Cancer and Infectious Diseases. *Chemistry - A European Journal* **2020**. https://doi.org/10.1002/chem.201903475.

(413) Mayorga-Martinez, C. C.; Pumera, M. Self-Propelled Tags for Protein Detection. *Advanced Functional Materials* **2020**. https://doi.org/10.1002/adfm.201906449.

(414) Mayorga-Burrezo, P.; Mayorga-Martinez, C. C.; Pumera, M. Light-Driven Micromotors

to Dissociate Protein Aggregates That Cause Neurodegenerative Diseases. *Advanced Functional Materials* **2022**. https://doi.org/10.1002/adfm.202106699.

(415) Wang, H.; Pumera, M. Coordinated Behaviors of Artificial Micro/Nanomachines: From Mutual Interactions to Interactions with the Environment. *Chemical Society Reviews* **2020**. https://doi.org/10.1039/c9cs00877b.

(416) La Asunción-Nadal, V. de; Pacheco, M.; Jurado-Sánchez, B.; Escarpa, A. Chalcogenides-Based Tubular Micromotors in Fluorescent Assays. *Analytical Chemistry* **2020**. https://doi.org/10.1021/acs.analchem.0c01541.

(417) Yuan, K.; de la Asunción-Nadal, V.; Li, Y.; Jurado-Sánchez, B.; Escarpa, A. Graphdiyne Micromotors in Living Biomedia. *Chemistry - A European Journal* **2020**. https://doi.org/10.1002/chem.202001754.

(418) Esteban-Fernández De Ávila, B.; Martín, A.; Soto, F.; Lopez-Ramirez, M. A.; Campuzano, S.; Vásquez-Machado, G. M.; Gao, W.; Zhang, L.; Wang, J. Single Cell Real-Time MiRNAs Sensing Based on Nanomotors. *American Chemical Society Nano* **2015**. https://doi.org/10.1021/acsnano.5b02807.

(419) Li, M.; Chen, T.; Gooding, J. J.; Liu, J. Review of Carbon and Graphene Quantum Dots for Sensing. *American Chemical Society Sensors* **2019**. https://doi.org/10.1021/acssensors.9b00514.

(420) Ananthanarayanan, A.; Wang, X.; Routh, P.; Sana, B.; Lim, S.; Kim, D. H.; Lim, K. H.; Li, J.; Chen, P. Facile Synthesis of Graphene Quantum Dots from 3D Graphene and Their Application for Fe3+ Sensing. *Advanced Functional Materials* **2014**. https://doi.org/10.1002/adfm.201303441.

(421) Xie, R.; Wang, Z.; Zhou, W.; Liu, Y.; Fan, L.; Li, Y.; Li, X. Graphene Quantum Dots as Smart Probes for Biosensing. *Analytical Methods*. **2016**. https://doi.org/10.1039/c6ay00289g.

(422) Li, L.; Wu, G.; Hong, T.; Yin, Z.; Sun, D.; Abdel-Halim, E. S.; Zhu, J. J. Graphene Quantum Dots as Fluorescence Probes for Turn-off Sensing of Melamine in the Presence of Hg2+. *American Chemical Society Applied Materials & Interfaces* **2014**. https://doi.org/10.1021/am405305r.

(423) Zhao, J.; Zhao, L.; Lan, C.; Zhao, S. Graphene Quantum Dots as Effective Probes for Label-Free Fluorescence Detection of Dopamine. *Sensors and Actuators, B: Chemical* **2016**. https://doi.org/10.1016/j.snb.2015.09.105.

(424) Peng, B.; Chen, L.; Que, C.; Yang, K.; Deng, F.; Deng, X.; Shi, G.; Xu, G.; Wu, M. Adsorption of Antibiotics on Graphene and Biochar in Aqueous Solutions Induced by π-π Interactions. *Scientific Reports* **2016**. https://doi.org/10.1038/srep31920.

(425) McGaughey, G. B.; Gagné, M.; Rappé, A. K. π-Stacking Interactions. Alive and Well in Proteins. *Journal of Biological Chemistry* **1998**. https://doi.org/10.1074/jbc.273.25.15458.

(426) He, S.; Song, B.; Li, D.; Zhu, C.; Qi, W.; Wen, Y.; Wang, L.; Song, S.; Fang, H.; Fan, C. A Craphene Nanoprobe for Rapid, Sensitive, and Multicolor Fluorescent DNA

Analysis. *Advanced Functional Materials* **2010**. https://doi.org/10.1002/adfm.200901639.

(427) Maria-Hormigos, R.; Jurado-Sánchez, B.; Escarpa, A. Graphene Quantum Dot Based Micromotors: A Size Matter. *Chemical Communications* **2019**. https://doi.org/10.1039/c9cc02959a.

(428) Jurado-Sánchez, B.; Pacheco, M.; Rojo, J.; Escarpa, A. Magnetocatalytic Graphene Quantum Dots Janus Micromotors for Bacterial Endotoxin Detection. *Angewandte Chemie - International Edition* **2017**. https://doi.org/10.1002/anie.201701396.

(429) Peter, C.; Meusel, M.; Grawe, F.; Katerkamp, A.; Cammann, K.; Börchers, T. Optical DNA-Sensor Chip for Real-Time Detection of Hybridization Events. *Analytical and Bioanalytical Chemistry* **2001**. https://doi.org/10.1007/s002160101006.

(430) Indrawattana, N.; Promptmas, C.; Wat-Aksorn, K.; Soontornchai, S. Real-Time Monitoring of DNA Hybridization for Rapid Detection of Vibrio Cholerae O1. *Analytical Methods* **2014**. https://doi.org/10.1039/c4ay01162g.

(431) Loo, A. H.; Sofer, Z.; Bouša, D.; Ulbrich, P.; Bonanni, A.; Pumera, M. Carboxylic Carbon Quantum Dots as a Fluorescent Sensing Platform for DNA Detection. *American Chemical Society Applied Materials & Interfaces* **2016**. https://doi.org/10.1021/acsami.5b10160.

(432) Feng, F.; Chen, W.; Chen, D.; Lin, W.; Chen, S. C. In-Situ Ultrasensitive Label-Free DNA Hybridization Detection Using Optical Fiber Specklegram. *Sensors and Actuators, B: Chemical* **2018**. https://doi.org/10.1016/j.snb.2018.05.099.

(433) Ray, P. C.; Darbha, G. K.; Ray, A.; Walker, J.; Hardy, W. Gold Nanoparticle Based FRET for DNA Detection. *Plasmonics* **2007**. https://doi.org/10.1007/s11468-007-9036-9.

(434) Zhou, S.; Xu, H.; Gan, W.; Yuan, Q. Graphene Quantum Dots: Recent Progress in Preparation and Fluorescence Sensing Applications. *Royal Society of Chemistry Advances* **2016**. https://doi.org/10.1039/c6ra24349e.

(435) Benítez-Martínez, S.; Valcárcel, M. Graphene Quantum Dots in Analytical Science. *TrAC - Trends in Analytical Chemistry* **2015**. https://doi.org/10.1016/j.trac.2015.03.020.

(436) Zhang, Z.; Zhang, J.; Chen, N.; Qu, L. Graphene Quantum Dots: An Emerging Material for Energy-Related Applications and Beyond. *Energy and Environmental Science* **2012**. https://doi.org/10.1039/c2ee22982j.

(437) Wong, K. L.; Liu, J. Factors and Methods to Modulate DNA Hybridization Kinetics. *Biotechnology Journal* **2021**. https://doi.org/10.1002/biot.202000338.

(438) Esteban-Fernández De Ávila, B.; Lopez-Ramirez, M. A.; Báez, D. F.; Jodra, A.; Singh, V. V.; Kaufmann, K.; Wang, J. Aptamer-Modified Graphene-Based Catalytic Micromotors: Off-On Fluorescent Detection of Ricin. *American Chemical Society Sensors* **2016**. https://doi.org/10.1021/acssensors.5b00300.

(439) Shi, J.; Chan, C.; Pang, Y.; Ye, W.; Tian, F.; Lyu, J.; Zhang, Y.; Yang, M. A

Fluorescence Resonance Energy Transfer (FRET) Biosensor Based on Graphene Quantum Dots (GQDs) and Gold Nanoparticles (AuNPs) for the Detection of MecA Gene Sequence of Staphylococcus Aureus. *Biosensors and Bioelectronics* **2015**. https://doi.org/10.1016/j.bios.2014.09.059.

(440) Bharathi, G.; Lin, F.; Liu, L.; Ohulchanskyy, T. Y.; Hu, R.; Qu, J. An All-Graphene Quantum Dot Förster Resonance Energy Transfer (FRET) Probe for Ratiometric Detection of HE4 Ovarian Cancer Biomarker. *Colloids and Surfaces B: Biointerfaces* **2021**. https://doi.org/10.1016/j.colsurfb.2020.111458.

(441) Fu, S.; Zhang, X.; Xie, Y.; Wu, J.; Ju, H. An Efficient Enzyme-Powered Micromotor Device Fabricated by Cyclic Alternate Hybridization Assembly for DNA Detection. *Nanoscale* **2017**. https://doi.org/10.1039/c7nr01168g.

(442) Wu, J.; Balasubramanian, S.; Kagan, D.; Manesh, K. M.; Campuzano, S.; Wang, J. Motion-Based DNA Detection Using Catalytic Nanomotors. *Nature Communications* **2010**. https://doi.org/10.1038/ncomms1035.

(443) Zhang, X.; Chen, C.; Wu, J.; Ju, H. Bubble-Propelled Jellyfish-like Micromotors for DNA Sensing. *American Chemical Society Applied Materials & Interfaces* **2019**. https://doi.org/10.1021/acsami.9b00605.

(444) Báez, D. F.; Ramos, G.; Corvalán, A.; Cordero, M. L.; Bollo, S.; Kogan, M. J. Effects of Preparation on Catalytic, Magnetic and Hybrid Micromotors on Their Functional Features and Application in Gastric Cancer Biomarker Detection. *Sensors and Actuators, B: Chemical* **2020**. https://doi.org/10.1016/j.snb.2020.127843.

(445) Wang, Q.; Wang, Y.; Guo, B.; Shao, S.; Yu, Y.; Zhu, X.; Wan, M.; Zhao, B.; Bo, C.; Mao, C. Novel Heparin-Loaded Mesoporous Tubular Micromotors Formed via Template-Assisted Electrochemical Deposition. *Journal of Materials Chemistry B* **2019**. https://doi.org/10.1039/c9tb00131j.

(446) Wang, Y.; Mayorga-Martinez, C. C.; Moo, J. G. S.; Pumera, M. Structure-Function Dependence on Template-Based Micromotors. *American Chemical Society Applied Energy Materials* **2018**. https://doi.org/10.1021/acsaem.8b00605.

(447) Manesh, K. M.; Cardona, M.; Yuan, R.; Clark, M.; Kagan, D.; Balasubramanian, S.; Wang, J. Template-Assisted Fabrication of Salt-Independent Catalytic Tubular Microengines. *American Chemical Society Nano* **2010**. https://doi.org/10.1021/nn1000468.

(448) Zha, F.; Wang, T.; Luo, M.; Guan, J. Tubular Micro/Nanomotors: Propulsion Mechanisms, Fabrication Techniques and Applications. *Micromachines*. **2018**. https://doi.org/10.3390/mi9020078.

(449) Manjare, M.; Yang, B.; Zhao, Y. P. Bubble-Propelled Microjets: Model and Experiment. *Journal of Physical Chemistry C* **2013**. https://doi.org/10.1021/jp311977d.

(450) Pacheco, M.; López, M. Á.; Jurado-Sánchez, B.; Escarpa, A. Self-Propelled Micromachines for Analytical Sensing: A Critical Review. *Analytical and Bioanalytical Chemistry*. **2019**. https://doi.org/10.1007/s00216-019-02070-z.

(451) Liu, J.; Li, J.; Jiang, Y.; Yang, S.; Tan, W.; Yang, R. Combination of π-π Stacking and Electrostatic Repulsion between Carboxylic Carbon Nanoparticles and Fluorescent Oligonucleotides for Rapid and Sensitive Detection of Thrombin. *Chemical Communications* **2011**. https://doi.org/10.1039/c1cc14445f.

(452) Martín, A.; Jurado-Sánchez, B.; Escarpa, A.; Wang, J. Template Electrosynthesis of High-Performance Graphene Microengines. *Small* **2015**. https://doi.org/10.1002/smll.201500008.

(453) Jiang, G.; Susha, A. S.; Lutich, A. A.; Stefani, F. D.; Feldmann, J.; Rogach, A. L. Cascaded FRET in Conjugated Polymer/Quantum Dot/Dye-Labeled DNA Complexes for DNA Hybridization Detection. *American Chemical Society Nano* **2009**. https://doi.org/10.1021/nn901324y.

(454) Zhang, J.; Lang, H. P.; Yoshikawa, G.; Gerber, C. Optimization of DNA Hybridization Efficiency by PH-Driven Nanomechanical Bending. *Langmuir* **2012**. https://doi.org/10.1021/la205066h.

(455) Rashid, J. I. A.; Yusof, N. A. The Strategies of DNA Immobilization and Hybridization Detection Mechanism in the Construction of Electrochemical DNA Sensor: A Review. *Sensing and Bio-Sensing Research* **2017**, *16*, 19–31. https://doi.org/10.1016/j.sbsr.2017.09.001.

(456) Saeki, K.; Kunito, T.; Sakai, M. Effect of Tris-HCl Buffer on DNA Adsorption by a Variety of Soil Constituents. *Microbes and Environments* **2011**. https://doi.org/10.1264/jsme2.ME10172.

(457) Jeong, S.; Pinals, R. L.; Dharmadhikari, B.; Song, H.; Kalluri, A.; Debnath, D.; Wu, Q.; Ham, M. H.; Patra, P.; Landry, M. P. Graphene Quantum Dot Oxidation Governs Noncovalent Biopolymer Adsorption. *Scientific Reports* **2020**. https://doi.org/10.1038/s41598-020-63769-z.

(458) Faridbod, F.; Sanati, A. L. Graphene Quantum Dots in Electrochemical Sensors/Biosensors. *Current Analytical Chemistry* **2018**. https://doi.org/10.2174/1573411014666180319145506.

(459) Yew, Y. T.; Loo, A. H.; Sofer, Z.; Klímová, K.; Pumera, M. Coke-Derived Graphene Quantum Dots as Fluorescence Nanoquencher in DNA Detection. *Applied Materials Today* **2017**. https://doi.org/10.1016/j.apmt.2017.01.002.

(460) Magdanz, V.; Guix, M.; Schmidt, O. G. Tubular Micromotors: From Microjets to Spermbots. *Robotics and Biomimetics* **2014**. https://doi.org/10.1186/s40638-014-0011-6.

(461) Zhao, G.; Sanchez, S.; Schmidt, O. G.; Pumera, M. Poisoning of Bubble Propelled Catalytic Micromotors: The Chemical Environment Matters. *Nanoscale* **2013**. https://doi.org/10.1039/c3nr34213a.

(462) Hu, L.; Wang, N.; Tao, K. Catalytic Micro/Nanomotors: Propulsion Mechanisms, Fabrication, Control, and Applications. In *Smart Nanosystems for Biomedicine, Optoelectronics and Catalysis*; **2020**. https://doi.org/10.5772/intechopen.90456.

(463) Wu, Z.; Lin, X.; Zou, X.; Sun, J.; He, Q. Biodegradable Protein-Based Rockets for Drug Transportation and Light-Triggered Release. *American Chemical Society Applied Materials & Interfaces* **2015**. https://doi.org/10.1021/am507680u.

(464) Draz, M. S.; Kochehbyoki, K. M.; Vasan, A.; Battalapalli, D.; Sreeram, A.; Kanakasabapathy, M. K.; Kallakuri, S.; Tsibris, A.; Kuritzkes, D. R.; Shafiee, H. DNA Engineered Micromotors Powered by Metal Nanoparticles for Motion Based Cellphone Diagnostics. *Nature Communications* **2018**. https://doi.org/10.1038/s41467-018-06727-8.

(465) Kim, J. K.; Kim, S. J.; Park, M. J.; Bae, S.; Cho, S. P.; Du, Q. G.; Wang, D. H.; Park, J. H.; Hong, B. H. Surface-Engineered Graphene Quantum Dots Incorporated into Polymer Layers for High Performance Organic Photovoltaics. *Scientific Reports* **2015**. https://doi.org/10.1038/srep14276.

(466) Suryawanshi, A.; Biswal, M.; Mhamane, D.; Gokhale, R.; Patil, S.; Guin, D.; Ogale, S. Large Scale Synthesis of Graphene Quantum Dots (GQDs) from Waste Biomass and Their Use as an Efficient and Selective Photoluminescence on-off-on Probe for Ag+ Ions. *Nanoscale* **2014**. https://doi.org/10.1039/c4nr02494j.

(467) Saad, S. M.; Abdullah, J.; Rashid, S. A.; Fen, Y. W.; Salam, F.; Yih, L. H. A Fluorescence Quenching Based Gene Assay for Escherichia Coli O157:H7 Using Graphene Quantum Dots and Gold Nanoparticles. *Microchimica Acta* **2019**. https://doi.org/10.1007/s00604-019-3913-8.

(468) Abbas, A.; Tabish, T. A.; Bull, S. J.; Lim, T. M.; Phan, A. N. High Yield Synthesis of Graphene Quantum Dots from Biomass Waste as a Highly Selective Probe for Fe3+ Sensing. *Scientific Reports* **2020**. https://doi.org/10.1038/s41598-020-78070-2.

(469) Lu, L.; Guo, L.; Wang, X.; Kang, T.; Cheng, S. Complexation and Intercalation Modes: A Novel Interaction of DNA and Graphene Quantum Dots. *Royal Society of Chemistry Advances* **2016**. https://doi.org/10.1039/c6ra00930a.

(470) Maity, N.; Kuila, A.; Das, S.; Mandal, D.; Shit, A.; Nandi, A. K. Optoelectronic and Photovoltaic Properties of Graphene Quantum Dot-Polyaniline Nanostructures. *Journal of Materials Chemistry A* **2015**. https://doi.org/10.1039/c5ta06576c.

(471) Zhang, Y.; Zheng, B.; Zhu, C.; Zhang, X.; Tan, C.; Li, H.; Chen, B.; Yang, J.; Chen, J.; Huang, Y.; Wang, L.; Zhang, H. Single-Layer Transition Metal Dichalcogenide Nanosheet-Based Nanosensors for Rapid, Sensitive, and Multiplexed Detection of DNA. *Advanced Materials* **2015**. https://doi.org/10.1002/adma.201404568.

(472) Lu, C.; Huang, P. J. J.; Liu, B.; Ying, Y.; Liu, J. Comparison of Graphene Oxide and Reduced Graphene Oxide for DNA Adsorption and Sensing. *Langmuir* **2016**. https://doi.org/10.1021/acs.langmuir.6b03032.

(473) Wu, M.; Kempaiah, R.; Huang, P. J. J.; Maheshwari, V.; Liu, J. Adsorption and Desorption of DNA on Graphene Oxide Studied by Fluorescently Labeled Oligonucleotides. *Langmuir* **2011**. https://doi.org/10.1021/la1037926.

(474) Liu, B.; Salgado, S.; Maheshwari, V.; Liu, J. DNA Adsorbed on Graphene and Graphene Oxide: Fundamental Interactions, Desorption and Applications. *Current Opinion in*

Colloid and Interface Science **2016**. https://doi.org/10.1016/j.cocis.2016.09.001.

(475) Qin, F.; Wu, J.; Fu, D.; Feng, Y.; Gao, C.; Xie, D.; Fu, S.; Liu, S.; Wilson, D. A.; Peng, F. Magnetically Driven Helical Hydrogel Micromotor for Tumor DNA Detection. *Applied Materials Today* **2022**. https://doi.org/10.1016/j.apmt.2022.101456.

(476) Pashazadeh, P.; Mokhtarzadeh, A.; Hasanzadeh, M.; Hejazi, M.; Hashemi, M.; de la Guardia, M. Nano-Materials for Use in Sensing of Salmonella Infections: Recent Advances. *Biosensors and Bioelectronics* **2017**. https://doi.org/10.1016/j.bios.2016.08.012.

(477) Stephen Inbaraj, B.; Chen, B. H. Nanomaterial-Based Sensors for Detection of Foodborne Bacterial Pathogens and Toxins as Well as Pork Adulteration in Meat Products. *Journal of Food and Drug Analysis* **2016**. https://doi.org/10.1016/j.jfda.2015.05.001.

(478) Guo, J.; Chan, E. W. C.; Chen, S.; Zeng, Z. Development of a Novel Quantum Dots and Graphene Oxide Based Fret Assay for Rapid Detection of Inva Gene of Salmonella. *Frontiers in Microbiology* **2017**. https://doi.org/10.3389/fmicb.2017.00008.

(479) Country Outbreak of Salmonella Typhimurium Linked to Chocolate Products – Europe and the United States of America. **2022**. https://www.who.int/emergencies/disease-outbreak-news/item/2022-DON369

(480) Johnson, R.; Mylona, E.; Frankel, G. Typhoidal Salmonella: Distinctive Virulence Factors and Pathogenesis. *Cellular Microbiology* **2018**. https://doi.org/10.1111/cmi.12939.

(481) Commission Regulation EC No 2160/2003 of 17 November 2003 on the Control of Salmonella and Other Specified Food-Borne Zoonotic Agents. *Regulation*. **2003**. https://eur-lex.europa.eu/legal-content/EN/TXT/PDF/?uri=CELEX:02003R2160-20130701&from=EN

(482) Commission Regulation (EC) No 2073/2005 of 15 November 2005 on Microbiological Criteria for Foodstuffs. *Official Journal of the European Union* **2005**. https://eur-lex.europa.eu/legal-content/EN/TXT/PDF/?uri=CELEX:02005R2073-20140601&rid=1

(483) Kumar, R.; Surendran, P. K.; Thampuran, N. Evaluation of Culture, ELISA and PCR Assays for the Detection of Salmonella in Seafood. *Letters in Applied Microbiology* **2008**. https://doi.org/10.1111/j.1472-765X.2007.02286.x.

(484) Kasturi, K. N.; Drgon, T. Real-Time PCR Method for Detection of Salmonella Spp. in Environmental Samples. *Applied and Environmental Microbiology* **2017**. https://doi.org/10.1128/AEM.00644-17.

(485) Croci, L.; Delibato, E.; Volpe, G.; De Medici, D.; Palleschi, G. Comparison of PCR, Electrochemical Enzyme-Linked Immunosorbent Assays, and the Standard Culture Method for Detecting Salmonella in Meat Products. *Applied and Environmental Microbiology* **2004**. https://doi.org/10.1128/AEM.70.3.1393-1396.2004.

(486) Brigmon, R. L.; Zam, S. G.; Wilson, H. R. Detection of Salmonella Enteritidis in Eggs

and Chicken with Enzyme-Linked Immunosorbent Assay. *Poultry science* **1995**. https://doi.org/10.3382/ps.0741232.

(487) Saikia, K.; Deb, P.; Kalita, E. Sensitive Fluorescence Response of ZnSe(S) Quantum Dots: An Efficient Fluorescence Probe. *Physica Scripta* **2013**. https://doi.org/10.1088/0031-8949/87/06/065802.

(488) Jana, D.; Matti, C.; He, J.; Sagle, L. Capping Agent-Free Gold Nanostars Show Greatly Increased Versatility and Sensitivity for Biosensing. *Analytical Chemistry* **2015**. https://doi.org/10.1021/acs.analchem.5b00014.

(489) Unser, S.; Bruzas, I.; He, J.; Sagle, L. Localized Surface Plasmon Resonance Biosensing: Current Challenges and Approaches. *Sensors (Switzerland)*. **2015**. https://doi.org/10.3390/s150715684.

(490) Zheng, X. T.; Ananthanarayanan, A.; Luo, K. Q.; Chen, P. Glowing Graphene Quantum Dots and Carbon Dots: Properties, Syntheses, and Biological Applications. *Small* **2015**. https://doi.org/10.1002/smll.201402648.

(491) Alocilja, E. C.; Radke, S. M. Market Analysis of Biosensors for Food Safety. In *Biosensors and Bioelectronics* **2003**. https://doi.org/10.1016/S0956-5663(03)00009-5.

(492) Liu, G.; Mao, X.; Phillips, J. A.; Xu, H.; Tan, W.; Zeng, L. Aptamer-Nanoparticle Strip Biosensor for Sensitive Detection of Cancer Cells. *Analytical Chemistry* **2009**. https://doi.org/10.1021/ac901889s.

(493) Chen, H.; Wang, Z.; Zong, S.; Chen, P.; Zhu, D.; Wu, L.; Cui, Y. A Graphene Quantum Dot-Based FRET System for Nuclear-Targeted and Real-Time Monitoring of Drug Delivery. *Nanoscale* **2015**. https://doi.org/10.1039/c5nr03454j.

(494) Agarwal, K.; Rai, H.; Mondal, S. Quantum Dots: An Overview of Synthesis, Properties, and Applications. *Materials Research Express* **2023**. https://doi.org/10.1088/2053-1591/acda17.

(495) Chen, Y.; Cao, Y.; Ma, C.; Zhu, J. J. Carbon-Based Dots for Electrochemiluminescence Sensing. *Materials Chemistry Frontiers* **2020**. https://doi.org/10.1039/c9qm00572b.

(496) Li, Z.; Bai, L.; Zhou, C.; Yan, X.; Mair, L.; Zhang, A.; Zhang, L.; Wang, W. Highly Acid-Resistant, Magnetically Steerable Acoustic Micromotors Prepared by Coating Gold Microrods with Fe3O4 Nanoparticles via PH Adjustment. *Particle and Particle Systems Characterization* **2017**. https://doi.org/10.1002/ppsc.201600277.

(497) Morales-Narváez, E.; Guix, M.; Medina-Sánchez, M.; Mayorga-Martinez, C. C.; Merkoçi, A. Micromotor Enhanced Microarray Technology for Protein Detection. *Small* **2014**. https://doi.org/10.1002/smll.201303068.

(498) Beltrán-Gastélum, M.; Esteban-Fernández de Ávila, B.; Gong, H.; Venugopalan, P. L.; Hianik, T.; Wang, J.; Subjakova, V. Rapid Detection of AIB1 in Breast Cancer Cells Based on Aptamer-Functionalized Nanomotors. *ChemPhysChem* **2019**. https://doi.org/10.1002/cphc.201900844.

(499) Pacheco, M.; Jurado-Sánchez, B.; Escarpa, A. Sensitive Monitoring of Enterobacterial

Contamination of Food Using Self-Propelled Janus Microsensors. *Analytical Chemistry* **2018**. https://doi.org/10.1021/acs.analchem.7b05209.

(500) Pacheco, M.; Jurado-Sánchez, B.; Escarpa, A. Transition Metal Dichalcogenide-Based Janus Micromotors for on-the-Fly Salmonella Detection. *Microchimica Acta* **2022**. https://doi.org/10.1007/s00604-022-05298-2.

(501) Pacheco, M.; Asunción-Nadal, V. de la; Jurado-Sánchez, B.; Escarpa, A. Engineering Janus Micromotors with WS2 and Affinity Peptides for Turn-on Fluorescent Sensing of Bacterial Lipopolysaccharides. *Biosensors and Bioelectronics* **2020**. https://doi.org/10.1016/j.bios.2020.112286.

(502) Jyoti, Jose Muñoz, and M. P. Quantum Material-Based Self-Propelled Microrobots for the Optical "On-the-Fly" Monitoring of DNA. *American Chemical Society Applied Material and Interfaces* **2023**. https://doi.org/10.1021/acsami.3c09920.

(503) Dong, Y.; Shao, J.; Chen, C.; Li, H.; Wang, R.; Chi, Y.; Lin, X.; Chen, G. Blue Luminescent Graphene Quantum Dots and Graphene Oxide Prepared by Tuning the Carbonization Degree of Citric Acid. *Carbon* **2012**. https://doi.org/10.1016/j.carbon.2012.06.002.

(504) Mansuriya, B. D.; Altintas, Z. Applications of Graphene Quantum Dots in Biomedical Sensors. *Sensors (Switzerland)* **2020**. https://doi.org/10.3390/s20041072.

(505) Kumar, Y. R.; Deshmukh, K.; Sadasivuni, K. K.; Pasha, S. K. K. Graphene Quantum Dot Based Materials for Sensing, Bio-Imaging and Energy Storage Applications: A Review. *Royal Society of Chemistry Advances* **2020**. https://doi.org/10.1039/d0ra03938a.

(506) Chattopadhyay, S.; Choudhary, M.; Singh, H. Carbon Dots and Graphene Oxide Based FRET Immunosensor for Sensitive Detection of Helicobacter Pylori. *Analytical Biochemistry* **2022**. https://doi.org/10.1016/j.ab.2022.114801.

(507) Mujtaba, J.; Liu, J.; Dey, K. K.; Li, T.; Chakraborty, R.; Xu, K.; Makarov, D.; Barmin, R. A.; Gorin, D. A.; Tolstoy, V. P.; Huang, G.; Solovev, A. A.; Mei, Y. Micro-Bio-Chemo-Mechanical-Systems: Micromotors, Microfluidics, and Nanozymes for Biomedical Applications. *Advanced Materials* **2021**. https://doi.org/10.1002/adma.202007465.

(508) Jurado-Sánchez, B. Microscale and Nanoscale Biosensors. *Biosensors* **2018**. https://doi.org/10.3390/bios8030066.

(509) Simmchen, J.; Magdanz, V.; Sanchez, S.; Chokmaviroj, S.; Ruiz-Molina, D.; Baeza, A.; Schmidt, O. G. Effect of Surfactants on the Performance of Tubular and Spherical Micromotors-a Comparative Study. *Royal Society of Chemistry Advances* **2014**. https://doi.org/10.1039/c4ra02202e.

(510) Wang, H.; Zhao, G.; Pumera, M. Crucial Role of Surfactants in Bubble-Propelled Microengines. *Journal of Physical Chemistry C* **2014**. https://doi.org/10.1021/jp410003e.

(511) Kreissl, P.; Holm, C.; De Graaf, J. The Efficiency of Self-Phoretic Propulsion

Mechanisms with Surface Reaction Heterogeneity. *Journal of Chemical Physics* **2016**. https://doi.org/10.1063/1.4951699.

(512) Naeem, S.; Naeem, F.; Zhang, J.; Mujtaba, J.; Xu, K.; Huang, G.; Solovev, A. A.; Mei, Y. Parameters Optimization of Catalytic Tubular Nanomembrane-Based Oxygen Microbubble Generator. *Micromachines* **2020**. https://doi.org/10.3390/MI11070643.

(513) Cao, F.; Li, Y.; Wu, J.; Liu, W.; Ngai, T. Measurements of Interactions between Fluorescent Molecules and Polyethylene Glycol Self-Assembled Monolayers. *Soft Matter* **2022**. https://doi.org/10.1039/d1sm01329g.

(514) Choi, D.; Tsang, R. S. W.; Ng, M. H. Sandwich Capture ELISA by a Murine Monoclonal Antibody against a Genus-specific LPS Epitope for the Detection of Different Common Serotypes of Salmonellas. *Journal of Applied Bacteriology* **1992**. https://doi.org/10.1111/j.1365-2672.1992.tb01814.x.

(515) Sannigrahi, S.; Arumugasamy, S. K.; Mathiyarasu, J.; K, S. Magnetosome-Anti-Salmonella Antibody Complex Based Biosensor for the Detection of Salmonella Typhimurium. *Materials Science and Engineering C* **2020**. https://doi.org/10.1016/j.msec.2020.111071.

(516) Wang, X.; Zhu, P.; Pi, F.; Jiang, H.; Shao, J.; Zhang, Y.; Sun, X. A Sensitive and Simple Macrophage-Based Electrochemical Biosensor for Evaluating Lipopolysaccharide Cytotoxicity of Pathogenic Bacteria. *Biosensors and Bioelectronics* **2016**. https://doi.org/10.1016/j.bios.2016.03.007.

(517) Wu, S.; Hulme, J. P. Recent Advances in the Detection of Antibiotic and Multi-Drug Resistant Salmonella: An Update. *International Journal of Molecular Sciences* **2021**. https://doi.org/10.3390/ijms22073499.

(518) Wang, M.; Zhang, Y.; Tian, F.; Liu, X.; Du, S.; Ren, G. Overview of Rapid Detection Methods for Salmonella in Foods: Progress and Challenges. *Foods* **2021**. https://doi.org/10.3390/foods10102402.

(519) Lee, K. M.; Runyon, M.; Herrman, T. J.; Phillips, R.; Hsieh, J. Review of Salmonella Detection and Identification Methods: Aspects of Rapid Emergency Response and Food Safety. *Food Control* **2015**. https://doi.org/10.1016/j.foodcont.2014.07.011.

(520) Shen, Y.; Xu, L.; Li, Y. Biosensors for Rapid Detection of Salmonella in Food: A Review. *Comprehensive Reviews in Food Science and Food Safety* **2021**. https://doi.org/10.1111/1541-4337.12662.

(521) Du, J. Biosensor Detection Methods for Salmonella: A Review. *Advances in Engineering Technology Research* **2023**. https://doi.org/10.56028/aetr.6.1.337.2023.

(522) Asunción-Nadal, V. de la; Maria-Hormigos, R.; Jurado-Sánchez, B.; Escarpa, A. Optical Motion Control of Catalytic WS2 and MoS2 Micromotors. *Applied Materials Today* **2022**. https://doi.org/10.1016/j.apmt.2022.101664.

(523) Presutti, D.; Agarwal, T.; Zarepour, A.; Celikkin, N.; Hooshmand, S.; Nayak, C.; Ghomi, M.; Zarrabi, A.; Costantini, M.; Behera, B.; Maiti, T. K. Transition Metal Dichalcogenides (TMDC)-Based Nanozymes for Biosensing and Therapeutic

Applications. *Materials* **2022**. https://doi.org/10.3390/ma15010337.

Chapter 8

Appendix

Al_2O_3/Covalent Organic Framework on 3D-Printed Nanocarbon Electrodes for Enhanced Biomarker Detection

Published: ACS Appl. Nano Mater. 2022, 5, 9719−9727